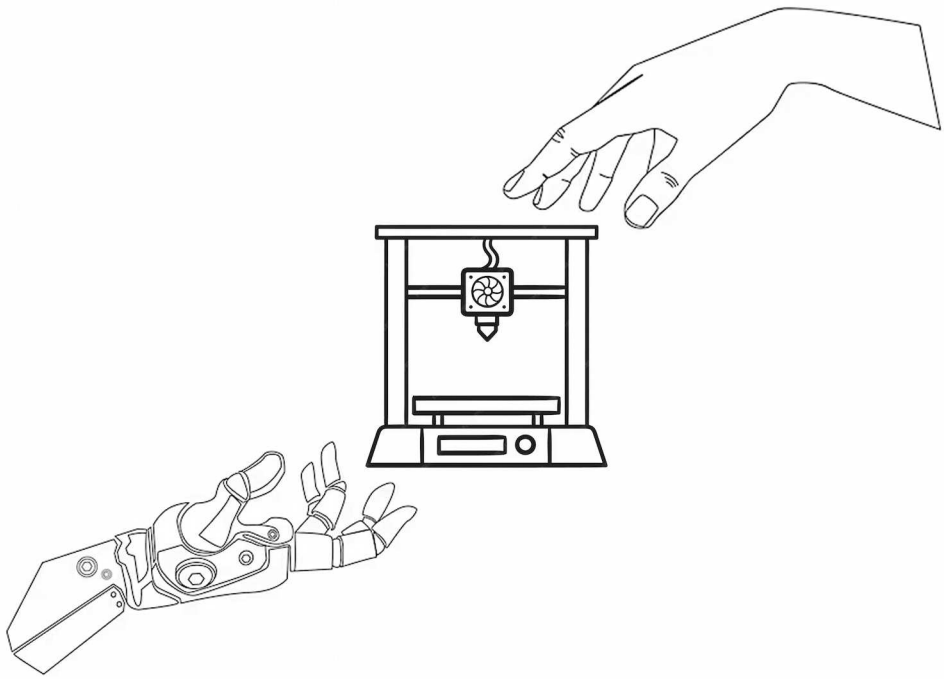
Valentina Venditoli



Artificial Intelligence-based Optimization and Material Ageing Studies to improve geometrical and mechanical performances of parts manufactured through Additive Manufacturing processes

UNIVERSITÀ DEGLI STUDI DI CASSINO E DEL LAZIO MERIDIONALE
CORSO DI DOTTORATO IN METODI, MODELLI E TECNOLOGIE PER L'INGEGNERIA
DIPARTIMENTO DI INGEGNERIA CIVILE E MECCANICA

Artificial Intelligence-based Optimization and Material Ageing Studies to improve geometrical and mechanical performances of parts manufactured through Additive Manufacturing processes

Valentina Venditttoli
valentina.venditttoli1@unicas.it

In Partial Fulfillment of the Requirements for the Degree of
PHILOSOPHIAE DOCTOR in
Civil and Mechanical Engineering

18/12/2024

TUTOR
Prof. Wilma Polini
Prof. Luca Sorrentino
Prof. Michael S.J. Walter

COORDINATOR
Prof. Fabrizio Marignetti

XXXVII Cycle

UNIVERSITÀ DEGLI STUDI DI CASSINO E DEL LAZIO MERIDIONALE

CORSO DI DOTTORATO IN METODI, MODELLI E TECNOLOGIE PER L'INGEGNERIA

Date: 18/12/2024

Author: **Valentina Venditoli**

Title: **Artificial Intelligence-based Optimization and Material Ageing Studies to improve geometrical and mechanical performances of parts manufactured through Additive Manufacturing processes**

Department: **DIPARTIMENTO DI INGEGNERIA CIVILE E MECCANICA**

Degree: **PHILOSOPHIAE DOCTOR**

Permission is herewith granted to university to circulate and to have copied for non-commercial purposes, at its discretion, the above title upon the request of individuals or institutions.

Valentina Venditoli

Signature of Author

THE AUTHOR RESERVES OTHER PUBLICATION RIGHTS, AND NEITHER THE THESIS NOR EXTENSIVE EXTRACTS FROM IT MAY BE PRINTED OR OTHERWISE REPRODUCED WITHOUT THE AUTHOR'S WRITTEN PERMISSION.
THE AUTHOR ATTESTS THAT PERMISSION HAS BEEN OBTAINED FOR THE USE OF ANY COPYRIGHTED MATERIAL APPEARING IN THIS THESIS (OTHER THAN BRIEF EXCERPTS REQUIRING ONLY PROPER ACKNOWLEDGEMENT IN SCHOLARLY WRITING) AND THAT ALL SUCH USE IS CLEARLY ACKNOWLEDGED.

"It's funny how you wake up each day and never really know if it will be one that will change your life forever."

— The Secret World of Arrietty

Abstract

Additive Manufacturing has emerged as a transformative technology to produce complex geometries and customized parts across a range of sectors. Nevertheless, considerable obstacles remain in optimizing the mechanical properties and dimensional precision of manufactured parts, as well as addressing concerns regarding the sustainability of the materials used. This thesis investigates the integration of Artificial Intelligence techniques and Multi-Objective Optimization methods to enhance the performance of AM processes.

In the Fused Filament Fabrication process, artificial intelligence-driven models were employed to optimize the performance indices. This approach permitted the concurrent enhancement of mechanical strength and dimensional precision in Polylactic Acid components, thereby facilitating multi-objective optimization for industries necessitating high-precision manufacturing. This approach markedly diminishes the necessity for trial-and-error procedures and augments the predictability of AM outcomes.

While in Selective Laser Sintering, this thesis develops predictive models for mechanical properties derived from degraded Polyamide 12 powder. The present study investigates the effects of repeated thermal cycling on mechanical properties and crystallinity. The relationship between the degree of crystallinity and the ultimate tensile strength of the parts was established, thereby offering a practical method for predicting mechanical strength and determining the optimal reuse of aged powder, with the dual objective of ensuring both sustainability and part integrity.

The research was conducted along three primary avenues: (i) the creation of performance indices that unify mechanical and dimensional properties into a single optimization value; (ii) AI-driven optimization of these indices in Fused Filament

Fabrication, improving both mechanical and dimensional properties; and (iii) predictive modeling of mechanical properties from degraded Polyamide 12 powder in Selective Laser Sintering, enabling sustainable material reuse.
The results illustrate that AI-driven optimization techniques yield enhanced precision in mechanical performance predictions, while the proposed recycling strategies for PA12 contribute to more sustainable AM practices. The findings provide substantial insights into the application of AI for both industrial manufacturing optimization and environmental sustainability in AM processes.

Keywords: Additive Manufacturing; Artificial Intelligence; Performance Index; Multi-Objective Optimization; Sustainable Manufacturing.

Table of contents

Abstract vii

Table of contents i

List of Abbreviations iii

General Introduction 19

Chapter 2 An overall performance index to quantify dimensional accuracy and mechanical strength of parts manufactured through VAT photopolymerization in biodegradable and non-biodegradable resin 41

Chapter 3 From MSLA to FDM: Process Control and Performance Indices in AM 63

Chapter 4 Geometrical Deviations of green Parts due to Additive Manufacturing: a Synthetic Geometrical Performance Index 67

Chapter 5 Two Performance Indices of Parts in Polylactic Acid Manufactured Through a Material Extrusion Process: Analysis of Their Dependence on Process Parameters 83

Chapter 6 Introducing Artificial Neural Networks to predict the dimensional and micro-geometrical Deviations of additively manufactured Parts 103

Chapter 7 Using Bayesian regularized Artificial Neural Networks to predict the Tensile Strength of additive manufactured Polylactic Acid Parts 117

Chapter 8 Artificial Intelligence Tool to Optimize Geometrical and Mechanical Performances of Parts Manufactured Through Additive Manufacturing Processes 137

Chapter 9 Multi-Response Optimization of the dimensional and mechanical Properties of 3D-printed Polylactide Acid part by Response Surface Methodology 159

Chapter 10 From FDM to SLS: Enhancing Material and Process Efficiency in AM 191

Chapter 11 Overview of Structural, Mechanical and Geometrical Characteristics of Parts in Polyamide 12 Manufactured with Laser Powder Bed Fusion: Outcome and Future Development 197

Chapter 12 A Novel Approach on Artificial Aging of Nylon 12 Powder for Laser Powder Bed Fusion 225

Chapter 13 Predictive Modeling of Mechanical Properties from Degraded Polyamide 12 Powder in Laser Powder Bed Fusion 245

Summary and Conclusion 265

References 271

Appendix 307

List of publications 317

About the author 319

List of figures

Figure 1.1 (a) Schematic of the MSLA process; (b) Representation of the manufactured part. 22

Figure 1.2 Schematic of the FDM process. Reprinted with permission from Ref. [28]. 25

Figure 1.3 Schematic of the SLS process. Courtesy of Materialgeeza, SLS, Wikipedia from Ref. [48]. 29

Figure 1.4 Taxonomy of ML applications in the AM domain. X_1; X_2; … X_n represent the input vector, and Y represents the output. Adapted with permission from Ref. [75]. 35

Figure 1.5 Outline of the thesis. 38

Figure 2.1 Benchmark design, all dimensions in mm [106]. 46

Figure 2.2 (a) Tensile specimen according to ASTM-D 638-99, all dimensions in mm [109]; (b) Flexural specimen according to ASTM-D 790-03, all dimensions in mm [110]. 47

Figure 2.3 (a) Benchmark; (b) Tensile specimens; (c) Flexural specimens 48

Figure 2.4 (a) Measurement system overview; (b) Image capture process. 50

Figure 2.5 (a) Specimen position; (b) End of the test. 51

Figure 2.6 Tensile specimens before and after the test: (a, c) Prusa resin; (b, d) Anycubic resin (specimens with delamination are highlighted in red). 52

Figure 2.7 (a) Specimen position; (b) Crosshead motion. 53

Figure 2.8 Flexural specimens before and after the test: (a, c) Anycubic resin; (b, d) Prusa resin (specimens with delamination are highlighted in red). 54

Figure 2.9 Tensile stress-strain curve. The maximum stress is highlighted on the curves. 57

Figure 2.10 Flexural stress-strain curve. The maximum stress is highlighted on the curves. 58

Figure 4.1 Considered benchmark. 72

Figure 4.2 (a) Ultimaker S3 machine; (b) Printing of the parts. 72

Figure 4.3 Image capture process. 75

Figure 4.4 Reference points on part's surfaces: (a) top; (b) bottom; (c) curved; (d) lateral. 75

Figure 4.5 Construct process on GOM Inspect. 76

Figure 5.1 Benchmark's technical drawing, dimension in mm. 88

Figure 5.2 (a) Ultimaker S3 printer, and (b) Printed specimens. 88

Figure 5.3 Box-plot representation of the distribution of DPI categorized by the Taguchi's run. 91

Figure 5.4 Box-plot representation of the distribution of PI categorized by the Taguchi's run. 92

Figure 5.5 The effects of input parameters on the DPI. 94

Figure 5.6 Normal probability plot for the residual (based on regression model 1). 95

Figure 5.7 The effects of input parameters on the PI. 98

Figure 5.8 Normal probability plot for the residual (based on regression model 2). 100

Figure 6.1 (a) Benchmark design (all dimensions in mm); (b) Printed specimens. 108

Figure 6.2 Artificial Neural Network architecture. 110

Figure 7.1 Tensile test specimen (all dimensions in mm). 124

Figure 7.2 (a) Setup of the tensile test machine right before starting the test procedure; (b) Tensile specimens after the test. 126

Figure 7.3 Artificial Neural Network Architecture. 128

Figure 7.4 (a) A BR learning rate curves and (b) the learning curves for the non-regularized trained model. 130

Figure 8.1 Methodology and structure of the paper. 144

Figure 8.2 (a) Benchmark design; (b) Finished specimens inside the chamber. 146

Figure 8.3 Artificial Neural Network Architecture. 149

Figure 8.4 (a) Validation test specimen position before testing; (b) DPI specimens; (c) PI specimens. 151

Figure 9.1 Nominal dimensions of the specimen (according to the ASTM D638-22 standard). 166

Figure 9.2 Main effect plots showcasing the influence of input parameters on internal feature dimensions (diameter, square length, and square width). The axes represent parameter levels and their corresponding effects. 170

Figure 9.3 Main effect plots depicting the influence of input parameters on external dimensions: length, width, thickness, and neck dimensions. The axes represent parameter levels and their corresponding effects 174

Figure 9.4 The effects of input parameters on the UTS. The axes represent parameter levels and their corresponding effects. 180

Figure 9.5 Composite desirability plot illustrating optimal parameter combinations for maximizing dimensional accuracy and mechanical strength. The axes display input parameter ranges, while the gradient indicates desirability. 185

Figure 9.6 (a) Specimens from the validation print before and (b) after the tensile test. 186

Figure 11.1 (a) Tensile specimen according to ASTM-D 638-22, all dimensions in mm [109]; (b) Printing preview during the AM pre-processing. 202

Figure 11.2 XRD patterns of virgin and 5-times used powders. 206

Figure 11.3 XRD patterns of virgin and 5-times used powder and of the corresponding sintered parts. 206

Figure 11.4 XRD patterns of the two opposite sides of sample obtained by sintering the 5-times used powder. 207

Figure 11.5 DSC curves of virgin powder. ((1) Melting temperature peak; (2) Crystallization temperature peak; (3) Sintering window (Tm-onset- Tc-onset); (4) Tm-endset; (5) Tc-endset.) 207

Figure 11.6 SEM Micrographs of virgin (a, c) and 5-time used (b, d) powders. 210

Figure 11.7 Particle Size Distribution of virgin powder. 210

Figure 11.8 SEM Micrographs of top (a, b, c) and bottom (d, e, f) surfaces of the SLS part obtained using virgin powder. 212

Figure 11.9 SEM micrographs of the opposite sides (a, c, e) and (b, d, f) of the specimen obtained using SLS of 5-times used powder. 213

Figure 11.10 Internal cross-sectional SEM micrographs of the sintered parts obtained using virgin (a, c, e and g) or 5 times used (b, d, f and h) powder. 214

Figure 11.11 Roughness results. 216

Figure 11.12 (a) Definition of the measurement sequence (blue numbers), and (b) their position on the specimen. 216

Figure 11.13 Dimensional results for (a) square pocket and (b) round hole of the tensile specimens at each reusing cycle. 217

Figure 11.14 Dimensional results for (a) width and (b) neck of the tensile specimens at each reusing cycle. 218

Figure 11.15 Dimensional results of the positions with respect to the specimen for (a) square pocket and (b) circle hole at each reusing cycle. 219

Figure 12.1 SLS printer's main components: (a) photograph showing the position of the overflow bin; (b) photograph showing the positions of the feed chamber, print chamber, and recoater direction. Figure by authors. 231

Figure 12.2 Schematic temperature-time-curve of the SLS phases: (1) warming phase; (2) printing phase; (3) cooling phase. Figure by authors. 232

Figure 12.3 Flowchart of the proposed novel method ("n" is the number of processing cycles). Figure by authors. 234

Figure 12.4 Temperature trend to which the powder inside (a) feed and bin chambers; (b) print chamber was submitted. Figure by authors. 236

Figure 12.5 Volume particle size distribution (a) difference between 2-times powder from a real printing cycle and artificially aged; (b) difference between 5-times powder from a real printing cycle and artificially aged (the circles correspond to the part where the curves differ as visible in Table 8.3). Figure by authors. 239

Figure 12.6 Microscopic analyses of artificially aged powder with respect to virgin powder. (a) virgin powder; (b, c, d, e, f) successive building cycles. Figure by authors. 241

Figure 12.7 Melting enthalpy behavior. Figure by authors. 242

Figure 12.8 Degree of crystallinity variation between methods. Figure by authors. 243

Figure 13.1 (a) Tensile specimen according to ASTM-D 638-99, all dimensions in mm [109]; (b) Printing preview (screenshot from the pre-processing software Sinterit Studio). 252

Figure 13.2 (a) Powder sample after sieving and printing specimens after each printing process; (b) Sinterit Powder sieve. 253

Figure 13.3 (a) Specimens positioning; (b) Tensile specimens after the test. 254

Figure 13.4 Normal probability plot for the residual (based on regression model 1). 260

Figure 13.5 The effects of powder reuse on the final part's UTS. 260

Figure 13.6 Normal probability plot for the residual (based on regression model 2). 261

Figure 13.7 The effects of powder reuse on the degree of crystallinity of the powder. 262

List of tables

Table 2.1 Biodegradable resin properties. 47

Table 2.2 Non-biodegradable resin mechanical properties. 48

Table 2.3 Values of used printing parameters. 49

Table 2.4 ATOS Core 200® Technical data. 50

Table 2.5 Biodegradable resin and non-biodegradable resin dimensional results. 55

Table 2.6 ANOVA results of UTS and maximum strain value from tensile tests (DF = Degree of Freedom; Seq SS = Sequential sums of squares; Adj SS = Adjusted sums of squares; Adj MS = Adjusted mean squares). 57

Table 2.7 Biodegradable resin and non-biodegradable resin mechanical results. 57

Table 2.8 ANOVA results on UFS and maximum strain value from flexural tests (DF = Degree of Freedom; Seq SS = Sequential sums of squares; Adj SS = Adjusted sums of squares; Adj MS = Adjusted mean squares). 58

Table 2.9 Dimensional Performance Index (DPI). (Smaller is better). 59

Table 2.10 ANOVA results on DPI values (DF = Degree of Freedom; Seq SS = Sequential sums of squares; Adj SS = Adjusted sums of squares; Adj MS = Adjusted mean squares). 59

Table 2.11 Complex index of each benchmark per mechanical strengths (bigger is better). 60

Table 2.12 Complex index for both resins. It was taken into consideration separately the mechanical strengths (bigger is better). 60

Table 4.1 Values of printing parameters. 74

Table 4.2 Technical data of ATOS Core 200®. 75

Table 4.3 Dimensional results. 77

Table 4.4 Geometrical results. 78

Table 4.5 Synthetic Geometrical Performance Index (SGPI) (a smaller SGPI corresponds to a higher geometrical accuracy). 80

Table 4.6 SGPI for each part. 81

Table 5.1 Fractional Taguchi L16 combinations. 89

Table 5.2 ANOVA results of DPI values (DF = Degree of Freedom; Seq SS = Sequential sums of squares; Adj SS = Adjusted sums of squares; Adj MS = Adjusted mean squares). 93

Table 5.3 ANOVA of interactions between process parameters for DPI values (DF = Degree of Freedom; Seq SS = Sequential sums of squares; Adj SS = Adjusted sums of squares; Adj MS = Adjusted mean squares). 96

Table 5.4 ANOVA results of PI values (DF = Degree of Freedom; Seq SS = Sequential sums of squares; Adj SS = Adjusted sums of squares; Adj MS = Adjusted mean squares). 98

Table 5.5 ANOVA of interactions between process parameters for PI values (DF = Degree of Freedom; Seq SS = Sequential sums of squares; Adj SS = Adjusted sums of squares; Adj MS = Adjusted mean squares). 101

Table 6.1 3D printing parameters for the fractional-factorial Design of Experiments. 107

Table 6.2 Database output variation from nominal. 111

Table 6.3 ANN performance. 112

Table 6.4 Combination for ANN testing. Experimental data (Internal and external feature dimensions are in mm, micro-geometry is in μm). 114

Table 6.5 Percentage variation of each predicted output from the experimental value (all dimensions in %). 115

Table 7.1 3D printing parameters and levels from a fractional-factorial DOE. 124

Table 7.2 L16 DOE. 125

Table 7.3 Experimental data. 131

Table 7.4 ANN performance. 131

Table 7.5 Input-Hidden-Output Connection Weights. 132

Table 7.6 Connection Weight Approach. 133

Table 7.7 Additional combination for ANN test. 134

Table 7.8 Test performance. 134

Table 7.9 Experimental and predicted data from the test. Percentage variation of each predicted output from the experimental value. 134

Table 8.1 Taguchi fractional DOE L16. 148

Table 8.2 Evaluation of the ANN prediction quality. (R^2 = 100 %: highest prediction quality, R^2 = 0 %: lowest prediction quality; MSE, MAE=0: highest prediction quality and MSE, MAE=1: lowest prediction quality). 152

Table 8.3 Evaluation of the ANN prediction quality by COP (COP = 100 %: highest prediction quality, COP = 0 %: lowest prediction quality). 152

Table 8.4 Additional combination for ANN test. 153

Table 8.5 Evaluation of the ANN test prediction quality. (R^2 = 100 %: highest prediction quality, R^2 = 0 %: lowest prediction quality; MSE, MAE=0: highest prediction quality and MSE, MAE=1: lowest prediction quality). 153

Table 8.6 Percentage variations from experimental data (all values in %). 154

Table 8.7 Optimal process parameters from the pattern search algorithm. 154

Table 8.8 Pattern search optimized output (all dimensions in mm; UTS in MPa). 155

Table 8.9 Validation results from the indices optimization with average (μ) and standard deviation (σ) of all validation printed parts (all dimensions in mm; UTS in MPa). 156

Table 8.10 Percentage variation of the experimental data from the numerical model predictions (all values in %). 156

Table 9.1 Parameter combinations for the Taguchi L16 design used in the study. 167

Table 9.2 ANOVA results of the circle's diameter (DF = Degree of Freedom; Seq SS = Sequential sums of squares; Adj SS = Adjusted sums of squares; Adj MS = Adjusted mean squares). 171

Table 9.3 ANOVA results of the square length. 172

Table 9.4 ANOVA results of the square width. 173

Table 9.5 ANOVA results of the length. 176

Table 9.6 ANOVA results of the width. 177

Table 9.7 ANOVA results of the neck. 178

Table 9.8 ANOVA results of the thickness. 179

Table 9.9 ANOVA results of the UTS. 181

Table 9.10 Consolidated Summary of ANOVA Results for dimensional accuracy of internal and external features, and mechanical performance. 182

Table 9.11 RSM predictive regression models and corresponding R^2(adj). 184

Table 9.12 RSM-optimized response parameters. 186

Table 9.13 Model validation of predicted process conditions. Values of experimental tests (X1, X2 and X3) and prediction results at the optimal conditions (all dimensions in mm; UTS in MPa). 187

Table 11.1 Sinterit PA12 properties [268]. 201

Table 11.2 Sinterit LISA technical specification. 202

Table 11.3 DSC results. 209

Table 11.4 Density and porosity of PA12 powders. 211

Table 11.5 ANOVA results on UFS and maximum strain value from flexural tests (DF = Degree of Freedom; Adj SS = Adjusted sums of squares; Adj MS = Adjusted mean squares). 220

Table 11.6 Tensile properties of samples printed horizontally for different printing cycles. 221

Table 11.7 ANOVA results on UFS and maximum strain value from flexural tests (DF = Degree of Freedom; Adj SS = Adjusted sums of squares; Adj MS = Adjusted mean squares). 222

Table 12.1 Printing process parameters. Table by authors. 235

Table 12.2 Particle size distribution percentiles of the powder at different stages of reuse (virgin = 0, 2 times and 5 times reused, 2 times and 5 times artificially aged). Table by authors. 238

Table 12.3 Volume particle size distribution of the powder at different reuse stages (virgin = 0, 2 times and 5 times reused, 2 times and 5 times artificially aged). Table by authors. 240

Table 13.1 DSC test results. 256

Table 13.2 Mechanical performances of specimens printed with virgin and reused powder (μ: mean; σ: standard deviation). 257

Table 13.3 ANOVA results of UTS value from tensile tests (DF = Degree of Freedom; Seq SS = Sequential sums of squares; Adj SS = Adjusted sums of squares; Adj MS = Adjusted mean squares). 259

Table 13.4 ANOVA results of degree of crystallinity from DSC test (DF = Degree of Freedom; Seq SS = Sequential sums of squares; Adj SS = Adjusted sums of squares; Adj MS = Adjusted mean squares). 261

Table 13.5 Comparison between predicted and measured UTS values. 263

List of Abbreviations

3D	Three-dimensional
ABS	Acrylonitrile Butadiene Styrene
AESO	Acrylated epoxidized soybean oil
AI	Artificial Intelligence
AM	Additive Manufacturing
ANN	Artificial Neural Network
ANOVA	Analysis of Variance
ASTM	American Society for Testing and Materials
BJ	Binder Jetting
BNN	Bayesian neural networks
BR	Bayesian Regularization
CAD	Computer-aided design
CD	Crystallinity degree
CNN	Convolutional Neural Networks
COP	Coefficient of Prognosis

CV	Cross-Validation
DBN	Deep Belief Networks
DED	Direct Energy Deposition
DF	Degree of Freedom
DGEBA	Diglycidylether of bisphenol-A
DL	Deep Learning
DLP	Digital Light Processing
DOE	Design of Experiments
DPI	Dimensional Performance Index
DSC	Differential Scanning Calorimetry
ESO	Epoxidized soybean oil
FDM	Fused Deposition Modeling
FFF	Fused Filament Fabrication
GWO	Grey-Wolf optimization Genetic Algorithm
ISO	International Organization for Standardization
LCD	Liquid Crystal Display
LOO	Leave-One-Out
LS	Laser Sintering
LTLS	Low-temperature Laser Sintering
MA-BSA	Methacrylated Bovine Serum Albumin
MAE	Mean Absolute Error
ME	Material Extrusion

MFR	Melt Flow Rate
MJ	Material Jetting
ML	Machine Learning
MS	Mean Squares
MSE	Mean Squared Error
MSLA	Masked Stereolithography
MVR	Melt Volume-Flow Rate
NLL	Nonlinear Laser Lithography
PA	Polyamide or Nylon
PBF	Powder Bed Fusion
PC	Polycarbonate
PEEK	Polyether Ether Ketone
PEGDA	Polyethylene Glycol Diacrylate
PET	Polyethylene Terephthalate
PETG	Polyethylene Terephthalate Glycol
PI	Performance Index
PLA	Polylactic Acid
PSA	Pattern Search Algorithm
PSO	Particle Swarm Optimization
R^2	Coefficient of Determination
RNN	Recurrent Neural Networks
RSM	Response Surface Methodology

SEM	Scanning Electron Microscopy/Microscope
s.e.m.	Standard errors on the mean
SGPI	Synthetic Geometrical Performance Index
SL	Sheet Lamination
SLA	Stereolithography
SLS	Selective Laser Sintering
SS	Sum of Squares
STL	Standard Triangle Language
TPE	Thermoplastic Elastomer
TPU	Thermoplastic Polyurethane
UFS	Ultimate Flexural Strength
UTS	Ultimate Tensile Strength
UV	Ultraviolet
VED	Volumetric Energy Density
VP	Vat Photopolymerization
XRD	X-ray Diffractometric Analysis

General Introduction

Valentina Vendittoli[1]

[1] Department of Civil and Mechanical Engineering, University of Cassino and Southern Lazio, via G. di Biasio 43, 03043 Cassino, Italy

1.1 Overview of Additive Manufacturing

A process of joining materials to create objects from three-dimensional model data, usually layer by layer, as opposed to subtractive manufacturing methodologies [1].

Additive Manufacturing (AM), popularly known as 3D printing, brings a step change in manufacturing technology that affords excellent design freedom and customization. Unlike conventional subtractive manufacturing, where removals reduce an initial solid block of material, AM builds three-dimensional complex objects by carefully adding layer-by-layer material guided by a digital model. This new creation process made possible a range of possibilities for constructional geometries and structures previously inaccessible or too costly with conventional methods [1]. AM technologies, one of the widest ranges of processes, mechanisms, and applications, have evolved quickly over the last two decades. The driving force behind this development came from new advances in material science and process optimization, coupled with innovative digital tools for manufacturing. This new value chain extended to aeronautic, health, automotive, and consumer products industries that require lightweight, complex, and customized parts more than ever before [2]. It can even carry out multi-material parts to integrate different material properties into a single part. Besides, the very nature of the additive manufacturing process guarantees minimal waste and consumption of raw materials [3].

However, AM is not entirely free from challenges. The cost-per-part is relatively high compared to traditional manufacturing, making it less suitable for mass production. 3D printing parts are too expensive for many applications, limiting additive manufacturing to niche, high-value applications [4]. Lowering the price per part could accelerate AM adoption and scalability, as performance benefits outweigh the costs. Besides, the mechanical properties of the parts depend so much on such process parameters and materials that the strength and durability of AM-made parts might strengthen their foothold in some critical industries [5]. Consequently, AM is often seen as a supporting technology rather than directly replacing conventional manufacturing methods. According to the ISO/ASTM standard, a few primary groups can be distinguished concerning additive manufacturing processes: Binder Jetting (BJ), Direct Energy Deposition (DED), Material

Extrusion (ME), Material Jetting (MJ), Powder Bed Fusion (PBF), Sheet Lamination (SL), And Vat Photopolymerization (VP). Technologies are included in each category, with unique benefits that answer needs specific to various applications.

1.1.1 Masked Stereolithography

Stereolithography (SLA) represents a pioneering technology in the field of AM. A layer-by-layer process employs a laser to cure liquid resin into a hardened plastic material. In SLA, a UV laser is used to selectively solidify the resin following the cross-sectional design of the 3D model. This process continues until the entire object is completed, resulting in highly accurate and detailed parts. The original SLA technology was invented in 1984 by Charles Hull, who filed the first patent for this technology, marking the advent of 3D printing [6]. Hull's invention became commercially available in 1988, revolutionizing manufacturing by enabling the creation of complex geometries and smooth surfaces with precision [7]. However, despite its precision, SLA has certain limitations, particularly regarding build speed and the size of parts that can be produced efficiently—a variant known as Masked Stereolithography (MSLA) was developed to address these issues. MSLA is an advanced variant of traditional stereolithography SLA that employs an LCD screen to mask the entirety of a resin layer during the curing process (see Figure 1.1.a). This allows for the simultaneous exposure of the entire layer, in contrast to the point-by-point laser approach utilized by SLA, thereby making MSLA more rapid and efficient. MSLA technology is particularly valued for its ability to produce high-resolution models with intricate details, especially in applications where precision is critical, such as dental prostheses and bio-microfluidics [8] (see Figure 1.1.b).

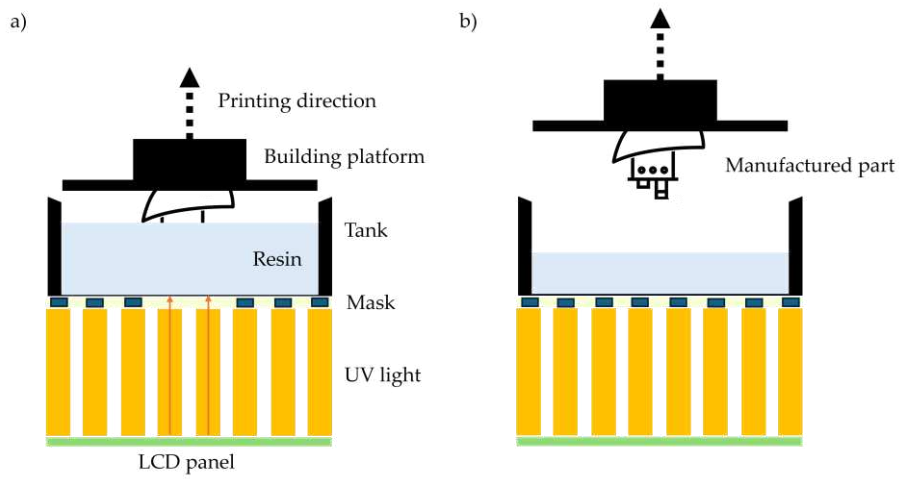


Figure 1.1 (a) Schematic of the MSLA process; **(b)** Representation of the manufactured part.

In MSLA, a digital mask is created using an LCD, which blocks the light in specific areas, thereby enabling the selective hardening of the resin through UV light. This process results in a more efficient use of time and materials than SLA, as the entire layer is cured simultaneously. The materials employed in MSLA are primarily photopolymer resins that undergo a chemical reaction in the presence of UV light. These resins include acrylate-based photopolymers, commonly utilized due to their mechanical properties and capacity for biocompatibility in medical applications such as tissue engineering and regenerative medicine [9]. Moreover, biodegradable and plant-based resins are emerging as sustainable alternatives that address environmental and health concerns. Recent research has underscored the utility of bio-based resins, including Acrylated Epoxidized soybean oil (AESO) and plant-derived Polyethylene Glycol Diacrylate (PEGDA). These resins are gaining prominence in medical applications due to their biodegradability and adaptability for different applications [10]. Furthermore, these bio resins can be combined with nanoparticles, such as hydroxyapatite, to enhance their mechanical properties, rendering them ideal for bone tissue engineering and other regenerative medical applications [11]. One illustrative example is Methacrylated Bovine Serum Albumin (MA-BSA) resins, formulated into hydrogels for three-dimensional printing applications. These resins exhibit excellent mechanical strength and support cell viability, rendering them suitable for intricate tissue engineering applications [12]. Biodegradable resins based on Polylactic Acid (PLA)

have also garnered attention for their potential use in personalized medical devices, such as implants and scaffolds, that degrade safely within the body [13]. These resins are not only biocompatible but also offer tunable degradation rates, which is critical in medical applications where the material needs to be absorbed by the body over time without leaving harmful residues. Developing these advanced bio resins opens new possibilities for sustainable and efficient medical treatments, further advancing the boundaries of additive manufacturing in healthcare [14].

1.1.1.1 Studies on mechanical properties of MSLA parts

The mechanical properties of MSLA parts are contingent upon several parameters. The post-curing phase is a crucial step in the strengthening process, as it allows for the completion of the polymerization process, improves tensile and bending strength, and enhances surface hardness. Insufficient post-curing can result in diminished mechanical properties and reduced durability [15]. Moreover, elevated post-curing temperatures have improved toughness and mechanical strength by facilitating more complete cross-linking in resins [16]. The layer thickness is another crucial parameter. Thinner layers allow for more intricate prints, but it may result in weaker interlayer bonding, reducing the part's overall mechanical strength. The build orientation also influences the mechanical strength of the resulting part. Vertical orientations have been observed to result in weaker parts due to the stress concentration between layers [17]. Furthermore, extended washing periods during the post-processing stage may result in a slight reduction in strength. In contrast, inadequate washing can lead to the retention of unpolymerized resin, potentially compromising the mechanical integrity of the part [18].

1.1.1.2 Studies on the quality of MSLA parts

The quality of MSLA parts is contingent upon several parameters, including exposure time, layer height, and further post-processing parameters, such as temperature and exposure time. It is essential to utilize the appropriate exposure times to achieve accurate geometrical fidelity and create smooth surfaces. Excessive exposure can result in excessive curing, leading to geometrical inaccuracies. Conversely, inadequate exposure may result in weak and incomplete parts [9].

Additionally, layer height is a significant parameter, as reducing the layer height allows for finer details but increases surface roughness and the potential for print defects [19]. Post-curing methods, such as UV curing, have significantly enhanced surface smoothness and mechanical properties. Using distinct post-curing methodologies can improve flexural strength and mitigate surface roughness, which is particularly significant for components designed for medical applications [20].
Furthermore, build orientation and print resolution are essential parameters that can influence the quality of the final product. If these settings are not optimal, it can result in geometrical errors and surface flaws, ultimately affecting the overall quality of the part [21, 22]. In this work, the term geometrical deviation is used to describe inaccuracies in dimensions (diameter, length, width) [23] as well as geometrical inaccuracies of parts (parallelism, roundness, flatness) [24].
Furthermore, the quality of MSLA parts is also affected by the printer type and material selection. The resolution and light exposure methods employed by printers utilizing LCD technologies influence the level of accuracy with which the resin is cured layer-by-layer. The interaction between the printer and the material used can result in disparate outcomes concerning surface smoothness, geometrical accuracy, and mechanical strength [20]. The selection of an appropriate resin is also of considerable importance. Newer bio-based and hybrid resins offer enhanced mechanical properties and are gaining popularity for applications in medical and sustainable manufacturing [16].

1.1.2 Fused Deposition Modeling

Fused Deposition Modeling (FDM), also called Fused Filament Fabrication (FFF) is one of the most popular AM technologies, mainly because it is relatively cheap, easy to use, and versatile. The process involves extruding thermoplastic material through a heated nozzle to form layers that build up the final object, as depicted in Figure 1.2. The process, without exception, starts with a digital 3D model, most likely created within a CAD software environment. Afterwards, the specialized pre-processing software slices the model into several thin layers, which are read by the FDM printer; they form the path for the movements of the print head [25]. This has further been adapted to the prototyping, educational, and low-volume manufacturing environments, with its popularity brought about by the low costs of producing models and the availability of a wide range of materials [26]. This key ability has made FDM a valuable tool to designers and engineers for the

experience of quickly produced functional prototypes and end-use parts. The critical steps of the FDM process must be controlled so that the quality of the final part is guaranteed. First, in the print head liquefier, the thermoplastic filament is heated, and later, it is melted and extruded through a nozzle. The movement of this nozzle along the X and Y axes is continuously precisely fastened, reacting to the sliced layer data of the digital model. After the deposition of the single layer, the build platform lowers, or the nozzle is raised, by a predetermined layer height in preparation for the subsequent layer deposition, and this is repeated until the object is fully built [27].

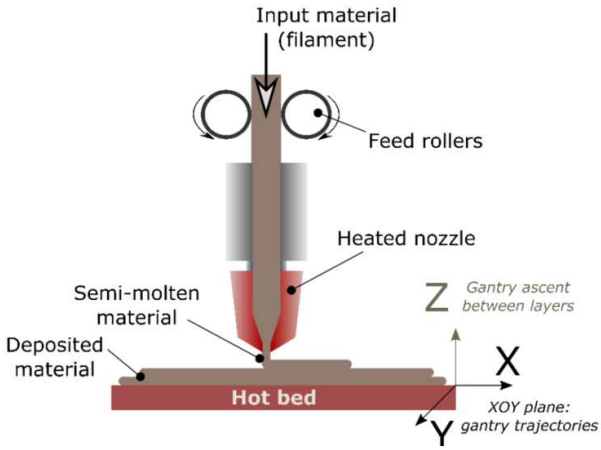


Figure 1.2 Schematic of the FDM process. Reprinted with permission from Ref. [28].

Generally, the accuracy of the FDM process for building parts is mainly dependent on the accuracy of the CAD model, slicing software, and the printer's mechanical components. The geometrical errors and the bad surface qualities of the final parts are either the results of errors or variations in these parameters [29]. Thus, current research in FDM is concerned with enhancing the precision and repeatability of the process through improving hardware, software, and materials [30].
It can be applied to many thermoplastic polymers with different mechanical and thermal properties. Acrylonitrile Butadiene Styrene (ABS) and PLA are the mainstream materials used in FDM. ABS is famous for its great impact resistance, robustness, and cost-effectiveness, which enable it to be applied to tough prototypes or final-use parts. PLA is derived from renewable resources, and it carries biodegradability and biocompatibility features desirable for green applications [31].

Polyethylene Terephthalate Glycol (PETG) is as strong as ABS, with improved flexibility and raised temperature. It would find applications around functional prototypes and hard-pressing end-applications. Polycarbonates (PC) and Nylons are engineered for high-strength and thermal stability applications. PC has excellent impact tolerance and temperature tolerance. At the same time, Nylons offer high strength, great toughness, and resistance to chemicals and abrasion, which, as a result, are widely used in applications from functional prototypes up to end-use in really demanding applications [32].

1.1.2.3 Studies on mechanical properties of FDM parts

The mechanical properties of FDM parts are subject to a complex interplay of material properties, process parameters and design choices. One of the most significant parameters is the anisotropy introduced by the layer-by-layer deposition process, which can result in variations in strength and failure behavior depending on the orientation of the layers [33]. Incomplete fusion between layers, frequently attributed to insufficient printing temperature or rapid cooling, can precipitate the formation of weak interfaces and an increased propensity for failure under stress. Optimizing printing parameters, such as temperature control and cooling rates, is essential to improving interlayer adhesion and overall mechanical performance [34].

The rapid heating and cooling cycles inherent to FDM can also induce residual stresses, further compromising printed parts' mechanical integrity. These stresses, often concentrated at layer interfaces or within areas of complex geometry, can result in geometrical inaccuracies, warping, and reduced mechanical performance. Mitigation strategies for these stresses, such as preheating the build chamber or post-processing annealing treatments, are the subject of ongoing research [35, 36]. The selection of an infill pattern and its density also has significant consequences regarding the mechanical properties of FDM parts. Higher infill densities typically result in increased strength and stiffness, often accompanied by greater material consumption and longer printing times [37]. The choice of infill pattern and density is of great consequence, as different patterns, such as rectilinear, honeycomb, or gyroid structures, exhibit distinct mechanical properties. It is, therefore, essential to optimize the pattern for the specific load case to achieve the desired performance while minimizing material usage [38]. FDM-printed components' long-term performance and durability under various environmental

conditions, including creep, fatigue, and degradation due to UV exposure or moisture absorption, are crucial factors to consider when expanding the application of FDM in demanding environments. Ongoing research must be conducted into the effects of these factors on FDM-printed components to ensure their reliability and longevity in real-world applications [39]. The utilization of advanced modelling and simulation techniques, including data-driven approaches that employ machine learning algorithms, is becoming increasingly prevalent in predicting the mechanical properties of FDM parts. These models, trained on experimental data, can inform material selection, process optimization, and part design, thereby enabling the achievement of the desired mechanical performance and facilitating the broader adoption of FDM in high-performance applications [40].

1.1.2.4 Studies on geometrical accuracy and surface finish of FDM parts

The geometrical accuracy of an FDM-printed part is a critical parameter affecting the printed object's quality and functionality. The layer-by-layer fabrication process inherently introduces challenges in maintaining precise geometries, as slight variations in process parameters have the potential to propagate through the layers, leading to significant geometrical deviations [41].

It is crucial to optimize process parameters, including layer height, nozzle diameter, printing temperature and speed, to minimize geometrical errors. While the use of thicker layers enables faster build times, it has been observed that this approach often compromises accuracy [42]. Conversely, the use of finer layers has been shown to enhance the accuracy of the printed object; however, this does come with the disadvantage of longer printing durations. Therefore, it is necessary to consider the specific application requirements when establishing the optimal layer thickness. Furthermore, material shrinkage during the cooling and solidification stages of FDM represents an additional challenge to achieving high geometrical accuracy. Deviations from the intended dimensions may result from shrinkage, which is particularly prevalent in parts with complex geometries. It was demonstrated the efficacy of incorporating shrinkage compensation parameters into slicing software, thereby facilitating more precise prediction and mitigation of geometrical errors [43]. Furthermore, closed-loop control systems that monitor and adjust printing parameters in real time based on measured geometrical deviations show promise for achieving unprecedented accuracy in FDM. The surface roughness of FDM-printed parts represents a further critical aspect,

affecting both the aesthetic appeal and functional properties of the final product. The stair-stepping effect, which is a consequence of layer-by-layer deposition, is especially noticeable on curved or angled surfaces. Layer height is a primary determinant of surface roughness, in fact thinner layers result in a smoother finish, although this is achieved at the expense of longer printing times [44].
Additionally, the diameter of the nozzle has a considerable impact on the quality of the surface. The use of smaller nozzles enables the deposition of finer material beads, resulting in the formation of smoother surfaces on small features or intricate details. However, this approach necessitates slower printing speeds and increases the probability of nozzle clogging. Furthermore, the orientation of the part in relation to the build platform can impact the visibility of layer lines and influence the perceived surface roughness. The strategic orientation of the part can assist in reducing the visibility of these steps, thereby enhancing the overall surface smoothness [45].
Subsequent processing techniques, including mechanical sanding, polishing, and chemical treatments such as vapor smoothing or solvent polishing, are frequently employed to attain a genuinely smooth surface. While these methods can significantly enhance surface quality, they must be applied with precision and caution to avoid any alteration to the part's geometry or mechanical properties. Furthermore, coatings and other surface treatments can be employed to enhance the surface finish while simultaneously imparting functional properties, such as enhanced durability or improved aesthetics [46]. It is of great importance to achieve high geometrical accuracy and a smooth surface finish in FDM to broaden its application in industry where precision and quality are of the utmost importance. As research continues to explore the intricate relationships between material properties, process parameters, and part geometry, the discrepancy between the designed and fabricated dimensions will continue to diminish, thereby paving the way for the wider adoption of FDM in demanding applications.

1.1.3 Selective Laser Sintering

Selective Laser Sintering (SLS) represents a pioneering PBF technology in the domain of additive manufacturing, having received considerable acclaim for its capacity to produce durable and sophisticated components exhibiting intricate geometries. The versatility of SLS technology ensures its suitability for use across a variety of industries, including aerospace, automotive, medical, and prototyping.

SLS is characterized by its capacity to fabricate parts without the necessity for support structures, which represents a substantial advantage when producing geometries with overhangs or internal cavities [47]. The SLS process begins with the uniform distribution of a thin layer of powdered material onto a build platform within a heated chamber. A high-powered laser, guided by digital 3D model data, selectively scans and sinters (partially melts and fuses) the powder particles in designated areas, tracing the contours of each cross-sectional layer. Subsequently, the build platform is lowered to the requisite layer height, and a new layer of powder is distributed over the previously sintered layer. This process of powder deposition, selective laser sintering and platform lowering is repeated iteratively until the entire 3D object has been fabricated as shown in Figure 1.3.

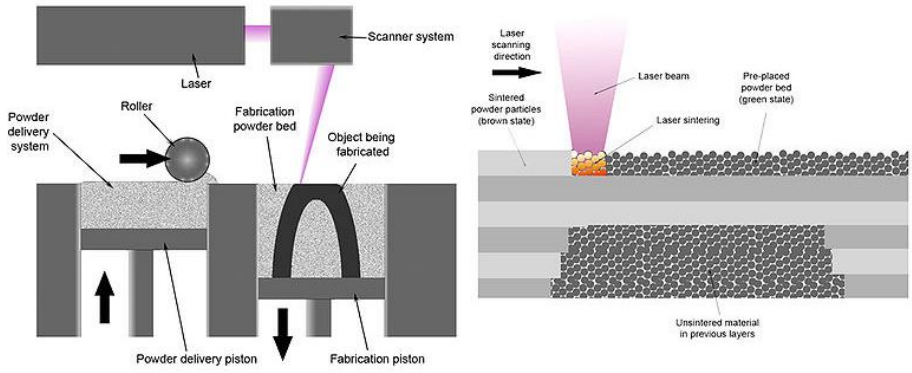


Figure 1.3 Schematic of the SLS process. Courtesy of Materialgeeza, SLS, Wikipedia from Ref. [48].

The versatility of SLS is reflected in its compatibility with a wide array of materials, including polymers, metals, and ceramics. Nevertheless, polymers are predominantly utilized due to their advantageous processing characteristics, mechanical properties and extensive applicability across numerous industries, particularly polyamides or nylons (PA). PA12 is the most frequently utilized polymer in SLS due to its exceptional balance of mechanical properties, including high tensile strength, robust impact resistance, and chemical resistance. It is employed in the production of functional prototypes, tooling, and end-use parts across a diverse range of industries [49, 50]. In comparison to PA12, PA11 is extracted from renewable resources and exhibits enhanced ductility and impact resistance, rendering it an optimal material for applications where a higher degree of flexibility and resilience is required. Its utilization in SLS is particularly beneficial in

applications where the mechanical performance under conditions of dynamic loading is of significance.
In addition to PA12 and PA11, other polyamides are available on the market, including PA6 and PA66. Among other composite materials, glass-filled or carbon-fiber-reinforced polyamides are gaining interest in SLS to meet the requirements of potential applications. These outcomes result in further enhanced mechanical properties, for example, in terms of increased stiffness and strength, thus extending the possibilities for applications of SLS [51]. The principal characteristics of Thermoplastic Polyurethanes (TPU) are their high elasticity and their high resistance to abrasion. Consequently, they are widely employed in the manufacture of flexible components, including seals, gaskets and footwear. The potential for the manufacture of such components via SLS represents a further development in the field of this technology. Polyether Ether Ketone (PEEK) is a high-performance thermoplastic that is becoming increasingly utilized in SLS, offering high mechanical properties, coupled with chemical resistance and high-temperature performance. It is particularly well-suited to utilization in challenging aerospace and medical applications, given the demanding conditions under which materials are required to perform [50].

1.1.3.5 Thermal and structural properties of PA12

PA12 is the most frequently utilized material in SLS, employed in a multitude of applications. Its popularity can be attributed to its ability to offer a balanced range of properties, both thermally and structurally. PA12 is distinguished by a relatively high melting point, which is approximately 178-180°C, as well as good thermal stability and a low coefficient of thermal expansion. These properties permit PA12 to retain elevated temperatures while maintaining geometrical stability across a broad temperature range, thereby rendering it suitable for functional prototypes and end-use parts subjected to rigorous conditions [52]. The PA12 exhibits excellent mechanical properties, including high tensile strength, good impact resistance, and good fatigue behavior. Its relatively good chemical resistance and low friction coefficient make it well suited for a wide range of applications, from structural components to functional prototypes and tooling. The semicrystalline nature of PA12 contributes to favorable mechanical strength, making it an optimal choice for durable and reliable products [53]. The properties of SLS-printed parts are influenced by a combination of the material's inherent characteristics, the

process parameters, and the environmental conditions during processing. It is of paramount importance to gain an understanding of the way these parameters interact, particularly in the context of material degradation, to guarantee the quality and reliability of SLS parts. During the SLS process, the elevated temperatures necessary for sintering can induce thermal degradation in polymers, resulting in a reduction in molecular weight. This degradation manifests as a reduction in mechanical properties, including strength and ductility. Thermal degradation represents a significant concern for materials such as PA12 and PA11, where prolonged exposure to elevated temperatures can result in a loss of part performance [54, 55]. The presence of oxygen within the SLS chamber can result in oxidation, particularly at elevated temperatures. Oxidation can result in the breaking of chemical bonds and the formation of new ones, which can have a detrimental impact on the mechanical and thermal properties of the printed parts. The formation of volatile by-products due to oxidation can result in further degradation of the material. Therefore, it is essential to exercise caution and control the chamber environment to minimize exposure to oxygen [56]. Polymers employed in SLS, particularly polyamides, exhibit hygroscopic properties, whereby they readily absorb environmental moisture. The moisture can act as a plasticizer during the processing of the printed parts, affecting their sintering behavior, mechanical properties and geometrical stability. It is of the utmost importance to ensure the correct storage and handling of the powder to minimize the absorption of moisture and its subsequent negative effects on the final product [57].

1.1.3.6 Studies on the mechanical and geometrical performance of parts manufactured with virgin and aged PA12 powder

In the pursuit of sustainability and cost-effectiveness, the repeated use of unsintered PA12 powder is a common practice in SLS. However, each thermal cycle subjects the powder to high temperatures, which can result in progressive degradation that may affect the powder's characteristics and the properties of the final parts. The repeated application of thermal cycling can result in a reduction in the molecular weight of PA12 powder, an alteration in its particle size distribution, and the formation of volatile by-products. Such alterations can have a detrimental impact on the powder's flowability, packing density, and laser energy absorption, which in turn affects the printed parts' sintering process and quality. It has been demonstrated that the degradation of PA12 powder results in a reduction in

mechanical properties and an increase in brittleness in parts produced with aged powder [47, 58].

The utilization of aged PA12 powder in SLS has been associated with a reduction in the mechanical properties of the printed parts, including a decline in tensile strength and elongation at break. Research has revealed the damaging effects of powder ageing, including an increase in brittleness and a reduction in impact strength, which can lead to a loss of structural integrity in the parts. Furthermore, the degradation of PA12 powder affects the geometrical accuracy and stability of parts produced via SLS. As powder ageing affects the flowability and packing density of the powder, the uniformity of the powder bed can be compromised, which may result in geometrical variations within the printed parts [57, 59, 60]. Furthermore, the altered thermal properties of aged powder can influence shrinkage and warpage during the cooling phase, thereby intensifying geometrical inaccuracies.

Several strategies have been put forth as potential means of counteracting the effects of PA12 powder ageing. The incorporation of a proportion of virgin powder into aged powder can facilitate the restoration of powder characteristics and enhance the quality of printed parts. Therefore, powder refreshment strategies could mitigate some of the adverse effects of ageing. Furthermore, techniques such as thermal treatment or post-processing of aged powder have been investigated with a view to reversing some of the degradation effects and enhancing powder properties [61, 62, 63].

Moreover, modifying the laser parameters and scanning strategies can assist in compensating for the altered sintering behavior of aged powder, thereby enhancing the quality of printed parts. Further research in this field is investigating how precise adjustments to these parameters can counteract the effects of powder ageing, thereby ensuring that SLS-printed components maintain the requisite quality and performance standards [64]. A comprehensive understanding of the degradation mechanisms of PA12 powder during SLS and their impact on the mechanical and geometrical performance of printed parts is crucial for optimizing process parameters, developing effective powder management strategies, and guaranteeing the long-term reliability of SLS-manufactured components [65].

1.2 Applications of Artificial Intelligence in the Optimization of AM processes

> *Artificial Intelligence is the study of how to make computers do things which, at the moment, people do better [66].*

Artificial Intelligence (AI) is a transformative technology that encompasses a range of techniques and methods designed to enable machines to perform tasks that have previously been the domain of human intelligence, including learning, reasoning and problem-solving. Subfields of AI, such as Machine Learning (ML) and Artificial Neural Network (ANN), have had a particularly significant impact. ML focuses on creating algorithms that can learn and improve based on experience while ANNs are inspired by the neural structure of the human brain and excel in pattern recognition and predictive modelling [67].

The integration of AI into the field of AM has led to significant advancements in the industry, with notable improvements in process efficiency, accuracy, and quality. AI enables the optimization of intricate AM processes by anticipating the behavior of materials and modifying parameters to attain the desired outcomes. This reduces the reliance on trial-and-error approaches and enhances the reliability of manufacturing processes [68]. Moreover, AI-driven systems provide real-time monitoring and control, thus enabling the early detection of defects and automatic adjustments to maintain product quality. Additionally, AI plays an important role in generative design, wherein algorithms generate design alternatives that satisfy defined constraints and objectives. This approach is particularly beneficial in the context of AM, where design flexibility is of paramount importance. The application of AI to the design process enables the optimization of structures in terms of weight, strength and material usage, thereby facilitating the creation of more efficient and innovative products [69, 70].

ANNs have already been demonstrated to be particularly effective in predicting the mechanical properties of AM parts, including tensile strength and flexibility, based on input parameters such as layer thickness and print speed [68, 39]. Such predictions permit process adjustments that optimize the final product, this reduces the reliance on extensive physical testing, thereby leading to significant time and cost savings in the manufacturing process [71].

Figure 1.4 illustrates the ML taxonomy and the corresponding implementations in AM. The employment of ML models, including advanced Deep Learning (DL) techniques, enables the dynamic optimization of AM process parameters, thereby improving the geometrical accuracy and surface finish of components. Techniques such as BR have been instrumental in the development of models that predict optimal conditions for the minimization of defects, such as warping or delamination, and the enhancement of the overall quality of AM-produced parts. For instance, ML algorithms have been successfully used to optimize the process parameters in FDM to achieve the desired surface finish and geometrical accuracy [72]. Furthermore, CNNs are employed for the detection of defects and the assurance of quality control, thereby guaranteeing that the manufactured parts comply with rigorous industry standards [73]. Furthermore, AI plays a pivotal role in the design of materials for AM. For example, ML algorithms are employed to forecast material properties and refine the composition of novel materials for AM applications, thus accelerating the development of advanced materials [74].

AI is revolutionizing manufacturing by facilitating more intelligent, expedient, and dependable production procedures [40]. This integration is of great consequence for the resolution of the complexities inherent to AM, facilitating the technology's scalability and adaptability across a multitude of industrial sectors.

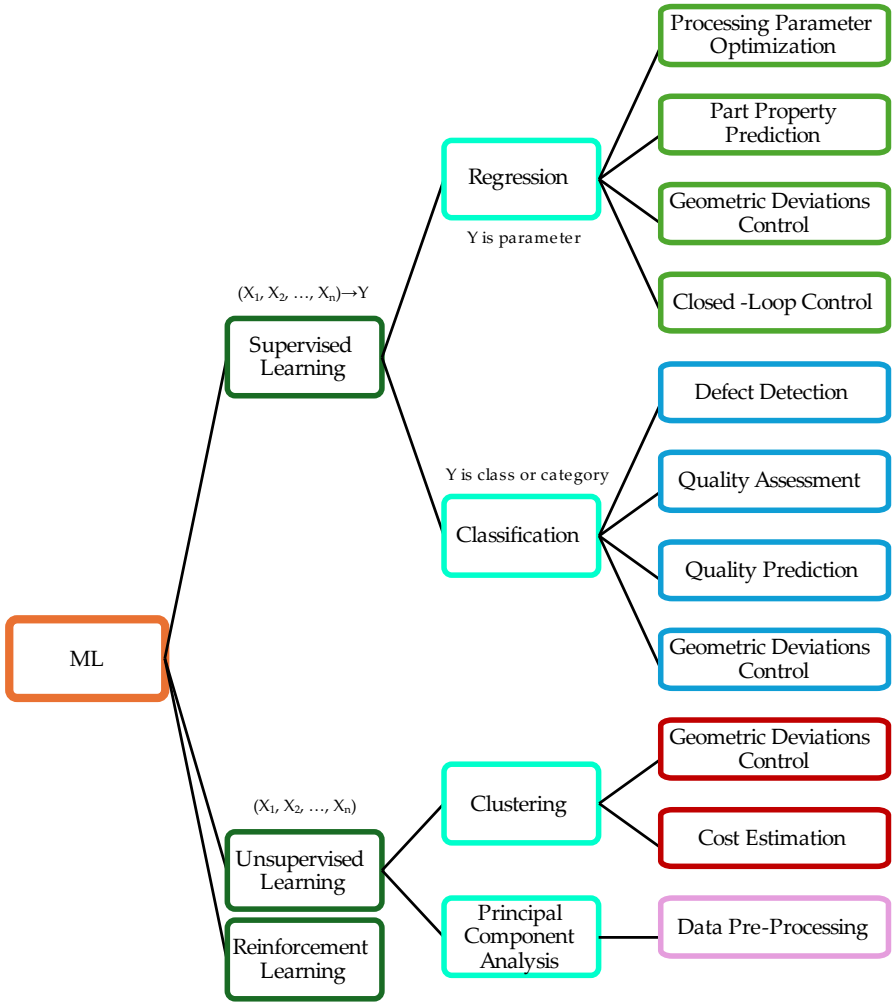


Figure 1.4 Taxonomy of ML applications in the AM domain. X_1; X_2; … X_n represent the input vector, and Y represents the output. Adapted with permission from Ref. [75].

1.3 Motivation

Rapid advancements in AM technologies, particularly SLS and FDM, have transformed the production of complex geometries and customizable parts. Despite these technological advancements, significant barriers prevent AM from becoming widely adopted in the industry. These challenges include optimizing both the mechanical properties and the geometrical accuracy of printed parts, as well as the sustainable reuse of materials, particularly in the context of recycling unsintered powders using SLS. The need to address these challenges comprehensively drives this research. This research aims to bridge existing knowledge and practice

gaps by focusing on AM process optimization and material sustainability, thereby contributing to the enhancement of AM's industrial viability and environmental sustainability.

1.3.1 Multi-objective optimization

AM processes such as SLS and FDM involve complex interactions between many parameters. These parameters significantly affect the final product's mechanical properties and geometrical accuracy. Traditionally, optimization efforts in AM have focused on independently improving either mechanical strength or geometrical accuracy. However, in industrial applications, it is crucial to balance these two aspects to ensure producing high-quality parts. The gap in the existing literature lies in the lack of integrated strategies that simultaneously address both objectives, the mechanical and the accuracy performance. This research seeks to fill this gap by developing and applying advanced multi-optimization techniques, enabling the specification and production of parts that meet stringent industrial standards for strength and accuracy.

1.3.2 Challenges in recycling unsintered powder

One of the most significant sustainability challenges in SLS is finding ways for an effective recycling of unsintered powder. While SLS is acknowledged for its material efficiency, repeated thermal cycling of unsintered powder can cause significant material degradation. This degradation includes variations in molecular weight, particle size distribution, and flowability, all of which can harm the quality of future prints. Current powder recycling practices are limited by a lack of understanding of the long-term effects of repeated recycling on material properties, as well as the absence of effective mitigation strategies. Addressing these challenges necessitates a thorough investigation into the degradation mechanisms of n-times recycled powders, as well as the development of novel recycling strategies that maintain or even improve material quality across multiple cycles. This study aims to provide such insights, contributing to more sustainable AM practices.

1.4 Research objectives

The primary objective of this research is to advance the field of AM by addressing key challenges related to the optimization of mechanical properties, geometrical accuracy, and material sustainability. Specifically, four research aims arise:

1. Develop and implement multi-optimization strategies that enhance both the mechanical performance and geometrical accuracy of parts produced through AM processes such as MSLA, SLS and FDM.
2. Investigate the degradation mechanisms associated with the repeated use of unsintered powder in SLS and propose effective methods to mitigate these effects, thereby improving powder recyclability.
3. Explore the relationship between process parameters, material properties, and the resulting part quality to establish guidelines for optimizing AM processes in industrial applications.
4. Contribute to the broader adoption of sustainable AM practices by providing insights into optimizing and recycling materials used in these processes.

1.5 Outline of the thesis

This thesis is structured into fourteen chapters, each addressing specific aspects of the above research objectives. The visual outline of the thesis is shown in Figure 1.5.

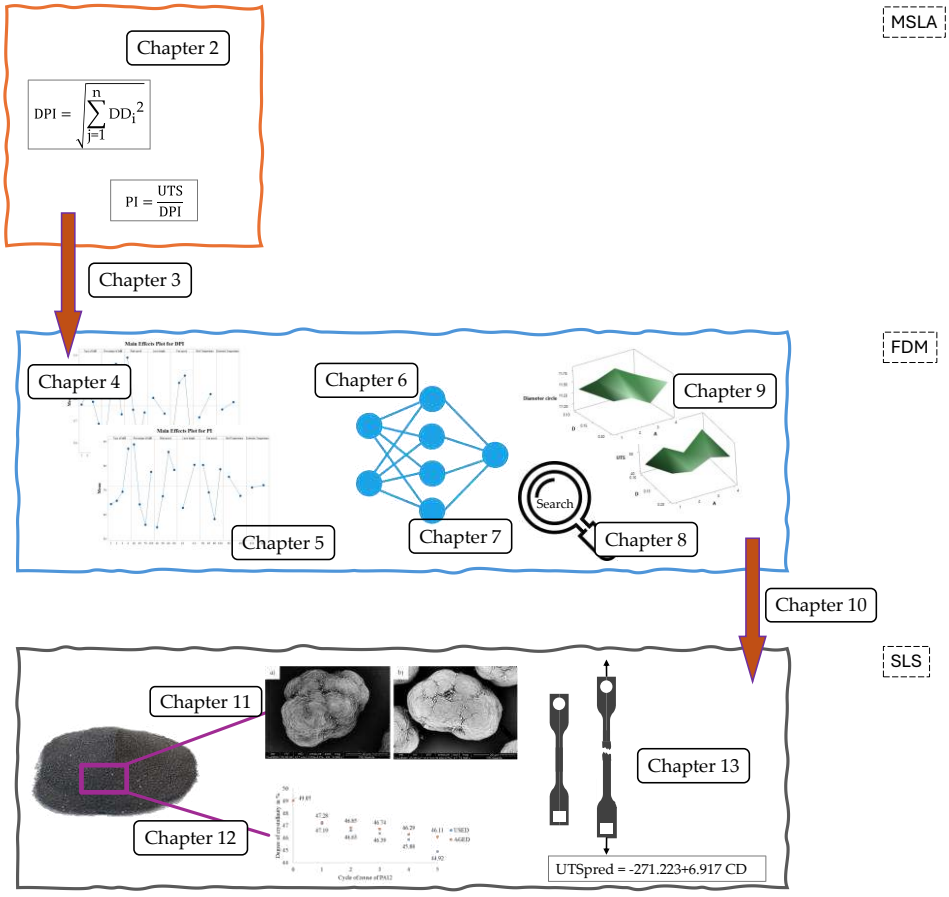


Figure 1.5 Outline of the thesis.

- Chapter 1 introduces the fundamentals of AM with a strong focus on SLS and FDM and identifies the research gaps that motivate this study and results in the four detailed research aims.
- Chapter 2 presents an overall performance index designed to quantify the geometrical accuracy and mechanical strength of parts manufactured through MSLA using both biodegradable as well as non-biodegradable

resins. Furthermore, it highlights the relevance of balancing mechanical properties and geometrical quality in AM components.

- Chapter 3 explores the transition from MSLA to FDM, highlighting the importance of adequately adjusting mechanical performance and geometrical accuracy to address specific requirements efficiently achievable through careful process control.
- Chapter 4 introduces a Synthetic Geometrical Performance Index (SGPI) to assess deviations in green parts resulting from FDM. This chapter puts forth novel methodologies for assessing and enhancing geometrical precision in components produced via AM.
- Chapter 5 analyses process parameters and their effects on two performance indices in polylactic acid parts manufactured through FDM. This chapter delves into the relationship between process settings and the resulting mechanical and geometrical qualities of the parts, setting the stage for the multi-optimization strategies discussed later.
- Chapter 6 introduces BR-ANN, a method for predicting the dimensional and micro geometrical deviations of parts produced through additive manufacturing processes. It demonstrates the use of AI to enhance the predictive accuracy of manufacturing outcomes.
- Chapter 7 presents a detailed exploration of BR-ANN and its application in predicting the tensile strength of additive-manufactured PLA parts. This chapter provides foundational insights into using advanced computational techniques to optimize AM mechanical performance.
- Chapter 8 introduces an artificial intelligence tool designed to optimize the geometrical and mechanical performances of parts produced through FDM. The chapter discusses the development and validation of this algorithm, demonstrating its potential to enhance AM outcomes through intelligent optimization.
- Chapter 9 extends the discussion on optimization by applying Response Surface Methodology (RSM) to achieve multi-response optimization of the dimensional and mechanical properties of 3D-printed PLA parts. The methodologies and results presented in this chapter provide practical insights into achieving balanced performance in AM parts.
- Chapter 10 explores the transition from FDM to SLS, highlighting material and process efficiency enhancements that can be achieved through

careful process control. This chapter bridges the gap between different AM technologies and discusses the implications for material sustainability.

- Chapter 11 provides a comprehensive overview of the structural, mechanical, and geometrical characteristics of parts manufactured with PA12 using SLS. The findings presented in this chapter inform the subsequent discussions on material degradation and recycling.
- Chapter 12 presents a novel approach to artificially ageing PA12 powder used in SLS. This chapter investigates the effects of repeated powder reuse on material properties and proposes innovative techniques to mitigate degradation.
- Chapter 13 builds on the previous chapters by focusing on the predictive modelling of mechanical properties from degraded PA12 powder in SLS. The models developed in this chapter aim to guide future material reuse and sustainability efforts in AM.
- Chapter 14 concludes the thesis with a general discussion of the findings, their implications for the field of AM and potential directions for future research.

Chapter 2 An overall performance index to quantify dimensional accuracy and mechanical strength of parts manufactured through VAT photopolymerization in biodegradable and non-biodegradable resin

Valentina Vendittoli[1], Wilma Polini[1] and Michael S. J. Walter[2]

[1] Department of Civil and Mechanical Engineering, University of Cassino and Southern Lazio, via G. di Biasio 43, 03043 Cassino, Italy

[2] Faculty of Engineering, University of Applied Sciences Ansbach, Residenzstr. 8, 91522 Ansbach, Germany

Published in: The International Journal of Advanced Manufacturing Technology (2023), 128, pp. 5491-5502
https://doi.org/10.1007/s00170-023-12285-1

Abstract

Epoxy resins are widely used polymers in the automotive and aerospace fields. Different blends of novel biodegradable resins have been studied in the last years in order to provide sustainability while maintaining the same properties of epoxy resins. Bio-based thermoset resins made with acrylated epoxidized soybean oil are well-studied in different vat polymerization techniques. The present work compares a bio-based resin and a petroleum-based resin.

A benchmark with different features was designed and manufactured by a VAT photopolymerization process using both materials; measured with an optical scanning device; thus, the dimensional deviations were analyzed through inspection software. Tensile and flexural specimens were manufactured with the same procedure and tested with a dynamometer machine. Therefore, the comparison between a biodegradable resin and a petroleum-based resin is discussed in terms of the quality and mechanical performances of manufactured parts, considering the use of identical printing conditions.

Some parts are required to satisfy both the requirements at the same time, such as the gears. Therefore, dimensional accuracy and mechanical strength need to be controlled and evaluated in a unique final quantification. This work proposes a novelty performance index to quantify dimensional accuracy and mechanical strength simultaneously. By combining the two aspects is possible to define the overall performance obtained with the used material, optimizing the manufacturing process by choosing the proper material for each purpose.

Keywords: Additive manufacturing; VAT photopolymerization; Bio resin; Epoxy resin; Dimensional accuracy; Mechanical performance; Performance index.

2.1 Introduction

Epoxy resins are polymers commonly used in various industries, such as adhesives, coatings, and insulations. Their important role in the automotive and aerospace fields leads to a variety of hybrid resins along with the creation of high-performance composite blends.

However, epoxy resins are not environmentally friendly, made of chemical monomers, which involve hazardous waste. Eco-sustainability has become a foundational issue; this has increased research into alternative resins created from natural blends that would maintain the same chemical and physical properties as petroleum-derived resins [76, 77, 78]. Moreover, a new field of interest for this application has been medical, which leads to the realization of non-toxic devices used for orthopedic and prosthetic purposes [79, 80]. Commonly, bio-resins are characterized by being only partly based on green resources; further studies have been made to produce full bio-resins that are equivalent in requirements and mechanical characterizations to petroleum-based resins [81]. Nowadays, the most studied bio-sources seem to be plant oils, lignin, and furanyl. Plant oils are triglycerides and fatty acids. The multiples carbon-carbon double bonds in the chemical chains are useful for polymerization [82, 83, 84]. Soybean seeds contain 40% protein and 20% oil. Epoxidized soybean oil (ESO) is used to produce bio-resins for SLA 3D printers [83]. ESO is made by epoxidizing the double bond of soybean oil triglyceride with hydrogen peroxide in formic acid or acetic acid. AESO is made by the reaction of ESO with acrylic acid. It can be UV cured by adding a photo-initiator [84, 85, 86]. Some studies on bio-based resin with AESO proved to be advantageous compared to other existing resins for different vat polymerization techniques, such as Digital Light Processing (DLP) or Nonlinear Laser Lithography (NLL), while retaining more than 60% bio-renewable carbon [87, 88]. The photopolymerization process is primarily influenced by light power and exposure time [89], since the liquid-to-solid transformation occurs due to light radiation passing through the material being absorbed by photo-initiators. The light source strikes the liquid bath's surface and disperses inside the resin.

The transparency of the resin is important for light absorption and proper polymerization [90]. Adding the color pigment in the composition can change the dimensional accuracy [91]. The quality of parts made of resins is also affected by the building's orientation. Generally, the alignment of the part with respect to the printer's axes is considered. Considering the longitudinal axis of the specimens

placed on the xy-plane the most accurate parts are obtained with a building angle of 0° respect to x, however 90° leads to less consumption of resin [92, 93, 94]. Layer thickness is another parameter influencing accuracy along the vertical z-axis. Researchers studied the effect of models printed at 25, 50, and 100 μm. The findings provide that the smaller the layer thickness, the better the surface finish. This is a direct consequence of the staircase phenomenon, where the different layers are visible in the printed parts. However, the possibility of inaccuracy increases with the number of printed layers, which is the case of a small layer thickness. In this case, a layer thickness of 100 μm provides the best performance in terms of dimensional accuracy and printing time [95, 96]. Another investigation on the layer thickness, using 0.01 mm, 0.1 mm, 0.2 mm, and the exposure time, with the values of 6 s, 13 s, and 20 s, provided a better understanding of the linear dimensional accuracy of the printed specimens. The best results are provided along the x and z axes with a layer thickness of 0.1 mm and an exposure time of 6 seconds, whereas along the y-axis, the best result is achieved with a layer thickness of 0.2 mm [97].

There is also a dependency between printing parameters and the mechanical properties of the final part. Higher layer thickness leads to the formation of voids, which decreases component density and lowers the part's strength. Research agrees with choosing 100 μm as layer thickness for the best tensile strength [98]. Furthermore, under different strain rates of parts produced with resins, the resin's behavior depends on the post-curing process. To finalize the polymerization, the right amount of time under UV light is needed to improve the strengthening process [99]. The degree of cure defines the conversion of the monomer in the resin into polymer chains, which implies a fully cured material [100]. The time frame of UV post-curing was critical in improving the mechanical characteristics, mainly hardness, and impact resistance. There is an increase as the duration range from 0 to 4 hours [101]. The crosslinking ratio improves the resistance against several organic solvents [94]. Blends of epoxidized soybean oil with composite are the focus of multiple works. Concerning the thermal and mechanical properties analysis, the authors state that bio-based resins are an excellent alternative to petroleum ones demonstrating that the glass transition temperature (Tg) of the polymer raised as the epoxy value of ESO increased and that the thermal stability of the polymer has a strong association with the degree of crosslinking [102, 103, 104]. Furthermore, ESO was also used to replace the diglycidylether of bisphenol-

A (DGEBA) in an epoxy matrix to investigate the toughening effects of reducing the consumption of petroleum materials. The DGEBA/ESO blends have an increase in impact strength. The blend's adhesive lap shear strength was improved by raising the ESO component to 40% by weight. The flexural strength and elastic modulus at low ESO concentrations were comparable to those of the pure DGEBA. This demonstrated how ESO can be used as a toughening agent [105].
Recent author's works investigated both dimensional and geometric deviations using FFF and MSLA techniques, revealing the possibility of synthesizing the geometrical information of a benchmark using a synthetic performance index [106, 107]. In this work, parts manufactured through a VAT photopolymerization process in both a bio-based resin and a petroleum-based one are compared in terms of dimensional deviations and mechanical strengths through tensile and 3 points flexural tests. The works in the literature studied the dimensional accuracy and the mechanical performances connected to the manufacturing process separately. However, some parts are usually required to satisfy both requirements simultaneously, such as the gears. Therefore, those two aspects must be evaluated, quantified, and put together in a unique final evaluation. For this reason, this work combines the quality of the parts manufactured by VAT photopolymerization, represented by an index connected with the dimensional deviations of the part surfaces already presented in [106, 107], and its mechanical strength through a unique performance index.
In detail, the comparison between a biodegradable resin and a petroleum-based resin is discussed in terms of quality and mechanical performances connected with the manufactured parts by considering the use of the same printing conditions. Starting from the data, the unique performance index is estimated in both cases. The paper is organized as follows: section 2 details the materials, the benchmarks used for the experimental tests, and the manufacturing process. The measuring procedure of the manufactured parts is also illustrated. Section 3 reports the mechanical tests carried out on the two sets of specimens. Section 4 shows the preliminary results in terms of dimensional accuracy and mechanical strength of both materials. Section 5 introduces the proposed Performance Index. In conclusion, Section 6 summarizes the findings and discusses potential future research for the topic.

2.2 Material and methods

An entirely experimental approach was used, which started by designing benchmarks to evaluate dimensional deviations and mechanical strength of parts manufactured using MSLA technology with biodegradable and epoxy resin. Once designed and manufactured, the benchmarks were measured using a 3D scanner. The specimens for bending and tensile tests were submitted to a dynamometer machine. The different steps of the adopted experimental approach are detailed in the following.

2.2.1 Benchmark

Many benchmarks have already been proposed by the literature [108]. They are characterized by protrusions or only cylindrical hollows. The need to introduce a further benchmark was due to the focus on different hollows inside the benchmark (see Figure 2.1) [106]. To test the mechanical properties of the two materials, a tensile specimen following the ASTM-D 638-99 was designed (see Figure 2.2.a). It was preferred the Type IV specimen among the other type due to the dimensions in x and y of the building plate of the printer. Then a specimen for flexural tests was designed following the ASTM-D 790-03 (see Figure 2.2.b).

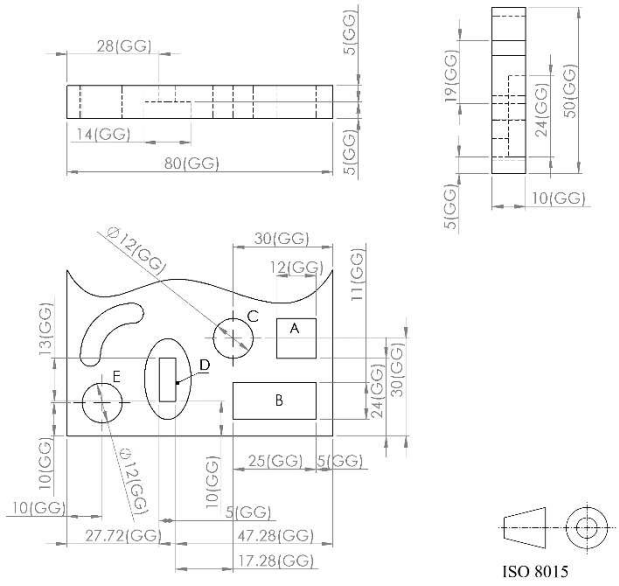


Figure 2.1 Benchmark design, all dimensions in mm **[106]**.

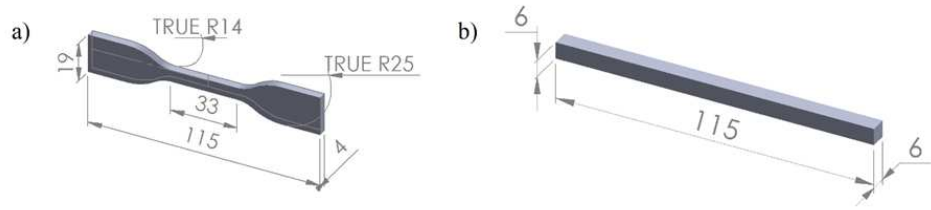


Figure 2.2 (a) Tensile specimen according to ASTM-D 638-99, all dimensions in mm **[109]**; **(b)** Flexural specimen according to ASTM-D 790-03, all dimensions in mm **[110]**.

2.2.2 Materials

Two different resins were used for the experiment. The first is a biodegradable liquid resin made of 45% soybean oil. The ANYCUBIC Plant-based UV Resin is composed of:

- 45% concentration of Fatty acids, soya, epoxidized, Bu esters;
- 30% isooctyl acrylate;
- 15% 2 - [[2,2 - Bis [[(1 - oxoallyl) oxy] methyl] butoxy] methyl] - 2 - ethyl - 1,3 - propanediyl diacrylate;
- 5% 2 - hydroxy -1 - (4 - (4 - (2 - hydroxy - 2 - methylpropionyl) benzyl) phenyl) - 2 - methylpropan - 1 - one;
- 5% colour pigment.

Table 2.1 shows its main properties.

Table 2.1 Biodegradable resin properties.

Property	Standard	Value
Hardness	ISO 2039-2	84 D
Shrinkage	ISO 294-4	3.72-4.24 %
Viscosity	ISO 1628-5	150-300 MPa*s (25 °C)
Glass transition temperature	ISO 75-2	100 °C
Thermal deformation	ISO 11359-2	80 °C
Thermal expansion	ISO 11357-2	95*E-6
Tensile strength	ISO 527	36-52 MPa
Elongation at break	ISO 527	11-20 %
Flexural strength	ISO 178	59-70 MPa

The second type of resin used for this experiment is the PRUSA THOUGH, a non-biodegradable resin. Its composition is:

- 40%-50% Epoxy resin;
- 20%-40% Monomer;
- 2%-5% Color pigment;
- 3%-5% Photoinitiators.

Table 2.2 presents its mechanical properties taken from the technical datasheet.

Table 2.2 Non-biodegradable resin mechanical properties.

Property/Print direction	Method	Uncured XY	Cured XY
Tensile strength	ISO 527	36.0±1.9 MPa	52.0±2.7 MPa
Elongation at break	ISO 527-1	3.00±1.12 %	4.20±0.19 %
Tensile Modulus	ISO 527	1.14±0.08 GPa	1.25±0.09 GPa
Impact strength - Charpy un-notched	ISO 179	22.1±3.5 kJ/m^2	19.8±4.4 kJ/m^2
Impact strength - Charpy notched	ISO 179	5.93±0.26 kJ/m^2	2.50±0.53 kJ/m^2

2.2.3 Manufacturing process

The first step in manufacturing the sample was designing the file of the CAD's benchmarks and saving them as an STL file. Prusa Slicer® the slicing software was used to display the two benchmarks virtually in the printer's building platform [111]. Both specimens were printed flat on the building plate to optimize the printing time and the material consumption (see Figure 2.3).



Figure 2.3 (a) Benchmark; **(b)** Tensile specimens; **(c)** Flexural specimens

Four benchmarks and ten specimens for both tensile and flexural tests were printed using the MSLA Original Prusa SL1 by Prusa Research for each used resin. The used printing parameters are shown in Table 2.3, where the layer height stands for the height of every single layer, and exposure time is the number of

seconds of curing of each layer during the manufacturing process. The first layer has a longer exposure time than the others to prevent bad adhesion since the print is upside down. The exposure time values were set according to the resin manufacturer specifications for the specific adopted layer thickness value, which was taken from the literature [95, 96, 97]. This technique requires further post-processing operations since printing is made inside the tank. The contours of the final part are impregnated with liquid resin. Therefore, the first step consists of washing the benchmark in isopropanol alcohol to remove the residues, drying it in hot air to eliminate all the alcohol and the final step is the curing process to reach the highest strength and stability of the part. The three steps involve 5 minutes, 3 minutes, and 3 minutes respectively. For that purpose, the Original Prusa CW1 was used.

Table 2.3 Values of used printing parameters.

Parameter	Biodegradable Resin	Non-biodegradable Resin
Print Orientation	0°	0°
Layer Height	0.1 mm	0.1 mm
Initial layer height	0.1 mm	0.1 mm
Exposure time	13 seconds	13 seconds
Initial exposure time	70 seconds	45 seconds

2.2.4 Measurement process

The four benchmark parts in Figure 2.1 were measured using an optical measurement system based on fringe projection. This method is based on scanning the object from different angles to obtain the 3D model. It was used the ATOS Core 200 by GOM, which is a scanner for components up to 500mm [112]. If the part is larger than the measuring area, it is possible to make successive scanning acquisitions on different areas of the part that are put together in order to obtain the 3D CAD model of the part. The technical information is shown in Table 2.4.

Table 2.4 ATOS Core 200® Technical data.

Data	Value
Measuring area	200 x 150 mm
Working distance	250 mm
Max resolution	0.08 mm
Sensor dimensions	206 x 205 x 64 mm

The scanning device comprises two cameras and a fringe projection unit that projects precise fringe patterns on the printed part (see Figure 2.4). Using the Triple Scan Principle, the cameras can calculate the coordinates from three different ray intersections resulting in a point cloud mesh. To prevent reflection onto the object's surface, Aedrox NQ1 spray was applied to reach the best scanning quality. Then, some reference markers were implemented to let the GOM Scan software automatically recognize all the photograms and combine those properly to create the 3D mesh in an STL file.

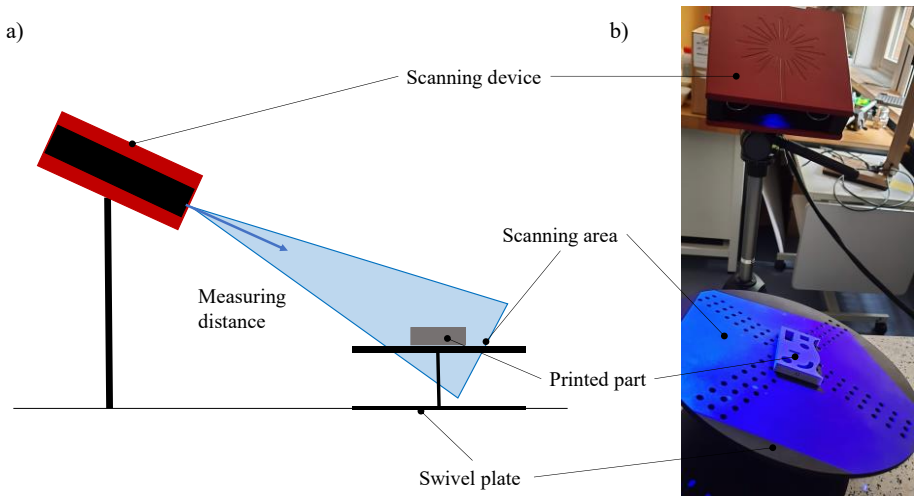


Figure 2.4 (a) Measurement system overview; **(b)** Image capture process.

The second step loaded the STL file into another software called GOM Inspect [113], together with the CAD model of the benchmark. By combining the CAD model and the STL file, it was possible to analyze the deviations between the measured part's dimensions and those nominals' dimensions.

2.2.5 Tensile test

Under the ASTM D638, twenty type IV tensile specimens were tested, ten for each of the two resins. An Instron 5586 universal testing machine with a load cell of 5kN was used for the test. The gap between the clamps was 70mm (see Figure 2.5.a), and the testing speed was 5 mm/min, in accordance with the classification of the material described in the ASTM D883 [114]. The procedure started by inserting the specimens between the clamps and blocking the specimens to prevent some slippery during the traction phase. To keep the specimens in tension, a preload of 0.1 kN was applied. Then the test started until the specimen broke (see Figure 2.5.b).

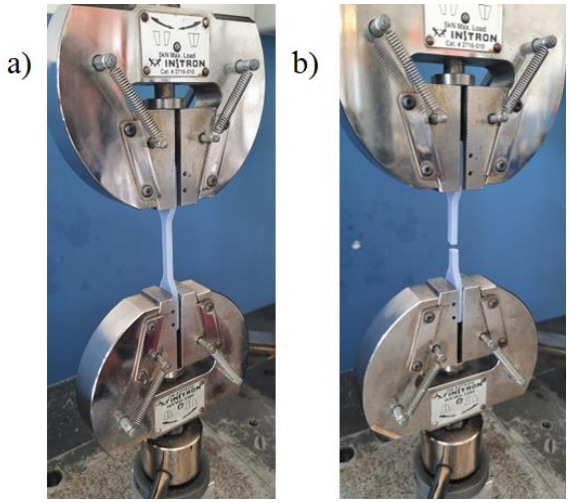


Figure 2.5 (a) Specimen position; **(b)** End of the test.

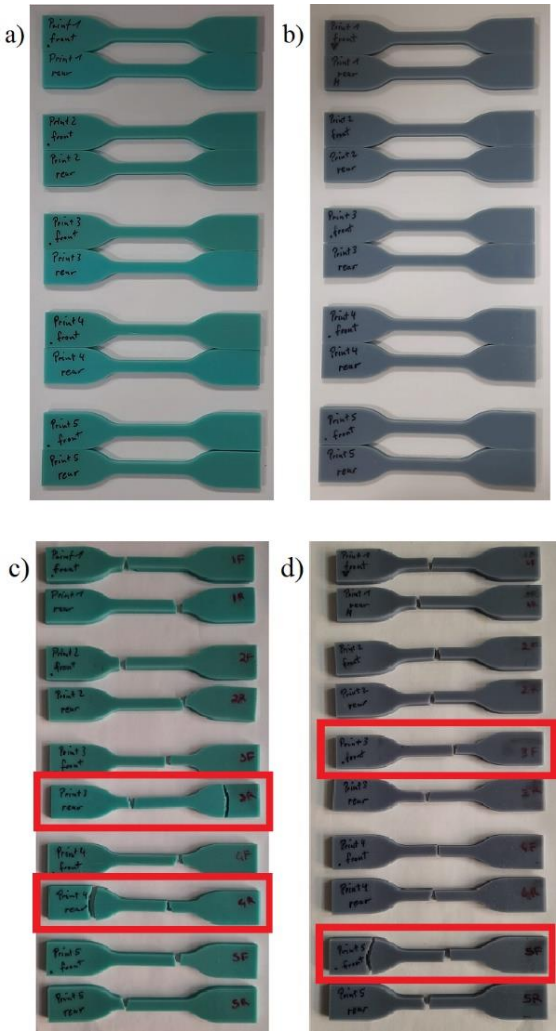


Figure 2.6 Tensile specimens before and after the test: **(a, c)** Prusa resin; **(b, d)** Anycubic resin (specimens with delamination are highlighted in red).

Two of the ten specimens manufactured with the non-biodegradable resins were considered defective since they broke inside the clamps. In contrast, one specimen had the same problems for the biodegradable resin, and another was removed for a delamination problem during the print. Hence, they were not considered in further analysis (see Figure 2.6.c, d).

2.3 Mechanical tests

2.3.1 Three-points flexural test

The machine used for the tensile tests was used for the three points flexural ones. The method used for the test followed the standard. The radii of the supports were 5 mm each with a distance, also called support span, of 96 mm, 16 times the thickness of the specimens. Even the radius of the loading nose was 5 mm.
Once the width and the thickness of each specimen were calculated with a micrometer, the specimen was placed on the two inferior supports at a distance previously defined (see Figure 2.7.a); the loading nose had to be moved to touch the surface of the specimen for all the tests, and the supports must be parallel. By following the Procedure A of the ASTM-D 790-03 standard, the rate of crosshead motion was 2.56 mm/min (see Figure 2.7.b).

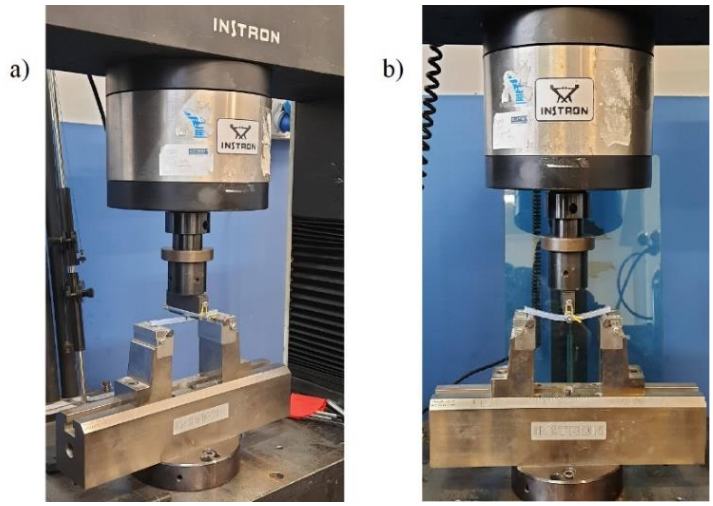


Figure 2.7 (a) Specimen position; **(b)** Crosshead motion.

The test continued until the sample broke. Not all the specimens were considered for the analysis for some delamination defects or wrong breaking during the test (see Figure 2.8.c, d).

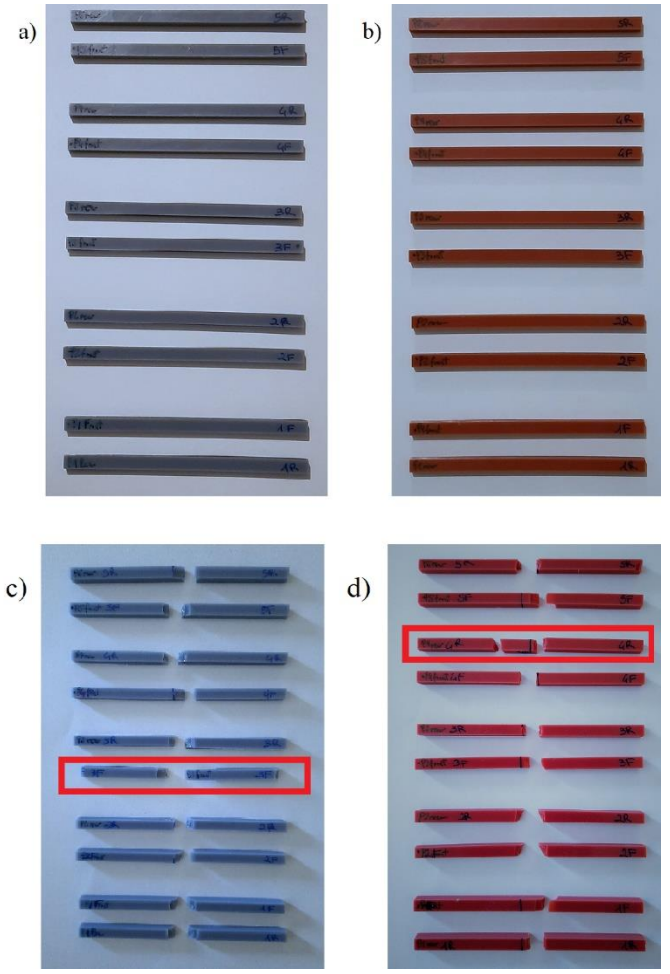


Figure 2.8 Flexural specimens before and after the test: **(a, c)** Anycubic resin; **(b, d)** Prusa resin (specimens with delamination are highlighted in red).

2.4 Results

2.4.1 Measurement results

All the benchmark features were nominated starting from the square and rectangular pockets, as shown in Figure 2.1. Once measured; the obtained dimensions x_i were compared with the nominal ones $x_{i,nominal}$. The features were divided into two main categories, internal and external. The external features define the boundary of the part where the material is inside it. On the other hand, internal features define the boundaries of the part surrounded by the material.

Table 2.5 shows the measurement results of all the benchmark features in terms of the average value and the standard deviation calculated on the four measured parts. Moreover, the percentage difference between the average of the measurement values and the nominal value is called Variation Var_i according to:

$$Var_i = \frac{\mu - x_{i,nominal}}{x_{i,nominal}} \cdot 100\ \% \qquad (2.1)$$

where μ stands for the average of the measurement values for each dimension.

Table 2.5 Biodegradable resin and non-biodegradable resin dimensional results.

			Biodegradable Resin			Non-biodegradable Resin		
Type of feature	Measurements	Nom value in mm	μ in mm	σ in mm	Variation in %	μ in mm	σ in mm	Variation in %
Internal	Length	80	80.029	0.025	0.04	80.143	0.089	0.18
	Thickness	10	10.018	0.007	0.18	9.858	0.065	-1.42
External	Diameter C	12	11.939	0.016	-0.51	11.951	0.048	-0.41
	Diameter E	12	11.944	0.023	-0.47	11.993	0.037	-0.06
	Length D	13	12.972	0.030	-0.22	12.999	0.044	-0.01
	Width D	5	4.976	0.071	-0.48	5.017	0.030	0.35
	Length A	12	11.989	0.004	-0.09	11.916	0.028	-0.70
	Width A	12	11.966	0.028	-0.28	11.884	0.027	-0.97
	Length B	25	24.859	0.047	-0.56	24.850	0.033	-0.60
	Width B	11	11.028	0.040	0.26	11.048	0.033	0.44

For the bio-resin, the percentage difference values range from 0.04 % to 0.18 % for the dimensions of external surfaces and from -0.56 % to 0.26 % for internal ones. Considering the parts made with non-bio resin, the values of the external dimensions range from -1.42 % to 0.18 %, and the internal ones from -0.97 % to 0.44 %. The biodegradable resin shows narrower ranges of variation than non-bio resin. This is due to the different shrinkage of crosslinking the two distinct resins [18].

2.4.2 Mechanical results

An Analysis of Variance (ANOVA) was performed through the software Minitab19 to investigate the influence on the mechanical response using biodegradable and non-biodegradable resins [115]. The results in Table 2.6 demonstrate how the difference between bio and non-bio resins is statistically significant in strength and strain. Its p-value is extremely low, and according to the high F-value, the resin type greatly influences the tensile response. The average value from the tensile test, in terms of Ultimate Tensile Strength (UTS_μ) and elongation at break (ε_μ), shows that the bio-resin strength is lower than the non-bio resin; conversely, its elongation is higher (see Table 2.7).

Figure 2.9 shows that the non-biodegradable resin has the lowest strain, indicating that the molecules in the cured resins have high interatomic bonding due to creating a three-dimensional network and strong chains, making the material tough [116].

Since its difficult to absorb stress, the tensile strength of non-bio resin is higher than bio-resin; this leads to the conclusion that rigid structure contributes to higher mechanical properties [117].

Table 2.7 shows the results from the flexural tests, considering the average Ultimate Flexural Strength (UFS_μ) and elongation at break (δ_μ). The bio-resin demonstrates more ductility in this case, leading to a more extended elongation before breakage; this difference is statistically significant, as shown by the ANOVA results of Table 2.8, with a p-value lower than 0.05. The ESO inside the resin acts as a plasticizer, imparting more flexibility to the chains and enchanting flexibility properties (see Figure 2.10) [118]. In addition, it is demonstrated that epoxy resins reinforced with a biodegradable polymer, such as ESO, provide good mechanical properties that are similar to those of a non-bio resin, as shown by the ANOVA results of Table 2.8, and could be used as a toughening agent [105].

Table 2.6 ANOVA results of UTS and maximum strain value from tensile tests (DF = Degree of Freedom; Seq SS = Sequential sums of squares; Adj SS = Adjusted sums of squares; Adj MS = Adjusted mean squares).

UTS						
Source	**DF**	**Seq SS**	**Adj SS**	**Adj MS**	**F-value**	**p-value**
Material	1	832.11	832.11	832.11	175.45	0.000
Error	14	66.40	66.40	4.74		
Total	15	898.51				
ε						
Material	1	0.0016736	0.0016736	0.0016736	84.42	0.000
Error	14	0.0002763	0.0002763	0.0000197		
Total	15	0.0019499				

Table 2.7 Biodegradable resin and non-biodegradable resin mechanical results.

Resin	**Tensile Test**		**Three-points Flexural Test**	
	UTS_μ in MPa	**ε_μ in mm/mm**	**UFS_μ in MPa**	**δ_μ in mm/mm**
Biodegradable Resin	50.65±2.06	0.085	67.99±5.96	14.80
Non-biodegradable Resin	65.61±6.48	0.066	62.53±26.49	9.86

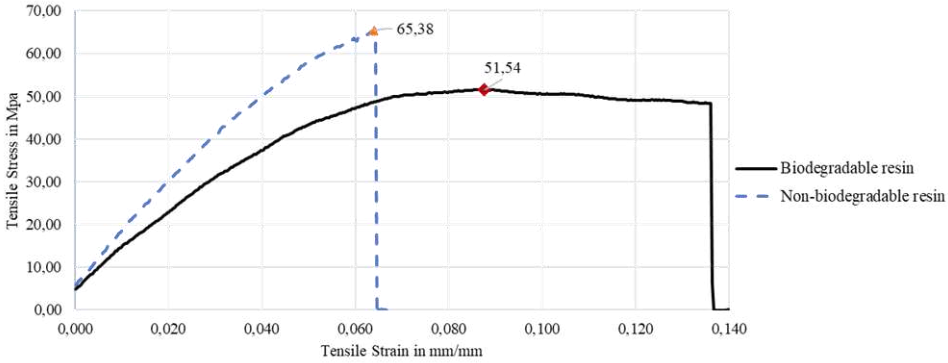


Figure 2.9 Tensile stress-strain curve. The maximum stress is highlighted on the curves.

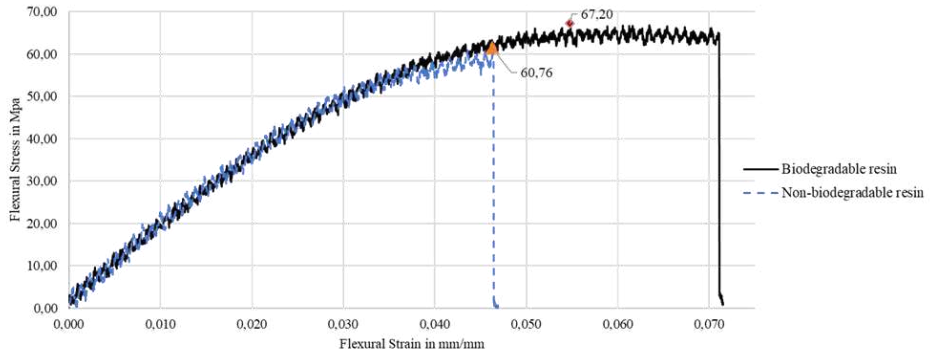


Figure 2.10 Flexural stress-strain curve. The maximum stress is highlighted on the curves.

Table 2.8 ANOVA results on UFS and maximum strain value from flexural tests (DF = Degree of Freedom; Seq SS = Sequential sums of squares; Adj SS = Adjusted sums of squares; Adj MS = Adjusted mean squares).

UFS						
Source	**DF**	**Seq SS**	**Adj SS**	**Adj MS**	**F**	**p-value**
Material	1	104.41	104.41	104.41	2.03	0.180
Error	12	617.23	617.23	51.44		
Total	13	721.74				
δ						
Material	1	0.0012957	0.0012957	0.0012957	65.18	0.000
Error	12	0.0002683	0.0002683	0.0000197		
Total	13	0.0015342				

2.5 Discussion

Commonly a manufactured part involves many features and, therefore, many dimensional deviations of these features. To characterize the part's quality, it is necessary to put together the dimensional deviations in a unique parameter. This is the aim of the Dimensional Performance Index (DPI) associated to a manufactured part [99]:

$$DPI_{Part} = \sqrt{\sum_{j=1}^{m} \sum_{i=1}^{n} DR_{ij}^{2}} \text{ in mm} \qquad (2.2)$$

where DR_{ij} stands for the i-th dimensional deviation associated with j-th feature of each manufactured part. The dimensional deviations were evaluated as the difference between the measured and the nominal values.

Table 2.9 shows that DPI values are stable for the two resins, but the biodegradable one shows a better dimensional accuracy of its parts, since DPI values are smaller than those due to the non-biodegradable resin. The ANOVA was performed on the DPI to verify the influence of the resins. This difference is statistically significant, as shown by the p-value less than 0.05 in Table 2.10. This means that bio-resin allows for manufacturing parts more accurately.

Table 2.9 Dimensional Performance Index (DPI). (Smaller is better).

	DPI_{Part} in mm	
Benchmark	**Biodegradable Resin**	**Non-biodegradable Resin**
1	0.19	0.31
2	0.18	0.30
3	0.17	0.30
4	0.19	0.29

Table 2.10 ANOVA results on DPI values (DF = Degree of Freedom; Seq SS = Sequential sums of squares; Adj SS = Adjusted sums of squares; Adj MS = Adjusted mean squares).

Source	**DF**	**Seq SS**	**Adj SS**	**Adj MS**	**F**	**p-value**
Material	1	0.035280	0.035280	0.035280	128.62	0.000
Error	7	0.001920	0.001920	0.000274		
Total	8	0.037200				

Since a manufactured part has its use and should withstand efforts, as well as having a certain dimensional quality, an overall Performance Index (PI) that takes into consideration both mechanical strength and dimensional deviations was created as follows:

$$PI_{Part} = \frac{US_{Avg}}{DPI_{Part}} \text{ in MPa/mm} \quad (2.3)$$

where DPI_{Part} is the dimensional index, and US_{Avg} is the ultimate strength of the material with which the part is manufactured. Considering that in a printing process, more than one part is built, the average value of the complex index is:

$$PI = \frac{US_{Avg}}{DPI_{Part_{Avg}}} \text{ in MPa/mm} \quad (2.4)$$

where $DPI_{PartAvg}$ represents the average value of the n manufactured parts.

The PI increases if the mechanical strength increases and the DPI decreases. Therefore, the bigger the PI value better the manufactured product.

Table 2.11 shows the two resins' PI values connected with tensile and flexural strengths. The first two columns show that the bio resin's PI is better because the quality defined with the DPI is so much lower than non-bio resin that puts in the denominator of a ratio where the numerator of the tensile strength of biodegradable resin is lower than the non-biodegradable one, causing the overall index to be higher.

The last two columns show that bio-resin is better in both flexural strength and dimensional quality; therefore, the overall index is significantly better than the overall index of non-biodegradable resin.

The percentage variation of PI among the four manufactured parts is at a maximum of 10%, so the performance index is stable.

Table 2.11 Complex index of each benchmark per mechanical strengths (bigger is better).

Benchmark	PI_{Part} in MPa/mm			
	Tensile Test		Three-points Flexural Test	
	Biodegradable Resin	Non-biodegradable Resin	Biodegradable Resin	Non-biodegradable Resin
1	266.56	211.64	357.87	201.72
2	281.37	218.69	377.75	208.44
3	297.92	218.69	399.97	208.44
4	266.56	226.23	357.87	215.63

Table 2.12 Complex index for both resins. It was taken into consideration separately the mechanical strengths (bigger is better).

Resin	PI in MPa/mm	
	Tensile Test	Three-points Flexural Test
Biodegradable Resin	277.51	372.57
Non-biodegradable Resin	218.69	208.44

Since the index is stable, it was averaged in Table 2.12. This index can be used to give a qualitative index of a set of parts produced under the same condition. The results obtained further emphasize what was explained earlier.

2.6 Conclusion

In the last decade, many substitutes for petroleum plastic have been investigated. Bio-based resin with ESO is one of those. This work investigates the possibility of substituting an epoxy resin with a bio-based resin to obtain parts by VAT photopolymerization. An experimental approach was used to achieve this aim: some benchmarks were designed and manufactured with biodegradable (Anycubic Plant-UV) and non-biodegradable (Prusa Though) resins through an MSLA printer and measured using a scanner.

The first comparison deals with the accuracy of the manufactured parts.

According to the measurement results, the percentage difference between the measured and nominal dimensions for Anycubic varies from 0.04 % to 0.18 % for exterior dimensions and from -0.56 % to 0.26 % for interior dimensions. The percentage difference between the exterior dimensions of the benchmark manufactured with Prusa resin and the nominal ones varies from -1.42 % to 0.18 %, and the interior dimensions range from -0.97 % to 0.44 %. The first comparison shows that bio-based resin manufactures parts dimensionally more accurately than traditional resin does.

The second comparison takes into account the part strength. some parts are required to satisfy both the requirements at the same time, such as the gears. Therefore, those two aspects need to be controlled and put together in a unique final evaluation. Tensile and flexural specimens using both resins were manufactured and tested. Non-biodegradable resin is more rigid once cured, so its UTS is higher than biodegradable resin; the values are 65.61 MPa and 50.65 MPa, respectively. Although between the bio-based specimens, the variation is smaller, so it could be denoted that there is a better repetition in the tests. Regarding flexural strength, bio-based specimens show enchanting flexibility with higher elongation and the same UFS as petroleum resin. The ANOVA tests supported the results, showing a statistical dependency on strength and strain, considering the type of resin used. In conclusion, the biodegradable resin can be used as a substitute for response to a more ductile behavior in the part.

A DPI was calculated to express the quality of the part manufactured by MSLA. It was estimated with the part by combining the dimensional deviations connected with the part features. The smaller its value, the greater the quality of the part.

Finally, a PI was calculated considering the mechanical strength applied to the benchmark area. Since the bio-based resin has lesser dimensional deviations than non-bio, the PI is higher when considering the tensile strength. Likewise, the flexural strength is better than the petroleum-based resin, so the overall index is also better. The percentage variation of the PI is 10 %, so it is considered stable.

Those two indexes could be used to compare different technologies using one benchmark. Furthermore, it is possible to make tests on multiple materials and choose the best one for the needed application. By optimizing the specimens, it will be possible to acknowledge how the mechanical performance is affected by the features in the part and choose the optimal one.

Further studies aim to extend the use of a performance index by considering geometrical deviations and other additive manufacturing technologies.

Chapter 3 From MSLA to FDM: Process Control and Performance Indices in AM

Valentina Vendittoli[1]

[1] Department of Civil and Mechanical Engineering, University of Cassino and Southern Lazio, via G. di Biasio 43, 03043 Cassino, Italy

3.1 Introduction

AM technologies, such as MSLA and FDM, offer unique advantages depending on their intended applications. This chapter facilitates a transition between the discussion of MSLA, which was presented in Chapter 2, and the subsequent focus on FDM, which will be addressed in Chapters 4 to 9. MSLA and FDM are potent technologies, with MSLA excelling in high-resolution, intricate parts and FDM being more suited to larger-scale production with a broader range of materials. This chapter aims to elucidate the distinctions between these technologies regarding their intended applications and establish a foundation for comprehending the role of FDM in the subsequent series of chapters.

3.2 Review of MSLA: Achievements and Limitations

Chapter 2 introduced MSLA, a resin-based AM process that uses UV light to selectively cure layers of photopolymer resin. This process enables the creation of intricate, high-precision parts, making it particularly suitable for applications that require fine geometric detail and smooth surface finishes. MSLA has proven effective in medical devices, dental prosthetics, and other sectors where precision is paramount. The Chapter also introduces two key metrics, DPI and PI, which evaluate the dimensional accuracy and mechanical strength of parts produced using MSLA. Its ability to deliver finely detailed components aligns it with applications where such precision is essential. However, the scale and mechanical requirements of certain parts may call for alternative approaches, particularly in cases where production needs to be more cost-effective or adaptable to higher volumes. MSLA's resin-based processes focus on highly specialized use cases where material properties such as biocompatibility or surface finish quality are top priority.

3.3 Rationale for Transitioning to FDM

As the focus of this thesis shifts to FDM, it becomes clear that the technology's broader application stems from its inherent adaptability and material versatility. Known for extruding thermoplastic filaments, FDM offers a broader range of material options, allowing the use of biodegradable polymers such as PLA and engineering materials such as ABS and PETG. The continued development of new filaments, including composites and reinforced materials, has expanded FDM's role in the automotive, aerospace and consumer goods industries. This

continuous innovation in filament technology enables FDM to meet various industrial needs, from prototyping to functional end-use parts [119]. The widespread use of FDM across industries can also be attributed to its scalability and cost-effectiveness. Compared to other AM processes, FDM is particularly advantageous for applications requiring large build volumes, where cost control and material flexibility are critical factors, and the availability of a wide range of thermoplastic filaments, which continue to evolve with improved mechanical properties and sustainability, positions FDM as a versatile solution for a wide range of applications. In contexts where rapid prototyping and functional testing are prioritized, FDM offers an efficient and adaptable route to production [4]. Despite the differences in their processes, MSLA and FDM are evaluated using performance indices that assess dimensional accuracy and mechanical strength. The emphasis on evaluating these indices highlights the importance of balancing accuracy and mechanical properties by considering the specific functional requirements [120]. FDM's number of process parameters offers greater flexibility, making it easier to fine-tune the printing process for optimal results. The use of ANN models, discussed in Chapter 6, introduces advanced predictive capabilities that can improve the dimensional accuracy and mechanical performance of FDM parts. Such optimization techniques are valuable for applications that require precision in larger or more complex structures, where real-time adjustments can improve overall performance [121]. In this context, the transition to FDM reflects a technological shift and an expansion of the scope of the thesis to explore a broader range of materials and scalable production techniques. As FDM continues to be refined through material advancements and AI-driven optimization, its applicability across multiple sectors continues to grow. Moreover, the transition from MSLA to FDM technology demonstrates that the indices and the methodologies used to optimize more than one part's performance are completely general.

3.4 Conclusion

This chapter has delineated the principal reasons for transitioning from MSLA to FDM, underscoring the interdependent strengths of these technologies. FDM offers advantages in terms of cost-efficiency, scalability, and material flexibility, which makes it a more suitable option for applications that require more extensive, more substantial parts. Furthermore, the integration of ANN for real-time optimization enhances the potential of FDM to achieve high-quality parts. As the

thesis progresses, Chapters 4 to 9 will examine these benefits in greater detail, focusing on how AI-driven optimization can further improve FDM's performance indices.

Chapter 4 Geometrical Deviations of green Parts due to Additive Manufacturing: a Synthetic Geometrical Performance Index

Valentina Vendittoli[1], Wilma Polini[1] and Michael S. J. Walter[2]

[1] Department of Civil and Mechanical Engineering, University of Cassino and Southern Lazio, via G. di Biasio 43, 03043 Cassino, Italy

[2] Faculty of Engineering, University of Applied Sciences Ansbach, Residenzstr. 8, 91522 Ansbach, Germany

Published in: Procedia CIRP (2022), 114, pp. 159–164
https://doi.org/10.1016/j.procir.2022.10.036

Abstract

This work presents a synthetic geometrical performance index that combines all dimensional and geometrical deviations of a printed part to express its quality. The smaller the value of this index, the greater is the part quality. The paper demonstrates the effectiveness of this index by printing a set of parts through Fused Filament Fabrication in a biological polymer. These parts, characterized by representative hollows, were measured by optical scanning technology. The proposed methodology shows the advantages of this index thus future work can focus on further printing techniques and varying process parameter values.

Keywords: Fused Filament Fabrication; PLA; geometrical deviation; additive manufacturing.

4.1 Introduction

AM is a new industrial process with which objects of various shapes and sizes are made, by the deposition of layers of material on a build plate. For complex printing, support structures are usually created to stabilize the part and to reduce deformations that may occur during printing. Among the main advantages, there is the possibility to increase the complexity of the part geometry, especially of inside pockets. Moreover, there is the printing speed, depositing layers of material, often reducing the time of manufacturing of the part compared to the realization of the same with traditional techniques.

This also brings less waste of materials, once the part is made and submitted to post-processing operations, only supports are considered printing waste. Furthermore, manufacturing parts with AM techniques leads to minimizing final printing costs.

FFF is widely spread among all AM techniques due to its ease of use. This technique is very cheap compared to other AM technologies. Some printers are equipped with more than one nozzle that leads to the minimization of the printing time [122]. Furthermore, where necessary, support can be printed with materials (such as dissolvable) using a second nozzle, to let them easy to remove.

In general, printed parts do not need post-processing operations other that the disposal of supports. One of this includes the removal of the build plate adhesion. Among all, most of the printing involves the use of the skirt type of build adhesion. This helps to ensure that the filament is well melted and to check if the plate is well levelled.

Different types of thermoplastic polymers can be used with FFF printers, with different mechanical characterizations. Some of them include ABS, PLA, Nylon, Polyethylene Terephthalate (PET), and Thermoplastic Elastomer (TPE) [123]. Among all materials, PLA is a widely used material in AM since it is a polymer made from renewable sources such as corn starch, sugar cane or wood [31]. This semi-crystalline polymer is widely in demand due to its ease of use and uses in different areas including biomedical engineering due to its biodegradability and non-toxicity [124]. Furthermore, it is resistant to a wide range of chemical solvents and denotes good mechanical characteristics.

The manufacturing of parts in biodegradable PLA by FFF is the focus of this work; it is in line with the concept of green manufacturing or sustainable manufacturing

as a method for manufacturing that minimizes waste and reduces the environmental impact. Sustainable manufacturing may be defined as a system that integrates product and process design issues with issues of manufacturing, planning, and control in such a manner as to identify, quantify, assess, and manage the flow of environmental waste to ultimately reduce the environmental impact to that of the self-recovery capability of the Earth could deal with while also trying to maximize resource efficiency. When it comes to preparing a good print, different parameters are considered to fulfill the given requirements of the final part. Moreover, PLAs of different manufacturers have different characteristics, and this can occur to filaments of the same brand but different colors. This might bring different specimen weights due to the type of colorant used in the chemical composition [125].

Furthermore, choosing the optimal configuration of an FFF printed part imply the outcome of dimensional deviations [126]. Deviations indicate how the dimensions of a printed part approach the nominal values. This also represents the accuracy of the printer used. To achieve good results and define a model with optimal parameters to directly insert, different combinations of parameters have been analyzed and the effects studied in multiple works.

Since there is gravity's influence, it is important to choose the correct position on the building plate to prevent distortions. In addition, to minimize geometrical deviations, layer thickness should be proportional to the nozzle diameter and adjust with the feed rate. In addition, the height of the printed part should be an integer multiple-layer thickness. Building orientation determinates also changes in the mechanical properties of the printed parts because it changes the direction of deposition of the layers and surface roughness [127]. Flat orientation determinates the minimum flatness error compared to the other building orientations. This depends on the direction of extrusion of the material and on how to set the optimal cooling process [128].

The combination of the print head speed and excess of material deposited on the plate, bring to the "bathtub ring" [125, 129, 130]. According to layer height, the extrusion temperature should be adapted as the temperature rises, the effect on deviations is more significant. Furthermore, molted material tends to become more fluid (lower viscosity) and flow uncontrollably from the nozzle [129, 131]. The warp deformation of the printed parts was correlated to layer thickness and extrusion velocity, while the dimensional deviations with filling velocity and line

width compensation in [132]. Some methods to reduce warp deformation were discussed in [133]. Models based on correction factors on printing parameters are created to prevent dimensional deviations. This involves many parameters that need to be studied [134, 135].

This work aims to study both dimensional and geometrical deviations of parts manufactured with FFF technology, using PLA. The study of dimensional and geometrical deviations connected with a manufacturing process is very important to achieve high-quality parts and to be able to assemble the obtained parts to arrive at assembly products with the desired functional requirements [136, 137].

Previous works of the literature studied geometrical deviations of cylindrical or planar features as a function of process parameters [135, 138]. This paper aims to consider many different geometrical deviations of hollows created inside a part since they involve a more difficult heat exchange during part cooling down. The paper aims to show an index to express synthetically the geometrical quality of a part or a feature of it that is printed by FFF in PLA.

In the following, the paper presents the considered benchmark, its manufacturing process, and the adopted procedure used to measure the manufactured parts. Then, the obtained different geometrical deviations are shown in detail, and they are summarized by the developed synthetic index of quality.

4.2 Material and methods

Many different parts were proposed by the literature to investigate the geometrical performances of AM processes [108]. However, they are made mainly by protrusions, while the aim of this paper is to focus on hollows created inside a part, since they involve more difficult heat exchanges during cooling down. Moreover, many different hollows were considered to focus the attention on as many geometrical deviations of different surfaces as possible. The considered benchmark is a rectangular parallelepiped of 80 mm x 50 mm x 10 mm, of which one of the lateral surfaces was modified using a B-Spline function, to create a smooth curve (see Figure 4.1). It is characterized by three square pockets, two holes, one elliptical pocket and one curvilinear buttonhole. The benchmark was produced through the FFF S3 printer by Ultimaker [139]. It has a fixed build plate and a print head that makes all the movements in the three axes. It was equipped with a print head composed of a nozzle of 0.4 mm diameter. It adopts the FFF by manufacturing AM parts through the melt of thermoplastic materials extruded

through a nozzle (see Figure 4.2). At the beginning, the material is in a solid-state in the form of a filament spool. The process is made inside the extrusion head, which is composed of some resistances that heat the wire to make it soft enough to let it pass into a nozzle, where the passage from solid to liquid takes place. At this point, the drops of liquid material are placed on the building platform in layers. Every layer after the deposition is cooled down in atmosphere or through the printer head's fans, depending on the type of material used.

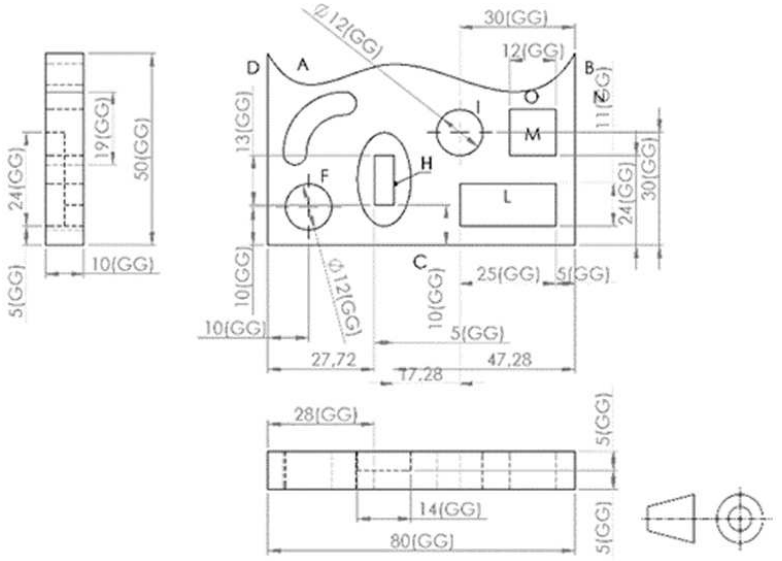


Figure 4.1 Considered benchmark.

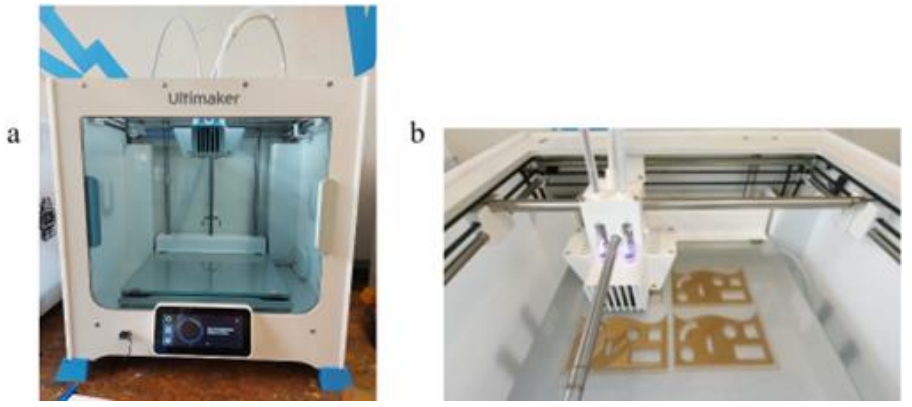


Figure 4.2 (a) Ultimaker S3 machine; **(b)** Printing of the parts.

The parts were made using a PLA filament manufactured by BASF 3D Printing Solutions B.V (a European company in the chemical and oil sector). The filament

has a diameter of 2.85 mm. This Ultrafuse PLA natural filament is obtained by the condensation of lactic acid obtained by corn starch and can be biodegraded if composted. The first step to realize the sample was the construction of the file of the CAD's benchmark by SolidWorks® software and it was saved as .STL file. The part was sliced with Ultimaker Cura®, a software whose aim is to display the part in a virtual printer's build plate to set all the printing parameters and simulate the realization of the part [139]. Therefore, four parts were manufactured, to have statistically significant measures for a demonstrative study as reported in [140], and to cover the building platform so that in the experiment the deviations that occurred in the different positions were taken into account. The positioning of the parts is predefined by the slicing-software following its standards. For this work, the values of some process parameters were chosen according to the default settings of the Cura, combined with optimal parameters that could be found in the literature [129, 128, 131]. They are shown in Table 4.1, where layer thickness indicates the height of every material layer deposed from the print head, the first layer is set with a higher height for making the adhesion stronger. Furthermore, the infill pattern represents the internal structure of the benchmark with its infill percentage that determines how much material is printed inside the shell. The printing temperature at which filament is melted is chosen following the material's datasheet and the chosen print speed. Since PLA filament, compared to other materials, is less affected by shrinkage, a skirt plate adhesion is preferred. This is a line printed around the part to prime the extrusion nozzle and clean it from residual filament before starting the actual print.

Table 4.1 Values of printing parameters.

Parameter	Value
Print Orientation	Horizontal
Layer Height	0.2 mm
Initial Layer Height	0.22 mm
Infill Percentage	20 %
Infill Pattern	Grid
Printing Temperature	220 °C
Printing Temperature Initial Layer	230 °C
Print Speed	80.0 mm/s
Wall Speed	50.0 mm/s
Outer Wall Speed	40.0 mm/s
Build Plate Adhesion Type	Skirt
Skirt Line Count	1
Skirt Distance	3.0 mm

4.2.1 Measurement procedure

The four manufactured parts were measured using an optical measurement system based on fringe projection. This method is based on scanning the object from different angles to obtain the 3D model. It was used a 3D scanner provided by GOM, the ATOS Core 200®, which can mesh components up to 500 mm, whose technical parameters are shown in Table 4.2. To carry out the measurement, fringe patterns are projected onto the surfaces of the part and recorded by two cameras that operate according to the Triple Scan Principle; it allows to calculate the coordinates of the 3D surface points from three different ray intersections. For better scanning quality, Aedrox NQ1 spray was used to give the parts a matt finish to prevent light reflections. The part, once prepared, was placed on the swivel plate to begin the image capture process (see Figure 4.3).

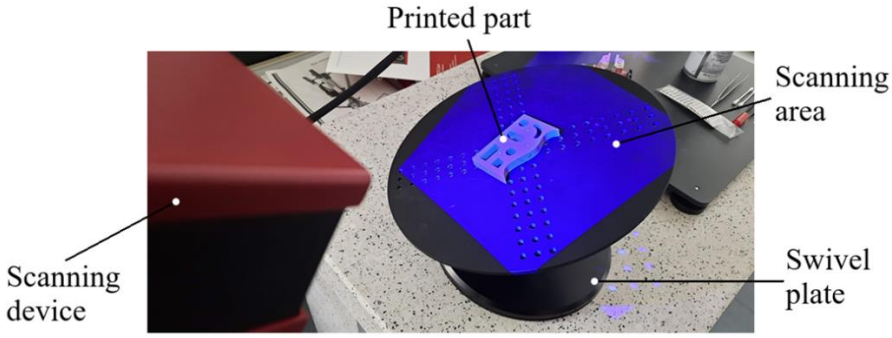


Figure 4.3 Image capture process.

Table 4.2 Technical data of ATOS Core 200®.

Data	Value
Measuring area	200 x 150 mm
Working distance	250 mm
Max resolution	0.08 mm
Sensor dimensions	206 x 205 x 64 mm

The measurement process started with the preparation of the single parts. On each part's surface, some markers were applied that were automatically detected by the camera during scanning and used to align the scans rightly (see Figure 4.4).

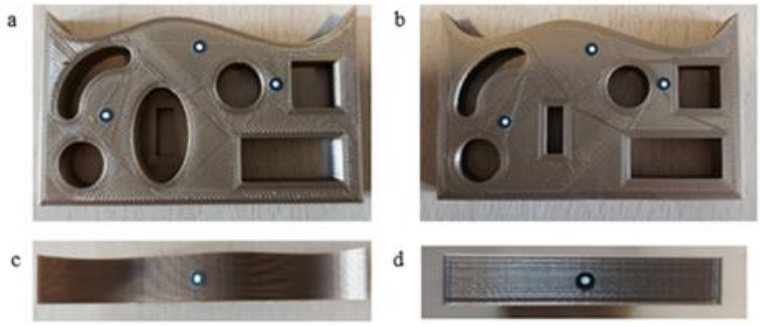


Figure 4.4 Reference points on part's surfaces: **(a)** top; **(b)** bottom; **(c)** curved; **(d)** lateral.

To acquire the photos and to transform them into 3D images of the measured part, software, known as GOM Scan was used. It automatically computes the photograms and creates the 3D mesh of the part. The GOM Inspect software was used to compare the CAD file in STL format with the measurement images of the part's

surfaces. The measurement points were registered as regards the 3D nominal model using the Gaussian best-fit Method (see Figure 4.5).



Figure 4.5 Construct process on GOM Inspect.

4.3 Results

The measured dimensions of the four printed parts are very similar; therefore, no significant influence of the location of the part on the build plate was observed.
The four values of each dimension were put together to evaluate the maximum, minimum, mean values, and standard deviations.
The distance of the measured average from the nominal values ranges from 0.02 mm to 0.51 mm. The percentage variation, reported in the last column of Table 4.3, was calculated as:

$$Variation = \frac{\mu - \text{Nominal}}{\text{Nominal}} \cdot 100 \text{ in } \% \qquad (4.1)$$

where μ stands for the average of each measurement.
Results in Table 4.3 indicate how the accuracy is greater for the external surfaces of the part than for the internal one. In fact, the percentage variation ranges from 0.2 % to 0. 4% for external surfaces and from -3.9 % to 3.6 % for internal surfaces. This is probably due to the cooling of the part that is easier and quicker for part external boundary than for internal one, thus involving a lower shrinkage on these surfaces.
The measured geometrical deviations of each considered feature are not affected by the position on the built plate. Therefore, the four values were put together to evaluate the average value of the measured geometrical deviations, shown in

Table 4.4. These values range from 0.01 mm to 0.31 mm, while the obtained standard deviation varies from 0.01 mm to 0.04 mm.

Table 4.3 Dimensional results.

Measurements	**μ in mm**	**σ in mm**	**Nominal value in mm**	**Variation in %**
Distance B-D	80.3	0.01	80	0.4
Length D	50.1	0.01	50	0.2
Distance O-N	10.0	0.03	10	0.2
Diameter cylinder F	11.5	0.02	12	-3.9
Diameter cylinder I	11.7	0.03	12	-2.8
Length H	12.5	0.03	13	-3.9
Width H	5.2	0.02	5	3.6
Length M	11.7	0.04	12	-2.5
Width M	11.7	0.02	12	-2.8
Width L	10.8	0.02	11	-1.8
Length L	24.6	0.01	25	-1.6

Table 4.4 Geometrical results.

Measurements	Max in mm	Min in mm	μ in mm	Range in mm	σ in mm
Circularity F	0.17	0.12	0.14	0.05	0.02
Cylindricity F	0.25	0.19	0.22	0.06	0.03
Location F	0.27	0.17	0.22	0.10	0.04
Perpendicularity F-N	0.06	0.02	0.04	0.04	0.02
Circularity I	0.16	0.14	0.15	0.02	0.01
Cylindricity I	0.23	0.21	0.22	0.02	0.01
Location I	0.16	0.13	0.15	0.03	0.02
Perpendicularity I-N	0.02	0.01	0.01	0.01	0.01
Location H	0.06	0.01	0.03	0.05	0.02
Location M	0.07	0.03	0.05	0.04	0.02
Location L	0.08	0.05	0.06	0.03	0.01
Flatness N	0.22	0.16	0.19	0.06	0.03
Flatness O	0.31	0.23	0.28	0.08	0.03
Parallelism D-B	0.26	0.22	0.24	0.04	0.02
Parallelism O-N	0.34	0.26	0.31	0.08	0.04
Perpendicularity B-O	0.26	0.20	0.24	0.06	0.03
Perpendicularity C-O	0.28	0.22	0.25	0.06	0.03
Perpendicularity D-O	0.22	0.18	0.21	0.04	0.02

4.4 Discussion

Considering the large number of dimensional and geometrical measurements that were carried out and that typically are industrially carried out on a part, it was looked for a way to quantify synthetically the quality of the part manufactured by FFF.

The deviation of the measured average value from a nominal dimension and the evaluated geometrical deviation (such as cylindricity, location, perpendicularity, and so on) represent the uncertainty connected with the FFF process to manufacture a part around the nominal value, that is the nominal dimension in the first

case and the zero value in the second one. Therefore, it is possible to combine the uncertainties connected with the different deviations of a part feature or all the features of a part by summing them. In this way, it was defined as a SGPI that was created and associated with each manufactured feature by combining its dimensional and geometrical deviations. The different contributions were considered independent.

$$SGPI_{Feature} = \sqrt{\sum_{i=1}^{n} DR_i{}^2} \quad (4.2)$$

where DR_i stands for i-th geometrical deviation associated with the manufactured feature among its n-deviations. The larger is SGPI value less accurate is the manufactured feature. The smaller its value, the greater the quality of the feature.

For dimensional tolerances, the deviation range was calculated as the difference between the largest and the smallest values of the manufactured parts. Instead of geometric deviations, the average values were taken into account.
To have a quick average evaluation of each contribution, the average SGPI of a feature was evaluated by dividing the SGPI value connected to each surface for the number of contributions:

$$SGPI_{Feature_{Avg}} = \frac{SGI_{Feature}}{n} \quad (4.3)$$

Table 4.5 shows the obtained results associated with all the features of the manufactured parts. $SGPI_{Feature}$ value ranges from 0.26 mm to 0.35 mm, except for surfaces H, M, L that present values much lower between 0.07 mm and 0.11 mm. The average SGPI value varies from 0.067 mm to 0.105, except for surfaces H, M, and L which presents a value between 0.02 mm and 0.037 mm. This different behavior requires further investigation.
Finally, it was calculated the SGPI of each manufactured part, whose values are shown in Table 4.6. It represents the quality of each part placed on the building platform.

$$SGPI_{Part} = \sqrt{\sum_{j=1}^{m} \sum_{i=1}^{n} DR_{ij}{}^2} \quad (4.4)$$

where DR_{ij} stands for i-th deviation range associated with the j-feature of the manufactured part. The values of the four indices are very similar because the location

on the building plate does not affect the geometrical results, as previously underlined.

Table 4.5 Synthetic Geometrical Performance Index (SGPI) (a smaller SGPI corresponds to a higher geometrical accuracy).

Feature	**Dimensional and geometrical deviations in mm**					**$SGPI_{Feature}$ in mm**	**$SGPI_{avg}$ in mm**
D	L: 0.03	W: 0.08	∥B: 0.24	⊥O: 0.21		0.330	0.083
B	L: 0.03	W: 0.08		⊥O: 0.24		0.255	0.085
C	L: 0.02	W: 0.08		⊥O: 0.25		0.263	0.088
N	L: 0.03	W: 0.02	▱: 0.19	⊥C: 0.25		0.316	0.079
O	L: 0.03	W: 0.02	▱: 0.28	∥ N: 0.31		0.419	0.105
F	Ø: 0.04	○: 0.14	⌭: 0.22	⊥N: 0.04	⌖: 0.22	0.346	0.069
I	Ø: 0.07	○: 0.15	⌭: 0.22	⊥N: 0.01	⌖: 0.15	0.314	0.063
H	L: 0.03	W: 0.06			⌖: 0.03	0.081	0.020
M	L: 0.09	W: 0.06			⌖: 0.05	0.110	0.037
L	L: 0.05	W: 0.05			⌖: 0.06	0.071	0.024

Table 4.6 SGPI for each part.

Benchmark	$SGPI_{Part}$ in mm
Left bottom	1.43
Right bottom	1.43
Left top	1.42
Right top	1.44

4.5 Conclusion

This work deals with green or sustainable manufacturing with a view to Industry 4.0. It aims to evaluate the dimensional and geometrical deviations of manufactured parts made with a biodegradable PLA filament using the FFF technology. This work aims to propose a synthetic geometrical index to give an idea of the quality of the part manufactured by FFF. The obtained results show that the location of the part on the building plate does not affect both dimensional and geometrical deviations of the part. Moreover, the accuracy seems greater for the external surfaces of the part than for the internal ones. The percentage deviation from nominal of the dimensions connected with the manufactured parts ranges from 0.2 % to 0.4 % for external surfaces and from -3.9 % to 3.6 % for internal surfaces. This is probably due to the cooling of the part that is easier and quicker for part external boundary surfaces than for internal ones, thus involving a lower shrinkage on these surfaces. The average value of the measured geometrical deviations ranges from 0.01 mm to 0.31 mm. It appears low for a printing process using polymeric material. A SGPI was calculated to express the quality of the part manufactured by FFF. It was associated with a feature of the part by adding the uncertainties connected with its geometrical deviations and to the part by adding the uncertainties connected with the geometrical deviations belonging to its features. The smaller is its value, the greater is the quality of the part. This index may be used to compare the geometrical performances of different printers to manufacture the same benchmark or to understand if a change in the values of the process parameters of a printing process gets better or worse results. Moreover, it may be used to find the process parameters that minimize its value, considering in one value both dimensional and geometrical deviations. Moreover, the use of a biodegradable filament in 3D printing part involves waste reduction, sustainable production.

Further study involves the use of the proposed index in the manufacturing of the same benchmark with different printing techniques or with different values of the FFF process parameters. Moreover, the independence between the dimensional and geometrical deviations of the same feature will be relaxed.

Other studies are oriented to understand the strength and environmental behavior of this kind of PLA natural filament, to understand in which application they can be substituted to traditional polymers considering also that PLA filaments are made with different renewable sources. To investigate its behavior, further study could be made on the type of infill pattern and percentage to characterize the mechanical strength.

Finally, the transfer of the dimensional and geometrical deviations from parts made with different materials to assembly will be another topic of study, since most industrial products are assemblies that need to be obtained despite the dimensional and geometrical deviations of their components associated with their manufacturing processes.

Chapter 5 Two Performance Indices of Parts in Polylactic Acid Manufactured Through a Material Extrusion Process: Analysis of Their Dependence on Process Parameters

Valentina Vendittoli[1], Wilma Polini[1] and Michael S. J. Walter[2]

[1] Department of Civil and Mechanical Engineering, University of Cassino and Southern Lazio, via G. di Biasio 43, 03043 Cassino, Italy

[2] Faculty of Engineering, University of Applied Sciences Ansbach, Residenzstr. 8, 91522 Ansbach, Germany

Published in: The International Journal of Advanced Manufacturing Technology (2024), 134, pp. 4689–4699
https://doi.org/ 10.1007/s00170-024-14380-3

Abstract

Industrially, some parts, such as gears, are manufactured through additive manufacturing processes. These processes require high mechanical strength and high geometric accuracy. Therefore, combining geometric accuracy with mechanical performances may provide a full understanding of the industrial product. The authors proposed two indices in previous works; the first combines all dimensional deviations from the nominal values, while the second combines the dimensional deviation with the mechanical performances.

This study aims to investigate the effects of printing process parameters on both indices. The results demonstrate the infill percentage, the print speed, the layer height, and the bed temperature exerted on the two proposed indices. The trend of the two indices versus the process parameter values is shown and quantified through relationships. These indices show significant correlations with process parameters, highlighting the need to consider individual and combined effects when optimizing 3D processes.

Understanding the relationships and optimizing these indicators facilitates the identification of optimal process parameters, which leads to improved efficiency and consistency in additive manufacturing operations.

Keywords: Additive manufacturing; Fused Filament Fabrication; PLA; Performance Index; Process parameters.

5.1 Introduction

AM has profoundly reshaped manufacturing processes by enabling the layer-by-layer construction of components, liberating design from the constraints of traditional methods. Among the diverse AM techniques, ME stands out as a 3D printing method that involves continuously depositing a fused filament to realize intricate 3D components [1]. FFF, one of the subsets of the broader field of material extrusion, has gained widespread adoption due to its versatility in processing a wide range of materials, including thermoplastic polymers, ceramics, and metals. While plastic materials are particularly favored due to their commendable mechanical properties and cost-effectiveness, using other materials is also becoming increasingly common. Notably, PLA has emerged as a leading material due to its composition derived from renewable sources such as corn starch or sugar cane, offering both environmental sustainability and material performance [141, 31].
The dimensional accuracy, surface roughness, mechanical performance of components produced using FFF technology, and an understanding of the influencing variables are significant areas of study in the literature [142]. An analysis of the variations in hole size within a linear U-shaped benchmark across three directions demonstrates an underestimation in XY dimensions and an overestimation in Z dimensions, with diameters consistently smaller than nominal values. Furthermore, there are distinct dimensional variations for internal and external features even under equal parameters [42, 41]. A paper identifies the optimal values for minimizing dimensional deviations in XYZ directions; they include an infill rate of 20 % and a layer height of 0.2 mm in Z direction [43]. Matching the extrusion temperature to the layer height is essential to mitigate variations, as these increase with temperature. However, elevated printing speeds can compromise surface quality due to incomplete solidification, while incorrect nozzle temperatures may result in incomplete melting or material flow issues. Key process parameters, such as the nozzle temperature and print speed, directly influence the bonding strength between layers [130, 45]. Typically, the build plate temperature ranges between 50 and 60 degrees Celsius, with central regions experiencing higher temperatures than the periphery. Enclosed printers address this issue through controlled workspaces and managed heat flow. Adjusting fan speed is vital for managing melt solidification and improving print quality, particularly to prevent deformation and enhance print definition during successive layer printing [30].

Further literature studies are focused on the impact of the critical process parameters on mechanical qualities. In a paper, the authors study the effects of printing speed, layer height, and extrusion temperature.
The findings revealed that higher extrusion temperatures led to enhanced interlayer adhesion, while printing speeds that were too high resulted in reduced tensile strength due to non-uniform layer deposition. The optimal parameters identified were a layer height of 0.15 mm, a printing speed of 48 mm/s, and an extrusion temperature of 220 °C [143]. Lower melting temperatures and suitable printing speeds maintain part integrity without compromising geometry. Higher extrusion temperatures enhanced material bonding for maximum tensile strength, while lower printing speeds, in conjunction with printing temperature, resulted in higher strain and stiffness. Moreover, higher cooling speeds were observed to improve geometric accuracy but diminish mechanical strength [144, 145]. A detailed analysis of the internal structure highlighted the influence of infill type, part fill percentage, number of perimeters, and shell thickness. Optimal configurations included a layer height of 0.1 mm, 6 perimeters, and a gyroid infill pattern [146]. In contrast, infill percentage was identified as the most influential parameter, followed by contour thickness and layer height, in determining optimal printing parameters [127]. The impact of layer thickness on the tensile strength of the printed material yielded conflicting results. While some studies observed an improvement in tensile strength with lower layer thickness, others reported an increase in strength with thicker layers [38, 147]. It is evident from previous investigations that the performances of a part obtained by an additive manufacturing process are defined in terms of geometric accuracy or mechanical strength. Scientific papers frequently explore these factors individually. The geometric accuracy is generally investigated through a large set of dimensional tolerances, thus making hard a clear part quality sight. The authors' previous research pursued the proposal of an index that synthetically incorporates a part's geometrical quality, combining all dimensions differences into a coherent dimensional performance index [106]. Industrially there are some sets of parts manufactured through additive manufacturing processes, such as gears, which both require a high mechanical strength and a high geometric accuracy. Therefore, a full knowledge of the industrial product may be obtained by combining geometric accuracy with mechanical performances. The authors proposed in previous works two indices the first combines all dimensional deviations from the nominal values, while the second puts

together the dimensional deviation with the mechanical performances. This composite measure delineates the component's dual quality features, resulting in a comprehensive assessment framework [148].

Currently, no consolidated indicators address the integrated evaluation of geometric deviations and mechanical performance. Although there are numerous specific approaches and tools for measuring each of these aspects individually, a comprehensive analytical framework that unifies them is lacking. This gap represents a significant challenge in the field of system evaluation, as it limits the ability to understand and improve overall performance. It is critical to recognize the interaction of the two indices with the process parameters of the printing approach. As a result, this research uniquely investigates the sensitivity of these indices to various process parameters within a controlled experimental setting. By systematically altering parameters such as printing speed, layer height, and extrusion temperature, this study provides new insights into the robustness and sensitivity of the proposed indices. This comprehensive analysis demonstrates the interaction between the indices and the process parameters, highlighting a novel and integrative perspective that enhances their combined effect on the overall performance of 3D printed parts. The obtained relationship between performance indices and the printing process parameters may be used to set the printing process on the industrial product's quality (mechanical and/or geometric). At the same time, these relationships may be used to improve product quality.

5.2 Material and methods

An experimental approach was adopted, starting with the choice of specimen geometry. Type IV tensile specimens were created following the ASTM-D 638-22 standard [109] and included geometric elements like square and hole pockets (see Figure 5.1). Two internal parts were included in the test specimen to assess geometric differences in the interior surfaces. It is important to note that these parts do not affect the tensile test results because they are situated inside the clamp, maintaining the test's integrity.

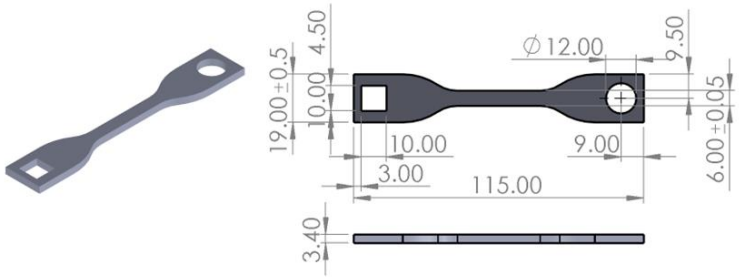


Figure 5.1 Benchmark's technical drawing, dimension in mm.

The Ultimaker S3 FFF printer (Ultimaker, Netherlands) used in this work has a construction volume of 230 by 190 by 200 mm³, presented in Figure 5.2.a, and a resolution of 6.9 μm in the XY direction and 2.5 μm in the Z direction [149]. It is equipped with a 0.4 mm diameter nozzle and the Ultrafuse PLA filament (BASF, Germany) was used. It is known for its high-quality printing, providing an ideal balance of strength and flexibility for a wide range of applications. PLA is a biodegradable and biocompatible substance derived from renewable resources like maize and sugarcane. Furthermore, PLA has high strength and stiffness, making it excellent for applications that need durability.

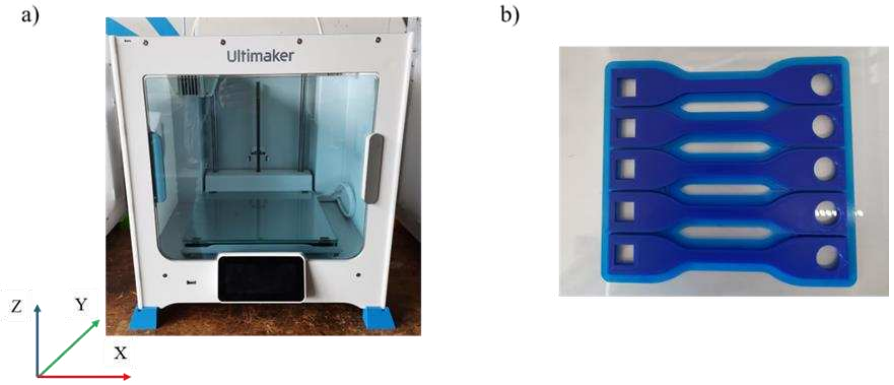


Figure 5.2 (a) Ultimaker S3 printer, and **(b)** Printed specimens.

Seven printing parameters were selected and examined using Taguchi's parametric Design of Experiment (DOE) technique [150]. Table 5.1 shows the sixteen combinations from the Fractional Taguchi L16 in which four parameters are assigned four levels of control, while the remaining two are assigned three levels. For each combination, five specimens were manufactured and analyzed. The fractional Taguchi method was chosen over a full factorial DOE to decrease the number of

experiments since this work aimed to investigate many printing parameters instead of going in depth into only those studied by the literature. The specimens were positioned flat on the XY plane to increase surface contact with the build plate, which reduces warping and maximizes mechanical performance (see Figure 5.2.b). The printing parameters levels, such as print speed, extrusion temperature, and bed temperature, were determined using the datasheet provided by the printer manufacturer [151]. Further parameter values were obtained using the literature [144, 145, 146, 127, 35, 26]. The other process parameters were left as default throughout the experimental plan because of their negligible impact on mechanical strength and dimensional accuracy.

Table 5.1 Fractional Taguchi L16 combinations.

Run	Type of infill	Infill in %	Print speed in mm/s	Layer height in mm	Fan speed in %	Bed temperature in °C	Extrusion temperature in °C
1	Grid	20	40	0.1	50	50	210
2	Grid	45	50	0.1	65	60	220
3	Grid	70	60	0.2	80	50	220
4	Grid	100	80	0.2	100	60	210
5	Triangles	20	50	0.2	50	60	210
6	Triangles	45	40	0.2	65	50	220
7	Triangles	70	80	0.1	80	60	220
8	Triangles	100	60	0.1	100	50	210
9	Cubic	20	60	0.1	100	60	220
10	Cubic	45	80	0.1	80	50	210
11	Cubic	70	40	0.2	65	60	210
12	Cubic	100	50	0.2	50	50	220
13	Zig Zag	20	80	0.2	65	50	220
14	Zig Zag	45	60	0.2	50	60	210
15	Zig Zag	70	50	0.1	100	50	210
16	Zig Zag	100	40	0.1	80	60	220

The dimensions of the manufactured specimens were measured and then the parts were mechanically tested. The 2D control measurement system used to

measure the dimensions of the internal and external features within the printed specimens was the Keyence Instant Measurement System Advantages IM-7000 (Keyence, Japan). This system provided high-resolution measurements of deviations from nominal values, ensuring an accurate assessment of geometrical accuracy, with a resolution of 0.1 μm and an accuracy of 2 μm. The measurements included the circle's diameter and the square's dimensions, as well as the external surfaces' length, width, thickness, and neck.

Following the measurement process, the mechanical properties of the samples were systematically characterized by tensile testing. This involved employing a dynamometric MTS Criterion 43 machine (MTS Systems Corporation, USA) equipped with a 5 kN cell, configured according to ASTM D638 standards, with a gauge length of 70 mm and a testing speed of 5 mm/min, as specified in ASTM D883 [114].

5.2.1 Data preprocessing and evaluation metrics

The quality of the manufactured specimen was evaluated by analyzing the deviations of its dimensions from the nominal (DD) in such a way:

$$DD = \text{Nominal - Experimental in mm} \quad (5.1)$$

Generally, each part has multiple surfaces that may deviate from the nominal; therefore, it is crucial to consolidate all the dimensional discrepancies into a single parameter for a comprehensive evaluation. The DPI, outlined in equation (5.2), achieves this objective. It is calculated as the square root of the sum of squares of the dimensional deviations for each surface, with 'n' representing the total number of considered surfaces.

$$DPI = \sqrt{\sum_{j=1}^{n} DD_i^{\,2}} \text{ in mm} \quad (5.2)$$

However, since a component's functionality depends on both its dimensional accuracy and mechanical strength, an aggregate PI was developed, as expressed in equation (5.3). The PI combines mechanical strength in terms of the UTS and DPI to provide an integrated assessment of both the component's dimensional quality and mechanical performance.

$$PI = \frac{UTS}{DPI} \text{ in MPa/mm} \quad (5.3)$$

5.3 Results and discussion

Once the deviations from nominal values of both internal and external surfaces, along with the UTS, were calculated, the DPI and PI were estimated. The obtained values of both indices were represented through boxplots divided by the 16 input combinations in Figures 5.3 and 5.4.

From eq. (5.2) and (5.3) it is clear that DPI increases as deviation growth increases, indicating that higher dimensional accuracy is associated with DPI values closer to zero, which indicates optimal performance. In parallel, PI shows a positive correlation with UTS, increasing as the latter increases and DPI decreases. An ideal PI approaches infinite values, indicating an optimal strength and dimensional accuracy combination. These trends demonstrate significant relationships among different material properties and propose optimization objectives to enhance overall performance. Therefore, the correlations between these two indices and the process parameter were deeply investigated through statistical tools.

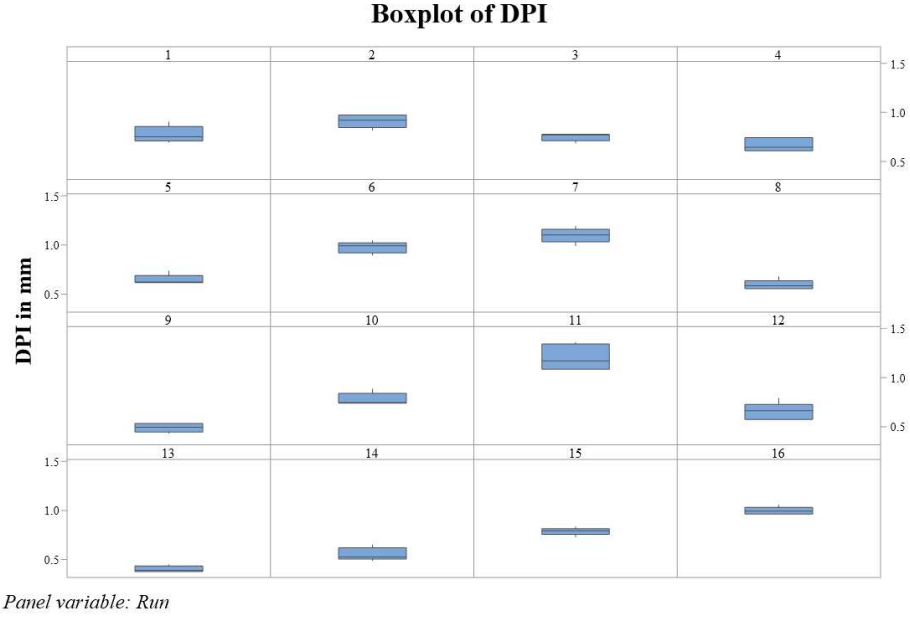


Figure 5.3 Box-plot representation of the distribution of DPI categorized by the Taguchi's run.

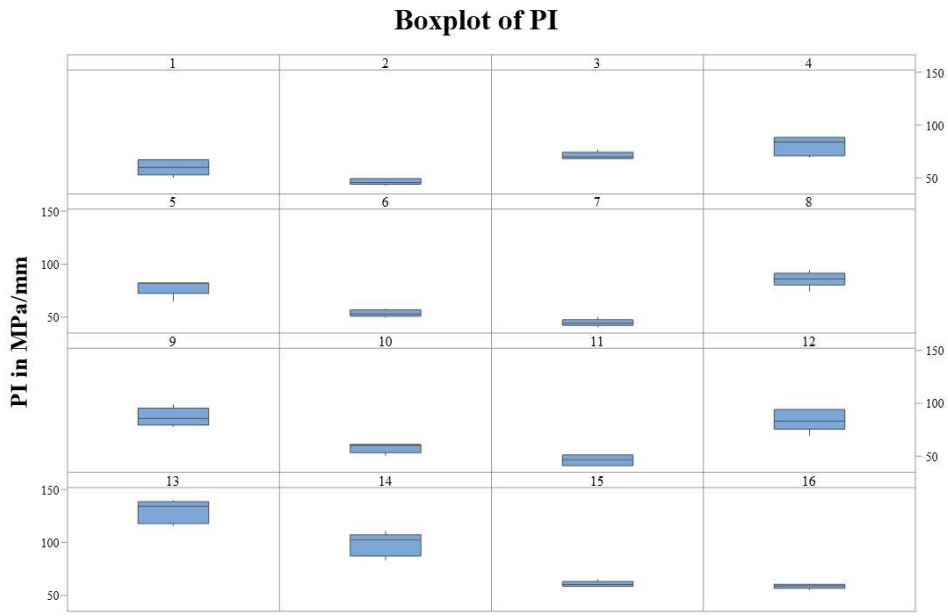


Figure 5.4 Box-plot representation of the distribution of PI categorized by the Taguchi's run.

5.3.1 Effect of input parameters on DPI

The experimental results were carefully collected and analyzed using a statistical software [152]. Table 5.2 presents the results of the ANOVA [115] conducted for the DPI. The percentage of infill, the print speed, the bed temperature, and the layer height appear to influence the DPI values, while the fan speed has a minor influence.

To provide a visual representation of the main effects of the parameters under consideration on the system responses, a main effects plot graph was created (see Figure 5.5). The results indicate that infill type significantly affects DPI, with variations observed among different types. Furthermore, it was discovered that augmenting the percentage of infill can increase the DPI of 65.50 %, from 20 % to 70 % of infill, by reducing the dimensional accuracy of the part, but exceeding the threshold of 70 % may enhance the final quality of the part with a reduction in the DPI value of 24.02 %. This is probably due to the fact that increasing the infill percentage involves increasing the quantity of material inside the part section and, therefore, its thermal distortion during cooling [29].

Table 5.2 ANOVA results of DPI values (DF = Degree of Freedom; Seq SS = Sequential sums of squares; Adj SS = Adjusted sums of squares; Adj MS = Adjusted mean squares).

Source	DF	Seq SS	Contribution	Adj SS	Adj MS	F-Value	p-Value
Infill	3	0.21086	5.32 %	0.210859	0.070286	16.33	0.000
Percentage of Infill	3	1.50130	37.88 %	0.639237	0.213079	49.49	0.000
Print speed	3	1.57559	39.75 %	0.644584	0.214861	49.91	0.000
Layer height	1	0.10604	2.68 %	0.071653	0.071653	16.64	0.000
Fan speed	3	0.06504	1.64 %	0.043440	0.014480	3.36	0.024
Bed Temperature	1	0.22913	5.78 %	0.229134	0.229134	53.22	0.000
Extrusion Temperature	1	0.00006	0.00 %	0.000058	0.000058	0.01	0.908
Error	64	0.27553	6.95 %	0.275534	0.004305		
Total	79	3.96354	100.00 %				

Print speed is also a critical variable, with optimal balance appearing to influence dimensional accuracy positively. Higher speed improved the overall dimensional quality by 39.50 %, while after a print speed of 60 mm/s, the behavior is inverted with a worsening of 23.37 %. This phenomenon is poorly understood, though it may result from a unique heat transfer or temperature gradient created when printing at that speed [130]. Additionally, bigger layers tend to reduce DPI by 9 %, suggesting that higher vertical resolution may favor the part's quality. Fewer layers will be needed, and the effect of distortion will be reduced as layer thickness increases [43].

Choosing the right bed temperature can improve the initial layer's adhesion with limited warping and deviations. Higher temperatures induce a higher DPI of 15 % [30]. Although they produced better geometric accuracy, faster cooling rates were found to have less mechanical strength [144]. The percentage difference between 50 % and 100 % fan speed is 3.42 %. These findings offer valuable insights for optimizing printing parameters and maximizing the dimensional accuracy of 3D printing parts, by reducing the DPI value. To investigate the complex relationship between the interactions of different input parameters and their effect on the DPI, a nonlinear model was created and examined, presented in equation 5.4.

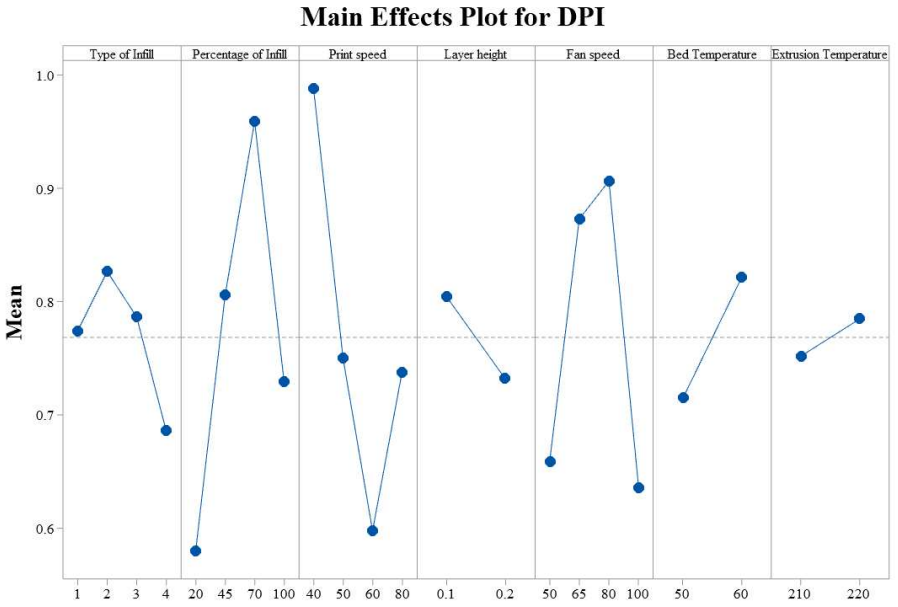


Figure 5.5 The effects of input parameters on the DPI.

Table 5.3 presents the results of the ANOVA conducted for the DPI. This approach enables the capture of not only the direct effect of each parameter but also the more intricate dynamics that emerge from the intertwining of variables. Such insight is crucial to a complete and reliable understanding of the process under consideration, providing a solid foundation for future optimizations and improvements in efficiency and quality of results. Extrusion temperatures exhibit significant interactions even though they are not statistically significant when evaluated individually. The consideration of interactions enhances the statistical power of the analysis, facilitating the detection of significant effects that may otherwise be obscured when only main effects are considered.

$$\begin{aligned} \text{DPI} = {} & 5.039 - 0.312\ \text{Type of Infill} + 0.001172\ \text{Percentage of Infill} \\ & - 0.07468\ \text{Print speed} - 1.958\ \text{Layer height} \\ & + 0.10474\ \text{Fan speed} - 0.05897\ \text{Bed Temperature} \\ & - 0.01924\ \text{Extrusion Temperature} \\ & - 0.03820\ \text{Type of Infill} * \text{Type of Infill} \\ & - 0.000789\ \text{Fan speed} * \text{Fan speed} \\ & + 0.740\ \text{Type of Infill} * \text{Layer height} \\ & + 0.005535\ \text{Type of Infill} * \text{Fan speed} \\ & + 0.01540\ \text{Percentage of Infill} * \text{Layer height} \\ & + 0.001296\ \text{Print speed} * \text{Bed Temperature} \end{aligned} \quad (5.4)$$

The estimated low p-value associated with the regression, coupled with the high R^2 of 93.02 %, R^2pred of 91.65 %, and R^2adj of 89.65 %, indicates that the regression model is highly significant and explains a significant portion of the variability in the DPI values. These results suggest a strong association between the input parameters and DPI, providing a valid basis for interpreting the analysis. Additionally, the normality of the residuals was analyzed, and the results showed a p-value of 0.180. The residuals plot in Figure 5.6 also indicates normally distributed errors, confirming the regression model's suitability for representing the experimental data.

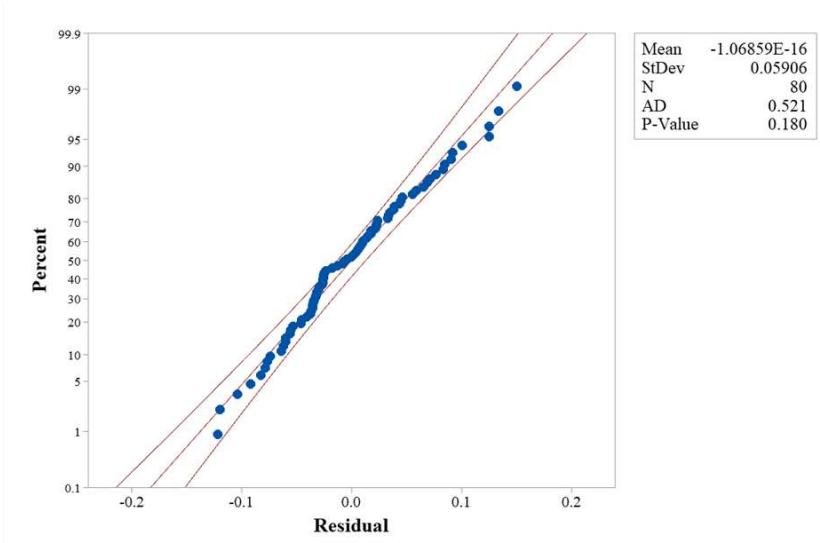


Figure 5.6 Normal probability plot for the residual (based on regression model 1).

Table 5.3 ANOVA of interactions between process parameters for DPI values (DF = Degree of Freedom; Seq SS = Sequential sums of squares; Adj SS = Adjusted sums of squares; Adj MS = Adjusted mean squares).

Source	DF	Seq SS	Contribution	Adj SS	Adj MS	F-Value	p-Value
Regression	13	3.68692	93.02 %	3.68692	0.28361	67.67	0.000
Type of Infill	1	0.09306	2.35 %	0.01758	0.01758	4.19	0.045
Percentage of Infill	1	0.30525	7.70 %	0.29313	0.29313	69.94	0.000
Print speed	1	0.53237	13.43 %	0.06609	0.06609	15.77	0.000
Layer height	1	0.10604	2.68 %	0.02606	0.02606	6.22	0.015
Fan speed	1	0.07880	1.99 %	0.03143	0.03143	7.50	0.008
Bed Temperature	1	0.22913	5.78 %	0.36421	0.36421	86.90	0.000
Extrusion Temperature	1	0.01800	0.45 %	0.48878	0.48878	116.62	0.000
Type of Infill*Type of Infill	1	0.11675	2.95 %	0.11675	0.11675	27.86	0.000
Fan speed*Fan speed	1	1.52879	38.57 %	1.84740	1.84740	440.78	0.000
Type of Infill*Layer height	1	0.00390	0.10 %	0.04404	0.04404	10.51	0.002
Type of Infill*Fan speed	1	0.23358	5.89 %	0.14335	0.14335	34.20	0.000
Percentage of Infill*Layer height	1	0.06234	1.57 %	0.03147	0.03147	7.51	0.008
Print speed*Bed Temperature	1	0.37890	9.56 %	0.37890	0.37890	90.40	0.000
Error	66	0.27662	6.98 %	0.27662	0.00419		
Lack-of-Fit	2	0.00109	0.03 %	0.00109	0.00054	0.13	
Pure Error	64	0.27553	6.95 %	0.27553	0.00431		0.882
Total	79	3.96354	100.00 %				

5.3.2 Effect of input parameters on PI

An ANOVA was conducted to assess the influence of input parameters on PI. Table 5.4 presents the results of the ANOVA for each parameter under consideration. The infill percentage, print speed, type of infill, layer height, bed temperature, and fan speed seem to influence the index PI significantly.

Figure 5.7 shows the Main Effect Plot for the PI. The selection of infill type is a critical factor in determining material performance during the printing process. The literature review reveals that the density and infill pattern directly affect the material's mechanical properties [153]. Some infill types, such as 'Grid' and 'Triangles', compromise performance, while 'Zig Zag' leads to an improvement in overall performance of 35.33 % compared to the Grid type. Additionally, the analysis of infill percentage revealed a non-linear relationship with PI. A high infill rate may initially affect performance at a 70 % percentage infill. This is due to the higher DPI. A reversal was observed above 70 %, with a significant performance improvement of 38.92 %. Choosing a proper infill percentage and pattern results in strong and durable parts with little weight [154]. The mechanical performances of products are all affected by infill density; as infill density increases, printed components grow stronger [155, 37]. Therefore, the appropriate selection of the infill rate is crucial for optimal performance in the printing process between dimensional accuracy and mechanical strength.

Table 5.4 ANOVA results of PI values (DF = Degree of Freedom; Seq SS = Sequential sums of squares; Adj SS = Adjusted sums of squares; Adj MS = Adjusted mean squares).

Source	DF	Seq SS	Contribution	Adj SS	Adj MS	F-Value	p-Value
Type of Infill	3	6619.8	15.85 %	6619.80	2206.60	47.20	0.000
Percentage of Infill	3	12704.1	30.41 %	5819.84	1939.95	41.49	0.000
Print speed	3	10837.6	25.94 %	8483.53	2827.84	60.48	0.000
Layer height	1	6216.1	14.88 %	1346.35	1346.35	28.80	0.000
Fan speed	3	1169.9	2.80 %	1153.75	384.58	8.23	0.000
Bed Temperature	1	1230.6	2.95 %	1230.61	1230.61	26.32	0.000
Extrusion Temperature	1	1.3	0.00 %	1.28	1.28	0.03	0.869
Error	64	2992.3	7.16 %	2992.30	46.75		
Total	79	41771.7	100.00 %				

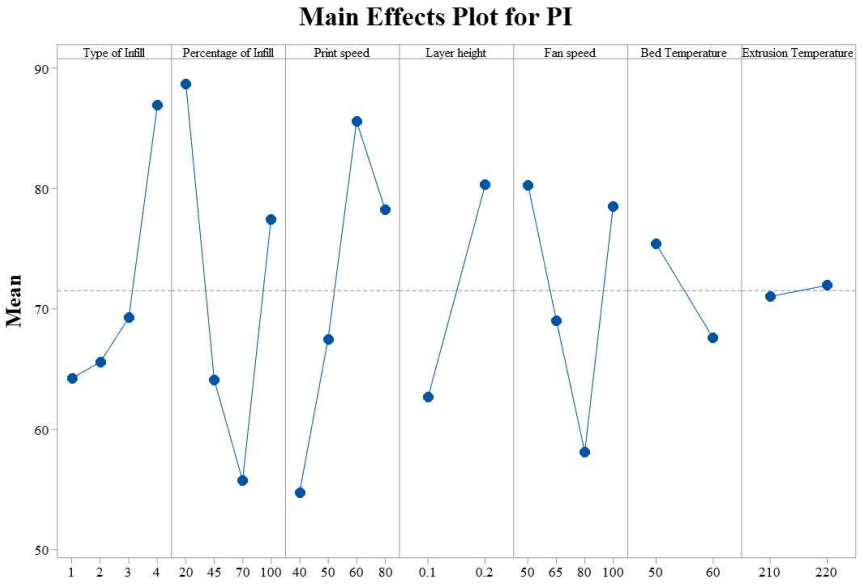


Figure 5.7 The effects of input parameters on the PI.

While a gradual increase in printing speed may appear to promote greater efficiency, it has been found that moderate speed is optimal for optimal performance. Between 40 and 60 mm/s, the PI increases by 56.43 %. At this speed, the layer arrangement is optimal, providing the lowest degree of porosity [26]. A decrease of 8.59 % may be observed when using a print speed of 80 mm/s.

Additionally, layer height has been shown to affect material performance significantly. An increase in layer height correlated with improved PI by 28.12 %, suggesting that a thicker layer could promote greater adhesion and solidity between the print layers [38, 147]. A slight increase in bed temperature tends to decrease the PI by 10.4 %. The heat fluxes in open-space 3D printers make establishing homogeneity of build plate temperature challenging. A closed work environment and regulated heat flow minimize this disadvantage for printers. The impact of the heat flux on ultimate tensile strength is minimal when the specimens are printed horizontally and high when the specimens are printed vertically [32]. Finally, the lowest fan speed positively impacts the PI [144].

Table 5.5 summarizes the comprehensive evaluation of the variation in PI to the interaction between printing parameters. It is possible to denote that the proportion of variance in PI explained by extrusion temperature is insignificant compared to the variance explained by other factors or their interactions. Given that PI incorporates both UTS and DPI, the total variability in PI may be predominantly influenced by different parameters, which could, in turn, reduce the apparent significance of extrusion temperature. However, the model has high explanatory power, with an R^2 of 92.78 %, a R^2pred of 91.36 %, and a R^2adj of 89.23 %. The analysis of variance reveals that the relationships between input parameters and PI are complex, reflecting the interplay among various factors affecting mechanical performance, as determined by the regression equation:

$$\begin{aligned} \mathrm{PI} = {} & -189.9 - 24.96\ \text{Type of Infill} - 4.824\ \text{Percentage of Infill} \\ & + 7.192\ \text{Print speed} - 123.0\ \text{Layer height} \\ & + 7.11\ \text{Fan speed} - 1.172\ \text{Bed Temperature} \\ & - 0.127\ \text{Extrusion Temperature} + 3.988\ \text{Type of Infill} \\ & * \text{Type of Infill} + 0.02496\ \text{Percentage of Infill} \\ & * \text{Percentage of Infill} - 0.0707\ \text{Print speed} \\ & * \text{Print speed} - 0.0453\ \text{Fan speed} * \text{Fan speed} \\ & + 141.2\ \text{Type of Infill} * \text{Layer height} \\ & + 0.0295\ \text{Percentage of Infill} * \text{Print speed} \end{aligned} \tag{5.5}$$

The residual plots assessment reinforces the validity of the model. Figure 5.8 shows that the data points closely align with the normal distribution line, and the p-value exceeds 0.05, indicating adherence to a normal distribution. This observation confirms the assumption of normally distributed errors, as validated by the normal probability plot of the residuals.

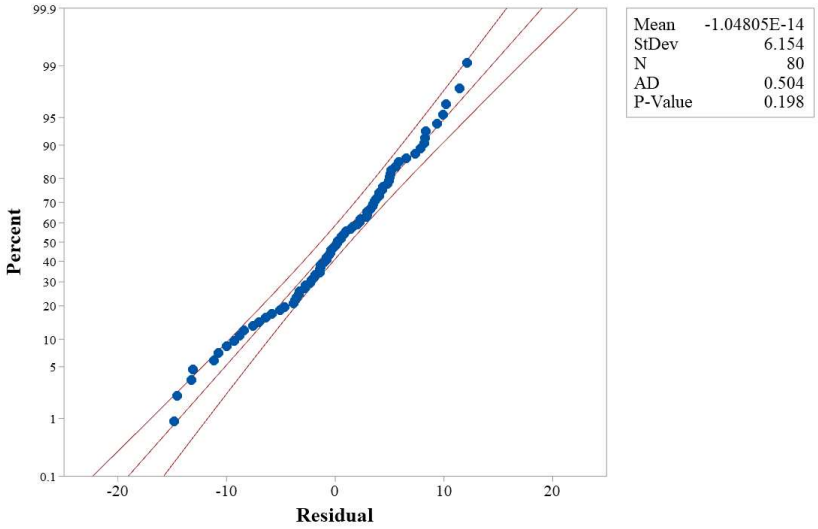


Figure 5.8 Normal probability plot for the residual (based on regression model 2).

Table 5.5 ANOVA of interactions between process parameters for PI values (DF = Degree of Freedom; Seq SS = Sequential sums of squares; Adj SS = Adjusted sums of squares; Adj MS = Adjusted mean squares).

Source	DF	Seq SS	Contribution	Adj SS	Adj MS	F-Value	p-Value
Regression	13	38757.7	92.78 %	38757.7	2981.36	65.29	0.000
Type of Infill	1	5151.9	12.33 %	1104.1	1104.15	24.18	0.000
Percentage of Infill	1	1416.1	3.39 %	1929.2	1929.23	42.25	0.000
Print speed	1	5963.3	14.28 %	4180.8	4180.81	91.55	0.000
Layer height	1	6216.1	14.88 %	6137.6	6137.57	134.40	0.000
Fan speed	1	218.2	0.52 %	1126.3	1126.35	24.66	0.000
Bed Temperature	1	1230.6	2.95 %	1489.5	1489.49	32.62	0.000
Extrusion Temperature	1	23.7	0.06 %	16.3	16.35	0.36	0.552
Type of Infill*Type of Infill	1	1331.9	3.19 %	1269.8	1269.84	27.81	0.000
Percentage of Infill*Percentage of Infill	1	11193.6	26.80 %	2999.5	2999.54	65.68	0.000
Print speed*Print speed	1	4030.9	9.65 %	1558.1	1558.07	34.12	0.000
Fan speed*Fan speed	1	14.9	0.04 %	423.3	423.33	9.27	0.003
Type of Infill*Layer height	1	1610.5	3.86 %	1960.9	1960.91	42.94	0.000
Percentage of Infill*Print speed	1	355.9	0.85 %	355.9	355.92	7.79	0.007
Error	66	3014.0	7.22 %	3014.0	45.67		
Lack-of-Fit	2	21.7	0.05 %	21.7	10.85	0.23	0.793
Pure Error	64	2992.3	7.16 %	2992.3	46.75		
Total	79	41771.7	100.00 %				

5.4 Conclusions

As the adoption of AM continues, it's crucial to comprehensively evaluate printed components' performance. Some industrial components require controlling both geometrical deviation and mechanical strengths. Moreover, many tolerances often describe geometrical deviations, such as flatness, parallelism, location, etc.

This work demonstrates the correlation of two indices, which the authors proposed to summarize the dimensional accuracy and the mechanical strengths of a

manufactured part with the parameters of an additive manufacturing process. The results of this work demonstrate the infill percentage, the print speed, the layer height, and the bed temperature exerted on the two proposed indices. The trend of the two indices versus the process parameter values is shown and quantified through relationships. The study highlights how the two proposed indices may be used to set up the process parameter values in additive manufacturing.

Optimizing metrics simplifies the mathematical problem of optimization and improves performance. Combining dimensional and mechanical performance metrics provides a comprehensive assessment of the quality and functionality of printed parts.

Optimizing these indicators helps to identify optimal process parameters, improving efficiency and consistency in AM operations. Using these indicators, manufacturers can achieve higher quality output, reduce production costs and accelerate innovation in additive manufacturing technologies. Further research will include experiments to test the forecasting performances of the proposed relationship between indices and process parameters and machine learning models to improve predictive capabilities.

Chapter 6 Introducing Artificial Neural Networks to predict the dimensional and micro-geometrical Deviations of additively manufactured Parts

Valentina Vendittoli[1], Wilma Polini[1], Michael S. J. Walter[2] and Stefan Geißelsöder[2]

[1] Department of Civil and Mechanical Engineering, University of Cassino and Southern Lazio, via G. di Biasio 43, 03043 Cassino, Italy

[2] Faculty of Engineering, University of Applied Sciences Ansbach, Residenzstr. 8, 91522 Ansbach, Germany

Published in: Procedia CIRP (2024), 129, pp. 181–186
https://doi.org/10.1016/j.procir.2024.10.032

Abstract

The dependencies between process parameters and the resulting geometrical accuracy of additively manufactured parts are usually highly non-linear and thus complex to investigate and mathematically quantify. Therefore, the application of artificial intelligence techniques is promising to generate mathematical models that reduce effort and increase the prediction quality. The overall goal is to establish a procedure to automatically determine the optimal settings of the manufacturing process parameters to guarantee the highest geometrical accuracy of parts in additive manufactured production. This paper presents the first step towards this fully automatic procedure – the training and evaluation of a mathematical model based on artificial neural networks to quantify the effects of varying process parameters of a material extrusion process on both macro- and micro-geometrical performances. Therefore, a dataset is established based on the Design of Experiment of an additively manufactured part made from Polylactic Acid filament. The dataset is then used to train an artificial neural network that predicts the dimensional and micro-geometrical deviations of the manufactured parts. Finally, the evaluation of the network's prediction quality and reliability indicates that it is possible to predict the parameters linked to resulting print quality with a mean absolute error from 0.0004 to 0.036.

Keywords: Additive Manufacturing; Artificial Neural Networks; Geometrical Accuracy; Roughness; Material Extrusion Process.

6.1 Introduction

ME is a technique that continuously deposits a fused filament to realize the 3D component [1].

FFF is an extrusion-based technique, one of the most common and widely used in the AM world. Thermoplastic polymers, composites, ceramics, and metals can be used. However, plastic materials are preferred, considering their good mechanical and dimensional properties and lower costs [141]. PLA stands out as an extensively utilized material in AM due to its composition as a plastic polymer derived from renewable sources like corn starch, sugar cane, or wood [31]. Dimensional accuracy, surface roughness, mechanical performances of components manufactured utilizing FFF technology, and the influencing variables are prominent research topics in literature [142].

According to a study by Moza, process parameters affect accuracy in the XY and Z planes differently [43]. An investigation of hole size variations within a linear U-shaped benchmark in the three directions shows that the dimensions are underestimated in XY, while in Z, they are overestimated. Furthermore, it was noted that the diameter is always smaller than the nominal value [42]. Furthermore, for equal parameters, there are different dimensional variations for internal and external features [41].

An Infill rate of 20 % is considered an optimum value to minimize dimensional deviations in the XYZ directions, and a layer height of 0.2 mm is functional in the z direction [43]. The extrusion temperature should be matched to the layer height, as variations increase with temperature. Nonetheless, elevated printing speeds may detrimentally influence surface quality by causing incomplete solidification, while nozzle temperatures set too low or high can lead to incomplete melting or issues in material flow. Thus, the extrusion temperature should be matched to the layer height, as variations increase with temperature. Key process parameters shape the temperature profile, such as nozzle temperature and print speed. Consequently, these factors directly impact the bonding strength between layers in the printed object [130, 45]. The build plate temperature is typically configured within the 50-60 °C range. Generally, the building plate's central regions experience higher temperatures than the periphery. This drawback is addressed in enclosed printers through a controlled workspace and managed heat flow [30]. Adjusting the fan speed is important to manage the melt's solidification and improve

the print's quality. Usually, when printing successive layers, it is useful to cool the newly deposited material quickly to avoid deformation and improve the definition of the print characteristics. Therefore, many are the process parameters to manage to minimize the macro and micro geometrical deviations [156, 157, 148]. At the same time, many are the dimensional variables to evaluate the quality of a part [158, 107]. Artificial intelligence tools may help take into account so many variables and parameters.

Therefore, this work considers the seven process parameters that influence the printing quality to create a dataset based on a Taguchi Design Experiment of an FFF-manufactured part made from PLA filament. The complete dataset was then used to train and test an ANN for forecasting manufactured parts' quality performance, both on internal and external features and the specimens' roughness.

The network's predictive accuracy and reliability are thoroughly assessed, and a final testing dataset is used to evaluate the network's ability to foresee unknown values.

The paper concludes with a comprehensive evaluation of the effectiveness of the developed model in predicting quality metrics for manufactured components. This study provides valuable insights into the field of quality control in manufacturing processes.

6.2 Material and methods

The benchmark is a tensile specimen Type IV according to the ASTM-D 638-22 standard [109] (see Figure 6.1.a). Two internal geometric features (rectangular and cylindrical holes) were added to the model to provide further information on the dimensional deviations of internal structures.

For the work, seven printing parameters with a great influence on the geometrical and dimensional accuracy of FFF specimens were selected and investigated.

Considering there are so many parameters, Taguchi's parametric DOE was used. A fractional Taguchi design type L16 (2^3), (4^4) was adopted to carry out a limited number of experiments to have a reliable set of data to train the ANN (see Table 6.1), where three parameters were assigned two levels of control, and the remaining four levels of control [150]. The values were chosen according to studies from the literature and the material data sheet [43, 151, 35, 26]. The other parameters were kept constant for the entire DOE.

Table 6.1 3D printing parameters for the fractional-factorial Design of Experiments.

	Printing parameters						
Run	**A - Type of infill**	**B - Infill in %**	**C - Print speed in mm/s**	**D - Layer height in mm**	**E - Fan speed in %**	**F - Bed tempera-ture in °C**	**G – Extrusion temperature in °C**
1	Grid	20	40	0.1	50	50	210
2	Grid	45	50	0.1	65	60	220
3	Grid	70	60	0.2	80	50	220
4	Grid	100	80	0.2	100	60	210
5	Triangles	20	50	0.2	50	60	210
6	Triangles	45	40	0.2	65	50	220
7	Triangles	70	80	0.1	80	60	220
8	Triangles	100	60	0.1	100	50	210
9	Cubic	20	60	0.1	100	60	220
10	Cubic	45	80	0.1	80	50	210
11	Cubic	70	40	0.2	65	60	210
12	Cubic	100	50	0.2	50	50	220
13	Zig Zag	20	80	0.2	65	50	220
14	Zig Zag	45	60	0.2	50	60	210
15	Zig Zag	70	50	0.1	100	50	210
16	Zig Zag	100	40	0.1	80	60	220

The Ultimaker S3 printer was adopted to carry out sixteen prints, with five specimens each (see Figure 6.1.b), to have statistically significant measurements through the PLA filament supplied by BASF 3D, with a diameter of 2.85 mm.

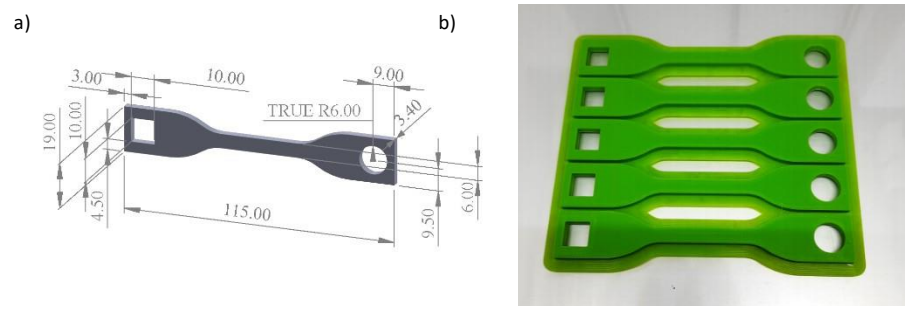


Figure 6.1 (a) Benchmark design (all dimensions in mm); **(b)** Printed specimens.

To improve adhesion between the specimens and the building plate to prevent the curling effect, an additional "brim" was added to the first print layer (see Figure 6.1.b). The specimen was oriented flat on the XY plane, so it had a large surface area in contact with the bed. Larger areas are more prone to warping or detachment during printing. Although PLA is known for its low warping tendencies, large flat surfaces can still be susceptible to warping, especially at the corners. The brim adds stability and prevents warping by securing the edges of the part to the build plate.

6.2.1 Measurement procedure

The macro-geometrical deviations were examined using a 2D control measurement system (Keyence Instant Measurement System Advantages IM-7000 [159]). This system allows the high-resolution 2D image of the object to be acquired, and deviations from the nominal can be measured from the creation of the measurements. The Capture Range was defined according to the following setting:

- Camera: Wide field with a resolution of 0.1 μm and an accuracy of ±5 μm
- Capture size: 150x150 mm
- Z-stage position: -0.999 mm

The lighting settings are:

- Back light Intensity: 100 %
- Exposure time: 16 ms

The roughness on the upper part of the tensile specimens was measured using the Waveline W20 instrument from Vista Instrument SDN BHD [160]. The instrument has a 2 μm radius tip. Measurement program 3 was chosen by ISO 16610-21 [161], using a cut-off of 2.5 mm and a surface traversing the length of the probe of 15 mm. For each specimen, three measures were taken: two measurements

transverse to the nozzle deposition near the internal features and one longitudinal measurement in the middle of the specimen neck.

6.2.2 Neural Network procedure

The ANN model was realized by means of MATLAB software R2022b [162]. The ANN has been trained and validated on the complete dataset of 16 combinations with 5 repetitions each. The input parameters considered are the ones listed in Table 6.1.
The diameter of the circle was selected as the internal feature, while the three dimensions of the specimen were chosen as the external feature. Finally, the three roughness values were included in the output as well.

Figure 6.2 represents the ANN architecture, with the following parameters:

- Learning algorithm: Bayesian Regularization (BR)
- Hidden layer activation function: Tansig
- Number of neurons: 11
- Output layer activation function: Purelin

Regularization is a technique generally used to prevent models from becoming too complex and overfitting the training data. Bayesian regularization is especially useful when dealing with limited or noisy data, as it allows for the expression of uncertainty in model parameters and can lead to more robust and generalizable models [163].
Due to the small number of data points, the approach used was the so-called "Leave-one-out" (LOO), which is a Cross-Validation (CV) technique commonly used in machine learning and statistical modelling [164]. LOO involves the usage of each data point in the dataset as the validation set while using the remaining data points for training. This process is repeated for each data point in the dataset. In this case, 80 neural networks were created and trained. Considering that at every iteration of validation, the other four repetitions are included in the training process, this method is used to report the stability of predicting combinations of input that the network already sees, estimating the natural variation within a set of parameters.

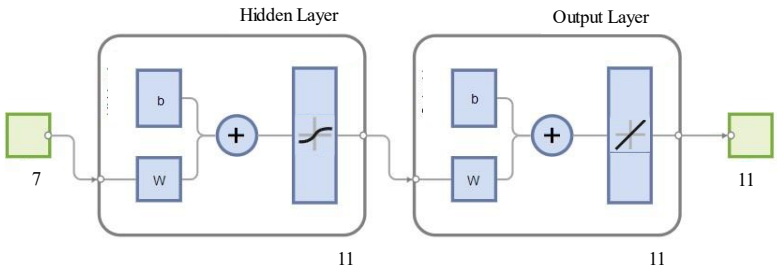


Figure 6.2 Artificial Neural Network architecture.

6.3 Results

The measurements of each of the five printed parts are considered similar (variation < 0.01 mm), so the average was calculated. Table 6.2 shows the measurement results in terms of percentage variation from the nominal.

The value of the roughness is represented as average. It should be noted that the internal features have smaller dimensions in every combination from -0.56 % to -8.66 %, and the external show an opposite trend that ranges from -0.59 % to 9.71 %. This difference in shrinkage between the external and internal surfaces is likely caused by the cooling process [106].

The specimen's neck tends to be rougher than its ends due to the material lay-up by the nozzle. This is due to the build-up of material by the nozzle, and given the narrow cross-section, an inaccurate definition of the process parameters will lead to problems, including burrs.

Table 6.2 Database output variation from nominal.

	Variation in %							Average in µm		
	Internal feature			External feature				Micro-geometry		
Run	Diameter circle	Length square	Width square	Length	Neck	Width	Thickness	Ra_{square}	Ra_{center}	Ra_{circle}
1	-5.25	-3.60	-3.07	0.07	3.48	0.58	0.29	0.739	4.043	2.124
2	-5.18	-6.27	-5.72	0.25	6.17	1.84	1.18	1.077	13.334	3.612
3	-4.44	-6.29	-6.09	0.13	6.03	1.27	2.65	2.909	8.608	3.778
4	-2.61	-2.27	-1.50	0.02	3.68	0.62	2.65	8.610	10.770	7.617
5	-2.36	-1.99	-0.56	-0.01	0.32	0.50	2.94	7.005	4.881	7.322
6	-5.61	-8.66	-7.33	0.32	4.02	1.17	9.71	9.599	42.520	11.821
7	-6.86	-6.95	-6.08	0.21	5.32	1.61	0.29	3.684	5.070	3.006
8	-2.14	-3.66	-2.13	0.13	3.08	1.41	1.47	3.040	3.268	2.456
9	-3.08	-4.75	-3.80	0.02	2.00	1.07	2.35	3.336	3.199	2.746
10	-3.88	-5.55	-4.81	0.32	4.97	1.71	1.18	3.668	4.262	2.691
11	-7.80	-5.57	-5.27	0.21	5.02	1.79	5.29	5.130	22.566	5.222
12	-3.56	-5.86	-4.52	0.02	2.75	1.40	5.88	6.988	23.126	5.518
13	-1.98	-5.01	-3.33	0.07	1.83	1.02	-0.59	6.750	3.471	8.074
14	-3.01	-5.14	-4.33	0.11	3.43	0.94	3.82	2.944	22.584	3.746
15	-4.83	-5.75	-4.93	0.17	5.42	1.82	-0.59	2.359	3.151	2.489
16	-5.79	-6.05	-5.78	0.31	6.67	2.34	5.88	13.891	44.341	10.598

To train the ANN, input, and output values were normalized. The purpose was to make data comparable or to scale it in a way that simplifies analysis or training processes. First, the nominal value was subtracted from each measurement for each repetition. The roughness values at this first stage were not changed.
Once the deviation from the nominal was obtained, the data were normalized using the following formula:

$$x_n = \frac{value_n - min_i}{max_i - min_i} \qquad (6.1)$$

where max and min are the maximum and minimum parameter values within the dataset; specifically, the maximum and minimum were chosen from the three outputs for the roughness data.

The same procedure is also applied to the outputs representing dimensions. This way, outputs representing information with the same units are more easily scaled and compared. Furthermore, during training, the network will be able to learn and generalize the problem more easily. Three performance indices were measured for each neural network. The R-squared (R^2) represents the proportion of the variance in the dependent variable that can be predicted from the independent variables in a regression model [165]. R-squared is commonly used to evaluate the model's goodness of fit. The Mean Absolute Error (MAE) is a goodness of fit parameter that quantifies the prediction accuracy of a predictive mathematical model. Therefore, it calculates the average absolute difference between the predicted value and the actual value for a number of input parameter combinations. Meanwhile, the Mean Squared Error (MSE) quantifies the average of the squared differences between the predicted and actual values.

$$R^2 = 1 - \frac{SS_{res}}{SS_{tot}} \quad (6.2)$$

where SS_{res} is the residual sum of squares and SS_{tot} represents the total sum of squares.
where n is the number of observations, x is the observed value, and y is the predicted value.

$$MAE = \frac{\sum_{i=1}^{n} |y_i - x_i|}{n} \quad (6.3)$$

$$MSE = \frac{1}{n}\sum_{i=1}^{n}(y_i - x_i)^2 \quad (6.4)$$

The average values μ were taken into account for the evaluation of the goodness of the LOO procedure, as shown in Table 6.3 with the relatively standard deviations σ.

Table 6.3 ANN performance.

	Training		**Evaluation**	
Performance	**μ**	**σ**	**μ**	**σ**
R^2 in %	94.41	0.15	91.22	8.67
MAE	0.029	0.0004	0.036	0.014
MSE	0.002	0.00004	0.003	0.002

The R^2 is above 90 % for the training and the evaluation. This implies a good generalization of the mathematical model by the networks. It is important to consider that the R^2 value of the evaluation is lower because each network learns four variations of the same combination and predicts the fifth. Generally speaking, the average value between the displayed variations will be predicted.
Both the average and standard deviation of MSE and MAE are very low. This suggests that the model's predictions are close to the actual values.

6.4 Discussion

In the LOO method, multiple models are fitted, and the dataset is divided into training, validation, and test sets. The training and validation set assists in model verification, while the test set evaluates the final model's predictive ability [166].
Three new input combinations were tested to evaluate the accuracy of the neural network in predicting previously unseen data. The combinations were within the range of the DOE and are shown in Table 6.4. Each combination was manufactured and measured. As for the previous DOE, each combination consisted of 5 repetitions, and the average was evaluated for each measurement as the difference was negligible.
The percentage variations of each predicted output concerning the actual measure were reported in Table 6.5. The dimensional variations are stable between -2.45 % to 7.33 %. The roughness presents higher variations between -25.08 % and 5.41 %, which could be due to the type of normalization; this needs further investigation.

Table 6.4 Combination for ANN testing. Experimental data (Internal and external feature dimensions are in mm, micro-geometry is in μm).

								Internal feature		
Combination	**A**	**B**	**C**	**D**	**E**	**F**	**G**	**Diameter circle**	**Length square**	**Width square**
C1	Zig Zag	20	60	0.2	50	50	210	11.361	9.395	9.436
C2	Zig Zag	20	60	0.2	100	50	210	11.782	9.771	9.928
C3	Zig Zag	20	60	0.1	100	50	210	11.834	9.667	9.818

	External feature			
	Length	**Neck**	**Width**	**Thickness**
C1	115.152	6.324	19.312	3.590
C2	115.023	6.084	19.176	3.550
C3	115.112	6.120	19.129	3.420

	Micro-geometry		
	Ra_{square}	**$Ra_{centralpart}$**	**Ra_{circle}**
C1	4.482	25.673	5.161
C2	7.255	10.269	6.365
C3	2.749	3.264	2.608

Table 6.5 Percentage variation of each predicted output from the experimental value (all dimensions in %).

	Internal feature			
Combination	**Diameter circle**	**Length square**	**Width square**	
C1	2.81	6.83	7.33	
C2	-1.33	2.39	2.41	
C3	-2.44	3.01	2.08	
	External feature			
	Length	**Neck**	**Width**	**Thickness**
C1	-0.10	-2.45	-1.02	-2.15
C2	-0.09	1.25	0.14	-0.58
C3	0.01	2.46	0.59	0.16
	Micro-geometry			
	Ra_{square}	**$Ra_{central}$**	**Ra_{circle}**	
C1	3.63	-25.08	-4.96	
C2	4.44	-11.91	-19.55	
C3	5.41	-23.74	-6.18	

6.5 Conclusion

Over the last decade, AM has undergone significant evolution and is increasingly being adopted due to its ability to produce components with wide geometries and complexity. However, FFF technology offers a wide range of process parameters that can be varied. To ensure that parts conform to specifications, it is essential to implement a mathematical model capable of predicting quality, as dependencies between process parameters can lead to different geometric deviations in components.

This study considers seven printing process parameters that influence the quality of parts made from PLA. A fractional Taguchi L16 DOE was implemented, and the manufactured parts were measured to assess the quality of each combination. Therefore, an artificial intelligence technique is implemented on the dataset. Using the LOO procedure, some neural networks equal to the number of data were trained and evaluated in performance using three metrics. The average R^2 of the training phase is 94.41 %, and the evaluation is 91.22 %. The MSE is 0.002 and 0.003, respectively, while the MAE is 0.029 and 0.036 for the evaluation. These

metrics show that, despite a small number of data points, the ANN can consistently predict any combination within the database with high accuracy. The implications of the network's predictions for the manufacturing process emphasize its potential impact on enhancing overall quality control.

Additional combinations were made within the input ranges to evaluate the accuracy of predicting unseen data. The neural network with the highest R^2 value, equal to approximately 67 %, was used to check the percentage variation between predicted and actual values. The dimensional variations remain stable within a range of -0.07 % to 7.42 %. Variations on roughness show high variations that may be due to normalization and different unit scales between outputs. Further analysis is required.

To conclude, this paper demonstrates the successful training of an artificial neural network for quality prediction and critically examines its performance, providing valuable insights for future research and applications in manufacturing quality assessment.

Future developments involve expanding the database to include more combinations and broader input limits. Additionally, mechanical performance will be incorporated into the dataset. Finally, the crucial step for application to real-life printing projects will be multi-objective optimization to find the optimal input combination while staying within the tolerances defined by the project.

Chapter 7 Using Bayesian regularized Artificial Neural Networks to predict the Tensile Strength of additive manufactured Polylactic Acid Parts

Valentina Vendittoli[1], Wilma Polini[1], Michael S. J. Walter[2] and Stefan Geißelsöder[2]

[1] Department of Civil and Mechanical Engineering, University of Cassino and Southern Lazio, via G. di Biasio 43, 03043 Cassino, Italy
[2] Faculty of Engineering, University of Applied Sciences Ansbach, Residenzstr. 8, 91522 Ansbach, Germany

Published in: Applied Science (2024), 14, pp. 3184
https://doi.org/10.3390/app14083184

Abstract

Additive manufacturing has transformed the production process by enabling the construction of components in a layer-by-layer approach. This study integrates Artificial Neural Networks to explore the nuanced relationship between process parameters and mechanical performance in Fused Filament Fabrication. Using a fractional Taguchi design, seven key process parameters are systematically varied to provide a robust dataset for model training. The resulting model confirms its accuracy in predicting tensile strength. In particular, the mean squared error is 0.002, and the mean absolute error is 0.024. These results significantly advance the understanding of 3D manufactured parts, shedding light on the intricate dynamics between process nuances and mechanical outcomes. Furthermore, they underscore the transformative role of machine learning in precision-driven quality prediction and optimization in additive manufacturing.

Keywords: Fused Filament Fabrication; Tensile strength; Artificial intelligence; Bayesian regularized artificial neural networks; Quality control.

7.1 Introduction

AM is revolutionizing production technologies by enabling the creation of components layer-by-layer without the limitations of traditional manufacturing methods. This technology also allows for the use of a variety of materials, making it highly attractive to industries such as automotive, aircraft, and medical [167, 148]. ME is a type of 3D printing process that involves selectively depositing material through a heated nozzle [1] and is one of seven categories of additive printing processes defined by the ASTM/ISO 52900 standard [1]. Extrusion-based technology can process a wide range of materials [3], making it suitable also for constructing complex parts [106, 68]. FDM, also known as FFF, is a 3D printing process that uses thermoplastic filament to create components layer by layer. The path of the nozzle is defined by the file codes generated during the design stage. The most used thermoplastic material for FDM is PLA, made from plant-based sources.
To ensure that FFF-made components meet their functional requirements, critical process factors must be examined to determine their impact on mechanical qualities. Several research have looked at the influence of the key process parameters. Taguchi orthogonal array was used to define the level of each factor, and the experimental data were analyzed using ANOVA to quantify the main effects of the parameters on the responses [68, 168, 169]. In a study using Taguchi's L9, the effects of printing speed, layer height, and extrusion temperature were analyzed, and the results showed that higher extrusion temperatures improved interlayer adhesion in the printed object. On the other hand, the use of printing speeds that are too high leads to a progressive reduction in the tensile strength because the deposition of the layers is not uniform. The optimal process parameters for this work are a layer height of 0.15 mm, a printing speed of 48 mm/s, and an extrusion temperature of 220 °C [170]. By using lower melting temperatures, at which printing speeds do not affect the geometry of the part while maintaining the necessary integrity of the structure. For the maximum tensile strength, higher extruding temperatures provide better material bonding. Lower printing speeds combined with the printing temperature led to higher strain and stiffness [143]. Moreover, higher cooling speeds were found to improve geometric accuracy but lower mechanical strength [144]. A detailed analysis of the specimen's internal structure was conducted to study the effects of infill type, percentage of part fill, number of perimeters, and shell thickness. The performance is influenced by the chosen infill

pattern and the number of contours, with optimal values being a layer height of 0.1 mm, 6 perimeters, and a gyroid infill geometry [145]. In contrast, ranked first in influence is infill percentage, followed by contour thickness and then the layer height. In Enemuoh et al.'s study, the most influential parameter for optimum printing parameters was found to be infill percentage, followed by contour thickness and layer height. Specifically, an infill density of 100 %, a shell thickness of 1.2 mm, a layer thickness of 0.2 mm, a cubic infill pattern, and a print speed of 40 mm/s were identified as optimal printing parameters [146]. Results on layer thickness are mixed. Caminero et al. observed that on-edge and flat orientations result in the highest mechanical properties with intra-layer failure. The study found that the tensile strength was highest at a lower layer thickness, which also had higher ductility. However, ductility decreased as the layer thickness increased [127]. Another study showed that increasing the layer height from 0.1 to 0.2 mm resulted in improving the tensile strength. Furthermore, the triangle pattern provides optimal mechanical strength while minimizing material consumption [38, 147].

ML is a subfield of artificial intelligence (AI) that uses algorithms to analyze data, recognize patterns, and make decisions without explicit instructions. It is based on objective analysis and logical structure. Within the field of ML, ANNs are modeled to simulate the working flow of the human brain and consist of interconnected nodes that mimic neurons. ANNs excel at learning intricate patterns and correlations in data, making them ideal for applications such as image identification, natural language processing, and predictive analytics. The development of deep neural networks has further improved the capability in processing various and complex data sets [67]. ANNs have played a crucial role in image recognition tasks, including object detection, facial recognition, and image classification. This has resulted in significant progress in areas such as self-driving cars, medical imaging, and security systems [171]. DL differs from traditional ANNs in its ability to automatically learn complex data representations through the use of deep neural networks with many hidden layers. Compared with traditional ML, DL can learn complicated representations of data sets automatically, without the need to manually extract relevant features. It enables more efficient and accurate learning from raw data, automatically uncovering complex patterns and relationships that may not be apparent upon initial analysis. Additionally, it can handle large amounts of data and adapt dynamically to changes, making it particularly suitable for applications with high data complexity and dimensionality [172]. On the

other hand, Deep Belief Networks (DBNs) are hierarchically structured ANNs that learn complex representations of input data using probabilistic methods. They have been used successfully in areas such as computer vision, natural language recognition, bioinformatics, and financial data analysis. Recent developments include hybrid architectures that combine DBNs with other deep learning techniques, such as Convolutional Neural Networks (CNNs) for image processing and Recurrent Neural Networks (RNNs) for sequential data processing. This combination improves model performance and increases flexibility when learning data representations. DBNs are increasingly being used on cloud platforms, allowing for more efficient data management and faster neural network training [172]. One of its applications is in smart cities to improve security and efficiency. It enabled anomaly detection, data encryption, intrusion detection, behavior analysis, and secure communication with significantly improvement overall security by providing effective tools for data protection and cyber threat prevention [173]. Moreover, to enhance the planning and administration of urban tunnel building projects, DBN is utilized to predict the performance of cantilever roadheaders in challenging terrain. This enables precise and timely control of factors that affect roadheader performance. The use of DBN allows for addressing issues related to the complexity of geological data and the non-linear correlations between excavation factors, resulting in more accurate projections that are adaptive to changing ground conditions [174]. High-resolution image processing is crucial in various industries, including medical analysis, satellite image processing, and computer graphics. Rehman et al. [175] proposed a cascade approach, where a CNN extracts DNN-based features from input image patches. These features are then fed into the DBN model for high-resolution image quality prediction. This study aims to improve the objective assessment of super-resolution image quality by providing an advanced, accurate approach without reference images. Bayesian neural networks (BNNs) are a type of neural network that treat model weights as random variables with probability distributions, rather than fixed parameters. This approach captures the uncertainty associated with the model weights and input data, resulting in more informative and robust predictions. Bayesian approaches enable the estimation of the posterior distribution of model parameters from observed data. This estimation can be used for model selection, prediction, and uncertainty quantification. Additionally, Bayesian approaches can improve the generalization performance of ANNs by reducing

overfitting and providing a principled method for selecting the appropriate model complexity. Bayesian methods have the advantage of incorporating prior knowledge into the model, which is useful when training data is limited. They are also robust to outliers and less sensitive to overfitting than non-Bayesian methods due to constraints on model complexity [176, 177]. The transition from the traditional Bayesian approach to BR is a significant advancement in the field of neural networks and ML. This approach improves network performance, making it more robust and better able to generalize to new data, without the full complexity of traditional Bayesian methods [178, 72]. Bayesian analysis is a suitable approach for addressing uncertainties in civil engineering problems such as materials, excitation, modeling, and emission for damage prediction [177]. Moreover, the approach has been utilized to address various challenges in the medical field, including predicting disease progression, identifying diagnostic biomarkers, and customizing treatments to individual patient characteristics [179].

Nowadays, digital technologies and solutions for calibration, prediction, learning, and self-optimization have been implemented in manufacturing to eliminate inefficiencies [180]. The combination of AM and ML techniques offers the ability to identify relationships in large manufacturing data sets, providing the possibility of obtaining components with improved performance [181]. Charalampous et al. [40] investigated tensile strength optimization by adopting an ML regression algorithm. Layer thickness, printing speed, and printing temperature were the process parameters considered. The results showed that a medium printing speed, temperature, and low layer thickness improved the tensile strength. Layer height, infill percentage, printing temperature, and printing speed were used as input to train an ML for simultaneously predicting minimum weight, minimum printing time, and maximum tensile strength. Although no unique optimal solution exists, the Pareto front provides an appropriate combination of input parameters to obtain the best trade-off between the outputs to meet the user's requirements [182]. The same printing processes were investigated by Jatti et al. using an ML nonlinear regression algorithm only for tensile strength prediction. The results were able to predict the tensile strength with a percentage error of less than 2.977 [39]. Models for predicting ultimate tensile strength were developed using ANN. The regression curve had a correlation coefficient of 0.999782. The input combinations between print speed, infill density, build orientation, temperature, and layer thickness were evaluated based on the Taguchi orthogonal array. Having

considered for each input three control levels, 33 experiments were performed for training and evaluation of a neural network. The error percentage value for the neural network is 1.10. The validation parameter indicates an error of 1.57 when comparing the actual and predicted outcomes using the ML method [183]. In the majority of the provided study, the best combination of process parameters was discovered through independent experimental trials, with the experimental outcome that produced a better solution being classified as the optimum solution [184]. However, the optimal process parameter combination may differ from the experimental combinations, and it must fall within the permitted range of process parameters [185]. Additionally, FFF involves a large number of process parameters that must be carefully controlled to ensure the proper formation of components. Therefore, it is essential to control the parameters that have an impact on mechanical performance [186].

This work aims to explore the complex relationship between process parameters and mechanical performance in FFF through the integration of ANNs. The study employs a fractional Taguchi design to systematically vary seven key process parameters and generate a comprehensive dataset for model training. The primary objective is to develop an accurate ANN model capable of predicting tensile strength in FFF-produced parts. The gained knowledge should contribute to the optimization and quality assurance of 3D printed parts. The investigation is structured as follows: section 2 discusses the materials, the benchmarks utilized in the experiments, and the manufacturing method along with the measuring procedure of the manufactured parts. Section 3 reports the mechanical tests carried out and the performance metrics for the evaluation of the ANN model. Section 4 shows validation through additional data points to assess the prognosis. Section 6 concludes by summarizing the findings and discussing prospective future study on the issue.

7.2 Materials and Methods

7.2.1 Printing Procedure

The FFF printer used for the experimental part is the Ultimaker S3, from Ultimaker equipped with a nozzle diameter of 0.4 mm. It has a building volume of 230 by 190 by 200 mm^3 and, a resolution of 6.9 μm in the XY direction and 2.5 μm

in the Z direction [149]. The 2.85 mm diameter PLA filament from BASF Ultrafuse was used for the realization of the components [151].

For the work, a tensile specimen Type IV was designed according to the ASTM-D 638-22 standard [109] to investigate the mechanical performance of PLA parts with a thickness of 3.4 mm. A square and a hole pocket were added as shown in Figure 7.1.

Seven printing parameters were defined to study the effect of varying printing process parameters on the tensile strength through Taguchi's parametric DOE. A fractional Taguchi L16 was adopted where two parameters were assigned three levels of control, and the other four parameters had 4 levels of control, as shown in Table 7.1 [150].

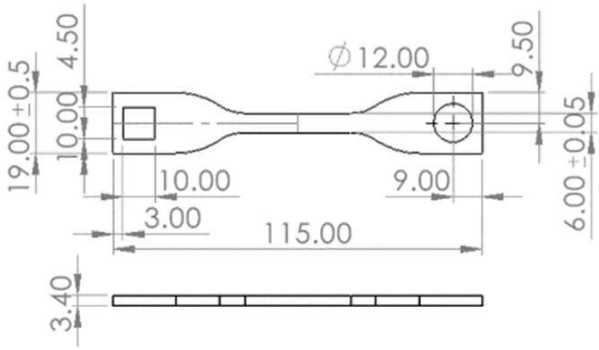


Figure 7.1 Tensile test specimen (all dimensions in mm).

Table 7.1 3D printing parameters and levels from a fractional-factorial DOE.

Factor	Low level (0)	(1)	(2)	High level (3)
A - Type of infill	Grid	Trian-gles	Cu-bic	Zig Zag
B - Infill in %	20	45	70	100
C - Print speed in mm/s	40	50	60	80
D - Layer in mm	0.1	0.2		
E - Fan speed in %	50	65	80	100
F - Bed temperature in °C	50	60		
G - Extrusion temperature in °C	210	220		

The sixteen combinations are shown in Table 7.2. The definition of the printing parameter levels, such as print speed, extrusion temperature, and bed temperature, were made according to the producer material's datasheet supplied by the printer manufacturer. Some further parameter values were set according to the literature [144, 145, 146, 127]. The remaining process parameters were left default for the entire experimental plan, based on their least influence on the mechanical performance. Knowing that the parts have anisotropic behavior, the specimens were printed flat on the XY plane, because they have the greatest strength [187]. Since the portion in contact with the building platform is prone to warping, especially the wider corner, a brim type of adhesion was used to prevent any parts' deformation from compromising the mechanical test results. Compared to the raft that creates a larger support structure beneath the model, the brim has minimal interference with the test specimen, ensuring its mechanical properties during tensile testing. For each combination, 5 specimens were printed, for a total of 80 specimens.

Table 7.2 L16 DOE.

Run	A	B	C	D	E	F	G
1	0	0	0	0	0	0	0
2	0	1	1	0	1	1	1
3	0	2	2	1	2	0	1
4	0	3	3	1	3	1	0
5	1	0	1	1	0	1	0
6	1	1	0	1	1	0	1
7	1	2	3	0	2	1	1
8	1	3	2	0	3	0	0
9	2	0	2	0	3	1	1
10	2	1	3	0	2	0	0
11	2	2	0	1	1	1	0
12	2	3	1	1	0	0	1
13	3	0	3	1	1	0	1
14	3	1	2	1	0	1	0
15	3	2	1	0	3	0	0
16	3	3	0	0	2	1	1

7.2.2 Mechanical test

The tensile tests were performed using a dynamometric MTS Criterion 43 machine (see Figure 7.2.a). A gap of 70 mm was adopted according to the standard

ASTM D638 [109]. The ASTM D883 [114] was consulted to choose the testing speed of 5 mm/min. Five specimens for each combination were tested. The test started until the specimen broke. The rupture occurred within the gauge, as is shown in Figure 7.2.b. The square and circle pockets created are not the subject of study for this paper, but it should be specified that they were placed at the clamping points, ensuring integrity throughout the test.

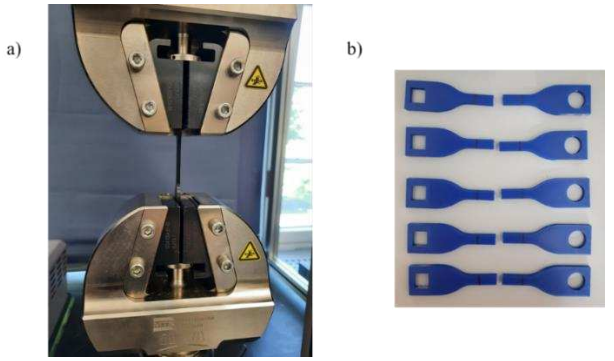


Figure 7.2 (a) Setup of the tensile test machine right before starting the test procedure; **(b)** Tensile specimens after the test.

7.2.3 Artificial Neural Network Architecture

The artificial neural network model was implemented using MATLAB software R2022b [162].

The ANN was trained and validated on a comprehensive dataset comprising 16 combinations with five repetitions each. The considered input parameters are outlined in Table 7.1. Figure 7.3 represents the ANN architecture. BR was used as a learning algorithm. Regularization is a widely employed technique to prevent models from becoming overly complex and overfitting the training data. Bayesian regularization, specifically implemented through the BR algorithm, proves particularly beneficial when dealing with limited or noisy data. BR allows for the expression of uncertainty in model parameters by incorporating a Bayesian framework, leading to the development of more robust and generalizable models [163].

In the context of neural networks, Bayesian Regularization helps prevent overfitting by introducing a probabilistic distribution over the weights. This approach is beneficial when the dataset is small or noisy, as it allows the model to consider multiple possible weight configurations, thus expressing uncertainty in its

predictions. As previously stated by the literature, it is not sensitive to overtraining and it is considered indifferent to the network's architecture [72]. The optimal number of hidden neurons is typically between the size of the input layer and the size of the output layer. In this study, each layer has 7 hidden neurons. For the hidden layer, the Tansig activation function was used. It introduces non-linearity to the model, which is crucial for capturing complex relationships within the data. Additionally, their bounded output range between -1 and 1 facilitates normalized outputs, which are often desirable in neural network models. The Purelin or linear function was used for the output layer, making it suitable for regression tasks where the goal is to predict continuous values.

Given the limited data points, the "Leave-One-Out" (LOO) approach, a cross-validation (CV) technique commonly utilized in machine learning and statistical modeling, was adopted [164]. In the LOO method, during each iteration of validation, the model is trained on all repetitions except one, which is reserved for verification. This systematic leave-one-out process provides a robust assessment of the model's performance and generalization ability, which is especially valuable in cases of limited data. It allows for the evaluation of the network's stability in predicting combinations of input and estimating the natural variation within a set of parameters. The process resulted in the creation and training of 80 neural networks, where 79 combinations were used for the training and 1 for the stability evaluation. In addition, 3 unseen combinations were finally used for the prediction test, to acquire the goodness of the model in predicting.

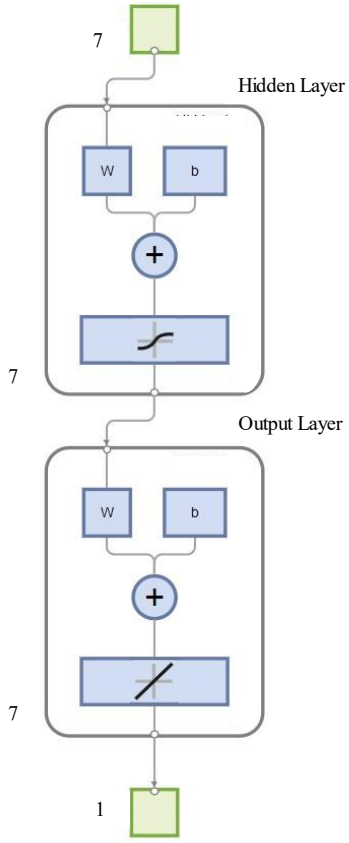


Figure 7.3 Artificial Neural Network Architecture.

7.2.4 Data preprocessing and evaluation metrics

To train the ANN, input, and output values were normalized. The purpose was to make data comparable or to scale it in a way that simplifies analysis or training processes.

Data normalization is the process of organizing data entries to ensure uniformity across all fields and records, making information easier to find, group, and analyze.

The data were normalized in the range 0-1 according to the following formula:

$$x_n = \frac{value_n - min_i}{max_i - min_i} \qquad (7.1)$$

concerning the maximum and minimum value of the i-th column.

The R^2 metric is used to evaluate the proportion of variance in the dependent variable that can be predicted from independent variables [165]. As an additional

method of evaluation, the MAE measures predictive model accuracy by calculating the average absolute difference between predicted and actual values. Similarly, the MSE provides insight into predictive performance by measuring the average of squared differences between predicted and actual values.

$$R^2 = 1 - \frac{SS_{res}}{SS_{tot}} \quad (7.2)$$

$$MAE = \frac{\sum_{i=1}^{n} |y_i - x_i|}{n} \quad (7.3)$$

$$MSE = \frac{1}{n}\sum_{i=1}^{n}(y_i - x_i)^2 \quad (7.4)$$

where SS_{res} is the residual sum of squares, SS_{tot} represents the total sum of squares, n is the number of observations, x is the observed value, and y is the predicted value.

A dedicated step involves assessing the prognosis quality using an independent coefficient to evaluate the approximation's quality thoroughly. This value assesses the agreement between actual test data and the predictions made by the meta-model. The Coefficient of Prognosis (COP) is applied for this purpose and offers an advantage over other error measures. It is worth noting that the COP automatic scale allows for a more nuanced interpretation of the results [188].

$$COP = \left(\frac{\sum_{i=1}^{n}(x_i - |\bar{x}|)\cdot(y_i - |\bar{y}|)}{\sigma_x \cdot \sigma_y \cdot (n-1)}\right)^2 \quad (7.5)$$

where $\bar{x}$ and $\bar{y}$ are the average values and σ_x and σ_y are the standard deviations of the samples.

7.3 Preliminary ANN settings

In the field of neural model optimization, regularization techniques are crucial for improving performance and preventing overfitting. Regularization adds penalizing terms to the objective function to control the model's complexity during training [189, 190]. This approach has several benefits, including reducing variance and improving the model's generalization to unseen data. Preliminary tests were conducted to investigate the differences between using the BR learning algorithm and the unregularized default training mode. As shown in Figure 7.4.a, the model trained with BR showed greater stability and less discrepancy between performance on the training data and test data than the model trained without it shown in Figure 7.4.b.

The results indicate that the regularized model with the Bayesian approach maintains low error on both training and test data compared to the unregularized model.

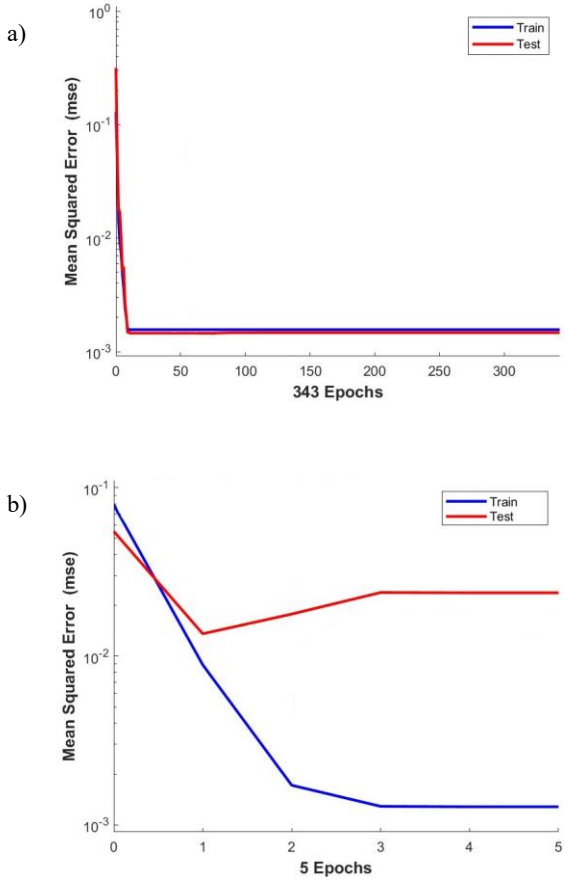


Figure 7.4 (a) A BR learning rate curves and **(b)** the learning curves for the non-regularized trained model.

7.4 Results

Table 7.3 shows the average UTS_{μ} values of the five repetitions, the maximum and minimum values, and the standard deviation σ for each combination. The measures exhibit very low variation, with a maximum standard deviation of 1.523.

The R^2 for the evaluation was not calculated since it is between two values. However, since the evaluation has the purpose of establishing the stability of the ANN predicting already seen values, with an MAE and MSE of 0.024 and 0.002 it is possible to confirm the statement that there is a good generalization and

prediction of the model (see Table 7.4). Furthermore, the reason behind an R^2 value of the training that is not perfectly 100 % is that the model is trained for each network on four variations of the same combination and predicts the fifth. The calculation of the COP was only possible for the training data, and the value of 97.40 % demonstrates how the predicted values are close to the actual ones. The COP on the evaluation was not possible since the prediction is based only on one row.

Table 7.3 Experimental data.

Run	UTS_{μ} in MPa	UTS_{MAX} in MPa	UTS_{MIN} in MPa	σ
1	45.799	48.587	44.257	1.523
2	41.822	43.289	40.105	1.073
3	52.736	54.380	52.207	0.825
4	53.113	53.783	51.772	0.718
5	50.217	51.360	47.556	1.363
6	52.019	52.539	51.614	0.359
7	48.809	4 9.369	48.463	0.338
8	50.593	51.432	49.815	0.598
9	42.995	43.452	42.543	0.308
10	45.523	46.199	45.182	0.351
11	55.892	56.233	55.400	0.348
12	55.054	55.628	54.446	0.484
13	51.960	52.608	50.868	0.601
14	54.177	54.407	54.058	0.121
15	47.789	48.656	46.767	0.615
16	58.647	58.996	58.465	0.190

Table 7.4 ANN performance.

	Training		Evaluation	
	μ	σ	μ	σ
R^2 in %	97.39	0.14	-	-
MAE	0.027	0.001	0.024	0.017
MSE	0.002	0.0001	0.002	0.005
COP in %	97.40	0.14	-	-

7.4.1 Connection weights to quantify variable importance

Weights are fundamental parameters in ANNs, determining the effectiveness and behavior of the network. They represent the importance of connections between

neurons in transmitting and transforming information. These weights determine how input is combined and weighted through the network's layers to produce the desired output. During training, weights are adjusted to minimize errors between predicted and desired output, ensuring accurate predictions. The connection between neural networks and their ability to process complex data enhances their effectiveness and efficiency [163, 191, 192]. The connection weights approach offers a straightforward evaluation of the inputs' relative importance in model prediction. It concentrates solely on the neural network's node connections' weights, providing a clear and immediate view of each input's contribution [192]. It assigns weights to input variables based on their relative importance in the network's output. The algorithm decomposes the weights of connections between input and hidden layers, allowing for a better interpretation of results and understanding of the relationships between input and output variables. Table 7.5 presents the weights of connections between neurons in the input, hidden, and output layers of the model.

Table 7.5 Input-Hidden-Output Connection Weights.

	Neuron 1	**Neuron 2**	**Neuron 3**	**Neuron 4**	**Neuron 5**	**Neuron 6**	**Neuron 7**
A	-0.395	-0.751	-0.341	-0.231	0.362	-0.151	-0.328
B	-0.414	-0.332	-0.347	-0.224	-0.330	-0.318	-0.383
C	-0.362	-0.166	-0.071	-0.187	-0.117	-0.131	-0.184
D	-0.465	-0.310	-0.330	-0.682	-0.524	-0.574	-0.570
E	-0.022	-0.036	0.377	0.624	0.279	0.521	0.521
F	-0.017	-0.024	-0.025	0.072	-0.379	0.064	-0.305
G	-0.014	-0.022	-0.023	0.013	-0.287	-0.016	-0.129
UTS	0.557	0.969	-0.357	-0.185	0.739	-0.108	-0.257

Table 7.6 evaluates the importance of different parameters in a neural network, revealing that the percentage of infill has the highest percentage contribution at 27.7 %, indicating its significant impact on the network's output. On the other hand, the extrusion temperature has the lowest percentage contribution at 5.7 %, indicating its least impact on the network's output [146, 127, 38, 147].

Table 7.6 Connection Weight Approach.

Input	Relative importance in %	Rank
A	16.9	3
B	20.2	1
C	13.3	4
D	20.0	2
E	11.4	5
F	10.0	6
G	8.1	7
Sum	100.0	

7.5 ANN validation

Three additional input combinations that differed from the initial DOE but still adhered to the input ranges presented in Table 7.7 were generated after completing training and evaluation. Each combination was printed with five repetitions and subjected to tensile testing.

The selection of three additional combinations was motivated by the need to test the ANN's ability to generalize to process conditions not yet observed during training. This approach helps ensure that the model can make accurate predictions over a wide range of printing scenarios, increasing its practical utility and reliability. The assessment evaluated the ability of ANN to predict and generalize scenarios, even when there are minor differences in printing circumstances. The three considered cases take into account the values of the layer height and fan speed that are different from those used for the training. The height of each layer has an impact on both the strength and surface quality of the printed component. Additionally, the speed of the fan can affect the cooling of the material during the printing process, which can ultimately impact the mechanical properties of the material, including its strength and ductility [144, 38, 147]. Table 7.8 displays the neural network's ability to predict new data. The R^2 value is above 70 %, indicating good capabilities, considering the limited number of data points used for the training part of the network.

Table 7.7 Additional combination for ANN test.

Combination	A	B	C	D	E	F	G
C1	3	0	2	1	0	0	0
C2	3	0	2	1	3	0	0
C3	3	0	2	0	3	0	0

Table 7.8 Test performance.

	Test	
	μ	σ
R^2 in %	92.48	4.90
MAE	0.070	0.017
MSE	0.006	0.002
COP in %	99.20	2.00

The other performance metrics demonstrate low prediction error, with an MAE and MSE of 0.070 and 0006, respectively. The low standard deviation values indicate low variability and high repeatability. Finally, the results show that an excellent prognosis quality can be achieved by using the optimal meta-model, and the estimated prognosis from the COP of 99.20 % indicates that the actual data closely matches that of the verification data set. Thus, the percentage difference between the data predicted by the ANN and the data obtained during the experimental campaign was calculated using the following formula:

$$Variation = \frac{UTS_{pred} - UTS_{real}}{UTS_{real}} \cdot 100\% \qquad (7.6)$$

Table 7.9 shows that the variations are minimal, ranging from -1.17 % to 2.56 %, indicating a low margin of error.

Table 7.9 Experimental and predicted data from the test. Percentage variation of each predicted output from the experimental value.

Combination	UTS in MPa	UTS_{pred} in MPa	$Variation_{UTS}$ in %
C1	54.945	54.325	-1.13
C2	52.671	52.054	-1.17
C3	42.554	43.643	2.56

7.6 Conclusions

In the field of additive manufacturing, FFF stands out as a transformative technology that enables the layer-by-layer construction of components without the

constraints of traditional manufacturing methods. Its versatility in material usage, particularly with thermoplastics such as PLA, has attracted attention in the automotive, aerospace, and medical industries. However, the ever-increasing demand for improved performance of 3D printed components has spurred the integration of advanced techniques, and this study explores the pivotal role of ML in achieving this goal.

The primary objective of this work was to exploit the capabilities of ANN to predict the mechanical performance of FFF-manufactured parts. As part of a comprehensive investigation, experiments were designed using Taguchi's parametric approach, with seven key process parameters carefully varied to study their influence on tensile strength. A fractional Taguchi L16 DOE was implemented, and the manufactured parts were tested to assess the mechanical performance of each combination.

The ANN showed the ability to predict tensile strength with an R^2 greater than 90 %. In addition, the LOO cross-validation approach provided a robust evaluation of the stability and generalization capabilities of the model with the MSE and MAE of 0.002 and 0.024. The ANN model, trained and evaluated on the dataset, demonstrated its effectiveness in predicting unknown values. The low margin of error observed on the subsequent independent test dataset further underscored the reliability of the developed model.

The neural network with the highest R^2 value, equal to approximately 97 %, was used to check the percentage variation between predicted and actual values. The best model has been selected according to the score on the training and validation. The variations on the UTS remain stable within a range of -1.17 % to 2.56 %.

In conclusion, this study not only advances our understanding of the intricate dynamics within FFF-manufactured parts but also underscores the transformative potential of ML in optimizing and predicting mechanical performance. As industries increasingly embrace additive manufacturing, the insights gained from this work serve as a beacon to guide the path toward more efficient, reliable, and precisely engineered 3D printed components. As demonstrated, the fusion of FFF and ML technologies drives toward a future where additive manufacturing is at the forefront of innovation and quality assurance. Future works will include a wider range of combinations and a greater expansion of input ranges to promote a more comprehensive and complete dataset. In this way, it will be possible to increase the representativeness of the database.

Chapter 8 Artificial Intelligence Tool to Optimize Geometrical and Mechanical Performances of Parts Manufactured Through Additive Manufacturing Processes

Valentina Vendittoli[1], Wilma Polini[1] and Michael S. J. Walter[2]

[1] Department of Civil and Mechanical Engineering, University of Cassino and Southern Lazio, via G. di Biasio 43, 03043 Cassino, Italy

[2] Faculty of Engineering, University of Applied Sciences Ansbach, Residenzstr. 8, 91522 Ansbach, Germany

This chapter has been submitted

Abstract

In Additive Manufacturing, the relationships between process parameters and part quality are challenging to identify and quantify. Artificial Intelligence techniques offer a promising avenue for developing computational models that precisely capture these relationships, thereby minimizing the effort required for process optimization and enhancing the overall prediction accuracy of part performance. This study presents a robust optimization framework designed for the production environment by integrating a Pattern Search Algorithm with an Artificial Neural Network. This integrated approach was employed to investigate the impact of various process parameters on the quality of parts produced via Fused Filament Fabrication. The key findings demonstrate that the Neural Network effectively predicts the outcomes of the printing process. At the same time, the Algorithm identifies optimal parameters that significantly enhance both dimensional accuracy and mechanical performance. The experimental validation of the optimized parameter sets revealed that the dimensional accuracy deviations were maintained within a range of -2.38 % to -4.65 %, while the ultimate tensile strength variations were between 1.14 % and 2.42 % relative to the predicted results. These findings confirm the effectiveness of the proposed optimization framework in producing high-quality printed components, emphasizing its potential for application in industrial additive manufacturing settings to achieve superior part performance.

Keywords: 3D Printing; Artificial Neural Network; Pattern Search Algorithm; Dimensional Accuracy; Mechanical Testing; Performance Index.

8.1 Introduction

The advent of AM has enabled the redesign of manufacturing processes, facilitating more flexible and customized production. In contrast to conventional subtractive manufacturing techniques, AM employs a layer-by-layer construction process, thereby reducing material wastage and enabling the fabrication of intricate, lightweight structures that are simultaneously more robust and efficient [193]. This capability is particularly advantageous in sectors such as aerospace and medical devices, where the design freedom afforded by AM can result in substantial enhancements in product performance and reductions in production costs [194, 4]. FFF or FDM is a material extrusion process that involves layering thermoplastic filaments to create a three-dimensional object [1]. PLA is widely utilized in FFF because of its biodegradable and biocompatible properties and ease of manufacturing and printing. Several studies have looked at how different input parameters influence the dimensions and mechanical properties of FFF-printed components. These studies have highlighted the complex relationships between process parameters and component quality, underlining the need for effective optimization processes [3].

AM significantly impacts supply chain dynamics by enabling localized and on-demand production, reducing inventory requirements and transportation costs. AM's agility allows companies to quickly reconfigure production lines for medical supplies, enhancing supply chain responsiveness and resilience [195]. FFF's flexibility and cost-effectiveness make it particularly advantageous for prototyping and small-batch production.

Gao et al. (2015) discussed the overall status and future of additive manufacturing, emphasizing how FFF facilitates the creation of complex designs without the need for extensive tooling [2]. Ford and Despeisse (2016) explored the sustainability of AM, highlighting FFF's potential for reducing waste and energy consumption compared to conventional manufacturing methods [5].

AM's flexibility is a key factor in creating agile production systems that can rapidly adapt to market changes [64]. The use of digital design and production capabilities allows manufacturers to quickly iterate designs and introduce new products, providing a competitive edge [196]. The optimization of process parameters is crucial for enhancing the performance and reliability of FFF-manufactured parts. Research has shown that meticulous control of parameters such as layer

thickness, print speed, and extrusion temperature can significantly improve the surface roughness, dimensional accuracy, and overall mechanical properties of the printed parts [44, 197, 198].

While FFF offers significant advantages, the quality of the produced products remains a top priority for customers. This aspect should be a key consideration in all research aimed at shaping the future of manufacturing. The Axiom of Manufacturing Imprecision emphasizes the importance of process control in AM to manage inherent variations and ensure high-quality output. The Axiom of Measurement Uncertainty emphasizes the need for real-time monitoring systems to ensure quality control in AM. Despite the advantages of AM, meticulous control and monitoring are crucial for achieving desired outcomes [120].

AM technology has the potential to significantly reduce the time to market of new products. This is achieved by enabling the rapid prototyping and direct production of items from digital designs. Consequently, the transition from concept to finished product can be accelerated, a significant advantage for companies operating within industries that experience rapid innovation cycles [199]. Additionally, FFF technology has been integrated with real-time process monitoring systems to improve quality control. These systems use various sensors to monitor key process parameters such as temperature and vibration, providing data that can be used to adjust the process in real time to prevent defects [34, 200].

The future of FFF and other AM technologies looks promising, with continuous advancements in materials, process control, and AI and machine learning integration for further optimization. As research progresses, FFF is expected to expand its applications and capabilities, making it an even more integral part of modern manufacturing systems [201]. Wu et al. (2018) demonstrated the efficacy of machine learning algorithms, including Random Forests and Support Vector Regression, in forecasting surface roughness in FFF processes [193]. The integration of AI offers considerable enhancements in prediction accuracy and process optimization, thereby further augmenting the potential of FFF in contemporary manufacturing systems [202].

8.2 Artificial Intelligence models for geometric and mechanical variation management in AM

AI and ML, in particular ANNs, have demonstrated considerable potential in optimizing AM processes [67, 180, 181]. Recent studies have shown significant improvements in parts' dimensional accuracy and mechanical performance by applying ANNs to FFF. Plaza et al. (2019) used ANN to model geometric properties in FFF, demonstrating the potential of ANN in optimizing printing parameters for better dimensional accuracy. In their study, the process parameters were varied between 200 °C and 220 °C for the printing temperature, 30-60 mm/s for the printing speed, and 0.1-0.3 mm for the layer thickness. The primary objective of their work was to optimize these parameters to enhance the dimensional accuracy of the printed parts. It was determined that the lowest dimensional deviations were achieved at a layer thickness of 0.06 mm and feed rates ranging from 20 mm/s to 50 mm/s. Specifically, the dimensional deviations were below 13 μm in the on-edge orientation. They ranged between 10 μm and 339 μm across various build orientations, indicating a significant enhancement in dimensional accuracy under optimal conditions [129].

In contrast, Abdulrazaqet et al. (2023) concentrated on optimizing the mechanical properties of 3D-printed parts using FFF. Twenty-seven samples were printed to evaluate tensile and compressive strength. A neural network model was developed to predict and optimize process parameters, focusing on three printing parameters: printing temperature, extrusion width, and number of shells. The full factorial design is used to conduct experiments to collect input-output data to train the ANN model. The maximum tensile and compressive strengths of 74.93 MPa and 67.43 MPa were obtained at a printing temperature of 210 °C, extrusion width of 0.64 mm, and four shells. The ANOVA revealed that the printing temperature is the most influential parameter on tensile strength, contributing 47.68 % to the variance. In comparison, the extrusion width significantly impacts compressive strength, accounting for 51.36 % of the variance. The ANN model demonstrated a high degree of concordance with the experimental results, with mean errors of 0.42 % for tensile strength and 0.45 % for compressive strength [203]. An FFF technology comparative study employed a neural network model and other optimization techniques to assess the dimensional accuracy and shape errors of gears printed in PLA and nylon. The process parameters were varied, including

printing temperatures between 200 °C and 240 °C, printing speeds between 30 mm/s and 70 mm/s, and layer thicknesses between 0.1 mm and 0.3 mm. The study revealed significant discrepancies in dimensional precision and shape fidelity between PLA and nylon. The application of the ANN model facilitated the optimization of the printing parameters, thereby enhancing the dimensional accuracy of the gears [204].

Seyedzavvar (2023) implemented a hybrid optimization methodology, incorporating ANN and Particle Swarm Optimization (PSO). The methodology aims to refine the mechanical properties of 3D-printed components by optimizing both material composition and process parameters. The process parameters analyzed included temperature between 200 °C and 230 °C, printing speed between 30 mm/s and 80 mm/s, and layer thickness between 0.1 mm and 0.3 mm. Hybrid optimization led to significant improvements in the mechanical properties of the parts [205]. The same printing parameters were analyzed through a multi-parametric evaluation with ANN to optimize the process parameters and analyze the mechanical response of 3D-printed PLA using FFF [206, 207] and metaheuristic approaches, integrating the Simulated Annealing (SA) algorithm with a hybrid optimizer [208].

8.3 Research gap and scope of the work

The existing literature indicates that maintaining dimensional accuracy and mechanical performance following requirements is a significant challenge due to the influence of numerous input parameters. However, the complex interdependencies among these parameters are not fully understood or effectively optimized holistically [194, 5]. Maximizing the mechanical strength and geometric quality of certain product categories, such as gear wheels, is crucial to ensure optimal performance and longevity [209, 210]. This reductive approach may limit the overall understanding of the interactions between the various process factors [195, 34]. Often, the complex nature of components, consisting of multiple features, requires simultaneous monitoring of numerous deviations to ensure that parts meet the requirements for assemblability, a crucial aspect in many industries [148, 106]. In addition, mechanical strength is a crucial element for many components that must be carefully matched to construction specifications. This matching is essential to ensure the component's durability and reliability under varying operating

conditions. The existing literature often lacks a comprehensive analysis integrating dimensional accuracy and mechanical performance [193, 3].

AM has demonstrated considerable potential in facilitating localized and on-demand production, reducing inventory requirements and transportation costs. The agility of AM enabled companies to rapidly reconfigure production lines for medical supplies, thereby enhancing the responsiveness and resilience of the supply chain [195]. The capacity to produce components on demand diminishes the necessity for substantial inventories and markedly reduces storage and transportation costs, enhancing cost-effectiveness [5]. Moreover, the high-speed prototyping capabilities of FFF reduce the time from design to production, enabling more agile product development and a faster time-to-market for new products [2].

Nevertheless, a significant gap remains in integrating advanced optimization techniques with production processes, aiming to improve the consistency and reliability of AM outputs. Integrating real-time monitoring systems and advanced optimization techniques, such as ANN and hybrid optimization approaches, can potentially enhance the dimensional and mechanical properties of FFF-printed parts. However, works treat these two distinct aspects separately, focusing on either dimensional accuracy or mechanical performance. This segmented approach may result in suboptimal solutions that fail to fully address the complexity of the fundamental problems encountered in advanced manufacturing [206, 182]. An integrated view that simultaneously considers the component's multiple process variables and functional requirements could offer more robust and applicable results.

This study addresses the earlier gap by integrating a Pattern Search Algorithm (PSA) with an ANN to create a robust FFF process parameter optimization framework. Integrating the ANN's predictive capabilities with the PSA's efficient design space exploration represents a comprehensive approach to simultaneously optimizing the dimensional accuracy and mechanical response of FFF-printed parts. Integrating the PSA with ANN in an optimization framework offers significant operational advantages for additive manufacturing. This approach improves dimensional accuracy and mechanical performance, reduces material waste and costs, and ensures consistent output quality. It optimizes workflows, reduces lead times, and encourages innovation, leading to higher customer satisfaction and sustainable manufacturing practices.

As illustrated in Figure 8.1, the methodology is divided into three main stages: Generation, Performance Index Optimization, and Validation. During the Generation phase, a comprehensive database is created to serve as the training ground for the models. The next stage focuses on refining the models to achieve optimal performance based on specific criteria. Various performance indices are calculated and optimized to ensure that the models are efficient and effective. In the Validation phase, the optimized models are subjected to thorough testing to confirm their efficacy and reliability.

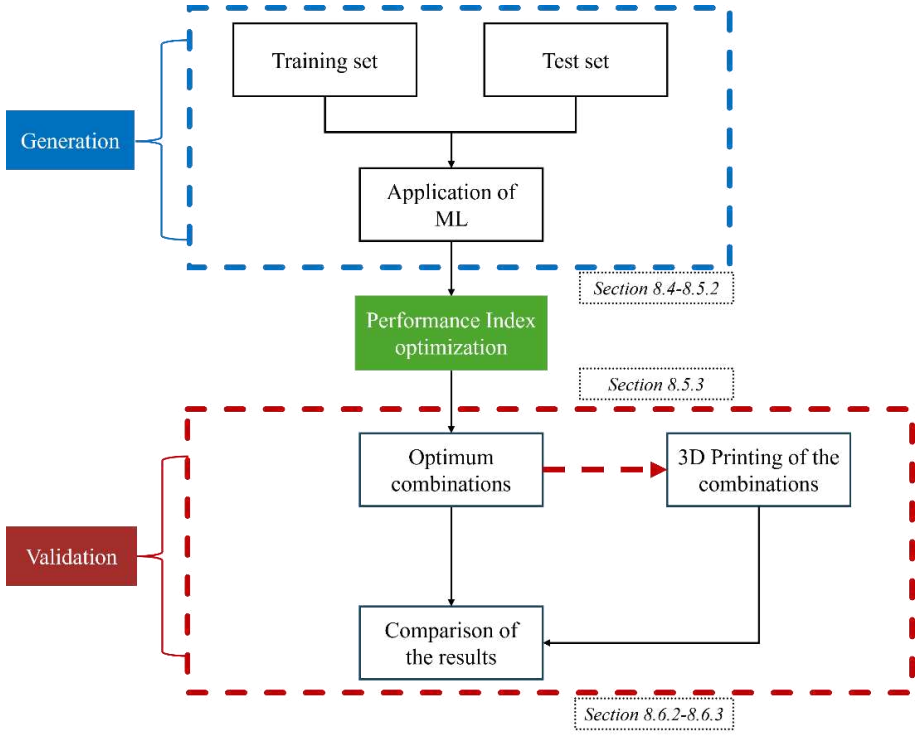


Figure 8.1 Methodology and structure of the paper.

8.4 Description of Neural Network Architecture and Optimization Method

Feedforward neural networks are well-suited for modeling complex nonlinear patterns due to their layered structure and ability to learn arbitrary functional mappings [211, 212]. The network's architecture includes a hidden layer employing a tangent hyperbolic (tanh) activation function. This function outputs values ranging from -1 to 1, adeptly handling positive and negative inputs. Using tanh

is crucial for capturing complex relationships and introducing non-linearity in the database. The output layer of this network employs a linear activation function, which is essential for tasks requiring a continuous spectrum of output values, such as regression problems. This setup allows the network to produce outputs that are a direct linear combination of the inputs from the last hidden layer. Training of the network was conducted using BR backpropagation. This method is renowned for reducing overfitting and enhancing the model's generalization across limited datasets. This is achieved by adjusting the network weights to minimize squared errors and weight magnitudes [163, 72].

A LOO cross-validation technique was employed to evaluate the model. Each data point in this approach is excluded from the evaluation set, while the remaining serve as the training set. This process is repeated until each data point has been used for assessment exactly once. This thoroughly evaluates the model's learning capacity and ability to generalize and understand the relationship between input and output. The decision to utilize LOO was motivated by the specific composition and size of the dataset [213]. This structure, characterized by repeated measurements, necessitates the implementation of a robust evaluation methodology to ensure that the model learns effectively from each unique combination and generalizes well across repeated and potentially similar observations [164].

The input and output data underwent normalization to establish values between 0 and 1. It was accomplished using the min-max normalization technique, which ensures that all features carry equal weight in the network's computations. This facilitates faster convergence during training as each dimensional output value was initially centered by subtracting its respective nominal value. The normalization was carried out according to the following formula:

$$x_{norm} = \frac{value_n - min_i}{max_i - min_i} \quad (8.1)$$

The neural network's performance was thoroughly evaluated using four key indices: R^2, MAE, MSE, and COP [165, 188]:

$$R^2 = 1 - \frac{SS_{res}}{SS_{tot}} \quad (8.2)$$

$$MAE = \frac{\sum_{i=1}^{n} |y_i - x_i|}{n} \quad (8.3)$$

$$MSE = \frac{1}{n}\sum_{i=1}^{n}(y_i - x_i)^2 \quad (8.4)$$

$$COP = \left(\frac{\sum_{i=1}^{n}(x_i - |\bar{x}|)\cdot(y_i - |\bar{y}|)}{\sigma_x \cdot \sigma_y \cdot (n-1)}\right)^2 \quad (8.5)$$

If a DOE considers more than j=1 output parameters, the ANN's resulting prediction quality must be evaluated by calculating the average of the normalized j-th key indices. In case of j=8, the resulting overall prediction quality of a MSE is:

$$MSE^* = \frac{1}{j}\sum_{1}^{j} MSE_j \quad (8.6)$$

The ANN's response was optimized using the Pattern Search Algorithm (PSA). Unlike gradient-based approaches, the PSA does not require gradient information. Instead, it conducts a structured exploration of the parameter space by assessing the objective function at a collection of locations known as "patterns" produced around the present solution. This derivative-free technique enables the PSA to avoid local minima in the complicated optimization issue of training an artificial neural network [214, 215].

8.5 Case study and experimental tests

The Ultimaker S3 3D printer was employed due to its reliability and precision, featuring dual extrusion with a nozzle diameter of 0.4 mm and a build volume of 230 x 190 x 200 mm^3 [149]. The printing material selected was Ultrafuse PLA, a biodegradable thermoplastic derived from renewable resources. It was chosen for its high rigidity and excellent strength and is suitable for both prototyping and final products [151]. For testing purposes, a Type IV tensile specimen was created under the ASTM D638-22 standard [109], incorporating specific geometric features such as square and hole pockets, was adopted. This allowed for the evaluation of the effect of process parameters on the Ultimate Tensile Strength (UTS) and internal and external geometries' deviations, as shown in Figure 8.2.a.

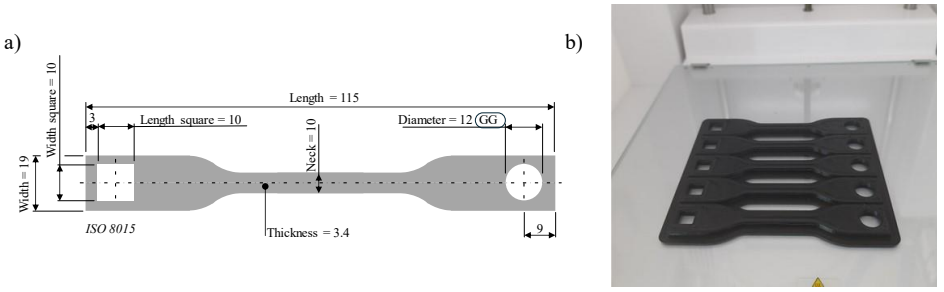


Figure 8.2 (a) Benchmark design; **(b)** Finished specimens inside the chamber.

The optimization of seven manufacturing processes was achieved through the utilization of a fractional Taguchi DOE, specifically an L16 orthogonal array described as L16 (2^4, 4^4) [150]. This fractional factorial design approach significantly reduces the number of experimental runs required by using orthogonal arrays to study parameter effects efficiently across a comprehensive experimental space. The experimental setup involved 16 experimental runs with four factors set at two levels and four factors set at four levels, allowing for a systematic investigation of the interactions between process parameters and their impact on the print quality, with a focus on enhancing both the dimensional accuracy and the mechanical properties of the 3D printed components (see Table 8.1). The process parameter levels were chosen according to the literature and the material data sheet [145, 146, 127, 151]. For each combination, five specimens were printed to ensure statistical reliability (see Figure 8.2.b).

Table 8.1 Taguchi fractional DOE L16.

Run	A - Type of Infill	B - Infill in %	C - Print speed in mm/s	D - Layer height in mm	E - Fan speed in %	F - Bed Tempera-ture in °C	G - Extrusion Temperature in °C
1	Grid	20	40	0.1	50	50	210
2	Grid	45	50	0.1	65	60	220
3	Grid	70	60	0.2	80	50	220
4	Grid	100	80	0.2	100	60	210
5	Trian-gles	20	50	0.2	50	60	210
6	Trian-gles	45	40	0.2	65	50	220
7	Trian-gles	70	80	0.1	80	60	220
8	Trian-gles	100	60	0.1	100	50	210
9	Cubic	20	60	0.1	100	60	220
10	Cubic	45	80	0.1	80	50	210
11	Cubic	70	40	0.2	65	60	210
12	Cubic	100	50	0.2	50	50	220
13	Zig Zag	20	80	0.2	65	50	220
14	Zig Zag	45	60	0.2	50	60	210
15	Zig Zag	70	50	0.1	100	50	210
16	Zig Zag	100	40	0.1	80	60	220

8.5.1 Dimensional Accuracy and Mechanical Testing methodologies

The dimensional accuracy of the 3D-printed specimens was evaluated utilizing the Keyence IM-7000 measurement system. The system employs a wide-field camera with a resolution of 0.1 μm and an accuracy of ±5 μm to capture high-resolution 2D images. The capture area was 150x150 mm, and the Z-stage was positioned at - 0.999 mm to ensure optimal focus. The lighting conditions were controlled by setting the backlight intensity to 100 % and the exposure time to 16 milliseconds, which proved crucial for capturing clear and precise images for measuring macro-geometric deviations [159].

Mechanical testing was conducted utilizing an MTS Criterion 43 dynamometer, each employing a standardized gauge length of 70 mm and a crosshead speed of 5 mm/min [114]. Tensile tests were conducted until failure to determine the material properties under stress accurately. To ensure consistency and statistical reliability of the results, five specimens were analyzed for each test combination, both in dimensional measurements and mechanical tests.

8.5.2 ANN training

The neural network was implemented and trained using MATLAB Release 2023b [162]. The network architecture is illustrated in Figure 8.3. The suggested neural network layout includes an input layer with seven input parameters and one hidden layer with n=11 neurons. The neurons within the hidden layer are capable of learning complex patterns as each neuron performs a weighted sum of the inputs, adds a bias term, and applies an activation function. The output of the hidden layer is then transferred to the output layer, which consists of eight neurons representing the eight output parameters.

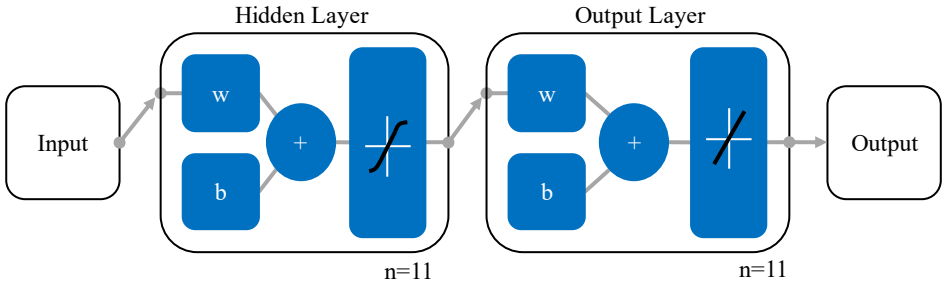


Figure 8.3 Artificial Neural Network Architecture.

Each of the 80 data points was excluded from the evaluation set, while the remaining 79 served as the training set. This process was repeated until each data point had been used for assessment exactly once, providing a rigorous evaluation of the model's learning capacity and ability to generalize and understand the relationship between input and output. The dataset comprised 16 distinct input combinations, each repeated five times, resulting in 80 data points.

8.5.3 Fitness function and Validation experiments

This study utilized two indices as fitness functions for the purpose of minimizing the variation in the printed parts: the DPI and the PI. Both were derived from previous studies [106, 148]. These indices are fundamentally important in the evaluation process. The DPI aggregates multiple dimensional discrepancies into a single, interpretable value, thereby facilitating the assessment and comparison of dimensional accuracy across diverse components. In contrast, the PI integrates the UTS (representing of the mechanical performance) with the dimensional accuracy, offering a comprehensive evaluation that reflects the manufactured parts' structural integrity and precision. This dual-focus metric is of particular value in applications where both mechanical and dimensional performance are critical for the component's functionality.

The DPI is calculated as the sum of the squared differences between the neural network outputs and their target values. This objective function aims to minimize the dimensional discrepancies and drive the neural network outputs towards their ideal target values of zero. The fitness function value is then calculated as the square root of the sum of the squared differences for the relevant outputs, representing an aggregated measure of the dimensional accuracy as shown in equations 8.7 and 8.8:

$$\text{fitness}_n = \sum_1^n (\text{predictedOutput}_i - \text{target})^2 \quad (8.7)$$

$$\text{DPI} = \sqrt{\sum_1^n \text{fitness}_i^2} \quad (8.8)$$

where fitness_n represents the fitness value for each of the n output predictions, predictedOutput_i is the predicted value for the i-th output parameter, and n is the number of output parameters being considered.

The PI objective function is calculated as the UTS divided by the DPI:

$$\text{PI} = \frac{\text{UTS}}{\text{DPI}} \quad (8.9)$$

Validating investigations were used to validate the optimized neural network's performance, comparing predictions to actual measurements of the manufactured components. This comparison evaluated the neural network's ability to accurately forecast the manufactured parts' dimensions and mechanical performance, ensuring the optimization strategy's stability and accuracy.

The validation approach involved producing three additional test specimens for each scenario and evaluating their dimensions and mechanical properties (see Figure 8.4). The values were then compared to those predicted by the improved neural network.

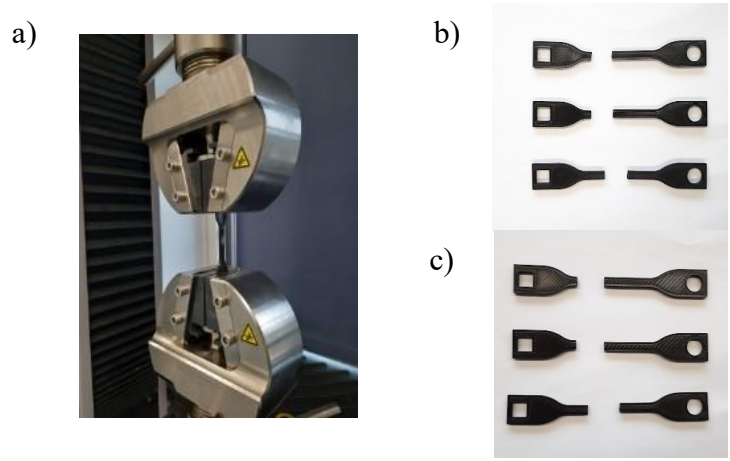


Figure 8.4 (a) Validation test specimen position before testing; **(b)** DPI specimens; **(c)** PI specimens.

8.6 Results and discussion

8.6.1 ANN Model Performance

The analysis of the ANN model's performance, as outlined in Table 8.2, demonstrates the model's robust predictive capabilities in learning and predicting the dimensional accuracy and mechanical response of parts produced through FFF. The high R^2 values, 94.34 % for the training phase and 91.34% for the evaluation phase, indicate that the ANN model can explain a substantial portion of the variance in the data. The low MSE and MAE values across both phases further underscore the model's precision, with the training errors being notably minimal and evaluation errors only slightly higher. These metrics collectively suggest that the ANN model is well-calibrated and generalizes effectively to new data, maintaining high accuracy and reliability in its predictions.

Table 8.2 Evaluation of the ANN prediction quality. (R^2 = 100 %: highest prediction quality, R^2 = 0 %: lowest prediction quality; MSE, MAE=0: highest prediction quality and MSE, MAE=1: lowest prediction quality).

	Training		**Evaluation**	
	μ	**σ**	**μ**	**σ**
R^2 in %	94.34	0.20	91.34	6.77
MSE	0.002	0.00001	0.003	0.002
MAE	0.031	0.0005	0.038	0.017

The COP results detailed in Table 8.3 provide further insights into the model's performance. Notably, the model exhibits overall high predictive accuracy. Low standard deviations indicate consistent performance. However, the model's predictive accuracy is comparatively lower for the neck and width.

Table 8.3 Evaluation of the ANN prediction quality by COP (COP = 100 %: highest prediction quality, COP = 0 %: lowest prediction quality).

Value	**Diameter circle**	**Length square**	**Width square**	**Length**	**Neck**	**Width**	**Thickness**	**UTS**
COP in %	93.80	75.65	81.37	81.00	59.57	36.29	95.19	96.82
σ of COP in %	0.42	0.94	0.71	1.02	1.73	2.35	0.43	0.37

The study used the LOO cross-validation technique to assess the model's performance. However, it should be noted that the final combination used for evaluation was one of the repetitions detected by the model during training. Therefore, three new combinations were introduced to provide a more rigorous assessment of the model's ability to generalize to new, previously unseen data (see Table 8.4). These additional combinations were explicitly chosen to allow the model's predictive capabilities to be thoroughly tested on previously unknown data. The input parameters for these new combinations were selected to be between the established upper and lower limits.

Table 8.4 Additional combination for ANN test.

Combination	Input parameters						
	A	**B**	**C**	**D**	**E**	**F**	**G**
C1	Zig Zag	20	60	0.2	50	50	210
C2	Zig Zag	20	60	0.2	100	50	210
C3	Zig Zag	20	60	0.1	100	50	210

Five repetitions were manufactured for each combination, and the average was used for the analysis, as the differences between the repetitions were negligible. The results from Table 8.5 indicate that the ANN model maintains a reasonable level of accuracy when predicting outcomes for unseen data, though with some expected reduction in performance compared to the training and evaluation phase.

Table 8.5 Evaluation of the ANN test prediction quality. (R^2 = 100 %: highest prediction quality, R^2 = 0 %: lowest prediction quality; MSE, MAE=0: highest prediction quality and MSE, MAE=1: lowest prediction quality).

	Test	
	μ	**σ**
R^2 in %	70.49	10.9
MSE	0.028	0.005
MAE	0.124	0.012

Table 8.6 reports the percentage variations between the predicted and the actual measured outputs. The dimensional variations were stable, ranging from -2.45 % to 7.33 %. For the mechanical properties, the percentage variation was limited to around -2.49 % to 1.63 %, confirming the stability of the predictive model.

Table 8.6 Percentage variations from experimental data (all values in %).

Combination	Output							
	Diameter circle	Length square	Width square	Length	Neck	Width	Thick-ness	UTS
C1	2.81	6.83	7.33	-0.10	-2.45	-1.02	-2.15	-0.22
C2	-1.33	2.39	2.41	-0.09	1.25	0.14	-0.58	-2.49
C3	-2.44	3.01	2.08	0.01	2.46	0.59	0.16	1.63

8.6.2 Pattern Search Algorithm Optimal Results

Table 8.7 presents the optimal process parameters identified by the PSA. The optimal combination for the DPI includes a specific infill pattern, print speed, layer height, fan speed, bed temperature, and extrusion temperature. For the PI, the same infill pattern is used with different settings for print speed, fan speed, and extrusion temperature. These parameters reflect the balance between dimensional accuracy and mechanical strength [38, 147, 35, 26].

Table 8.7 Optimal process parameters from the pattern search algorithm.

Combination	Input parameters						
	A	B	C	D	E	F	G
DPI	Zig Zag	20.00	70.01	0.20	72.73	60.00	210.31
PI	Zig Zag	100.00	71.25	0.20	79.12	60.00	210.00

Table 8.8 presents the optimized outputs achieved using the optimal process parameters for both scenarios. The results indicate that the optimized parameters improve dimensional accuracy and mechanical strength. The results from Tables 8.7 and 8.8 suggest that the PSA effectively identified optimal process parameters and their corresponding outputs.

Table 8.8 Pattern search optimized output (all dimensions in mm; UTS in MPa).

	Combination	
Output	**DPI**	**PI**
Diameter circle	11.841	11.404
Length square	10.086	9.951
Width square	10.149	9.991
Length	114.963	115.050
Neck	6.127	6.337
Width	19.101	19.292
Thickness	3.508	3.548
UTS	47.246	60.810

8.6.3 Comparative Validation Analysis

The validation of the model's prediction, as detailed in Tables 8.9 and 8.10, provides a comprehensive analysis of how well the ANN model predictions align with the actual experimental data for various geometric dimensions and mechanical properties of the 3D printed parts. Table 8.9 shows the experimental results, including each measured output's average and standard deviation. The low standard deviations indicate that the results are highly repeatable, demonstrating the consistency and reliability of the printing process.

Table 8.10 further analyses the percentage variation of the experimental data from the model predictions. The dimensional accuracy shows minor deviations from the predicted values, with the percentage variations for these dimensions ranging between -2.38 % to -4.65 % for the DPI-optimized parameters and -0.36 % to -3.97 % for the PI-optimized parameters. These minor discrepancies suggest that the ANN model is highly reliable in predicting the dimensions of the printed parts, with variations well within acceptable limits for practical applications.

The UTS for the DPI-optimized parameters shows a percentage variation ranging from 9.72 % to 11.16 %, while the PI-optimized parameters show a variation from 1.14% to 2.42%. The higher variation in UTS for the DPI-optimized parameters can be attributed to the objective function focusing solely on dimensional optimization, which resulted in more significant discrepancies.

Table 8.9 Validation results from the indices optimization with average (μ) and standard deviation (σ) of all validation printed parts (all dimensions in mm; UTS in MPa).

Output	DPI					PI				
	X_1	X_2	X_3	μ	σ	X_1	X_2	X_3	μ	σ
Diameter circle	11.56	11.56	11.47	11.53	0.04	11.28	11.36	11.31	11.32	0.04
Length square	9.68	9.76	9.72	9.72	0.03	9.61	9.649	9.62	9.63	0.02
Width square	9.69	9.73	9.68	9.70	0.02	9.60	9.63	9.59	9.61	0.01
Length	114.67	114.72	114.78	114.73	0.05	114.65	114.66	114.68	114.66	0.01
Neck	6.09	6.17	6.18	6.15	0.04	6.16	6.14	6.16	6.15	0.09
Width	18.90	18.89	18.98	18.92	0.04	18.98	18.85	18.96	18.93	0.06
Thickness	3.54	3.55	3.52	3.54	0.01	3.59	3.58	3.55	3.57	0.02
UTS	51.84	52.52	52.46	52.27	0.31	61.50	61.85	62.28	61.88	0.32

Table 8.10 Percentage variation of the experimental data from the numerical model predictions (all values in %).

Output	DPI			PI		
	X_1	X_2	X_3	X_1	X_2	X_3
Diameter circle	-2.42	-2.38	-3.10	-1.11	-0.36	-0.84
Length square	-4.03	-3.28	-3.64	-3.40	-3.04	-3.31
Width square	-4.50	-4.14	-4.65	-3.92	-3.65	-3.97
Length	-0.25	-0.21	-0.16	-0.34	-0.34	-0.33
Neck	-0.64	0.64	0.90	-2.84	-3.06	-2.74
Width	-1.08	-1.12	-0.66	-1.63	-2.29	-1.71
Thickness	0.91	1.20	0.34	1.19	0.91	0.07
UTS	9.72	11.16	11.04	1.14	1.71	2.42

8.7 Conclusions

This research presents a method for enhancing the dimensional quality and mechanical properties of FFF-printed parts by utilizing a combination of a Pattern Search Algorithm and an Artificial Neural Network within an optimization

framework. Utilizing a fractional Taguchi DOE approach (L16), the study systematically evaluated the influence of various process factors, establishing a minimal set of combinations to explain the process relationships effectively.

The ANN model trained using BR achieved great prediction accuracy, with R^2 values of 94.34 % for training and 91.34 % for assessment, suggesting strong model performance. Two performance indices were used as separate objective functions to optimize, improving either dimensional accuracy or a balance between dimensional accuracy and mechanical strength. The PSA successfully identified optimal process parameter sets, leading to notable improvements in the DPI and the PI. The optimal DPI parameter set resulted in enhanced dimensional accuracy with deviations within -2.38 % to -4.65 %. The optimal PI parameter set showed improved mechanical strength with ultimate tensile strength variations between 1.14 % and 2.42 %. Validation through experimental runs confirmed that the optimized parameters yielded parts with superior dimensional accuracy and mechanical integrity, closely aligning with the ANN's predictions.

Future work can extend this optimization framework to address broader aspects of additive manufacturing and further enhance the production of high-quality parts. An important direction is the integration of material-process-layout co-optimization to mitigate defects such as thermally induced distortion through comprehensive optimization strategies. Additionally, enhancing support structure design using topology optimization can improve manufacturability and reduce post-processing efforts. There is also potential in coupling process planning with machining requirements to evaluate how machining time and cost vary with the geometry and amount of supports.

In conclusion, integrating PSA and ANN for optimizing FFF printed components represents a significant advancement in additive manufacturing. This framework not only improves the dimensional accuracy and mechanical properties of printed parts but also sets a precedent for future research and development in the field, paving the way for producing high-quality, reliable, and commercially viable 3D printed components.

Chapter 9 Multi-Response Optimization of the dimensional and mechanical Properties of 3D-printed Polylactide Acid part by Response Surface Methodology

Valentina Vendittoli[1], Wilma Polini[1] and Michael S. J. Walter[2]

[1] Department of Civil and Mechanical Engineering,
University of Cassino and Southern Lazio, via G. di Biasio 43, 03043 Cassino,
Italy
[2] Faculty of Engineering,
University of Applied Sciences Ansbach, Residenzstr. 8, 91522 Ansbach,
Germany

This chapter has been submitted

Abstract

Industrial parts often demand high dimensional accuracy and mechanical strength. This study introduces a method using Response Surface Methodology and composite desirability to optimize these performances in components manufactured through additive processes simultaneously. The approach was validated on Polylactic Acid parts fabricated through Fused Filament Fabrication. Optimized process parameters included a print speed of 80 mm/s, a layer height of 0.2 mm, a fan speed of 50%, and an extrusion temperature of 210°C, yielding tensile strength of 53.27 MPa and dimensional deviations under 5%. Experimental validations showed less than a 5% deviation between predictions and outcomes. The findings provide valuable insights into improving the quality and performance of printed components in various industrial applications, such as gears, highlighting the significance of multi-response optimization in 3D printing processes. This study ultimately contributes to more efficient and cost-effective manufacturing processes.

Keywords: Additive manufacturing; Fused Filament Fabrication; Polylactic Acid; Response Surface Methodology; Optimization.

9.1 Introduction

AM has the potential to transform the production landscape, offering the possibility of creating complex geometries with high precision and minimal material waste. Among the various AM technologies, FFF has gained significant attention due to its accessibility and versatility in utilizing different thermoplastic materials [119, 148]. PLA is the most used material in FFF. It is biodegradable, and biocompatible, and makes the production of detailed prototypes and functional components easier across diverse fields, including biomedical engineering and sustainable manufacturing [106, 31]. PLA is a biodegradable and biocompatible thermoplastic derived from renewable sources, making it an environmentally friendly alternative. Additionally, its ease of printing and high availability makes it a popular choice for prototyping and functional parts [148]. However, its limitations, including low thermal resistance and moderate mechanical strength compared to alternatives like Acrylonitrile Butadiene Styrene (ABS) or Polyethylene Terephthalate Glycol (PETG), have been acknowledged. These characteristics position PLA as a compelling material for exploring multi-response optimization [119].

9.1.1 State of the art on optimizing the dimensional properties of PLA-printed parts

Studies focus on enhancing PLA-based components' mechanical properties and dimensional accuracy through process parameter optimization. Factors such as layer height (0.1-0.3 mm), printing speed (30-90 mm/s), nozzle temperature (190-230 °C), and type of infill significantly influence surface quality and dimensional accuracy. Reducing layer height and optimizing printing speed is crucial for minimizing dimensional errors and improving surface quality, with optimal settings including a layer height of 0.1 mm and a printing speed of 50 mm/s [206]. Using the Grey-Taguchi technique to measure the dimensional accuracy of PLA components, considering parameters like the number of shells [31, 206, 216], print temperature (190-210 °C), infill density (20-100 %), and print pattern (linear, zigzag), it was determined that nozzle temperature was the most critical parameter and that, adopting optimal temperatures, specimens exhibited minimum dimensional errors. The optimal parameters were a nozzle temperature of 200 °C and an infill density of 100% [216]. Also, the comparison between build orientation (0°, 45°, 90°), layer thickness (0.1-0.3 mm), and print speed (20-80 mm/s) was found to

affect the dimensional accuracy of PLA using a low-cost open-source 3D printer. Reduced layer thickness resulted in minor dimensional errors, although print speed had a less apparent effect on dimensional accuracy. A quasi-linear relationship was observed between flatness errors and surface texture, layer thickness, and feed rate. The optimal parameters were a layer thickness of 0.1 mm and a feeding speed of 40 mm/s [129]. Using the Taguchi L9 design to examine the dimensional accuracy of components made with PLA and ABS, varying the infill percentage (20 %, 50 %, 70 %), shell number (1, 2, 3), and layer height (0.1 mm, 0.2 mm, 0.3 mm) it was stated that PLA-printed components outperformed ABS components in dimensional accuracy [217]. Moreover, increased cooling rates improved geometric accuracy but decreased mechanical strength, with an optimal cooling rate of 5 m/s [144].

9.1.2 State of the art on optimizing the mechanical properties of PLA-printed parts

In addition to dimensional accuracy, the mechanical properties of PLA-printed parts significantly vary with printing parameters. Imperfections such as voids and irregularities in layer bonds reduce tensile strength by 30 %, from around 57 MPa to approximately 40 MPa. Optimal printing parameters included a nozzle temperature of 210 °C and a print speed of 60 mm/s, resulting in the highest flexural strength of around 65 MPa [218]. A 100 % infill further improved flexural properties [219]. A printing speed of 40 mm/s, a nozzle temperature of 200 °C, and a layer height of 0.2 mm produced a tensile strength of 58 MPa and a modulus of elasticity of 3.5 GPa [220]. Comparative investigations found that a nozzle temperature of 220 °C and a printing speed of 50 mm/s increased the tensile strength of PLA to around 55 MPa, with a layer height of 0.1 mm, further improving surface properties [221]. Further analysis showed that a printing speed of 30 mm/s, a nozzle temperature of 210 °C, and a layer height of 0.2 mm yielded the best combination of tensile strength of 60 MPa and flexural strength of 70 MPa [222]. Recent studies have increasingly focused on applying RSM to analyze and optimize the FFF parameters for printing with PLA. In the context of FFF printing, multi-response optimization plays a critical role in balancing multiple competing objectives, such as dimensional accuracy, surface finish, and mechanical strength, which are essential for producing high-quality prints. This approach is particularly important for demanding applications in sectors such as aerospace,

automotive, and biomedical engineering, where components must meet stringent tolerances while maintaining structural integrity. This robust statistical technique provides insight into the relationships between multiple process parameters and the resulting output characteristics. This enables the identification of optimal settings for enhanced performance by combining designed experiments with regression analysis to model and optimize processes. It is a widely used approach in various fields, including chemical and process industries [223, 224]. An investigation was conducted to optimize the PLA and wood composite 3D printing filament regarding their surface roughness through FFF. A Grey-Wolf optimization Genetic Algorithm (GWO) was employed in conjunction with RSM to investigate the impact of nozzle temperature (180-220 °C) and layer thickness (0.1-0.3 mm) on the properties of PLA/wood composite materials produced via FFF, finding that at a nozzle temperature of 190 °C and a layer thickness of 0.15 mm, the surface roughness can be significantly reduced [225]. To enhance the mechanical strengths of PLA parts, another inquiry implied the coalescing of the Taguchi method and RSM, intending to optimize FFF parameters. This study explored several parameters, including extruder temperature (200-240 °C), layer thickness (0.1-0.3 mm), raster width (0.4-0.6 mm), and printing speed (20-60 mm/s). Still, it was found that RSM produced better results, increasing tensile strength by 2.11 % and compressive strength by 8.15 % when compared to the Taguchi method. These optimal settings were determined to be an extruder temperature of 230 °C, a layer thickness of 0.2 mm, a raster width of 0.5 mm, and a print speed of 40 mm/s [226]. The combination of RSM and desirability function technique was used to identify the optimal conditions, including a 13.5° stacking angle, 145 % infill extrusion width, 0.2 mm layer thickness, and 110 °C bed temperature. These conditions significantly improved the tensile strength, tensile force, impact energy, and flexural strength of the printed parts with maximum values of 38.43 MPa, 1.48 kN, 1.86 J, and 32.36 MPa, respectively [227].

Expanding on these applications, recent studies have incorporated advanced hybrid models, such as artificial neural networks (ANN) and genetic algorithms (GA), with RSM to address complex, high-dimensional optimization problems. For instance, ANN-GA hybrid models achieved enhanced predictive accuracy, and modeling toughness with a 7.5% improvement in FFF-printed PLA parts. These approaches have demonstrated their utility in demanding fields like

aerospace and biomedical engineering, where precision, strength, and reliability are critical [228].

Moreover, multi-response optimization facilitates the concurrent improvement of multiple output characteristics, making it essential for achieving high-quality prints in industries requiring stringent tolerances. For instance, studies optimizing dimensional accuracy and mechanical strength in PLA components have demonstrated that adjusting nozzle temperature and print speed not only reduces dimensional errors but also enhances tensile strength, providing a balanced framework for application-specific designs [229].

These studies collectively highlight the importance of multi-response optimization in refining FFF processes to meet the increasingly complex requirements of industrial applications. By optimizing multiple outputs simultaneously, RSM ensures that components achieve the balance of precision, strength, and efficiency required in advanced manufacturing environments.

9.1.3 Research gap and resulting research objective

The existing literature reveals that many parameters influence printed parts' mechanical and dimensional properties. Despite notable developments in enhancing the precision and mechanical characteristics of 3D-printed PLA components, a substantial deficiency persists in the existing literature concerning comprehensive multi-response optimization. Most existing studies focus on either dimensional accuracy or mechanical properties rather than considering both in conjunction. This segmented approach is inadequate for simultaneously optimizing both aspects, essential for producing high-quality, robust PLA components. The gap has considerable potential benefits since multi-response optimization can develop PLA parts with superior performance characteristics, rendering them more suitable for a broader range of applications, such as gears. Applications extend to lightweight structural elements in aerospace, customized medical devices, and sustainable consumer products. These fields benefit from the balance of dimensional precision and mechanical robustness achieved through the proposed methodology, underscoring its versatility and industrial significance. Furthermore, such an approach can contribute to more efficient and cost-effective manufacturing processes to obtain parts that meet the design requirements and withstand the stresses they are subjected to during operations.

This study employs RSM to comprehensively optimize the dimensional and mechanical properties of 3D-printed PLA parts. By systematically varying key process parameters, the optimal combination of settings is identified, which maximizes both dimensional accuracy and mechanical strength. The proposed framework is designed to enhance the performance and reliability of PLA components, addressing the practical demands of additive manufacturing.

The investigation is structured as follows: Section 9.2 outlines the methodology employed to evaluate the dimensional and mechanical properties of printed parts. Section 9.3 presents the findings on the influence of process parameters, followed by Section 9.4, which evaluates and validates the RSM model through supplementary trials. A comparison of the predicted and experimental results validates the model's robustness. The paper concludes by summarizing the significance of multi-response optimization in 3D printing, highlighting its practical implications for industrial applications such as gears. It also discusses future research directions, including exploring this methodology for other materials and additive manufacturing techniques. This structured approach contributes valuable insights into 3D printing optimization, offering a scalable framework for improving the quality and performance of components across diverse industries. Furthermore, the methodology is adaptable to any additive manufacturing process or material, ensuring broad applicability.

9.2 Material and methods

The Ultimaker S3 FFF printer had a build volume of 230 x 190 x 200 mm^3, a resolution of 6.9 μm in the XY direction, and 2.5 μm in the Z direction. The printer is equipped with a 0.4 mm diameter nozzle [149]. It utilizes Ultrafuse PLA filament [151], which is renowned for its capacity to produce high-quality prints while maintaining an optimal equilibrium between strength and flexibility. PLA is a biodegradable and biocompatible material derived from renewable resources, including corn and sugarcane. Its use offers a sustainable approach to manufacturing while also providing favorable mechanical properties.

9.2.1 Design of Experiment

Type IV tensile specimens were constructed under the ASTM D 638-22 standard [109], which included additional geometric elements such as square and hole pockets (see Figure 9.1). The test specimen comprised two internal features, which

enabled the evaluation of geometric changes in the internal surfaces without compromising the tensile test results.

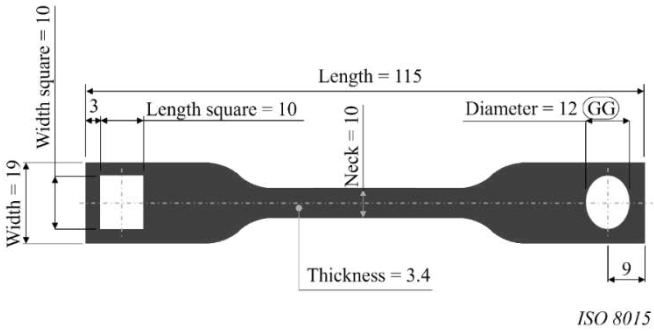


Figure 9.1 Nominal dimensions of the specimen (according to the ASTM D638-22 standard).

Using Taguchi's parametric DOE method, seven printing parameters were selected for testing. A fractional Taguchi L16 design [150] was selected to efficiently study the effects of multiple parameters with a reduced number of experiments while maintaining robust statistical power. Fractional factorial designs offer a beneficial compromise between the number of experiments and the capacity to discern interactions between factors. This approach permits a systematic investigation of the parameter space, thereby facilitating the identification of optimal conditions for the desired outcomes [213].

For this work, four parameters were assigned four levels of control, while the remaining three were assigned two levels. The parameter values were derived from the datasheet provided by the printer manufacturer [151], with supplementary values obtained from the literature based on their relevance to performance optimization, balancing dimensional accuracy, mechanical strength, and production efficiency. This approach ensures the study provides actionable insights for the manufacturing industry [119, 144, 43]. The extrusion temperature was varied at two levels, 210°C and 220°C, as this range is widely accepted as optimal for PLA printing, ensuring adequate flow, interlayer adhesion, and minimal thermal degradation [230]. Furthermore, the two levels allow for a comparative evaluation of dimensional accuracy, which is strongly influenced by thermal phenomena during material deposition and cooling. Similarly, the 100% infill level was chosen to achieve maximum mechanical strength and interlayer bonding, providing a reference point for comparisons of dimensional stability and quality with other infill

levels [231]. The Taguchi L16 fractional design comprises sixteen combinations, as illustrated in Table 9.1.

Table 9.1 Parameter combinations for the Taguchi L16 design used in the study.

Run	A	B	C	D	E	F	G
	Type of Infill	**Infill (%)**	**Print speed (mm/s)**	**Layer height (mm)**	**Fan speed (%)**	**Bed Temperature (°C)**	**Extrusion Temperature (°C)**
1	Grid	20	40	0.1	50	50	210
2	Grid	45	50	0.1	65	60	220
3	Grid	70	60	0.2	80	50	220
4	Grid	100	80	0.2	100	60	210
5	Triangles	20	50	0.2	50	60	210
6	Triangles	45	40	0.2	65	50	220
7	Triangles	70	80	0.1	80	60	220
8	Triangles	100	60	0.1	100	50	210
9	Cubic	20	60	0.1	100	60	220
10	Cubic	45	80	0.1	80	50	210
11	Cubic	70	40	0.2	65	60	210
12	Cubic	100	50	0.2	50	50	220
13	Zig Zag	20	80	0.2	65	50	220
14	Zig Zag	45	60	0.2	50	60	210
15	Zig Zag	70	50	0.1	100	50	210
16	Zig Zag	100	40	0.1	80	60	220

Five specimens were produced for each combination and subjected to testing, for a total of 80 specimens. The specimens were positioned in a level configuration on the XY plane to optimize mechanical performance and minimize warping [187]. The dimensions of the manufactured specimens were measured using the Keyence IM-7000 measurement system, which provided high-resolution

measurements of deviations from nominal values, thereby ensuring an accurate assessment of geometrical accuracy [159]. The mechanical properties of the samples were systematically characterized through tensile testing, which was conducted using an MTS Criterion 43 dynamometer machine [232], using a load cell of 5kN and configured under the ASTM D638 standards by setting a gauge length of 70 mm and the testing speed at 5 mm/min.

9.2.2 Optimization of Experiment

This study's process parameters were optimized using the RSM coupled with desirability functions, a method integral to multi-objective optimization. This approach, formulated by Derringer and Suich in 1980, utilizes desirability functions to transform each response variable into a scale ranging from zero to one, ideal settings. Such transformations allow for the simultaneous optimization of several responses by combining them into a single composite desirability score, thereby facilitating the maximization of this score to identify optimal conditions [233, 234, 235]. Initially, experiments are conducted, and models are fitted for each response to understand the behavior of each variable under study using statistical software [152]. Desirability functions are then defined for each response based on the optimization goal. These functions are generally classified into three types: "larger-the-better", where higher values are more desirable; "smaller-the-better", where lower values are preferable; and "target-the-best", where values closest to a target are ideal. Mathematically, each response y_i is converted into a desirability function di, ranging from 0 to 1. The overall desirability D is typically calculated as the geometric mean of these functions:

$$\mathrm{D} = (\mathrm{d}_1 \cdot \mathrm{d}_2 \cdot \ldots \cdot \mathrm{d}_\mathrm{n})^{\frac{1}{\mathrm{n}}} \qquad (9.1)$$

where n is the number of responses. For the larger-the-better (2) and smaller-the-better (3) scenarios, the desirability functions are formulated as follows:

$$d = \begin{cases} 0 & if\ y < L \\ \left(\frac{U-y}{U-T}\right)^r & if\ L < x \leq T \\ 1 & if\ y > T \end{cases} \qquad (9.2)$$

$$d = \begin{cases} 1 & if\ y = T \\ \left(\frac{U-y}{U-T}\right)^r & if\ T < x \leq U \\ 0 & if\ y > U \end{cases} \qquad (9.3)$$

where y is the output, L and U are the lower and upper bound of the response, and T is the target response value. The variable r represents the relative importance of each quality. In this study, all qualities are treated equally (r=1). This robust approach enables the navigation of complex decision-making scenarios in which multiple outcomes must be balanced to achieve optimal results. This optimization aimed to maximize the UTS while minimizing deviations from nominal dimensions. The optimal process parameters were identified using Minitab software, and these parameters were validated through experimental verification to ensure the reliability and practicality of the optimization results.

9.3 Results and discussion

9.3.1 Effect of process parameters on the internal features

Ensuring precise internal geometries for functional assemblies to guarantee dimensional accuracy and quality is crucial. This will allow the printed parts to fit perfectly in their final applications without additional adjustments or refinements. Properly managing these parameters is essential for maintaining precise dimensions and minimizing shape errors. Errors along the X and Y axes can lead to defective assemblies, wasted time and materials, and, in some cases, project failure [236]. Figure 9.2 presents the main effect plots of the internal surfaces. The dimensional accuracy of the diameter is influenced by increased print speed, which tends to improve dimensional accuracy [237]. A larger layer height, such as 0.2 mm compared to 0.1 mm, has been demonstrated to enhance the dimensional precision of the circle. This is because a larger layer height can facilitate layer adhesion and mitigate the likelihood of inaccuracies resulting from minor deviations in the printing process [238]. Furthermore, optimizing the extrusion temperature is important since high temperatures can result in undesirable thermal expansion. In contrast, extrusion temperatures below 210°C can lead to poor layer adhesion, negatively affecting dimensional accuracy [239]. This operational range of 210–220 °C aligns with the material's thermal properties, where the glass transition temperature (T_g) is approximately 60 °C, and the melting temperature (T_m) is 151°C, ensuring adequate flow and bonding without compromising dimensional stability. Dimensional accuracy is particularly susceptible to managing dimensions along the X and Y axes of the square. For instance, higher layer height has been demonstrated to reduce dimensional errors along both the X and Y axes

[240]. Furthermore, regulating the fan speed is crucial for maintaining uniform cooling of the material, preventing deformations, and enhancing the dimensional stability of the square along both axes [43] (see Figure 9.2).

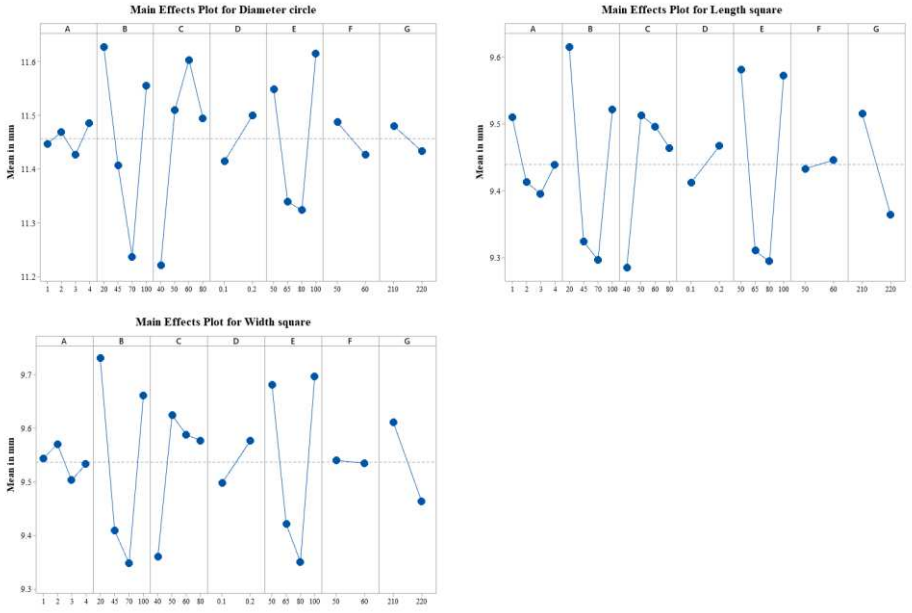


Figure 9.2 Main effect plots showcasing the influence of input parameters on internal feature dimensions (diameter, square length, and square width). The axes represent parameter levels and their corresponding effects.

The results of the ANOVA for the hole's diameter, as presented in Table 9.2, reveal several significant findings. The overall model exhibited a highly significant p-value, while the model's lack-of-fit was insignificant. Among the linear effects, parameter G is not statistically significant ($p = 0.406$), indicating that it does not exert a substantial linear impact. Notably, although G is not significant linearly, it becomes highly significant when interacting with A (AG), with a p-value < 0.001. This indicates that the interaction between A and G significantly affects the diameter. These results demonstrate that while some parameters may not be significant when considered individually, their interactions can play a critical role in determining the dimensional accuracy of the circle. The dimensional accuracy of the diameter is influenced by the layer height, followed by the fan speed. The interactions between extrusion temperature, print speed, and the type of infill are critical to achieving good heat distribution during layer deposition. An optimum combination of these factors will ensure that the material cools evenly, reducing

the risk of warping and maintaining the intended dimensions. In addition, the percentage of infill is closely related to fan speed; a higher fan speed may require adjustments to the percentage of infill to effectively manage thermal distribution. This highlights the importance of considering combined effects to optimize results. These findings align with prior studies on the role of layer height and cooling in maintaining geometric accuracy in FFF-printed components [238, 239].

Table 9.2 ANOVA results of the circle's diameter (DF = Degree of Freedom; Seq SS = Sequential sums of squares; Adj SS = Adjusted sums of squares; Adj MS = Adjusted mean squares).

Source	DF	Seq SS	Contribution	Adj SS	Adj MS	F-Value	p-Value
Model	11	3.87383	94.31%	3.87383	0.35217	102.51	0
Linear	7	1.08437	26.40%	1.32433	0.18919	55.07	0
A	1	0.00523	0.13%	0.03997	0.03997	11.63	0.001
B	1	0.10686	2.60%	0.24166	0.24166	70.34	0
C	1	0.55901	13.61%	0.47309	0.47309	137.7	0
D	1	0.14578	3.55%	0.19665	0.19665	57.24	0
E	1	0.15612	3.80%	0.05953	0.05953	17.33	0
F	1	0.07424	1.81%	0.0722	0.0722	21.02	0
G	1	0.03713	0.90%	0.00241	0.00241	0.7	0.406
Square	1	1.5445	37.60%	2.12793	2.12793	619.39	0
B*B	1	1.5445	37.60%	2.12793	2.12793	619.39	0
2-Way Interaction	3	1.24497	30.31%	1.24497	0.41499	120.79	0
A*G	1	1.07	26.05%	1.06395	1.06395	309.69	0
B*E	1	0.04574	1.11%	0.06138	0.06138	17.87	0
C*G	1	0.12923	3.15%	0.12923	0.12923	37.61	0
Error	68	0.23362	5.69%	0.23362	0.00344		
Lack-of-Fit	4	0.00281	0.07%	0.00281	0.0007	0.19	0.94
Pure Error	64	0.23081	5.62%	0.23081	0.00361		
Total	79	4.10745	100.00%				

In Table 9.3, the results of the ANOVA for the square length along the X-axis reveal that the print speed, extrusion temperature and layer height are significant

parameters. The remaining process parameters are significant if considered in interactions. Print speed and layer height play an important role in layer adhesion, while the percentage of infill is important since representing the internal structure, it supports the component during construction with the edges of the part [43].

Table 9.3 ANOVA results of the square length.

Source	DF	Seq SS	Contribution	Adj SS	Adj MS	F-Value	p-Value
Model	11	2.76888	76.98%	2.76888	0.25172	20.68	0
Linear	7	0.83834	23.31%	0.95999	0.13714	11.26	0
A	1	0.05431	1.51%	0.03752	0.03752	3.08	0.084
B	1	0.06694	1.86%	0.00013	0.00013	0.01	0.917
C	1	0.18489	5.14%	0.24955	0.24955	20.5	0
D	1	0.06056	1.68%	0.12199	0.12199	10.02	0.002
E	1	0.01694	0.47%	0.00579	0.00579	0.48	0.493
F	1	0.00334	0.09%	0.02459	0.02459	2.02	0.16
G	1	0.45137	12.55%	0.47295	0.47295	38.85	0
Square	1	1.3564	37.71%	1.03195	1.03195	84.76	0
B*B	1	1.3564	37.71%	1.03195	1.03195	84.76	0
2-Way Interaction	3	0.57413	15.96%	0.57413	0.19138	15.72	0
A*E	1	0.01281	0.36%	0.05863	0.05863	4.82	0.032
A*G	1	0.45945	12.77%	0.46806	0.46806	38.45	0
C*D	1	0.10187	2.83%	0.10187	0.10187	8.37	0.005
Error	68	0.82788	23.02%	0.82788	0.01217		
Lack-of-Fit	4	0.00216	0.06%	0.00216	0.00054	0.04	0.997
Pure Error	64	0.82572	22.96%	0.82572	0.0129		
Total	79	3.59676	100.00%				

As illustrated in Table 9.4, the ANOVA results for the square width along the Y-axis demonstrate that parameters print speed and extrusion temperature are significant parameters. Regulating the bed temperature and the extrusion temperature is crucial for maintaining uniform cooling of the material, preventing deformations considering the type of infill adopted. The control of both bed and

extrusion temperatures, together with the selection of the appropriate type of filler, is therefore essential to achieve high dimensional accuracy and minimize deformation in the final printed part as [129].

Table 9.4 ANOVA results of the square width.

Source	DF	Seq SS	Contribution	Adj SS	Adj MS	F-Value	p-Value
Model	10	3.55863	81.48%	3.55863	0.35586	30.36	0
Linear	7	0.91051	20.85%	0.7902	0.11289	9.63	0
A	1	0.00959	0.22%	0.00959	0.00959	0.82	0.369
B	1	0.04322	0.99%	0.04255	0.04255	3.63	0.061
C	1	0.27449	6.29%	0.13062	0.13062	11.14	0.001
D	1	0.12585	2.88%	0.10263	0.10263	8.76	0.004
E	1	0.02826	0.65%	0.00118	0.00118	0.1	0.752
F	1	0.00058	0.01%	0.00058	0.00058	0.05	0.825
G	1	0.42852	9.81%	0.43482	0.43482	37.1	0
Square	1	2.04145	46.74%	1.52794	1.52794	130.37	0
B*B	1	2.04145	46.74%	1.52794	1.52794	130.37	0
2-Way Interaction	2	0.60667	13.89%	0.60667	0.30333	25.88	0
A*F	1	0.15324	3.51%	0.11305	0.11305	9.65	0.003
A*G	1	0.45343	10.38%	0.45343	0.45343	38.69	0
Error	69	0.80869	18.52%	0.80869	0.01172		
Lack-of-Fit	5	0.03798	0.87%	0.03798	0.0076	0.63	0.677
Pure Error	64	0.7707	17.65%	0.7707	0.01204		
Total	79	4.36732	100.00%				

9.3.2 Effect of process parameters on the external features

In the context of 3D printing, the term "external surfaces" refers to the outermost layers or boundaries of a printed object that are exposed to the surrounding environment and define the shape and size of the part and are critical in determining the part's dimensional accuracy, surface finish, and overall aesthetic quality.
Figure 9.3 presents the main effect plots of the external surfaces. The length of 3D-printed parts can be affected mostly by variations in print speed and layer height. Higher print speeds generally lead to reduced dimensional accuracy due to the

reduced time for material deposition, causing over-extrusion or under-extrusion issues. Conversely, lower layer heights improve accuracy by allowing more precise control over material flow and better layer adhesion [241, 126]. Similarly, print speed and nozzle temperature influence the width of 3D-printed parts. Higher extrusion temperatures can lead to wider bead deposition as the material flows more efficiently, while lower temperatures result in narrower beads due to increased viscosity. Proper calibration of these parameters is essential to achieve desired dimensional tolerances [242]. The thickness of parts is primarily affected by the layer height setting and nozzle diameter. Smaller nozzle diameters and reduced layer heights enhance the accuracy of the printed part's thickness, enabling finer details and smoother surfaces, although this increases printing time. Larger nozzles and higher layer heights speed up the process but reduce accuracy [243]. The neck dimension is particularly sensitive to variations in print speed and cooling rates. Faster cooling can result in warping and shrinkage, negatively impacting the neck dimension. Controlled cooling strategies and optimized print speed can balance build time and dimensional accuracy [218].

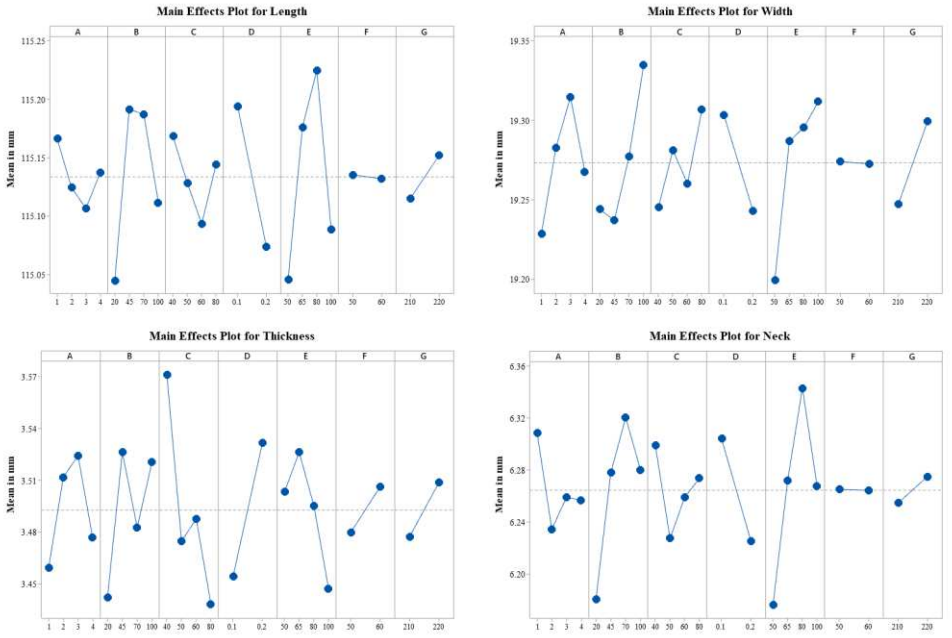


Figure 9.3 Main effect plots depicting the influence of input parameters on external dimensions: length, width, thickness, and neck dimensions. The axes represent parameter levels and their corresponding effects

The ANOVA results in Tables 9.5, 9.6, 9.7, and 9.8 offer insights into the significance of various parameters on the dimensional accuracy of 3D-printed PLA parts using FFF. Considering the external features (Tables 9.5 - 9.8), layer height is the most influential parameter affecting the dimensional accuracy of printed samples, contributing significantly to length variations. Studies have consistently shown that a lower layer height tends to improve dimensional accuracy by minimizing surface roughness and deviation from intended dimensions. In addition, fan speed and extrusion temperature, while less influential individually, are still critical, especially when considering their interactions with other parameters such as infill type and print speed, which can significantly alter the final dimensions of the sample [241, 242]. Furthermore, the width of a printed component is highly variable depending on both the printing speed and the cooling speed. Higher printing speeds typically result in an increase in width while faster cooling reduces width by limiting the flow of material post-deposition [244].

For the thickness of the printed component is significantly influenced by the printing temperature, with elevated temperatures resulting in enhanced material flow and, consequently thicker layers. Furthermore, the quantity of material deposited is subject to the layer height, which determine the density and overall material utilization in the printed structure [245]. The neck displays moderate sensitivity to temperature and infill, with elevated temperatures resulting in augmented material expansion and, consequently, an impact on the precision of this particular feature. The interaction between temperature, infill, and layer height has been demonstrated to influence the dimensional accuracy of printed components. An increase in temperature frequently gives rise to a notable increase in dimensional deviation [218]. These finding are consistent with findings reported in the literature [126, 242, 241].

Table 9.5 ANOVA results of the length.

Source	DF	Seq SS	Contribution	Adj SS	Adj MS	F-Value	p-Value
Model	11	0.82961	81.50%	0.829607	0.075419	27.24	0
Linear	7	0.40191	39.48%	0.337924	0.048275	17.43	0
A	1	0.01105	1.09%	0.009549	0.009549	3.45	0.068
B	1	0.03085	3.03%	0.067507	0.067507	24.38	0
C	1	0.00438	0.43%	0.00169	0.00169	0.61	0.437
D	1	0.28968	28.46%	0.235739	0.235739	85.13	0
E	1	0.04164	4.09%	0.038266	0.038266	13.82	0
F	1	0.00022	0.02%	0.000224	0.000224	0.08	0.777
G	1	0.02409	2.37%	0.02359	0.02359	8.52	0.005
Square	1	0.33529	32.94%	0.273527	0.273527	98.78	0
E*E	1	0.33529	32.94%	0.273527	0.273527	98.78	0
2-Way Interaction	3	0.0924	9.08%	0.092404	0.030801	11.12	0
A*G	1	0.04508	4.43%	0.067655	0.067655	24.43	0
B*G	1	0.02013	1.98%	0.014527	0.014527	5.25	0.025
C*D	1	0.0272	2.67%	0.027199	0.027199	9.82	0.003
Error	68	0.1883	18.50%	0.188299	0.002769		
Lack-of-Fit	4	0.0043	0.42%	0.004296	0.001074	0.37	0.827
Pure Error	64	0.184	18.08%	0.184003	0.002875		
Total	79	1.01791	100.00%				

Table 9.6 ANOVA results of the width.

Source	DF	Seq SS	Contribution	Adj SS	Adj MS	F-Value	p-Value
Model	10	0.45638	38.22%	0.45638	0.045638	4.27	0
Linear	7	0.28406	23.79%	0.37397	0.053424	5	0
A	1	0.02226	1.86%	0.10798	0.107983	10.1	0.002
B	1	0.10106	8.46%	0.1627	0.162704	15.22	0
C	1	0.03035	2.54%	0.03429	0.034291	3.21	0.078
D	1	0.07308	6.12%	0.02055	0.020546	1.92	0.17
E	1	0.00183	0.15%	0.06943	0.069428	6.49	0.013
F	1	0.00004	0.00%	0.09506	0.095058	8.89	0.004
G	1	0.05545	4.64%	0.0184	0.0184	1.72	0.194
Square	1	0.05131	4.30%	0.05131	0.051308	4.8	0.032
A*A	1	0.05131	4.30%	0.05131	0.051308	4.8	0.032
2-Way Interaction	2	0.12101	10.14%	0.12101	0.060506	5.66	0.005
A*C	1	0.06852	5.74%	0.12058	0.120577	11.28	0.001
A*E	1	0.05249	4.40%	0.05249	0.052494	4.91	0.03
Error	69	0.73762	61.78%	0.73762	0.01069		
Lack-of-Fit	5	0.01959	1.64%	0.01959	0.003919	0.35	0.881
Pure Error	64	0.71802	60.14%	0.71802	0.011219		
Total	79	1.194	100.00%				

Table 9.7 ANOVA results of the neck.

Source	DF	Seq SS	Contribution	Adj SS	Adj MS	F-Value	p-Value
Model	10	0.479961	60.39%	0.479961	0.047996	10.52	0
Linear	7	0.259494	32.65%	0.292052	0.041722	9.15	0
A	1	0.017096	2.15%	0.035495	0.035495	7.78	0.007
B	1	0.106261	13.37%	0.049731	0.049731	10.9	0.002
C	1	0.000395	0.05%	0.011076	0.011076	2.43	0.124
D	1	0.123795	15.58%	0.049219	0.049219	10.79	0.002
E	1	0.003132	0.39%	0.011544	0.011544	2.53	0.116
F	1	0.000009	0.00%	0.000031	0.000031	0.01	0.935
G	1	0.008806	1.11%	0.038461	0.038461	8.43	0.005
Square	2	0.196175	24.68%	0.220439	0.110219	24.16	0
A*A	1	0.02574	3.24%	0.046522	0.046522	10.2	0.002
E*E	1	0.170435	21.45%	0.186003	0.186003	40.77	0
2-Way Interaction	1	0.024293	3.06%	0.024293	0.024293	5.33	0.024
B*E	1	0.024293	3.06%	0.024293	0.024293	5.33	0.024
Error	69	0.314772	39.61%	0.314772	0.004562		
Lack-of-Fit	5	0.009867	1.24%	0.009867	0.001973	0.41	0.837
Pure Error	64	0.304905	38.37%	0.304905	0.004764		
Total	79	0.794734	100.00%				

Table 9.8 ANOVA results of the thickness.

Source	DF	Seq SS	Contribution	Adj SS	Adj MS	F-Value	p-Value
Model	13	0.514303	95.74%	0.514303	0.039562	114.06	0
Linear	7	0.33541	62.44%	0.219189	0.031313	90.28	0
A	1	0.004225	0.79%	0.007349	0.007349	21.19	0
B	1	0.036634	6.82%	0.000121	0.000121	0.35	0.557
C	1	0.140297	26.12%	0.063248	0.063248	182.35	0
D	1	0.120125	22.36%	0.073556	0.073556	212.07	0
E	1	0.000079	0.01%	0.00062	0.00062	1.79	0.186
F	1	0.014045	2.61%	0.008198	0.008198	23.63	0
G	1	0.020006	3.72%	0.007213	0.007213	20.8	0
Square	1	0.05	9.31%	0.005192	0.005192	14.97	0
A*A	1	0.05	9.31%	0.005192	0.005192	14.97	0
2-Way Interaction	5	0.128893	23.99%	0.128893	0.025779	74.32	0
A*F	1	0.027753	5.17%	0.00747	0.00747	21.54	0
B*F	1	0.028077	5.23%	0.025335	0.025335	73.04	0
C*D	1	0.012795	2.38%	0.010952	0.010952	31.57	0
C*G	1	0.058689	10.93%	0.035867	0.035867	103.41	0
E*G	1	0.001578	0.29%	0.001578	0.001578	4.55	0.037
Error	66	0.022892	4.26%	0.022892	0.000347		
Lack-of-Fit	2	0.000972	0.18%	0.000972	0.000486	1.42	0.249
Pure Error	64	0.02192	4.08%	0.02192	0.000343		
Total	79	0.537195	100.00%				

9.3.3 Effect of process parameters on the UTS

Figure 9.4 illustrates the main effect plot for the UTS of 3D-printed PLA specimens. Higher layer height has been observed to improve layer adhesion and reduce the formation of voids between layers, thereby increasing the tensile strength [38, 147]. Higher infill densities typically result in increased UTS, as more material is available to bear the load, thereby reducing the stress on individual layers. An infill density augment markedly enhances the mechanical properties, including tensile strength [246].

The relationship between print speed and UTS is complex. Higher speeds may reduce UTS due to insufficient bonding time between layers.
Conversely, lower print speeds (e.g., below 30 mm/s) do not significantly enhance the strength of the printed object, but increase the time required for printing, which in turn reduces production efficiency. Moderate print speeds (40–60 mm/s) provide an equilibrium between layer adhesion and build quality, thereby optimizing tensile strength [129, 247]. The attainment of optimal extrusion temperatures is paramount for realizing robust interlayer adhesion. Temperatures below 210°C can result in inadequate melting of PLA, leading to poor adhesion and structural weaknesses, while temperatures exceeding 220°C may cause material degradation due to thermal instability [30]. The orientation of the print layers in terms of loading direction has a considerable impact on the UTS. Parts printed with layers perpendicular to the load direction typically exhibit a higher tensile strength due to the continuous polymer chains being aligned with the stress.

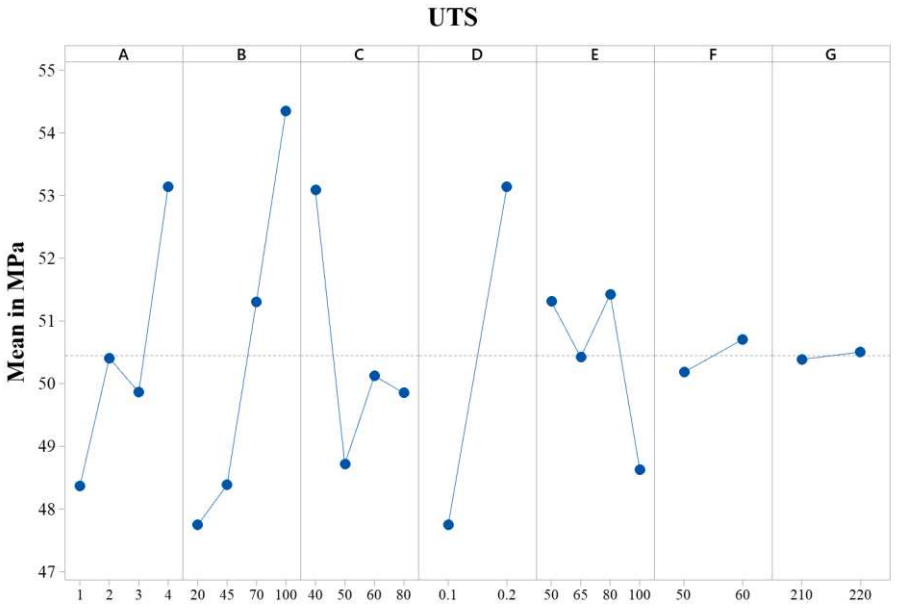


Figure 9.4 The effects of input parameters on the UTS. The axes represent parameter levels and their corresponding effects.

The ANOVA analysis of the UTS data indicated that several printing parameters significantly contributed. The overall model exhibited a highly significant p-value, indicating that the parameters under consideration significantly influence

the UTS. Furthermore, the model's lack-of-fit was insignificant, indicating that the ANOVA model adequately represents the experimental data with minimal fitting error. Table 9.9 delineates the contributions and significance of the various parameters, indicating that some linear terms, which were not significant on an individual basis, became significant when interacting with other parameters, demonstrating the intricate nature of the printing process, wherein the collective impact of multiple parameters can result in notable enhancements in UTS. The linear term E is not statistically significant when considered independently (P-Value = 0.652). However, it becomes statistically significant when interacting with G, as evidenced by the interaction term EG (P-Value = 0.000).

Table 9.9 ANOVA results of the UTS.

Source	DF	Seq SS	Contribution	Adj SS	Adj MS	F-Value	P-Value
Model	12	1669.76	97.30%	1669.76	139.147	201.19	0
Linear	7	1374.8	80.11%	967.82	138.26	199.91	0
A	1	189.99	11.07%	54.77	54.766	79.19	0
B	1	524.85	30.58%	156.83	156.829	226.76	0
C	1	51.57	3.01%	10.93	10.925	15.8	0
D	1	582.96	33.97%	395.6	395.598	571.99	0
E	1	19.82	1.16%	0.14	0.142	0.21	0.652
F	1	5.52	0.32%	6.15	6.155	8.9	0.004
G	1	0.1	0.01%	22.75	22.753	32.9	0
Square	1	69.07	4.03%	50.32	50.315	72.75	0
C*C	1	69.07	4.03%	50.32	50.315	72.75	0
2-Way Interaction	4	225.88	13.16%	225.88	56.471	81.65	0
A*F	1	131.74	7.68%	0.16	0.163	0.24	0.629
B*C	1	5.34	0.31%	3.32	3.319	4.8	0.032
B*E	1	68.31	3.98%	84.28	84.284	121.87	0
E*G	1	20.5	1.19%	20.5	20.5	29.64	0
Error	67	46.34	2.70%	46.34	0.692		
Lack-of-Fit	3	3.89	0.23%	3.89	1.297	1.96	0.13
Pure Error	64	42.45	2.47%	42.45	0.663		
Total	79	1716.1	100.00%				

The UTS is mostly influenced by the percentage of infill, layer height, type of infill and print speed. Increasing the layer height has been shown to improve the tensile strength of 3D printed products, particularly in cases where the layer height approaches the nozzle diameter, at the same time a higher infill percentage means more material is used within the part, resulting in greater bonding between layers and therefore improved mechanical strength [248, 249]. The combination of fan speed and temperature balance layer adhesion and build quality for realizing robust interlayer adhesion [49]. The part fill rate must be balanced with the layer height and print speed to achieve optimum bonding between layers [246].
To provide a concise overview of the ANOVA results, Table 9.10 consolidates the significant findings for all response variables. The table highlights the most influential parameters and their relative contributions to the variability observed, offering insights into the factors driving optimization.

Table 9.10 Consolidated Summary of ANOVA Results for dimensional accuracy of internal and external features, and mechanical performance.

Response Variable	Most Influential Parameters	% Contribution to Variance
Diameter circle	Type of infill, Infill, Print speed, Layer height, Fan speed, Bed temperature	94.31%
Length square	Print speed, Layer height, Bed temperature, Extrusion temperature	76.98%
Width square	Print speed, Layer height, Fan speed	81.48%
Length	Infill, Layer height, Fan speed, Extrusion temperature	81.50%
Width	Type of infill, Infill, Bed temperature	38.22%
Thickness	Type of infill, Print speed, Layer height, Bed temperature, Extrusion temperature	95.74%
Neck	Infill, Layer height, Extrusion temperature	60.39%
UTS	Type of infill, Infill, Print speed, Layer height, Bed temperature, Extrusion temperature	97.30%

9.4 Responses optimization and model validation

9.4.1 RMS model

The RSM represents a collection of mathematical and statistical techniques for modelling and analyzing problems in which several variables influence the response of interest. This study employed the RSM to optimize the process parameters for the dimensional and mechanical properties of 3D-printed PLA parts. The primary objective was to develop predictive regression models that could accurately forecast the outcomes of the experimental conditions, thus achieving the optimal response. Table 9.11 presents the RSM predictive regression models with their relative R^2(adj). The experimental data was then fitted to second-order polynomial equations. The equations were derived from the analyses conducted in Section 9.3; wherein various ANOVA tables are provided. The high R-squared values for most models indicate that they explain a significant proportion of the variability in the response variables. The model that predicts the hole's diameter achieved an adjusted R-squared value of R^2(adj) = 93.39%, demonstrating a high level of predictive capability. Similarly, the model for the UTS achieved an adjusted R-squared value of R^2(adj) = 96.82%, which underscores the robustness of the regression model in capturing the relationship between the input parameters and the response variable.

Nevertheless, it is notable that specific models exhibit relatively low R-squared values. The width is only explained by 29.27%. A low R-squared value indicates that the model cannot sufficiently explain the variability observed in the response variable. This may be attributed to several factors, including inherent variability in the 3D printing process, such as fluctuations in extrusion flow or filament consistency, as reported in prior studies [220]. Additionally, unmodeled interactions between parameters or environmental factors like room temperature and humidity may have played a role [222]. Even though the R-squared values were low, these models were included in the multi-objective optimization process to ensure a thorough approach. Including all responses in the optimization process makes it possible to ensure that the overall procedure is robust and that no potential influencing factor is left out.

Table 9.11 RSM predictive regression models and corresponding R^2(adj).

Response	Prediction model	R^2(adj)
Diameter circle	-20.50 + 10.391 A - 0.06905 B + 0.1353 C + 1.164 D - 0.00193 E - 0.00601 F + 0.15523 G + 0.000515 B*B - 0.04823 A*G + 0.000067 B*E - 0.000601 C*G	93.39
Length square	-2.81 + 6.54 A - 0.04497 B - 0.00192 C - 2.08 D - 0.00808 E + 0.00389 F + 0.0635 G + 0.000374 B*B + 0.00297 A*E - 0.03155 A*G + 0.0565 C*D	73.26
Width square	-3.83 + 6.98 A - 0.05296 B + 0.00340 C + 0.840 D + 0.000290 E + 0.01843 F + 0.0617 G + 0.000434 B*B - 0.00759 A*F - 0.03059 A*G	78.80
Length	110.212 + 1.278 A + 0.0322 B - 0.00473 C - 3.217 D + 0.03632 E - 0.00034 F + 0.01957 G - 0.000258 E*E - 0.00599 A*G - 0.000144 B*G + 0.02913 C*D	78.51
Width	18.684 - 0.626 A + 0.00521 B - 0.01983 C + 0.727 D - 0.00568 E + 0.01624 F + 0.00315 G - 0.0253 A*A + 0.00889 A*C + 0.00347 A*E	29.27
Thickness	-4.72 - 0.2064 A - 0.007766 B + 0.08034 C + 2.588 D + 0.0492 E - 0.01707 F + 0.04091 G - 0.01597 A*A + 0.00536 A*F + 0.000139 B*F - 0.03088 C*D - 0.000364 C*G - 0.000228 E*G	94.90
Neck	6.639 - 0.1589 A + 0.00434 B - 0.000908 C - 0.584 D + 0.03401 E - 0.00012 F - 0.00662 G + 0.02752 A*A - 0.000203 E*E - 0.000045 B*E	54.65
UTS	399.2 + 0.25 A + 0.0045 B - 0.5391 C + 53.82 D - 5.098 E - 0.1749 F - 1.553 G + 0.004719 C*C + 0.0226 A*F - 0.001002 B*C + 0.002468 B*E + 0.02304 E*G	96.82

9.4.2 Optimization of RSM models and Validation

Figure 9.5 illustrates the graphical representation of the composite desirability, which demonstrates the impact of varying combinations of process parameters on the overall desirability. Optimization consists of gradually adjusting the parameters to maximize the composite desirability value, thereby identifying the optimal settings for the desired outcomes; in this case, the solution will be a

compromise since the multi-objective function is trying to optimize both dimensions and strength.

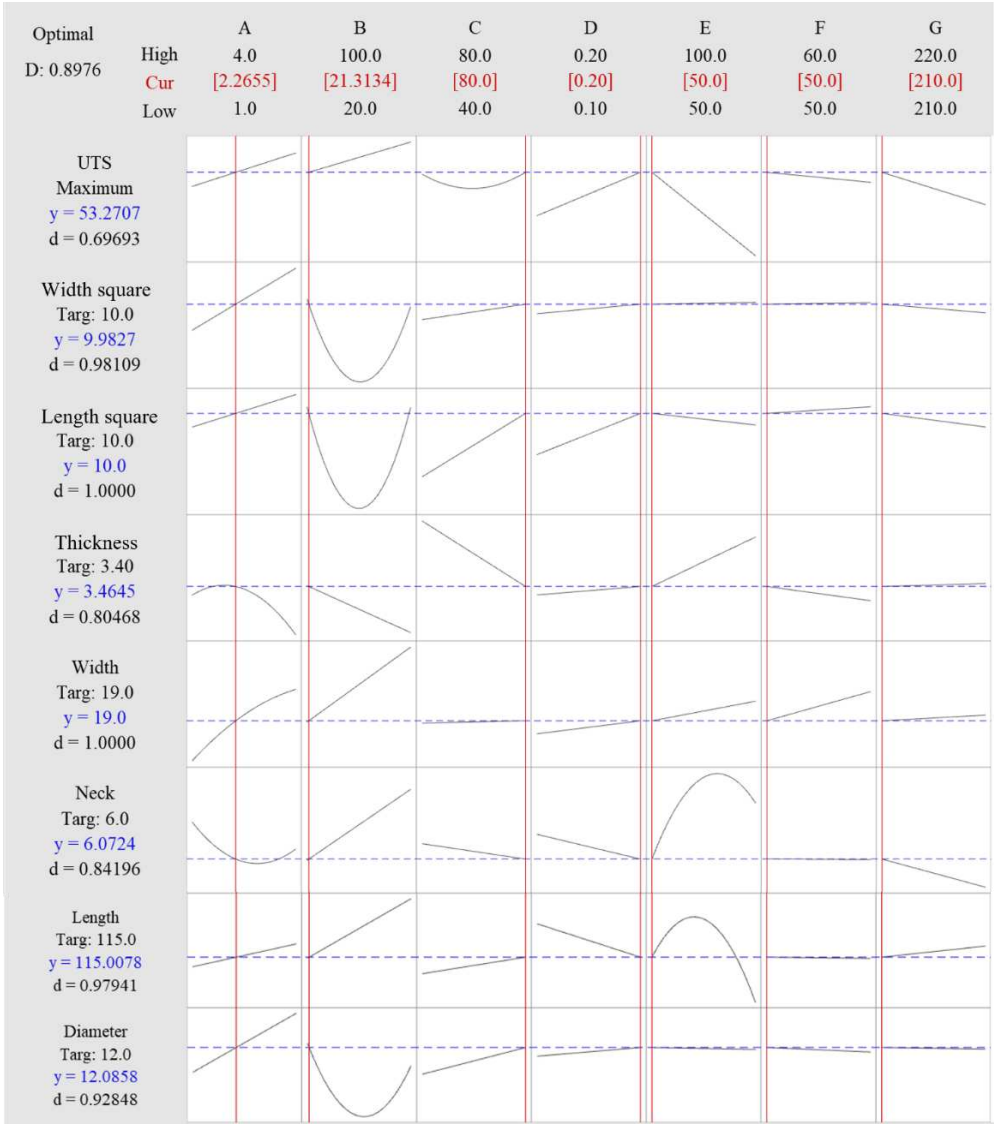


Figure 9.5 Composite desirability plot illustrating optimal parameter combinations for maximizing dimensional accuracy and mechanical strength. The axes display input parameter ranges, while the gradient indicates desirability.

Table 9.12 highlights the optimized settings for each input parameter.

Table 9.12 RSM-optimized response parameters.

Input variable	Optimal setting
A - Type of Infill	Triangle
B - Infill (%)	21.31
C - Print speed (mm/s)	80
D - Layer height (mm)	0.2
E - Fan speed (%)	50
F - Bed Temperature (°C)	50
G - Extrusion Temperature (°C)	210

Experimental tests were conducted under the optimal conditions identified by the RSM models to validate their predictive capability. The three specimens (see Figure 9.6) were produced using identical filaments and a 3D printer that was employed in creating the dataset. The validation specimens were subjected to the same dimensional and mechanical analyses as those on the original dataset.

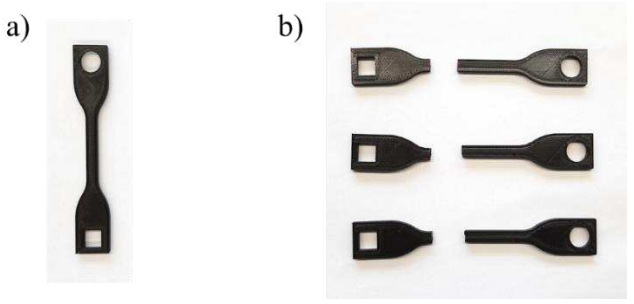


Figure 9.6 (a) Specimens from the validation print before and **(b)** after the tensile test.

The outcomes of these validation experiments are presented in Table 9.13, which compares the predicted outcomes and the experimental test values for a range of response parameters at optimal conditions. The percentage error was calculated to assess the precision of the predictions. Among all the parameters, the maximum observed variation was for the circle's diameter, with a maximum error of -5.01%. The minimum observed variation was for the length, with a maximum error of 0.01%. The low percentage of errors demonstrates the RSM models' reliability and effectiveness in predicting outcomes under specified conditions.

Table 9.13 Model validation of predicted process conditions. Values of experimental tests (X1, X2 and X3) and prediction results at the optimal conditions (all dimensions in mm; UTS in MPa).

Response	Prediction result	Experimental test			Error between experimental and predicted results in %		
		X1	X2	X3	E1	E2	E3
Diameter circle	12.086	11.548	11.480	11.483	-4.45	-5.01	-4.99
Length square	10.000	9.643	9.619	9.614	-3.57	-3.81	-3.86
Width square	9.983	9.682	9.652	9.637	-3.01	-3.31	-3.46
Length	115.008	114.960	115.018	115.002	-0.04	0.01	-0.01
Width	19.000	19.055	19.185	19.233	0.29	0.97	1.23
Thickness	3.464	3.510	3.560	3.550	1.31	2.76	2.47
Neck	6.072	6.306	6.381	6.356	3.85	5.08	4.67
UTS	53.271	52.634	53.110	53.394	-1.20	-0.30	0.23

The optimization framework presented in this study, based on RSM, empowers operators to strategically prioritize their objectives—dimensional accuracy or mechanical strength—depending on the specific requirements of the application. By defining acceptable ranges for key parameters such as layer height, print speed, and extrusion temperature, the operator can fine-tune the process to achieve the best possible outcome that aligns with industrial demands.

The RSM model provides a predictive tool that helps minimize trial-and-error approaches in production. While inherent limitations in the model might lead to slight deviations between predictions and experimental results, the validated optimization settings demonstrated errors within a manageable range (less than 5% for critical dimensions). This ensures that the final product closely meets the desired specifications. This flexibility makes the RSM-based optimization framework highly practical for real-world manufacturing, where different applications demand tailored trade-offs. By systematically balancing these parameters, operators can produce components that are not only functional but also meet stringent industrial standards efficiently and reliably.

9.5 Conclusion

This study aims to develop an RSM to achieve an optimal configuration in both dimensions and mechanical strength of PLA 3D-printed parts. Integrating these two aspects makes it possible to produce a component that fulfils the requisite functional assembly requirements and ensures prolonged operational reliability under stress. The experiments are designed following the fractional Taguchi L16 DOE, where seven printing parameters were analyzed, and the resulting data were subsequently analyzed using RSM. The samples were printed using an Ultimaker S3 FFF printer and subjected to tensile tests and measurements to evaluate their mechanical and dimensional properties. From the first analysis, the diameter of a circle is subject to influence by two key factors: printing speed and layer height. Higher printing speeds have been demonstrated to enhance precision, although a reduction in interlayer adhesion may accompany this. The dimensions of a square are influenced by the temperature at which the extrusion occurs and the fan speed, with the optimal temperature preventing heat expansion and the optimal fan speed ensuring uniform cooling. Higher printing speeds reduce dimensional accuracy, whereas lower layer heights enhance accuracy and adhesion. The thickness and width of parts are also influenced by extrusion temperature and fan speed. Controlled cooling prevents thermal deformation and maintains dimensional stability. The mechanical properties of 3D printed objects demonstrate that increasing layer height improves UTS adhesion and reduces void volume with 100 % infill density enhances UTS. At the same time, optimal extrusion temperature is crucial for strong adhesion. The optimization results revealed that the optimal printing parameters were a type of infill triangle, an infill percentage of 21.31 %, a print speed of 80 mm/s, a layer height of 0.2 mm, a fan speed of 50 %, a bed temperature of 50 °C, and an extrusion temperature of 210 °C. The experimental validation under these optimal conditions showed minimal percentage errors, confirming the reliability of the RSM models. Specifically, the maximum observed variation was -5.01 % for the hole's diameter, while the minimum observed variation was 0.01 % for length, demonstrating the accuracy of the models.

In conclusion, this study presents a comprehensive framework for optimizing FFF process parameters to produce high-quality PLA parts with exceptional dimensional precision and mechanical strength.

This research underscores the transformative potential of multi-response optimization in additive manufacturing. By systematically refining process parameters, manufacturers can achieve significant cost savings through reduced material waste and minimized trial-and-error iterations. Enhanced efficiency in achieving dimensional precision and mechanical strength simultaneously ensures that the printed components are ready for demanding applications. These advancements directly translate to improved performance, enabling greater adoption of additive manufacturing in critical industries such as aerospace, automotive, and healthcare. While the proposed framework is robust, its generalizability to other materials and manufacturing methods should be considered. The findings are validated for PLA, and extending the methodology to other thermoplastics such as ABS or PETG may require adjustments due to material property differences. Similarly, more complex geometries could introduce additional challenges, such as warping or support requirements, that were not evaluated in this study. Furthermore, while the framework is optimized for FFF, adaptations might be needed for other additive manufacturing techniques like SLA or SLS, where material deposition processes differ. These considerations open avenues for future research to expand the applicability of this approach. Furthermore, by integrating the optimization of dimensional accuracy and mechanical strength, the research has demonstrated the viability of producing 3D-printed parts that not only fulfil the functional requirements of assemblies but also withstand prolonged operational stresses. Further research could investigate the printing parameters of other thermoplastic materials, including ABS, PETG, and composites. This could facilitate the expansion of the scope of the findings. Moreover, research into advanced printing techniques, such as multi-material printing and hybrid manufacturing processes, could improve printed parts' intrinsic qualities. Integrating machine learning algorithms with RSM could also prove advantageous, as it would facilitate more efficient and precise prediction and optimization of printing parameters. Moreover, exploring its use in multi-material printing could unlock new possibilities for producing complex, functional assemblies with tailored material properties. Integrating machine learning algorithms with RSM could further enhance predictive accuracy and expedite optimization processes. Expanding the study to include other additive manufacturing techniques, such as hybrid or high-resolution methods, would also validate the generalizability of the approach.

Chapter 10 From FDM to SLS: Enhancing Material and Process Efficiency in AM

Valentina Vendittoli[1]

[1] Department of Civil and Mechanical Engineering, University of Cassino and Southern Lazio, via G. di Biasio 43, 03043 Cassino, Italy

10.1 Introduction

The objective of this Chapter is to present a comprehensive overview of the relationship between the research conducted on FDM and the subsequent exploration of SLS. This transition represents a strategic evolution in the approach to AM, addressing the inherent limitations of FDM and leveraging the advanced capabilities of SLS. Although FDM is widely acknowledged for its simplicity and cost-effectiveness, it is confronted with considerable challenges, particularly in attaining high mechanical performance and dimensional accuracy, which are fundamental for high-end applications [5]. SLS represents a promising alternative, offering superior material properties, increased design flexibility, and enhanced process efficiency. The transition to SLS is driven by the necessity to overcome the constraints of FDM in terms of material utilization, geometric complexity and environmental sustainability. This Chapter elucidates the scientific rationale behind this transition, emphasizing the potential benefits of SLS, such as enhanced mechanical strength, broader material compatibility and improved management of material ageing, which is particularly pertinent for PA12 employed in SLS processes [56].

10.2 Review of FDM: Achievements and Limitations

The research conducted on FDM has concentrated on the optimization of the mechanical properties and dimensional accuracy of parts produced using PLA.
Further progress is reflected in developing performance indices integrating both dimensional accuracy and mechanical strength, as explored in Chapter 4 and 5. These indices emphasize the necessity of considering process parameters' individual and combined effects, thereby facilitating a more comprehensive approach to optimizing 3D printing processes. Such an integrated methodology is essential for improving the quality of parts used in high-performance applications. A significant advancement has been made with the application of BR-ANN to predict dimensional accuracy tensile strength. This highlights the necessity to meticulously adjust process parameters, including infill percentage, print speed, and extrusion temperature, to optimize mechanical performance. This work, detailed in Chapter 6 and 7, represents a significant advancement in achieving precise control over the interaction between these parameters. Significant advancements have been made through integrating AI techniques, particularly ANN, and pattern

search algorithms. AI-driven models have facilitated a more precise prediction and control of the interaction between various process parameters, thereby enhancing product quality [207, 68]. This statement details further advancements in Chapter 8, which introduces an AI tool designed to optimize geometrical and mechanical performance. This tool refines predictive models and offers robust optimization techniques. Furthermore, utilizing RSM in Chapter 9 for multi-response optimization constitutes a novel advancement, further improving the overall quality of the 3D-printed parts by fine-tuning the process to achieve the best possible outcomes.

While PLA is biodegradable and easy to process, it may not always meet the mechanical requirements of more intensive applications. The need for support structures when producing complex geometries can lead to increased material usage and extended post-processing [4]. In addition, the environmental impact of non-recyclable waste material is a factor to consider, especially in high-volume production contexts [3]. However, FDM has seen significant advancements in material recycling techniques, allowing for efficient reuse of thermoplastic materials [250]. This development has reduced the environmental impact of FDM processes. As a result, research on recycling has been more focused on SLS, where challenges such as powder ageing and degradation make recycling less developed compared to FDM [251].

However, by carefully controlling parameters such as film thickness, print speed and extrusion temperature, significant improvements in surface roughness, dimensional accuracy and mechanical properties can be achieved [121].

10.3 Rationale for Transitioning to SLS

FDM technology, a dominant force within the material extrusion segment, has been extensively embraced across many industries, primarily due to its straightforward operational methodology and competitive cost structure. In 2023, FDM constituted a significant proportion of the 3D printing market, particularly in educational and prototyping applications [252]. However, technologies such as SLS are expected to experience the highest growth rates in the coming years [252]. These growth projections for the SLS are driven by their superior material properties and ability to produce complex geometries since it does not necessitate the incorporation of support structures at any stage of the manufacturing process. The production of complex internal structures, which are often required in

aerospace and biomedical applications, can be efficiently achieved using SLS, thereby expanding the potential applications of AM technologies [4], where the demand for durable, lightweight, and high-precision parts is important [253].
The enhanced mechanical properties of the parts are primarily attributable to the distinctive bonding mechanisms inherent to SLS, which form more dense and homogeneous parts. This renders SLS a particularly advantageous method for applications that require parts with superior structural integrity and durability [121].
The transition to SLS presents a promising avenue for environmental benefits, particularly in the context of material recycling. It has been demonstrated that carefully managing powder ageing, including mixing aged powder with virgin powder, can mitigate the negative effect of thermal treatment during the printing stage. This enhances the sustainability of the SLS process. This aspect renders SLS a more environmentally friendly option for large-scale additive manufacturing, where the minimization of waste is significant in reducing the carbon footprint [56]. Furthermore, recent developments in powder recycling techniques have further reduced the environmental impact of SLS, thereby establishing it as a leading choice for sustainable manufacturing practices [3]. In fact, companies such as 3devo have established processes for converting discarded SLS powder into premium-grade filament, thereby minimizing the environmental impact and operational costs for industries that employ 3D printing [254].

10.4 The Role of AI in AM Process Optimization

In FDM, ANN has been employed to optimize process parameters and predict the interactions between these parameters. These models have markedly enhanced the dimensional precision and mechanical attributes of FDM components by facilitating exact control over multiple process variables [255]. Additionally, AI models have been pivotal in reducing production time and material waste by improving the slicing process and predicting potential print failures [256]. The transition to SLS presents a novel opportunity for the application of AI that can be employed to optimize the more intricate process parameters in SLS, including powder characteristics. Furthermore, AI-driven models can predict the effects of powder ageing on part properties, thus facilitating more effective management of material reuse and improving the overall sustainability of the SLS process [253]. The incorporation of AI into SLS not only enhances the process's efficiency but

ensures consistent part quality across different production runs [3]. Moreover, AI can facilitate the development of novel materials optimized for SLS, optimizing both material properties and the printing process to achieve superior results [4].

10.5 Addressing Material Aging in SLS

The ageing of materials in SLS, particularly with PA12, represents a critical factor influencing the dimensional and mechanical properties of the resulting parts. The process of ageing affects the chemical and physical characteristics of the powder, resulting in alterations to the crystallinity, melting temperature, and mechanical strength. Without appropriate management, these changes can produce parts with inferior properties. It is, therefore, imperative to gain an understanding of and exert control over the ageing process if the durability and performance of SLS-manufactured parts are to be optimized [56]. Unlike FDM, where recycling and material reuse are more straightforward due to the thermoplastic nature of the filament and established recycling methods [250], SLS faces significant challenges in recycling due to powder degradation over successive thermal cycles [57]. The current methods employed, including adjusting the mixing ratios of virgin and recycled powder and refining process parameters, have thus far been unsuccessful in producing parts with mechanical properties equivalent to those made with virgin powder alone [61]. Therefore, future research must prioritize developing advanced techniques that facilitate the optimal utilization of recycled powder, thereby ensuring the long-term environmental and economic sustainability of SLS. Research on improving recycling in SLS is essential because the recycling processes are not as developed as in FDM, and material wastage has a more significant environmental impact [57, 250]. Other methods include adjusting the laser parameters to accommodate the aged powder's characteristics better. However, this requires careful optimization to avoid introducing new defects into the parts [257]. Nevertheless, the mechanical properties of components manufactured exclusively with reused powder remain inferior to those of parts produced with virgin powder. The current research is focused on developing methods that would allow for a fully recycled powder without compromising the mechanical integrity of the resulting product. Nevertheless, obtaining mechanical properties comparable to those of virgin powder continues to represent a substantial challenge within this field of research. It has been demonstrated that further developments in powder treatment and process optimization are necessary to facilitate

the complete reuse of SLS powders without compromising part quality [62]. These strategies are vital for maintaining the sustainability and cost-effectiveness of the SLS process, even when utilizing recycled materials. Furthermore, incorporating AI in forecasting aged powders' behavior can optimize recycling, ensuring consistent quality and performance in SLS-produced parts [3].

10.6 Conclusion

The following Chapters will undertake a detailed study of SLS, focusing on the impact of powder ageing across multiple reuse cycles on the mechanical properties of the resulting parts. It is essential to understand the degradation behavior of PA12 powder in the context of repeated thermal cycles to enhance the sustainability and efficiency of the SLS process. This research will contribute to the broader field of additive manufacturing by providing new insights into the interplay between material science and process engineering. It is currently not feasible to employ a method to reverse the effects of powder ageing. The following Chapters present a detailed examination of the effects mentioned above, focusing on evaluating these effects over multiple cycles of reuse.

Additionally, the research aims to identify the limits of powder reuse, exploring the extent to which aged powder can be reused before the properties of the produced parts are compromised beyond acceptable levels. It is crucial to ascertain the thresholds at which powder must be refreshed or replaced to maintain the quality of the parts produced. The transition from FDM to SLS is a crucial aspect of this research, as it allows for exploring advanced techniques to manage and potentially reverse the effects of powder ageing. For instance, the integration of AI could facilitate the development of predictive models that optimize the reuse of aged powders, enabling real-time adjustments to process parameters to maintain part quality. Furthermore, AI could be utilized to develop more sophisticated algorithms for predicting the optimal timing and methodology for refreshing or retiring powder from the process, thereby enhancing the overall sustainability and cost-effectiveness of SLS. This Chapter will connect the initial research on FDM and the forthcoming exploration of SLS, establishing a foundation for future studies that will seek to overcome these significant challenges. The goal is to achieve a process where reused powder can deliver mechanical properties comparable to those of virgin material, thereby enhancing the sustainability and cost-effectiveness of SLS while reducing its environmental impact.

Chapter 11 Overview of Structural, Mechanical and Geometrical Characteristics of Parts in Polyamide 12 Manufactured with Laser Powder Bed Fusion: Outcome and Future Development

Valentina Vendittoli[1], Maria Cristina Mascolo[1], Wilma Polini[1], Luca Sorrentino[1], Alexandru Sover[2] and Michael S. J. Walter[2]

[1] Department of Civil and Mechanical Engineering, University of Cassino and Southern Lazio, via G. di Biasio 43, 03043 Cassino, Italy

[2] Faculty of Engineering, University of Applied Sciences Ansbach, Residenzstr. 8, 91522 Ansbach, Germany

This chapter has been submitted

Abstract

Laser Powder Bed Fusion of Polymers is a widely used Additive Manufacturing technology that uses a laser to selectively sinter layers of a powder bed, with Polyamide 12 being a common material choice. Despite its favorable processability and component performance, the printing process leaves a significant amount of unsintered powder that undergoes heat treatment due to temperature gradients during printing, leading to material degradation over time. A deep comprehension of the aging behavior in the powder for rightly planning the successive building process is thus necessary to define the right recycling methods.

This paper presents a comprehensive study of the thermal and structural properties of Polyamide 12 after six successive reusing cycles, as well as the dimensional and mechanical characteristics of the corresponding printouts. The study includes tests on the powder that underwent successive building cycles and the parts manufactured using this powder. The results were compared to those obtained from virgin powder. These results were used to justify the differences in mechanical, macro-geometrical, and micro-geometrical performance between virgin and aged powder parts.

The results indicate that something occurred in the powder during aging that significantly reduced the mechanical strength and texture quality of parts made from aged powder.

Keywords: Additive manufacturing; Selective Laser Sintering; PA12; degradation; powder reuse.

11.1 Introduction

With the adventure of AM, the feasibility of producing different parts with the most varied features is possible. However, for some technologies, preventing waste from production is still impossible. According to the ASTM/ISO 52900 standard, the SLS technique, under the classification of the PBF family [1], is a 3D printing technique where the thermal energy of a laser selectively sinters portion of a powder to realize the layer.

Polymeric materials are preferred in the SLS technique for their good dimensional and mechanical properties while requiring low laser power and processing temperatures. PA12 is the most often used semicrystalline polymer [258, 259].

Compared to other technologies, supports are unnecessary since the component is built surrounded by unsintered powder. But, at the end of the process, this powder undergoes thermal cycles caused by the high temperatures in the printer, leading to powder degradation [65, 260].

Since this percentage of unsintered powder is almost 80 %, different solutions have been implemented to enchant the recycling process through reusing the unsintered powder and directly reducing the heating effect on the powder. The most common method is the powder refreshing with virgin powder at different percentages. Loper et al. studied different ratios in the mixture and successfully implemented an algorithm where only 30% of virgin powder is enough to enchant the mechanical properties in the printed specimens [59]. The Melt Flow Rate (MFR) test is used to verify if the mix is still printable. In this case, different range values can be applied to predict the possible surface quality of the parts [57]. This method does not take into account the mechanical performance connected with the degradation described by the flow index. However, this solution is not sustainable for a longer period the mixture will contain powder with different reusing stages and different characteristics, which makes it even more difficult to control recycling. Furthermore, the mixing method must be defined to pursue good homogeneity in the powder [60].

Acting directly on the PA12 chain with the use of a chain splitter allows the reverse of the effect of the post-condensation, thus adjusting the viscosity of the powder and its success in the printing process. By adding 5 wt% to the used powder, the flowability of the powder increases, reaching the results obtained with a mixture of virgin and used powder with a mixing ratio of 1:1 in weight. The

surface quality improves. However, some roughness is still present due to small chain splitter particles. The tensile strength and elongation are still lower than specimens made with only virgin powder but better compared to parts produced with 100 % used powder [261, 262].

A Low-temperature Laser Sintering (LTLS) has been developed to prevent powder degradation, in which the powder bed temperature is decreased at 140 °C. In this way, the unsintered powder undergoes less thermal damage by changing the process [263]. On the other hand, the laser's energy must be higher than the SLS to compensate for the lower heat, and the printing strategy must be adapted to the part geometry to obtain a well-sintered part.

Despite the improvement in the powder, the problem is shifted to the parts that need to be fixed on a rigid base to avoid the curling caused by the lower temperatures used for this type of technique [264]. In fact, the high gradient between the melt pool and the bed surface can cause the premature recrystallization and negatively impacting process stability [265]. All the methods described above do not fully repristinate the degradation and completely solve the problems on the final product or, in the case of LTLS, add more factors of influence that lead to worse performance in the parts. Understanding the ageing at different stages of reuse is important to analyze and correlate the different effects to define a new method to reduce the waste and reprocess all the powder multiple times without compromising the performance [266].

Eight building cycles with an initial batch of PA 2200 powder were carried out using the printer Formiga P110. Within the reusing cycles, the powder was analyzed at the virgin, second, fourth, sixth, and eighth build cycles for characterization. The number of cracks on the particles increases with reuse, and long exposure time leads to water and alcohol evaporation from the composition. Furthermore, the number of fine particles increases due to fragmentation [267]. The rough particle surface and the high viscosity do not facilitate the flowability of the powder in the printer, and the quality of the parts surface decreases [58]. The same brand of powder was subjected to different annealing times and temperatures in a nitrogen environment to simulate the different conditions and to analyze the effects of the temperature and time on the powder properties. Up to the third recycling state, the powder shows a decrease in the degree of crystallinity, which shows an opposite trend to the molecular weight [47]. However, there is a lack of studies on the effect of the degradation on the mechanical performances of the

printed parts made with successive reuse powders and the quantification of the surface quality in terms of roughness.

This paper will present an in-depth experimental analysis of the extensive reuse of the PA12 powder and the transfer of degradation effects from the powder to the part during the printing process in an oxygenated environment. A statistical analysis of the effect of the degradation on the performance of the printed parts was implemented. This will open a new field of study and more understanding to reach a more sustainable process in which the unsintered powder can be completely used and be equivalent to virgin powder by selectively acting on the right characterization.

The paper is organized as follows: Section 11.2 details the materials, the benchmarks used for the experimental tests, and the manufacturing process. The measuring procedure of the manufactured parts is also illustrated. In Section 11.3, the results are presented. Firstly, the effect of the degradation on the powder is reported in terms of density, porosity, and chemical behavior. Subsequently, the results obtained from the specimens' dimensional measurements, the statistical analysis, and the surface roughness are shown. Lastly, a report of the mechanical tests carried out is presented with a statistical analysis of the causes. In conclusion, Section 11.4 summarizes the findings and discusses potential future research for the topic.

11.2 Materials and method

11.2.1 Characterization of Virgin PA12

PA12 Smooth from Sinterit was used for the experimental setup. The main properties are listed in Table 11.1.

Table 11.1 Sinterit PA12 properties **[268]**.

Property and unit	Value
Particle size (μm)	18-90
Density of solid parts (g/cm^3)	0.92
Melting temperature (°C)	185
Tensile strength (MPa)	32
Young's modulus (MPa)	1470
Elongation at break (%)	10

11.2.2 Printing process

To investigate the dimensions and mechanical properties of the printed parts, a tensile specimen was designed according to the standard ASTM-D 638-22 (see Figure 11.1.a). Two internal geometric features (one round and one square hole) were added to the model to provide further features to measure the dimensional deviations of hollow structures. The modifications were applied to the part of the specimens that are fixed in the clamps of the testing rig to avoid any corruption during the mechanical tests.

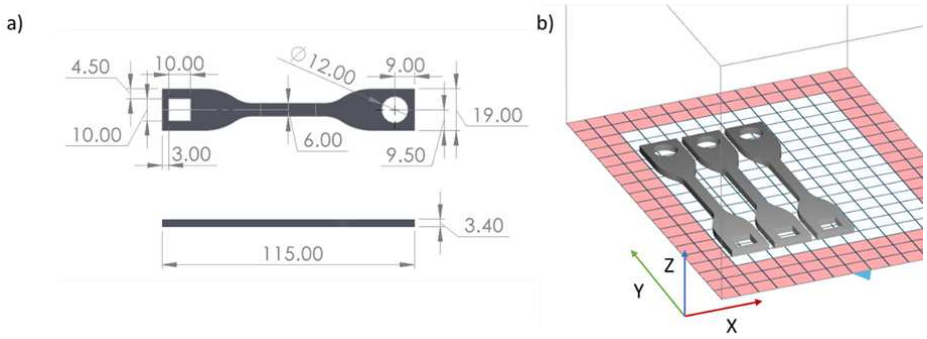


Figure 11.1 (a) Tensile specimen according to ASTM-D 638-22, all dimensions in mm **[109]**; **(b)** Printing preview during the AM pre-processing.

The process was made with a Sinterit LISA SLS printer. The specifications are reported in the Table 11.2 [269].

Table 11.2 Sinterit LISA technical specification.

Parameter and unit	Value
Build volume (mm*mm*mm)	150x200x150
Laser power (W)	5
Print bed temperature (°C)	5 below the T_m
Feed bed temperature (°C)	0 - 150
Print chamber temperature (°C)	0 - 140
Laser speed (mm/h)	Up to 3
Layer height (mm)	0.075 - 0.175

The recommended printing parameters from the manufacturer were set for this project: the chamber temperature is set to 140 °C and the surface printing temperature to 178 °C. The layer height was 0.1 mm. All the specimens were printed flat

on the build plate (see Figure 11.1.b). Six consecutive printing cycles were made with constant process parameters. Before every reuse, the powder collected from the printer was put in a sieve to remove the clumps [270].

11.2.3 X-Ray Diffraction (XRD) Analysis

The virgin and 5-times used powders and the corresponding sintered parts were characterized by X-ray Diffractometric Analysis (XRD) using a Philips diffractometer to detect the crystalline structure evolution of PA12.

11.2.4 Thermal Analysis Using Differential Scanning Calorimetry (DSC)

A Mettler Toledo DSC 3+ was used for thermal analysis on the powders. Three samples per powder were tested, and the average on the results was taken. Each sample weighs 10±0.5 μg and is sealed in aluminum pans [271]. It was subjected to a heating ramp from 120 °C to 200 °C at a constant rate of 10 K/min, then the temperature was kept constant for five minutes, then a cooling ramp with a constant rate of 10 K/min from 200 °C to 23 °C was applied. Finally, the temperature was kept constant for an additional five minutes. The measurements were carried out under a 30 mL/min nitrogen flow rate. To quantify the degradation effect of the printing process, the degree of crystallinity was calculated as follows:

$$Xc(\%) = \frac{\Delta H_f}{\Delta H_f^0} * 100 \qquad (11.1)$$

where ΔH_f is the heat of fusion from the DSC results, and ΔH^o_f is the heat of fusion of 100 % crystalline PA12. The ΔH^o_f is 209.3 J/g, according to the literature [52].

11.2.5 Scanning Electron Microscopy (SEM)

The morphological analysis of the surface of the sample was performed by Scanning Electron Microscopy (SEM) adopting a Philips microscopy (XL series, Almelo, Nederland).

11.2.6 Size distribution

A Mastersizer 2000 from Malvern that uses laser diffraction [272] was used for measuring the size distribution of the powder according to the standard ISO 13320:2020 [273]. Five measurements were carried out, and the average was considered since the observed variation was not significant. The percentile values at

10 %, 50 %, and 90 % (henceforth: d10, d50, and d90) and the volume distribution are reported.

11.2.7 Porosity

A Fluometer type ADP was used to calculate the bulk density of the powder, following the standard ISO 60 [274] as:

$$\rho_{bulk} = \frac{w_{powder}}{V_{cylinder}} \quad (11.2)$$

where w_{powder} is the weight of the powder in the cylinder, and $V_{cylinder}$ is the volume of the cylinder, which is 100 cm^3.
A Helium Pycnometer was used to measure the solid density of the powder according to the DIN 66137-2:2019-03 [275]. The formula for the porosity of the powder is:

$$\varepsilon = 1 - \frac{\rho_{bulk}}{\rho_{solid}} * 100 \quad (11.3)$$

where ϱ_{bulk} is the density of the bulk and ϱ_{solid} is the solid density.

11.2.8 Dimension and roughness analysis

Following the production of the samples, geometric deviations on the benchmark were investigated. The first step was to verify through a 2D control measurement system using the Instant Measurement System Advantages IM-7000 from Keyence. Two measurement programs were set up, one for each side (left and right, see Figure 7.1.a), to analyze the specimen's features with a high resolution. With the Waveline W20 device from the manufacturer Vista Instrument SDN BHD [160], the tensile specimens' roughness on the top and downside parts was measured. The downside surface is the one facing the building platform. It consists of a 2 µm radius tip and different measuring programs. For this purpose, program 2 was chosen under ISO 16610-21 [161]. The cut-off is 0.8 mm, and the traversing length of the probe on the surface is 4.8 mm.

11.2.9 Mechanical test

The tensile tests were carried out with an MTS Criterion 43 tensile testing machine using a load cell of 5 kN and following the standard ASTM D638-22 [109] for the definition of the gap between the clamps of 70 mm and the testing speed of 5

mm/min, following the classification of the material described in the ASTM D883 [114].

11.3 Results and discussion

11.3.1 Material characterization

PA-12 is a semi-crystalline polymer, and it exhibits two crystal structures, α- and γ-phases, and usually γ acts as its stable phase. XRD patterns of virgin and 5-times used powders are reported in Figure 11.2. Virgin and aged powder patterns show a single γ (0 0 1) peak at $2\theta = 21.5°$ and two weak reflections of the α-phase at 2θ equal to 11.2° and 21.5°, respectively, in agreement with other publication [276].

XRD pattern of 5-times used (aged) powder is characterized by a slightly more intense γ (0 0 1) peak compared to that of the virgin powder and, therefore, a crystallinity and, consequently, dimensions of the crystals slightly bigger. Moreover, γ (0 0 1) peak of aged powder is shifted to lower 2theta angle values. This indicates that, as a result of aging, the powders undergo a deformation due to the chain segment rearrangement. Furthermore, the peaks of the α-phase in the aged powder tend to decrease in intensity, thus favoring the formation of the more stable γ-phase. XRD patterns of the samples sintered from both the virgin and aged powders (Figure 11.3) show the presence of only the γ (0 0 1) peak, characterized by almost the same intensity and, therefore, the same crystallinity but greater intensity compared to the corresponding non-sintered samples and therefore by larger crystal dimensions. Moreover, γ (0 0 1) XRD peak of the sample obtained by sintering the 5-times used powder presents a shift towards the left compared to the same peak of the sample obtained starting from the virgin powder. This shift indicates an effect of a slight deformation justified by the fact that the sintering of the aging of the powder determines a different rearrangement of the chains compared to that of virgin powder due to a higher molecular weight and viscosity which disfavor the mobility of the chain [277, 278].

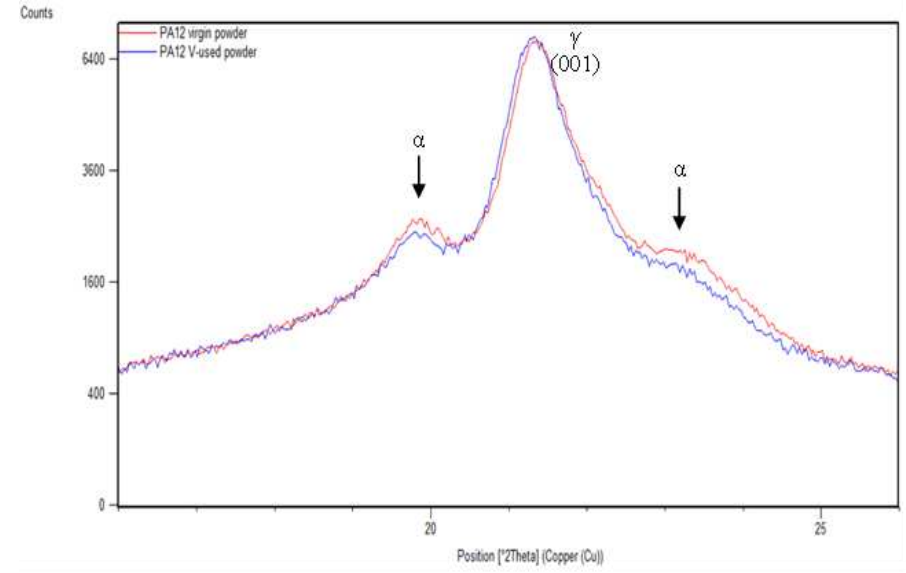


Figure 11.2 XRD patterns of virgin and 5-times used powders.

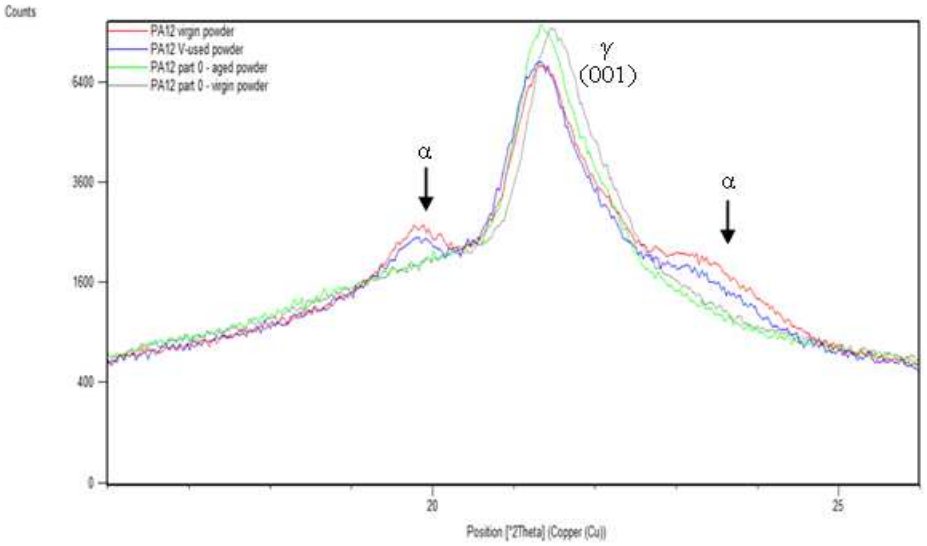


Figure 11.3 XRD patterns of virgin and 5-times used powder and of the corresponding sintered parts.

Figure 11.4 highlights the shift of the γ (001) peak between the two opposite sides of the same samples (obtained by sintering the 5-times used powder) due to the effect of layer sintering and, therefore, to different heating cycles of the subsequently deposited layers of material.

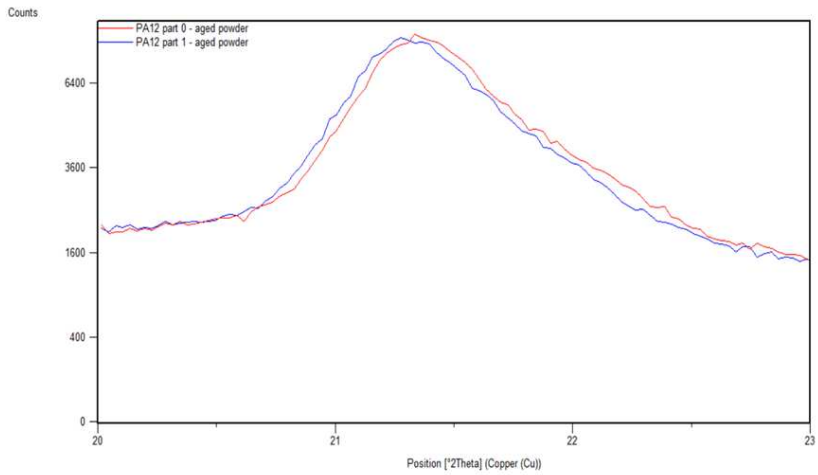


Figure 11.4 XRD patterns of the two opposite sides of sample obtained by sintering the 5-times used powder.

To obtain sintered products of desired quality, it is essential to understand the thermal behavior of the starting powder since in the SLS process the temperature is maintained in the sintering window [50]. The main reason is the adhesion between layers, ensuring good mechanical performances and pursuing the melt of the powder, avoiding unsintered particles in the parts. Figure 11.5 shows the heating and cooling curves of the virgin powder. The black area represents the energy absorbed during the melting, whereas the red one is the energy released from crystallization.

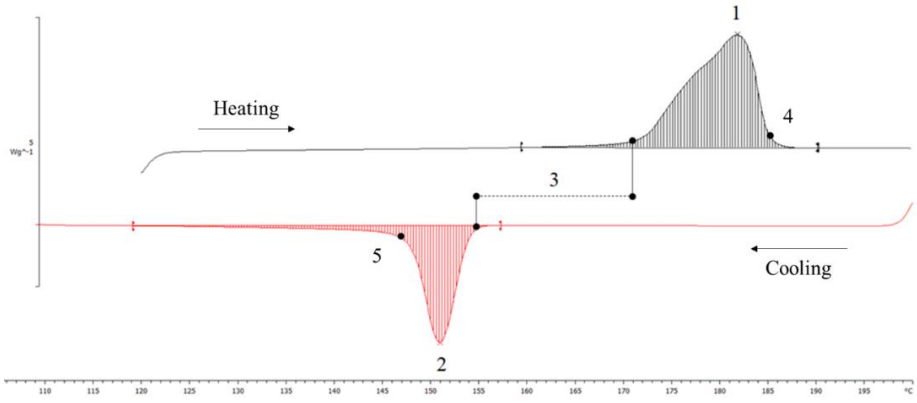


Figure 11.5 DSC curves of virgin powder. (**(1)** Melting temperature peak; **(2)** Crystallization temperature peak; **(3)** Sintering window (Tm-onset- Tc-onset); **(4)** Tm-endset; **(5)** Tc-endset.)

The temperatures related to the melting and the crystallization, along with energies and the degree of crystallinity from the DSC, are summarized in Table 11.3. From the virgin powder to the powder used five times, the melting peak Tm-peak shows an increase of 1.19 °C, while the crystallization peak Tc-peak also shows an increase of 0.796 °C. To properly examine the powder deterioration for recycling purposes, these temperature variations do not appear to be sensitive enough [47]. The increase in melting temperature, indicating preferential crystal form due to crystalline reorganization, is in line with other results in the literature [61, 59] and can be mainly attributed to the chain-scission degradation mechanism. In fact, the subsequent thermal cycles induce an increase in amplitude intramolecular vibrations, due to the heat, resulting in their rupture (chain-scission) [55, 54]. Both melting and crystallization onset and endset temperatures shift from the temperatures of virgin powder. Even if the shift is a few Celsius degrees, the sintering windows are broad because the change in the particle's size makes it difficult to melt them. Moreover, since the mobility of the chain decreases, the enthalpy associated with the melting process, ΔH_m, decreases [279]. Less energy can be needed for the molten phase if the powder has partly sintered particle agglomerates. As the powder degrades, some of its temperature history may be retained. Chain scission may also lead to the fragmentation of powder [61].

Table 11.3 DSC results.

	Number of Cycle of reuse of the powder					
	0	**1**	**2**	**3**	**4**	**5**
T_m-onset (°C)	171.42	175.05	174.68	174.63	174.78	174.39
T_m-endset (°C)	184.90	185.21	185.41	185.60	185.67	185.98
Melting shoulder (°C)	13.19	9.26	10.72	10.61	10.74	11.09
T_m-peak (°C)	179.83	180.30	180.75	180.61	180.55	181.02
T_c-onset (°C)	154.32	154.77	154.88	155.08	155.27	155.49
T_c-endset (°C)	148.27	148.80	148.83	148.89	148.95	148.84
Crystallisation shoulder (°C)	6.05	6.04	6.05	6.19	6.40	6.65
T_c-peak (°C)	152.14	152.68	152.71	152.86	152.89	152.93
ΔH_m (J/g)	101.71	98.77	98.06	97.37	96.02	94.03
ΔH_c (J/g)	58.34	57.54	57.54	57.38	58.00	56.93
Degree of crystallinity (%)	49.05	47.19	46.63	46.39	45.88	44.92

The crystallization enthalpy reduces the energy necessary for crystal development, or ΔH_c, similarly to how it reduces the melting enthalpy. Degradation activities, including further polymerization and cross-linking, may be responsible for this decline [280]. At the fifth reuse, the degree of crystallinity of succeeding powders indicates a gradual decrease of 8.42 %. The C-O links between the carboxyl and amine groups are broken during post-condensation to create new amide linkages. This decline results from solid-state condensation inside the powder throughout the building cycle. The effects of chain development and the rise in amorphous content during powder aging may be to blame for this result [267]. Due to the higher degree of crystallization in the virgin powder, the higher melting enthalpy suggests that more energy will be needed for the sintering process [281]. Figure 11.6 shows the SEM micrographs of the virgin powder (a, b) and the aged powder (b, d). The shape of the particles appears to be unchanged and almost spherical/oval (a, c). At the same time, the surface morphology of aged PA12 (Figure 7.6.d) powders seems to be more compact and shows increased cracking and porosity [282, 49] compared to that of virgin powder (Figure 11.6.c) due both to the evaporation of moisture or alcohol inside the powders when exposed to a

long period of pre-heating and sintering processes and to repeated phases of expansions/shrinkages in multiple heating and cooling cycles. Higher porosity in aged powders might also induce some porosity in the produced parts.

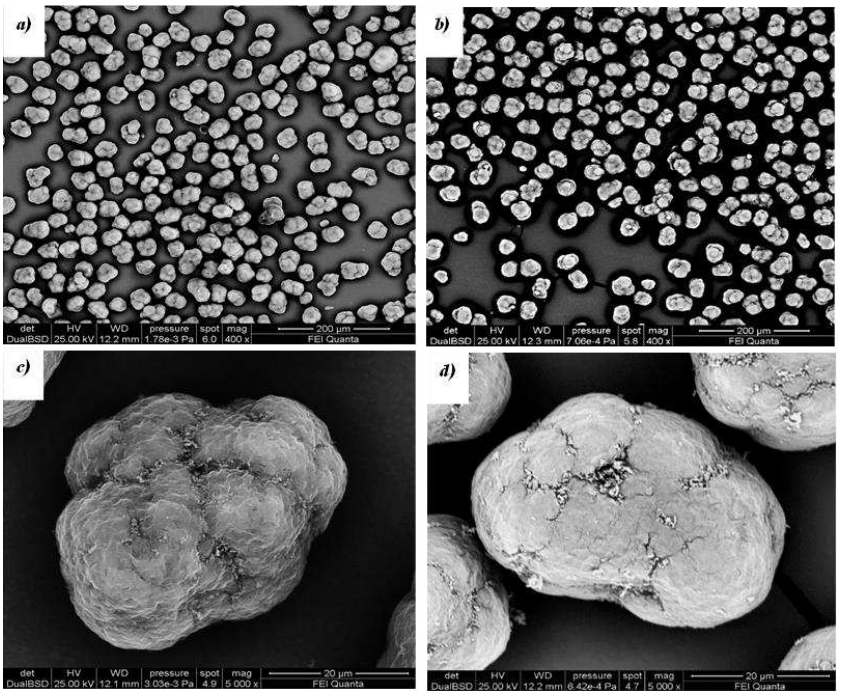


Figure 11.6 SEM Micrographs of virgin **(a, c)** and 5-time used **(b, d)** powders.

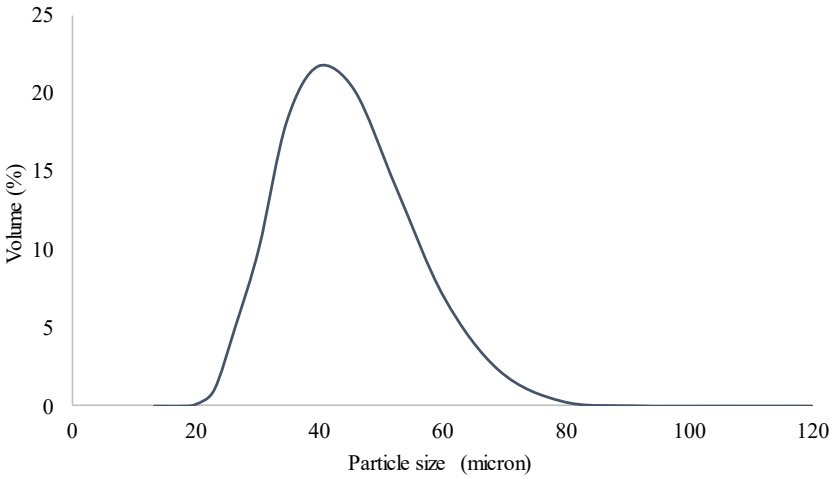


Figure 11.7 Particle Size Distribution of virgin powder.

Figure 11.7 shows the volume distribution of the particle sizes of the virgin powder. The aged powders have the same distribution as the virgin powder, confirming what was observed in the SEM micrographs (Figure 11.6.a, b).

Table 11.4 shows the density and porosity values of PA12 powders. The porosity increases with the aging of the powder and in particular undergoes an increase equal to 2.46 % with for the aged powder 5-times compared to the virgin one.

The spreading of powder plays a critical role in the SLS process. The quality of the powder particle size distribution on the bed directly impacts the overall quality of the produced parts. To ensure the deposition of uniform and compact layers of powder, the powder needs to possess good flowability. Reducing the porosity content in the powder leads to improved mechanical properties. Generally, the layer thickness in the SLS process ranges between 100-150 μm. Therefore, smooth particles with high sphericity are preferable to achieve the desired microstructure in the final sintered parts [283]. Meanwhile, the solid density is almost stable between printing cycles. The bulk density presents the same trend of porosity, with a decrease of 2.78 %. These results are connected with the surface of the particles. With the increment of the reprocessing cycle, the adhesion force between particles increases, and the flowability decreases. Moreover, an uneven distribution of the powder on the bed leads to pores on the printed parts [284, 285].

Table 11.4 Density and porosity of PA12 powders.

PA12 cycles	Bulk density (g/cm^3)	Solid density (g/cm^3)	Porosity (%)
0	0.50	1.06	52.85
2	0.49	1.06	53.51
5	0.48	1.06	54.15

Figures 11.8 and 11.9 show SEM micrographs of the top and bottom surfaces of sintered parts obtained from virgin and 5-used PA12 powders.

The top (Figure 11.8.a, b, c) and bottom (Figure 11.8.d, e, f) surface morphologies of SLS parts obtained using virgin powder are almost similar; in fact, for both surfaces, the PA12 particles and sintering necks are evident as well as the presence of some voids (Figure 11.8.b, c, e, f).

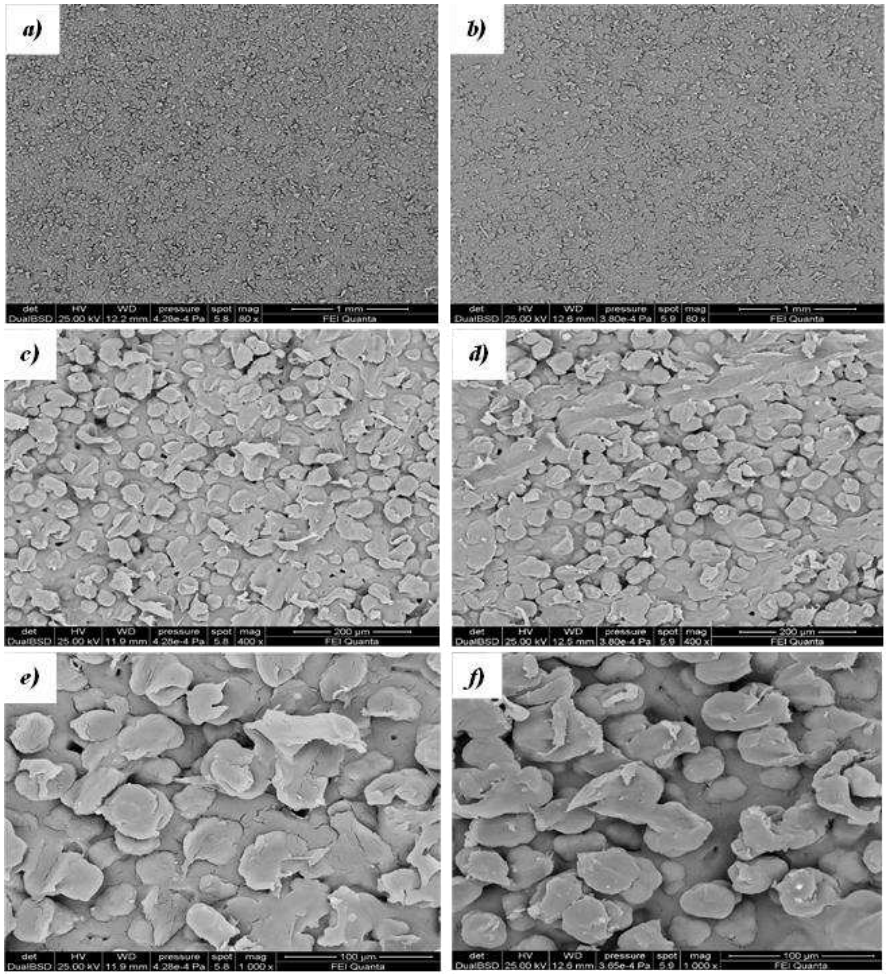


Figure 11.8 SEM Micrographs of top **(a, b, c)** and bottom **(d, e, f)** surfaces of the SLS part obtained using virgin powder.

SEM micrographs of the two opposite sides of the specimen obtained by sintering the powder used 5 times (Figure 11.9) show different surfaces. The first sintered side (Figure 11.9.a, c, e) is characterized by the presence of sintered areas and partially sintered particles with the presence of a sintering neck. A few well-sintered areas are on the last sintered side (Figure 11.9.b, d, f), and the presence is partially sintered. Moreover, many non-sintered powder particles can be seen attached to the surface due to partial fusion, which is responsible for high surface roughness.

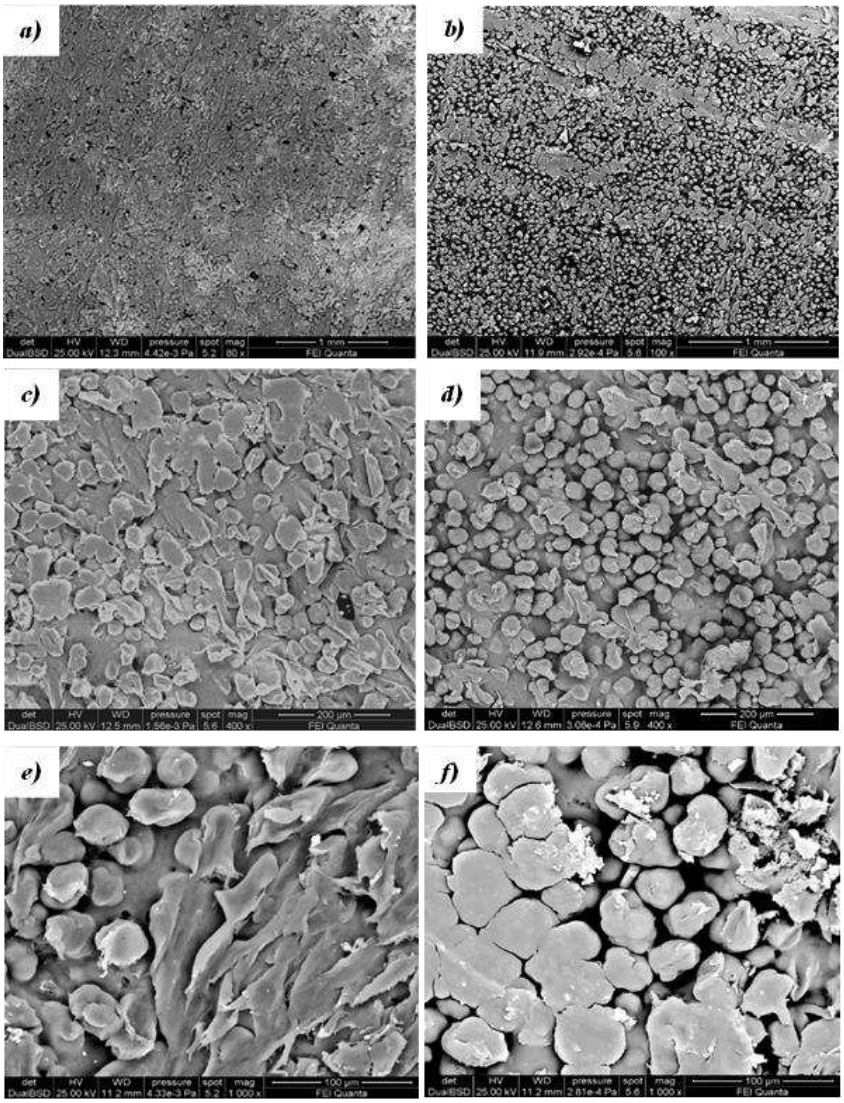


Figure 11.9 SEM micrographs of the opposite sides **(a, c, e)** and **(b, d, f)** of the specimen obtained using SLS of 5-times used powder.

Figure 11.10 compares the internal cross-sectional SEM micrographs of the sintered parts obtained using virgin (a, c, e, g) or 5 times used (b, d, f, h) powder. The section obtained from the sintered part using virgin powder appears, at low magnifications (Figure 11.10.a), homogeneous and any non-sintered particles are detected, unlike the section obtained from the sintered part using powder aged 5 times (Figure 11.10.b).

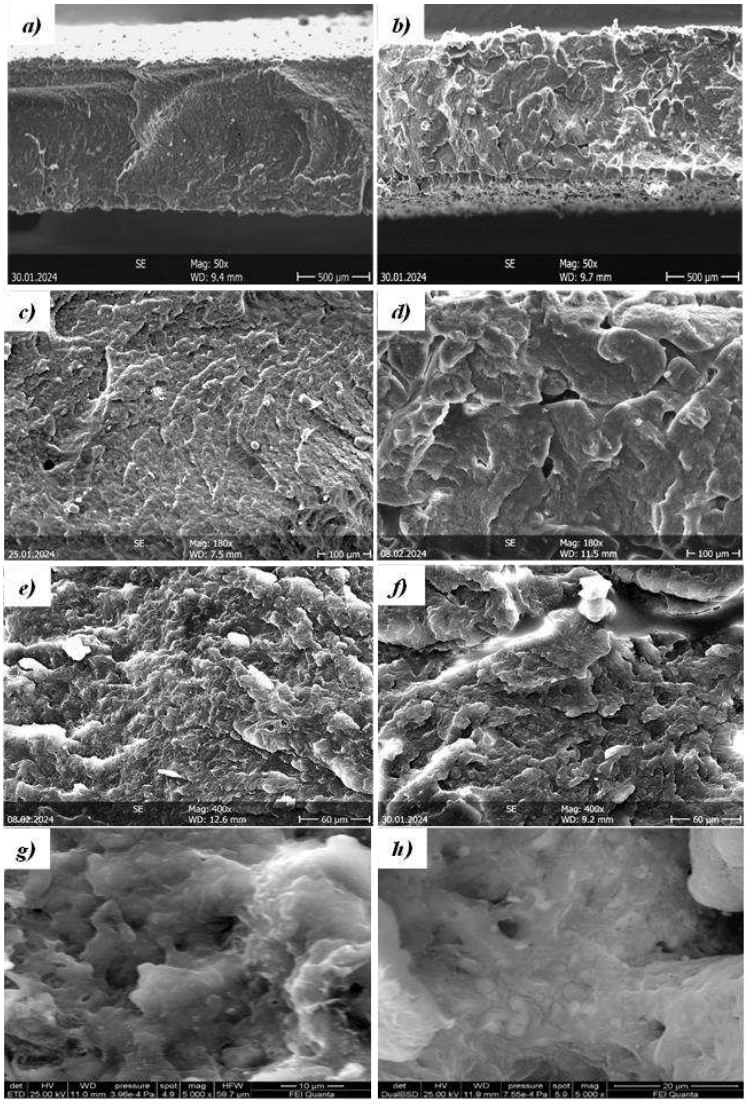


Figure 11.10 Internal cross-sectional SEM micrographs of the sintered parts obtained using virgin **(a, c, e and g)** or 5 times used **(b, d, f and h)** powder.

At higher magnifications, the various zones for the section with virgin powder (Figure 11.10.c, e, g) do not present morphological differences. The surface is spongier than the starting particles and has a smaller porosity than that of the sample's section obtained with aged powder (Figure 11.10.d, f, h).

In the section obtained with aged powder, the unmolten particle cores surrounded with spherulites are highlighted (Figure 11.10.h). The cores are the

unmolten central regions of the sintered powders coming out when these powders do not get enough energy and heat to melt fully.

The different morphologies between the parts obtained by SLS, starting from virgin powder and from powder used 5 times, lie in the fact that the unused PA12 powders, during sintering, remain at high temperatures, below the melting point, to a prolonged period, resulting in the formation of a denser crystalline morphology and an increase in the melting point of the powder as well as an increase in the chain length due to polycondensation in the solid state and this justifies their lower sinterability. Furthermore, to confirm what has been said, the sample obtained by sintering the powder used 5 times is characterized by pores of much larger dimensions compared to those present in the sample sintered using virgin powder.

The presence of void in the part can be linked to the decrease in the melting energy from the DSC results, an index of the missing portion of molten material. Furthermore, the presence of a void leads to weaker parts. The performance of the parts is also linked to the flowability of the powder during the printing process. The chemical structure of each polymer determines its flowability. Polymer chains with simple geometry and short lengths' slide' past one another with negligible flow resistance. In contrast, lengthy chains with complicated structures and high molecular weights have higher flow resistance [286].

In fact, works state that a high MFR is due to a lower molecular weight average and molecular number average. In other words, new PA12 powder with shorter chain molecules and higher-order areas might easily create parallel array chains [47].

11.3.2 Roughness analysis

It is fundamental to reach a good sintering of the powder to obtain a good quality. However, with degradation, the melting enthalpy decreases, leading to a decrease in the melting coalescence of the particle, which brings high porosity parts [65, 287].

The average roughness for the top and bottom surfaces of the tensile specimens, along with the standard deviation, are represented in Figure 11.11.

It is possible to notice how the upper part of the specimens presents a stable value of roughness which ranges around 7.90 μm for the part made with virgin powder and 5 times used.

On the other hand, the bottom part of the specimens has a higher variation with ageing. In fact, virgin-made specimens have an average Ra of 6.80 µm and 5 times one has 12.64 µm.

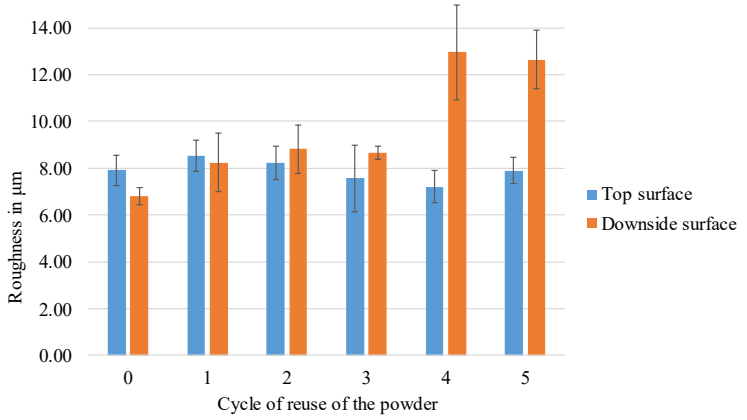


Figure 11.11 Roughness results.

11.3.3 Dimensional analysis

For every measurement, the average and the standard deviation between specimens were considered. In Figure 11.12, the list of the measurements is presented along with the representation of its position on the specimen.

a)

N.	Measurement item
1	Square length
2	Square width
3	Circle diameter
4	Width
5	Neck
6	Distance square left bottom
7	Distance square left
8	Distance circle bottom right
9	Distance circle right

b)

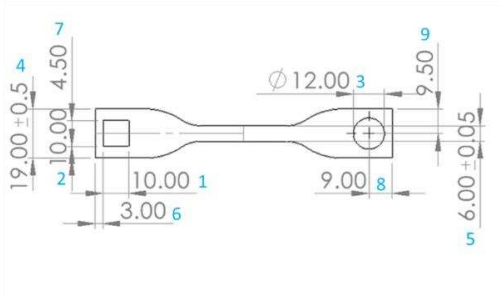


Figure 11.12 (a) Definition of the measurement sequence (blue numbers), and **(b)** their position on the specimen.

According to different works, the degradation of the powder leads to quality problems, such as surface finish, e.g., orange peel [47], and lower dimensional accuracy. Defining the right process temperatures helps obtain parts with no temperature-induced defects such as shrinkage and curling since no supports block the part besides the powder itself. Studies on the effect of the degradation of the powder on the part's quality found that it decreases by about 5 % - 10 % [282].

The current dimensional analysis was carried out on two classifications: internal and external features, with respect to the surroundings of the specimen. The length and width of the square built inside the specimens were measured and correlated with respect to the nominal value. Starting from the virgin-made specimens till the 5th time reuse, the values are reported in Figure 7.13.a. The percentage variation from the nominal length at different reuses ranges between -0.15 % and 1.29 %. The variation of the width along the building cycle varies from -0.68 % and 0.42 %. Even though there is a fluctuant variation between positive and negative values, the difference is very small, which can be caused by the cleaning process of the printed parts or the rumor during the acquisition of the measurements. The other internal feature is the circle where the diameter is checked. In this case, the dimension is always smaller than the nominal value, as reported in Figure 11.13.b, inside the following range: -2.72 % and -1.01 %. Also, the percentage variation of -1.01 % is small and thus can be considered negligible.

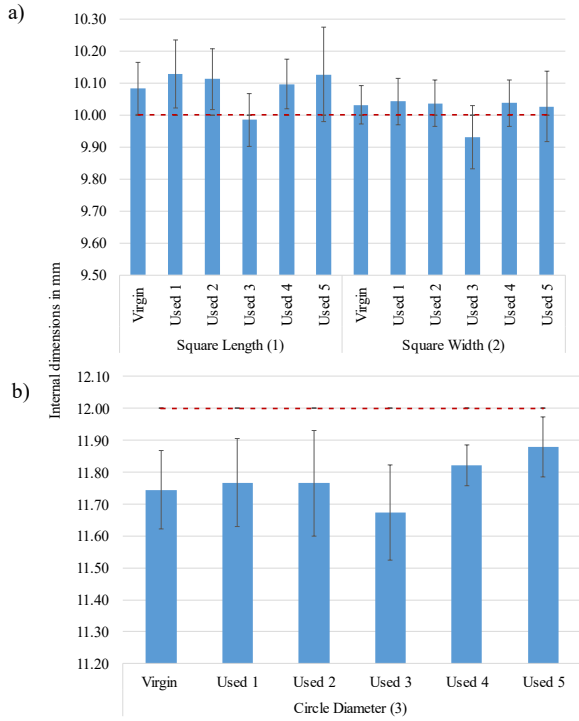


Figure 11.13 Dimensional results for **(a)** square pocket and **(b)** round hole of the tensile specimens at each reusing cycle.

The dimensions of the width and the neck of the tensile specimens are analyzed (see Figure 11.14). They were measured on the two sides of the specimens. Since there was no difference between the two sides, the average for each specimen was used.

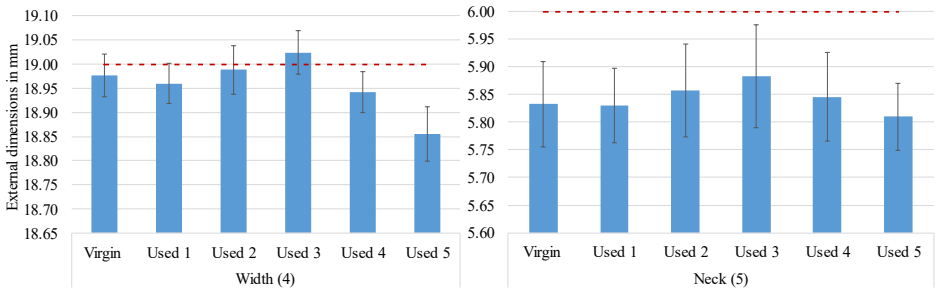


Figure 11.14 Dimensional results **for (a)** width and **(b)** neck of the tensile specimens at each reusing cycle.

The widths' variations from nominal vary inside the range -0.76% - 0.13 %. The variation of the neck dimension from nominal ranges from -3.17 % to -1.94 %.
The percentage values are small, so it is possible to declare that for the external features, no change occurs due to degradation and the shrinkage remains approximately the same.
Finally, the distances of the two external features from the specimens' border were evaluated and shown in Figure 11.15.

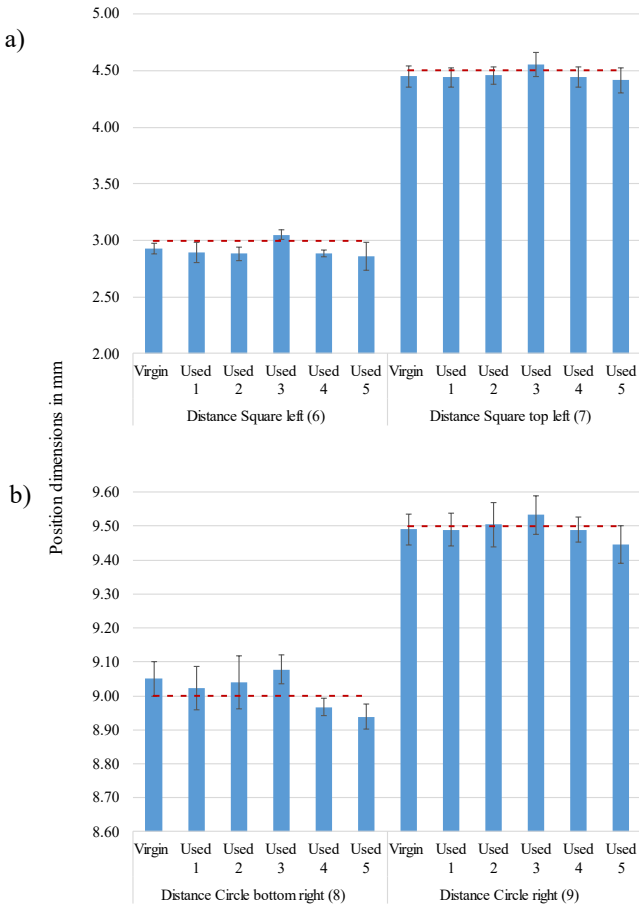


Figure 11.15 Dimensional results of the positions with respect to the specimen for **(a)** square pocket and **(b)** circle hole at each reusing cycle.

The percentage variation of the distance of the square calculated as the distance from its left surface and the left surface of the specimen ranges between -4.69 % and 1.71 %, whereas the one for the distance from the bottom surfaces of the square and the specimen varies inside the range -1.89 % - 1.22 %. The percentage distance between the center of the circle from both the bottom and the right side of each specimen ranges between -0.68 % and 0.87 % and -0.57 % - 0.34 %. Also, in this case, the variation is below the 5 % variation found in another study [282]. An ANOVA was performed to evaluate if the powder reusing caused the dimensional variations [152]. The results in Table 11.5 demonstrate how the powder reusing is not statistically significant since all the p-values are higher than 0.05.

Table 11.5 ANOVA results on UFS and maximum strain value from flexural tests (DF = Degree of Freedom; Adj SS = Adjusted sums of squares; Adj MS = Adjusted mean squares).

Length square					
Source	DF	Adj SS	Adj MS	F-value	p-value
Powder reusing	5	0.0432	0.0087	0.85	0.543
Error	12	0.1228	0.0102		
Total	17	0.1660			
Width square					
Powder reusing	5	0.0271	0.0054	0.79	0.580
Error	12	0.0830	0.0069		
Total	17	0.1102			
Diameter circle					
Powder reusing	5	0.0723	0.0146	0.90	0.512
Error	12	0.1943	0.0162		
Total	17	0.2672			
Width					
Powder reusing	5	0.0502	0.0101	0.82	0.560
Error	12	0.1472	0.01227		
Total	17	0.1974			
Neck					
Powder reusing	5	0.0097	0.0019	0.32	0.890
Error	12	0.0725	0.0060		
Total	17	0.0822			
Distance square left					
Powder reusing	5	0.0727	0.0145	2.74	0.071
Error	12	0.0637	0.0053		
Total	17	0.1363			
Distance square bottom					
Source	DF	Adj SS	Adj MS	F-value	p-value
Powder reusing	5	0.0352	0.0070	0.82	0.557
Error	12	0.1027	0.0086		
Total	17	0.1379			

(Table continues on the next page)

Distance circle right					
Powder reusing	5	0.0418	0.0086	3.07	0.052
Error	12	0.0327	0.0027		
Total	17	0.0745			
Distance circle bottom					
Powder reusing	5	0.0120	0.0024	0.88	0.526
Error	12	0.0329	0.0027		
Total	17	0.0449			

11.3.4 Mechanical characterization

Anisotropic mechanical characteristics characterize laser-sintered PA12 parts [288, 289]. This study only looks at the tensile characteristics of components printed perpendicular to the building direction. Three samples were evaluated for each circumstance. The rupture has occurred inside the gauge.

Table 11.6 Tensile properties of samples printed horizontally for different printing cycles.

Speci-men	**UTS_{μ} (MPa)**	**Std.dev$_{UTS}$**	**True $Strain_{\mu}$ (mm/mm)**	**Std.dev$_{STRAIN}$ (mm/mm)**	**E_{μ} (MPa)**	**Std.dev$_{E}$**
0	65.30	0.30	0.25	0.01	822.66	5.17
1	61.97	1.14	0.22	0.03	749.75	13.51
2	50.13	1.02	0.22	0.01	642.13	6.49
3	47.72	0.14	0.20	0.00	627.15	1.77
4	42.11	1.84	0.19	0.01	560.97	17.55
5	42.20	0.00	0.20	0.00	571.18	4.65

The average results of the tensile tests are shown in Table 11.6, together with their standard deviations. Reusing the powder results in a loss of strength and elongation capabilities, as would be predicted. The behavior was similarly described in earlier publications [267, 49].

The tensile strength of the component is reduced by 35.37 % after the fifth reuse when the powder is reused without being refreshed. In addition, the strain is 17.99 % lower than it was for the specimen made using virgin powder.

The weaker layer-to-layer solidification and decreased coalescence of the recycled PA12 particles account for the inferior mechanical properties [253, 46] (see

Figure 11.10). The usual crystal structure of PA12 is made up of two phases: α and γ. The more crystalline metastable α-phase is seen in the unprocessed powder. The chain changes into the stable γ-phase during the sintering process. The reduction in crystallinity in components made with old powder is brought about by increased short-molecule production [53].

Additionally, amorphous areas surround lamellae owing to the material's low crystallinity. As a result, the matrix's spherulites are distributed throughout and become coarser. It should be noted that the older material may have had rougher-looking spherulites due to the aggregation during the growth, which may have increased lamellar thickness. These microstructural alterations will be reflected in the final mechanical properties [284, 290].

From the results of the ANOVA in Table 11.7 on the UTS and strain, the high F-value and the p-values lower than 0.05 verify the high correlation of the reuse of the powder.

Table 11.7 ANOVA results on UFS and maximum strain value from flexural tests (DF = Degree of Freedom; Adj SS = Adjusted sums of squares; Adj MS = Adjusted mean squares).

UTS					
Source	DF	Adj SS	Adj MS	F-value	p-value
Powder reusing	5	981.929	196.386	202.22	0.000
Error	12	5.827	0.971		
Total	17	987.756			
True strain					
Powder reusing	5	0.0039	0.0008	5.08	0.036
Error	12	0.0009	0.0002		
Total	17	0.0048			

11.4 Conclusion and Outlook

This work aims to investigate the structural changes in the powder completely and the consequences in the printed specimens. An experimental setup was developed to pursue subsequent printing processes, using the unsintered powder from the previous cycle as an input. In total, six prints were carried out.

Initially, the PA12 powder exhibits a well-defined crystalline structure. However, distinctive trends emerge in the X-ray diffraction patterns with each successive printing cycle. The characteristic peak shows a slightly intensified increase and a shift towards lower angles, indicating a crystalline transition from the α to the γ phase. This phenomenon is accompanied by a reduction in the intensity of the α-phase peaks, favoring the formation of the more stable γ phase.

Concurrently, the morphological analysis of the particles indicates a structural transformation. Initially, the particles appear nearly spherical or oval, but with aging, they become more compact with increasing cracking and porosity.

Thermal trends show an increase in melting and crystallization temperatures. The melting temperature rises by 1.19 °C, while the crystallization temperature increases by 0.80 °C. These changes indicate a transformation in the thermal behaviors of the powder during printing cycles. Moreover, from the virgin to the fifth cycle of reuse, the degree of crystallinity drops by 8.42 %.

Successive thermal cycles impact the density and porosity of the powder. Density records a decrease of 2.78 %, while porosity exhibits an increase of 2.46 %. This may have implications for layer distribution during the printing process.

SEM analysis on virgin and 5-times printed specimens reveals distinct surface morphologies. Aging was found to cause denser crystalline structures, increased melting points, and longer chain lengths, ultimately reducing sinterability. This leads to challenges such as void formation, larger pores, and weaker parts.

The observed effects on the structural and thermal properties of the aged powder involve some worsening in the mechanical performances of the parts manufactured with this kind of powder. In fact, mechanical analysis revealed a significant reduction in the UTS by 35.37 % after the fifth reuse. Additionally, strain is notably 17.99 % lower than the virgin-made specimen, suggesting the potential occurrence of chain scission. Shorter chains exhibit increased mobility, complicating crystallization and leading to the presence of more amorphous regions, contributing to the observed mechanical deterioration.

Instead, no significant effect may be observed of the geometrical quality of the parts. In fact, the calculated dimensions of external and internal features, and their positions appear to assume the same values for the parts manufactured with both virgin and aged powder; the maximum deviation from nominal is under 5 %.

As the melting enthalpy decreases, causing reduced particle melting coalescence and producing high porosity components, surface quality changes. Interestingly,

the top surface displays a modest variation between the part made with virgin powder and the part subjected to five use cycles. Conversely, the bottom part exhibits a more substantial variation, reaching a Ra of 12.64 μm at the fifth reuse compared to the starting value of 6.80 μm in the virgin-made specimens.

This knowledge is critical for implementing an efficient powder recycling process of PA12. Future work is needed in order to improve the efficiency of the reuse of the powder, reducing waste while maintaining intact properties.

The powder should be subjected to in-depth studies to assess correlations and eliminate thermal history at every stage to ensure the best performance, regardless of the initial state of the powder.

Above all, the restoration of mechanical properties needs to be investigated. The adaptation of process parameters to different powder stages could be the subject of future work to see if sintering undergoes improvements in terms of surface and internally, in part, of better cohesion of the particles with a subsequent increase in the degree of crystallinity. Another solution is to investigate material modifications that can improve the stability and resilience of the polymer. This could include adding stabilizers or making alterations to the polymer chemistry.

Chapter 12 A Novel Approach on Artificial Aging of Nylon 12 Powder for Laser Powder Bed Fusion

Valentina Vendittoli[1], Wilma Polini[1], Michael S. J. Walter[2] and Jakob P. C. Stacheder[2]

[1] Department of Civil and Mechanical Engineering, University of Cassino and Southern Lazio, via G. di Biasio 43, 03043 Cassino, Italy

[2] Faculty of Engineering, University of Applied Sciences Ansbach, Residenzstr. 8, 91522 Ansbach, Germany

Published in: Rapid Prototyping Journal (2024), 30, pp. 1836–1845
https://doi.org/10.1108/RPJ-12-2023-0430

Abstract

Purpose - This study aims to address challenges in the Laser Powder Bed Fusion process of polymers, focusing on the considerable amount of unsintered powder left post-printing. The objective is to understand the altered properties of this powder and find solutions to improve the process, reduce waste, and explore re-using reprocessed powder.

Design/methodology/approach - A novel methodology is employed to generate reprocessed powder without traditional printing, reducing time, cost, and waste. The approach mimics the aging effects during the printing process, providing insights into particle size distribution and thermal behavior.

Findings - Results reveal insights into artificial aging, showing an 8.2 % decrease in particle size (60.256 - 69.183 μm) and a 9.1 % increase in particle size (17.378 - 19.953 μm) compared to unsintered powder. Thermal behavior closely mirrors used powders, with variations in enthalpy of fusion (-0.55 % to 2.69 %) and degree of crystallinity (0.19 % to 2.64 %). The proposed methodology produces results that differ from those due to printing under 3 % from a thermal point of view. The new process reduces the time needed for aged powder, contributing to cost savings and waste reduction.

Originality/value - The study introduces a novel method for reprocessed powder generation, deviating from traditional printing. The originality lies in artificially aging powders, providing comparable results to actual printing. This approach offers efficiency, time savings, and waste reduction in the Laser Powder Bed Fusion process, presenting a valuable avenue for further research.

Keywords: Additive manufacturing; Selective Laser Sintering; PA12; degradation; powder reuse; artificial ageing.

12.1 Introduction

AM is currently the most disruptive digital technology in the context of Industry 4.0, with the potential to challenge traditional manufacturing paradigms [65].
The manufacturing process is revolutionized: instead of removing material from a solid in the working process, as seen at the top, a 3D (virtual) model is created, and printing is undertaken using a precise layer-by-layer approach [261].
Additive manufacturing has various applications today, including in the aerospace, medical, and automotive fields [2]. They are connected with the complex shapes that can be produced whose geometry [106, 158, 107] and mechanical performances should be deeply demonstrated [148].
It is possible to classify AM technologies based on the energy source supplied during the process. PBF is an AM process that selectively melts regions of a powder bed using a heat source. According to the definition in the ASTM/ISO 52900 standard, SLS belongs to the PBF category [1].
SLS is an AM process that employs a laser's energy whose wavelengths are absorbed by the material, thus heating and sintering it in a build chamber and creating the desired part layer by layer.
Several SLS 3D printers are currently available and vary widely in the type of laser source they are equipped with. When selecting an SLS laser, it is important to consider the material being sintered. The resulting properties of a part, including surface quality and density, are greatly influenced by the type of laser, power, scan speed, scan spacing, and powder characteristics used. To achieve optimal part properties, it is crucial to adjust the laser wavelength to the powder's absorption capability [291]. These properties impact the laser's conversion of optical energy to heat energy, the depth of beam penetration, and, ultimately, the size of the melted zones. The laser interacts with the powders in reflection, absorption, and transmission. Since only a portion of the incident beam is absorbed in the outer surface, the remaining rays are repeatedly reflected and propagate freely towards the surface or interact with other powder particles. The amount of radiation absorbed and transmitted through a single particle is determined by the absorption behavior of the polymer material [292].
Most SLS machines use CO_2 lasers with a wavelength of 10.6 μm because their power is sufficient to sinter or fuse most polymeric materials. SLS printers also use diode lasers, solid-state lasers that emit light at a specific wavelength. Laser

printers in SLS mostly use wavelengths of blue (450 nm) or infrared (808 nm) [293]. Polymeric materials are commonly used for fabricating high-quality specimens with excellent mechanical performance, as they require lower process temperatures than other material categories. Most of the materials adopted for SLS are polyamide-based, especially PA12, which is a material with high market value [261]. One advantage of this technology is that support structures do not need to be added to the object during printing, as unsintered powder can act as support. However, a major disadvantage is that the powder that remains after the printing cycle has undergone thermal cycling at high temperatures, resulting in changed chemical and physical characteristics compared to the initial virgin powder [65]. An adverse outcome is observed, which negatively impacts the spread and flow of the powder, leading to inadequate powder distribution across each building layer. The result is an increased level of porosity in the final product [294, 295]. This hurts mechanical performances, resulting in weaker specimens [296]. Furthermore, repeated thermal cycles cause changes in the shape of particles, resulting in elongated potato-shaped forms or particle aggregation [297], which impact the thermal characteristics of the powders. Notably, as the crystallization temperature decreases, the peak melting temperature shifts towards higher values [58]. Additionally, aged powders exhibit lower levels of crystallinity than their virgin counterparts. During post-condensation, C-O bonds between the amine and carboxyl groups are broken, forming new amide linkages. This phenomenon may arise from chain growth and the increase in amorphous content during powder aging [267].

Reuse of reclaimed powder can be hazardous due to significant part weakening caused by powder degradation. Mixing aged powder with fresh powder is the most common technique for restoring its properties [62].

To ensure the successful recycling of the recovered powder, it is necessary to predict the final part quality through powder characterization. Quality control involves determining the minimum refresh rate of virgin powder to enhance the properties of parts printed from recycled powder. A specialized algorithm was utilized to analyze PA12 printed components produced using powder mixtures containing 0 %, 30 %, and 50 % virgin powder. These mixtures underwent five consecutive printing cycles without any replenishment. The algorithm's primary objective was to predict the minimum amount of virgin powder needed to prevent any degradation in properties, such as Young's modulus, tensile stress at

yield, and tensile stress at break. The study found that using solely used powder in mixtures resulted in a decline in properties. The algorithm determined that only 30% of virgin powder is needed to achieve an outstanding mechanical response [59].

The powder degradation is a significant issue since approximately 80% of it remains unsintered by the end of the printing process [298, 282]. Therefore, restoring the quality of the aged powder and improving the performance transferred to the final part is critical to keep using the reprocessed powder [290].

However, as it is one of the outputs of the printing process, it is necessary to print to obtain reprocessed powder, resulting in a waste of time and materials if it is not needed. One way to generate the aged powder and thus reduce waste could be through an artificial ageing approach. The need to generate aged powder is connected to the study of its effect on the performances of the printed parts and, especially, of the effects of the post-processing actions aiming to compensate for the negative effects of aging on the printed parts.

Drummer et al. (2015) developed a model to calculate Melt Volume-Flow Rate (MVR) values based on time and temperature during the laser melting process. The PA12 powder is stored in N_2 at 175 °C for varying durations of 0, 8, 16, 32, 64, and 128 hours. The funding shows that the viscosity increases with increasing storage time. This is probably due to post-condensation [299].

Innov'PA 1550 supplied by 3D System and White Xform SLS 100%, underwent artificial aging in a temperature-controlled oven (Mm Medcenter model Venticell 55) at 170 °C, 160 °C and 130 °C and for varying periods, from 6 to 24 hours. The materials' properties were evaluated every 3 hours. The materials show an increase in molecular weight and viscosity [300].

Pham et al. (2008) studied the effects of temperature and time on the powder properties. In a nitrogen-rich atmosphere, samples of new PA2200 powder supplied by EOS were placed in a temperature-controlled oven (Heraeus Instruments Vacuthermtype 6060M). The samples were heated at specified temperatures ranging from 100 to 180 °C. The heating periods ranged from 10 to 200 hours at each temperature. The results of the chemical characterization through DSC, MFR index, and gel permeation chromatography demonstrate that viscosity increases with degradation, and this could be attributed to the temperature and time at which the powder was exposed [47].

However, the named authors have mostly investigated the chemical properties resulting from oven aging of powders, without a comparison with powders that participated in an actual printing process.

Benz and Bonten (2019) conducted a study in which PA2200 from EOS was artificially aged in an oven filled with nitrogen at a temperature of 170 °C for 24 hours. Powder samples were taken at 1 h, 3 h, 8 h and 24 h. A PA12 that had undergone an actual laser-sintering process at an unknown frequency was used as a reference material. From the DSC results, even after 24 hours of storage in the oven, the values obtained from the powder taken from the actual SLS process were not reached [301].

The mentioned works only consider the surface temperature during printing as the temperature for treatment, without considering that the powder has undergone a warming phase at a lower temperature. Additionally, after a printing process, there will be residual powder in the material loading chamber and in the residual powder bin during the distribution of layers, which have not been warmed at the pre-heating temperature. In addition, it is crucial to control the various stages of aging that the powder undergoes to ensure it can be compared to the corresponding powder generated by an actual printing process.

This paper focuses on a novel method to simulate powder aging. Starting from the virgin state of the powder, successive oven aging is carried out by opportunely planning time and methods according to the real laser-sintering process. The proposed methodology in an oven allows to obtain any desired quantity of aged powder useful for subsequent analyses, whereas the printing machine requires a large amount of powder to start with the printing process and to generate an aged powder after a set of prints. Moreover, the time required for aging in the oven is smaller than that due to the printing machine. The obtained aged powder may be used to evaluate the thermal and structural changes in the powder due to aging and the way to overcome them.

Chemical and physical tests have been carried out on the powders, which are compared with equivalent powders taken after successive real printing processes. This will contribute to understanding the aged powder's degradation state compared to other works. The oven-ageing process can generate a minimal amount of powder that can be restored in future research. This improved powder can be used in industrial applications without the need to refresh it with virgin powder, thereby reducing material costs.

In section 12.2, the novel method and tests are described in detail; in section 12.3, the results are presented; and finally, in section 12.4, the results and future work are presented.

12.2 Experimental methodology

12.2.1 Material

For this purpose, virgin powder from the supplier Sinterit was used [268]. All powder used for this study was taken from the same manufacturing batch, as ensured by the individual lot number. Hence, any variation during manufacturing of batches is eliminated, and thus, the obtained results were compared with those due to the selective laser sintering process.

12.2.2 Selective Laser Sintering conditions

A SLS 3D printer consists of two chambers: the feed for the initial loading of the powder and the print where the layer-by-layer powder is moved to make the section of the object. There is also a bin to store the excess powder carried by the recoater (see Figure 12.1. a, b).

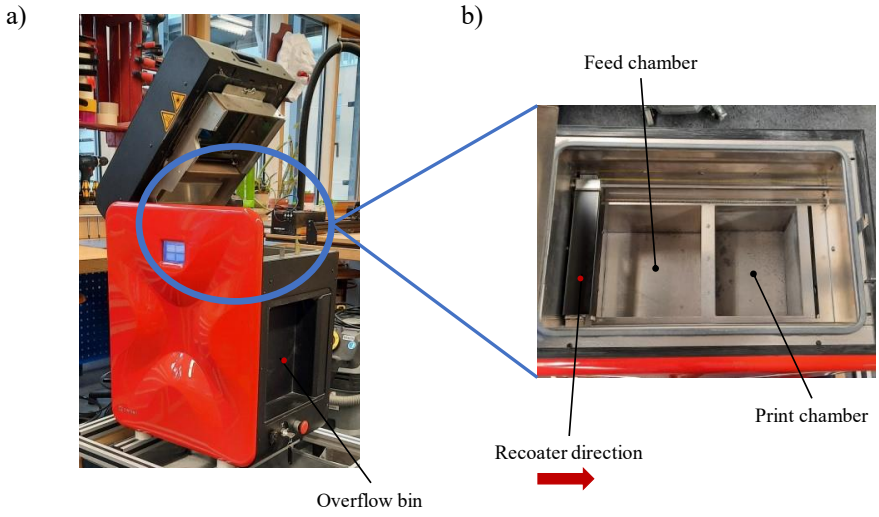


Figure 12.1 SLS printer's main components: **(a)** photograph showing the position of the overflow bin; **(b)** photograph showing the positions of the feed chamber, print chamber, and recoater direction. Figure by authors.

Throughout the printing process, different temperatures are relevant. The feed is intended to keep the powder at a constant temperature (chamber temperature T_C). At the same time, in the print bed, with each addition of a layer, bulbs irradiate the surface to bring the powder to a temperature about 5 °C lower than the melting temperature (pre-heating temperature T_{pH}). Finally, energy from a laser sinters the surface portions to make the section of the part, dispersing more heat. Figure 12.2 summarizes the sequence of stages in a printing process. Before removing the parts from the printer, waiting for the cooling down is required until a temperature of 20 °C is reached (T_f).

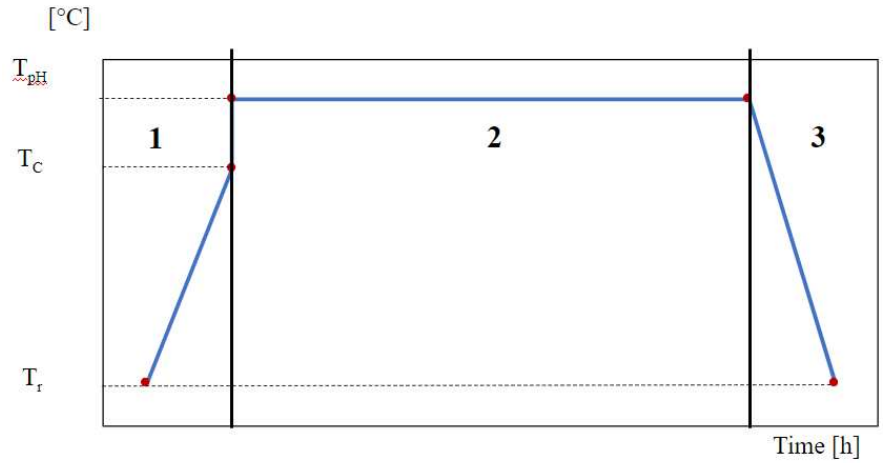


Figure 12.2 Schematic temperature-time-curve of the SLS phases: **(1)** warming phase; **(2)** printing phase; **(3)** cooling phase. Figure by authors.

12.2.3 Proposed novel method

The proposed novel method to simulate the actual aging of the powder during the printing process is based on the use of an oven to artificially age powder for further tests of post-processing activities.

To replicate the three compartments of the 3D printer, which are the relevant parts for the processes of "heating" and "cooling", the powder has to be divided into two equal quantities. The first one is heated to the T_C at which the powder inside the feed and bin chambers is maintained during printing. The powder is kept at this temperature for the involved time. The second one is heated up to the T_{pH}, to which the lamps heat the power below the melting temperature and keep it at this temperature for the time involved in the printing. This duration depends on the

layers' height; therefore, for the same temperature and object to be made, different times lead to different ageing. Therefore, the two spilt quantities of powder are cooled in the oven until they reach room temperature to simulate the cooling of the powder inside the printer at the end of the job. Finally, the two sets are mixed to produce a final artificially aged powder batch. This procedure must be replicated as often as needed to achieve the desired aging degree (see Figure 12.3).

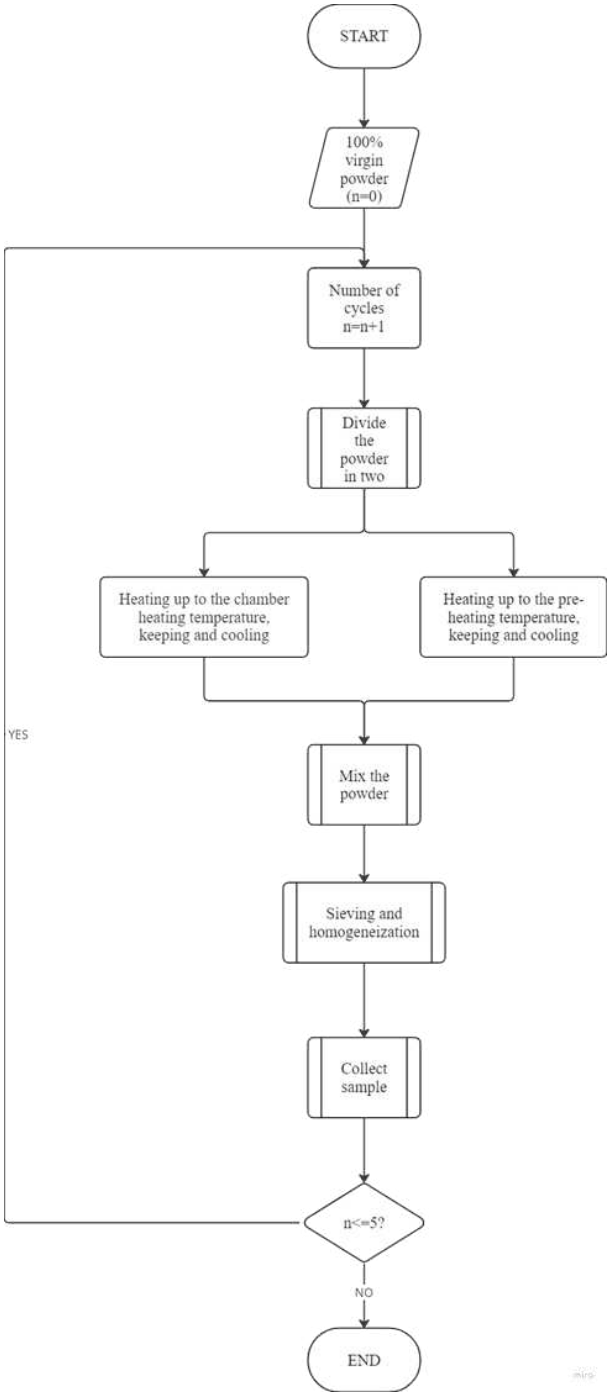


Figure 12.3 Flowchart of the proposed novel method ("n" is the number of processing cycles). Figure by authors.

12.2.4 Validation of the proposed method

The proposed artificial aging method was validated by comparing the obtained powder at the five aging stages with the non-sintered powder obtained by the SLS printing process during five consecutive prints.

It was used the printer model "Lisa" from the manufacturer Sinterit [269] to make components for tensile specimens, using a chamber temperature of T_C=140 °C and a powder surface temperature of T_{pH}=178 °C. Information about the .scode file is shown in Table 12.1. The printer is equipped with a 5W IR Laser Diode and operates in an oxygen environment.

Table 12.1 Printing process parameters. Table by authors.

Parameter	Value
Layer height	0.100 mm
Estimated total print time	6 h 36 m
Estimated powder needed in feed bed	1.68 L
Refresh powder needed after print	0.19 L
Laser power multiplier	1.00
Total model layers count	35
Models volume pro all prints in the chamber	18.14 cm^3
Estimated powder needed in feed bed (height)	4.2 cm
Total print height	2.35 cm
Estimated warmup time	65 min
Estimated active print time	3h 44m
Estimated cooldown time	1h 47m

A series of consecutive prints were made, where at the end of the printing process, the remaining powder was sieved out and reused in the next cycle so that the powder had undergone a series of continuous thermal cycles to highlight any effects on degradation. Samples of powder at each reusing state were collected. To enhance comprehension of the printing cycle, the initial powder is referred to as 'virgin', while subsequent powders are labeled with sequence numbers. The proposed novel method is general but it was applied to a sample of 500 g of virgin powder to demonstrate its efficiency in reproducing the thermal cycle of a regular SLS printer. This quantity is required to test the aged powder and thus, to compare the results with those achieved by regular printing starting with virgin

powder. The oven Memmert UNB 300 was used for this purpose [302]. It has a natural ventilation and a temperature resolution of ±0.5 °C. The incoming air is heated in a preheat chamber and enters the main chamber through ventilation slots in the side wall. The fan on the chamber's back wall produces a strong horizontal forced circulation of air, which is more intense than natural convection. The air intake and discharge rate are controlled by the air valve on the back of the oven. Exactly 250 grams of the 500 grams were used to simulate the feed and overflow bin heating, undergoing an initial preheating phase at T_C = 140 °C for 41 minutes and constant temperature maintenance for 67 minutes. The remaining 250 grams simulating the powder contained in the print chamber underwent a heating phase T_{pH} at 178 °C for 54 minutes and a holding for 67 minutes (see Figure 12.4 a, b), according to the following proportion:

$$V_{est}: V_{att} = t: x \qquad (12.1)$$

where V_{est} is the volume of powder required by the printer to make a real print, V_{att} is the amount in volume of powder to be artificially aged, and t represents the time in minutes for the two steps. 65 minutes represents the time required for a real preheating print, and 224 minutes is the active printing time.

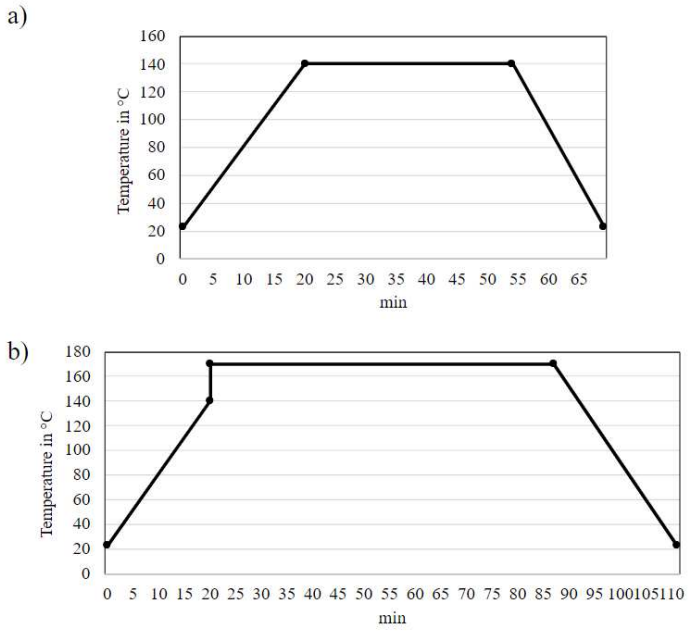


Figure 12.4 Temperature trend to which the powder inside **(a)** feed and bin chambers; **(b)** print chamber was submitted. Figure by authors.

12.2.5 Material characterization tests

The five sets of powder due to printer or artificial aging were submitted to different tests to compare them. The size distribution of the powder was measured using a Malvern Mastersizer 2000 [272]. This device employs laser diffraction and conforms to ISO 13320:2020 standards [273]. Five measurements were conducted, and their average value was computed since no considerable variation was detected. The volume distribution and percentile values d10, d50, and d90 are presented, which indicate the particle diameter below a certain quantity.

Images of the artificially aged powder were captured with the Digital Microscope VHX-7000 from Keyence [303]. The dual objective lens is the High-resolution zoom lens VH-ZST 20 to 2000x [304].

A Mettler Toledo DSC 3+ was employed to conduct thermal analysis on the powders. Three samples were tested per powder, and the average result was computed. Each sample weighs 10±0.5 μg and is secured in aluminum pans [271]. A heating ramp was run from 120 °C to 200 °C at a rate of 10 K/min; then the temperature was held constant for 5 min, then a cooling ramp was run at the same rate as the heating from 200 °C to 23 °C, then the temperature was held constant for 5 min. The experiments were conducted with a nitrogen flow rate of 30 mL/min.

To assess the impact of the printing process on degradation, the degree of crystallinity was computed as outlined below:

$$X_c(\%) = \frac{\Delta H_f}{\Delta H_f^\circ} \cdot 100\ \% \qquad (12.2)$$

where ΔH_f is the heat of fusion from the DSC results, and ΔH°_f is the heat of fusion of 100 % crystalline PA12. According to the literature, the value is 209.3 J/g [52].

12.3 Results and discussion

The size distribution percentiles for the powders used 2 times and 5 times, compared to artificially aged and virgin powder as a reference, are presented in Table 12.2. Two opposing phenomena can affect particle behavior, the first involving particle agglomeration at high temperatures during the printing process. The elevated temperatures cause the formation of fractures on the surface of the particles. This, in effect, causes the particles to break up into smaller particles when they are sieved. Both scenarios negatively impact the powder's spreadability and

flowability, which leads to the production of inferior-quality printed parts. The difficulty lies in distributing the individual layers evenly on the printing plate [305].

Table 12.2 Particle size distribution percentiles of the powder at different stages of reuse (virgin = 0, 2 times and 5 times reused, 2 times and 5 times artificially aged). Table by authors.

d(v) in μm	Type of PA12				
	VIRGIN	USED		AGED	
	0	2 times	5 times	2 times	5 times
d10	27.939	27.890	28.047	27.949	27.943
d50	38.264	38.213	38.427	38.313	38.311
d90	52.153	52.107	52.401	52.290	52.293

The analysis shows that the difference between the two types of powder is between 0.21 % and 0.35% for the 2-times powder and between -0.37 % and -0.21 % for the 5-times powder. These differences are exceedingly small and suggest an excellent simulation of the process.

Additionally, Figure 12.5 shows that the different powders have a particle diameter that ranges from 17.38 to 91.20 μm. The volume is analyzed in distinct size ranges.

The percentage difference in particle size between 2 times printed (used) and artificially aged powder ranges from -2.8 % in the 19.95 - 22.91 μm size range to 6.7 % in the 69.18 - 79.43 μm size range. On the other hand, the 5 times powder has a minimum variation of -8.2 % and a maximum variation of 9.1 % in the size ranges 60.26 - 69.18 and 17.38 - 19.95 μm, respectively between the artificially aged powder and the one that underwent five consecutive printing cycles.

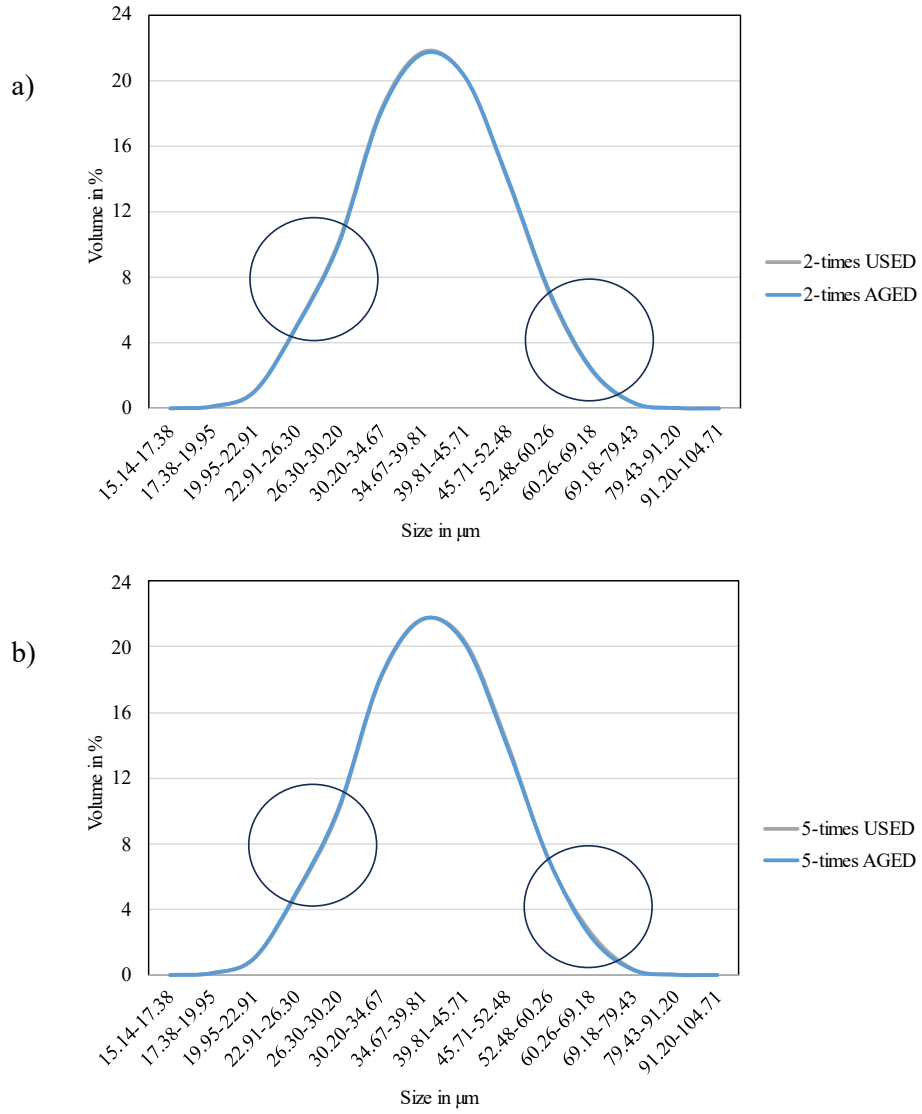


Figure 12.5 Volume particle size distribution **(a)** difference between 2-times powder from a real printing cycle and artificially aged; **(b)** difference between 5-times powder from a real printing cycle and artificially aged (the circles correspond to the part where the curves differ as visible in Table 8.3). Figure by authors.

For better visualization of the results, Table 12.3 was added with the additional particle size distribution of the given virgin powder.

Table 12.3 Volume particle size distribution of the powder at different reuse stages (virgin = 0, 2 times and 5 times reused, 2 times and 5 times artificially aged). Table by authors.

Size range in µm	Type of PA12				
	VIRGIN	USED		AGED	
	0	2 times	5 times	2 times	5 times
15.14-17.38	0	0	0	0	0
17.38-19.95	0.12	0.12	0.11	0.12	0.12
19.95-22.91	1.03	1.06	0.99	1.03	1.04
22.91-26.30	5.03	5.09	4.91	5.02	5.03
26.30-30.20	10.15	10.23	9.96	10.11	10.12
30.20-34.67	18.21	18.26	18.00	18.12	18.12
34.67-39.81	21.77	21.76	21.63	21.69	21.68
39.81-45.71	20.21	20.15	20.32	20.18	20.18
45.71-52.48	13.95	13.87	14.19	14.00	14.00
52.48-60.26	6.94	6.89	6.99	7.03	7.03
60.26-69.18	2.27	2.25	2.55	2.34	2.34
69.18-79.43	0.30	0.30	0.34	0.32	0.32
79.43-91.20	0.02	0.02	0.02	0.02	0.02
91.20-104.71	0	0	0	0	0

Figure 12.6 displays the microscopic analysis of the virgin powder (a) and the aged powder (b-f). The majority of the particles maintain their spherical/oval shape. With successive ageing states, some particles coalesce.

At the same time, the surface morphology of aged PA12 powder at successive ageing stages appears more compact and easily tends to stick together. It exhibits increased cracking and porosity compared to that of virgin powder. This is due to the evaporation of moisture or alcohol inside the powders during prolonged pre-heating and sintering processes and repeated phases of expansion and shrinkage in multiple heating and cooling cycles [49]. As this PA12 is a colored material, additional investigation of the powder is necessary to identify the black particles in the images.

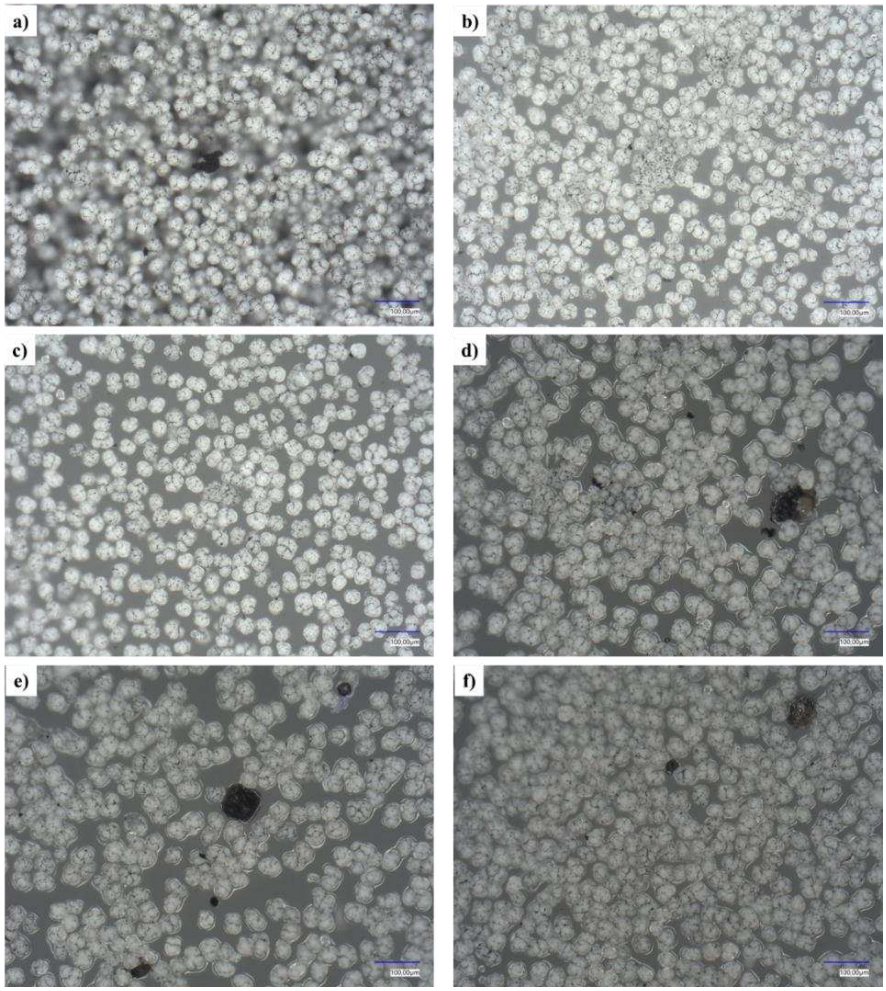


Figure 12.6 Microscopic analyses of artificially aged powder with respect to virgin powder. **(a)** virgin powder; **(b, c, d, e, f)** successive building cycles. Figure by authors.

Finally, it is crucial to understand the material's thermal behavior and compare it with the artificial method used. Therefore, Figures 12.7 and 12.8 display the analyzed melting enthalpy ΔH_m and degree of crystallinity in the powders.

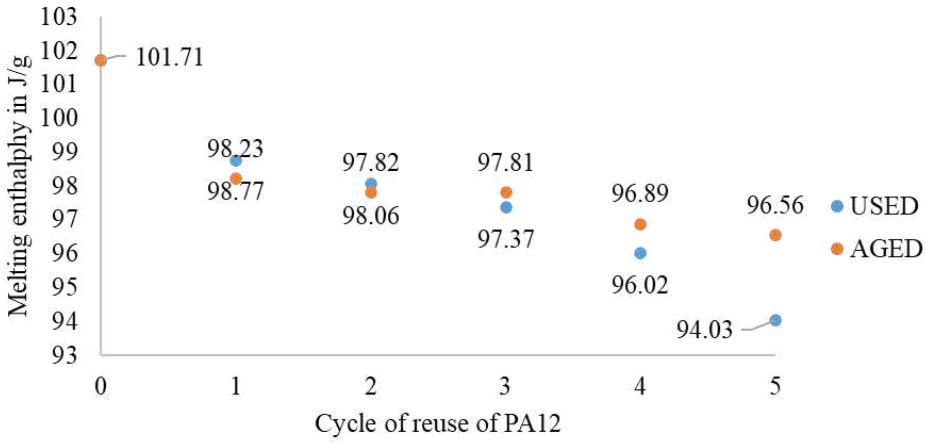


Figure 12.7 Melting enthalpy behavior. Figure by authors.

Both sets of powder exhibit a decrease in enthalpy due to degradation. The powder retains some of its thermal history. At high temperatures, the particles tend to aggregate and partially sinter, requiring less energy for complete sintering in the next print cycle. The degree of crystallinity also follows the same trend as the melting enthalpy. This effect is due to post-condensation, which causes new amide linkages to form as the amine and carboxyl groups break down. Technical term abbreviations have been explained when first used in the text. The initial powder comprises an α-type crystalline configuration, acknowledged as a metastable arrangement with a significant level of crystallinity. Through sintering and gradual cooling, the configuration transitions into γ. However, with subsequent thermal cycles, and the agglomeration of semi-sintered particles, both forms are present, leading to a gradual decrease in the degree of crystallinity in subsequent cycles of powder reuse [306, 49, 307, 308].

When examining the trends in the thermal behavior of artificially aged powders, it was found that they are comparable to those observed during the real printing process. Starting from the first reuse, the percentage changes in melting enthalpy for the artificially aged powder and the powder aged during printing are -0.55 %, -0.24 %, 0.45 %, 0.90 %, and 2.69 %, respectively. Additionally, the degree of crystallinity varies by 0.19 %, 0.49 %, 0.75 %, 0.90 %, and 2.64 %. These variations are low and therefore, they can be neglected. However, it is important to evaluate trends beyond the fifth recycling and use the aforementioned powder for component fabrication to assess how errors transfer to mechanical performance [290].

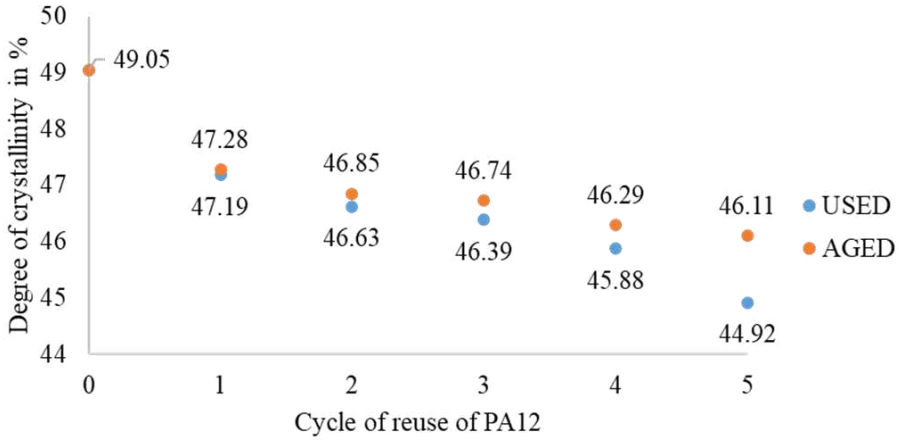


Figure 12.8 Degree of crystallinity variation between methods. Figure by authors.

12.4 Final discussion

Understanding the behavior of the material during the SLS process is crucial to minimize its impact. The ageing of PA12 material is influenced by the temperatures of the construction process. If the temperature is too high, particles will coalesce [284]. The post-condensation reaction increases molecular weight, thus decreasing the mobility and crystallization temperature of macromolecular chains. Moreover, it is suggested that the ageing behavior of the powder is highly influenced by the total printing duration [58]. Chain scission takes place during extended storage periods in the presence of oxygen, creating smaller particles with reduced flowability in general [61]. This research introduces a new approach to produce aged powder. It is crucial to investigate powder ageing without producing prints to obtain reprocessed powder. This is particularly important when examining subsequent building cycles, as printing becomes more burdensome. This method of artificial ageing is flexible and permits the amount of powder necessary for laboratory analysis to be determined, thus reducing waste from a circular economy perspective. Additionally, because the time is proportional to the amount of powder used, the actual time taken by the new method is less than the actual printing process, thus reducing the amount of powder used. These dual benefits result in lower costs. Since chosen process temperatures significantly affect the aging behavior of PA12 powder, it is helpful to perform an artificial ageing process that closely approximates the printer's actual behavior to ensure a faithful reproduction of the powder behavior. Therefore, a novel dual oven-based

artificial ageing process was developed to simulate the chamber temperatures in the printer in parallel.

12.5 Conclusion

SLS is a rapidly growing form of additive manufacturing that can create complex and high-quality products using various materials. However, because a large amount of unsintered powder with a thermal history remains at the end of the process, it is necessary to minimize losses and avoid reduced performance by re-using it. Studying the ageing of powder and its impact on the final product is crucial for effective restoration. Nevertheless, the exclusive means of obtaining aged powder is through printing processes, which can be time-consuming and require a sufficient amount of powder for analysis. One approach to reducing reliance on the printing process is by artificially aging the powder, to target the necessary amount of powder selectively and avoid wasting material in part production unless necessary. This study shows a novel method to artificially age the powder needed for further analyses. Powders produced from six consecutive print cycles were compared against artificially aged powders. The findings of the study indicate that the size distribution of 2-times and 5-times powders is similar. The percentage difference between the 2-times used and artificially aged powder ranges from -2.8 % for particles within the size range of 19.953-22.909 μm to 6.7 % for particles within the size range of 69.183-79.433 μm. In contrast, the 5-times powder has a minimum deviation of -8.2 % and a maximum deviation of 9.1 % in size ranges between 60.256 - 69.183 and 17.378 - 19.953 μm, correspondingly. The thermal behavior of synthetic powders is analogous to that of genuine aged powders, exhibiting a variation between -0.55 % and 2.69 % for melting enthalpy and between 0.19 % and 2.64 % for the degree of crystallinity. These variations in the analysis result from not considering the laser effect on the powder part neighboring the section of the parts during their manufacturing. To address this limitation, future work will involve further analysis on the artificially aged powder at different stages and testing the method beyond the five ageing. Moreover, manufacturing parts using artificially aged powder and comparing their properties with those created from reused powder to confirm if similar effects occur.

Chapter 13 Predictive Modeling of Mechanical Properties from Degraded Polyamide 12 Powder in Laser Powder Bed Fusion

Valentina Vendittoli[1], Maria Cristina Mascolo[1], Wilma Polini[1], Luca Sorrentino[1], Alexandru Sover[2] and Michael S. J. Walter[2]

[1] Department of Civil and Mechanical Engineering, University of Cassino and Southern Lazio, via G. di Biasio 43, 03043 Cassino, Italy

[2] Faculty of Engineering, University of Applied Sciences Ansbach, Residenzstr. 8, 91522 Ansbach, Germany

Published in: Journal of Materials Engineering and Performance (2024), https://doi.org/10.1007/s11665-024-10407-8

Abstract

Laser Sintering, also known as Powder Bed Fusion – laser beam, employs a laser to sinter powdered polymeric materials, such as Polyamide 12. Despite the process, a significant portion of the powder remains unsintered. However, due to elevated temperatures, material degradation occurs, altering its chemical characteristics. Industrially, a common practice involves utilizing a mixture of virgin and aged powder, with the latter having undergone multiple thermal cycles without sintering. Developing an effective powder recycling methodology is fundamental for fully realizing the potential of Polyamide 12. This work focuses the attention on reused powder to manufacture parts in Polyamide 12 through selective laser sintering and evaluates the correlation between the properties of reused powder and the strength of manufactured part through six consecutive printing processes. To achieve this, a wide experimental approach was planned and developed to arrive to establish a clear relationship between the degree of crystallinity of the powder and the Ultimate Tensile Strength of the part made from that powder. This relationship may be used to choose the kind of powder based on the strength required to the manufactured part in exercise. At the same time, if only a kind of powder is available, this relationship allows to predict the mechanical strength of the part manufactured.

Keywords: Additive manufacturing; Selective Laser Sintering; PA12; crystallinity degree; mechanical performance.

13.1 Introduction

In the last decades, AM has become an alternative manufacturing technology to the more mature ones, such as injection moulding, extrusion, and forming, thanks to the feasibility of producing complex parts using different materials [148, 283, 309].

Laser Sintering (LS), also known as SLS, is under the PBF family of 3D printing technology classified by the standard ASTM/ISO 52900 [1]. This 3D printing technique provides for the realization of polymeric parts. The material, which is in a powder state, is spread on a building plate and compressed for an even distribution of material; then a laser source hits the material, sintering the cross-section of the part; finally, the process is repeated layer-by-layer until the part is wholly realized [310]. Compared to other technologies, there is no need to make supports since the powder in the chamber supports the parts during fabrication. The powder bed support enables easy printing of complex geometries. The technology produces high-strength parts and offers a wide range of available materials. Additionally, SLS offers the advantage of sintering a range of biocompatible polymers.

Polymers were the first and most widely used appropriate materials for SLS because they are easy to process, have low laser power, and have lower temperatures than metallic materials. Last but not least, these materials make it possible to obtain very accurate parts. PA12 is the most often used semicrystalline polymer suitable for the medical, automotive, aerospace, and biomedical fields [65].

The mechanical properties of parts produced via SLS are significantly influenced by laser power, scanning speed, hatch spacing, and powder bed thickness [311]. The parameters mentioned above affect the energy input during the sintering process, and their collective impact is defined by the concept of Volumetric Energy Density (VED) which represents the total amount of laser energy applied to a given volume of material during the printing process and expresses in J/mm^3 [312]. It is, therefore, essential to achieve optimal combinations to produce mechanically robust and dimensionally precise parts. In that way, through this process index is possible to verify the influence of the parameters, defining that powder bed thickness has the most significant impact on scaffold mechanical characteristics, followed by laser scanning speed [313, 314]. Higher values of VED typically result in improved mechanical properties due to the enhancement of particle

fusion and sintering quality. An increase in VED to 0.9 J/mm³ resulted in a 79 % improvement in the tensile modulus of elasticity for PA12 parts and a 64 % improvement in tensile yield strength [315]; however, excessive values can result in adverse effects, including overheating and porosity, which can ultimately lead to a reduction in mechanical performance. In fact, when values exceed 0.9 J/mm³, there is a decline in mechanical properties due to degradation of the material caused by excessive heat [316]. The optimal VED range for achieving an equilibrium between mechanical strength and part accuracy is typically within the range of 0.5-0.9 J/mm³.

Furthermore, the dimensional accuracy of the final part is also significantly influenced by VED. On the contrary, lower VED values can result in incomplete fusion, affecting layer bonding and surface finish. However, when the laser power is set excessively high, the excess energy can cause distortion and reduce tensile strength [317].

Approximately 80% of the powder is left unsintered at the end of the printing process. Since the process occurs in a heated chamber, the unsintered powder degrades by changing its properties. Chemical degradation can alter the structures of polymer chains through chain scission, cross-linking, elongation, hydrolysis and post-condensation [318, 284, 281]. Moreover, the slow cooling phase at the end of the process prolongs the time at which is subjected to the temperatures.

Extensive studies on the changes in material properties after the printing process were done with a view to sustainability and finding a way to reuse the unsintered material to print new parts with similar characteristics to parts made using virgin powder (used in only one printing process and with known chemical and physical properties) [298, 62]. Some works focused on evaluating the degradation of the powder through the MFR test, which measures the molten polymer's flow viscosity. The higher the result, the less deteriorated the powder. According to the funding, the powder is discarded when the MFR value falls below 18 g per 10 min and is no longer used to create a new mix. Then, the results are used to calculate the appropriate ratio of virgin to used powder [57]. This was explained by a rise in molecular weight, which may have resulted from the "cross-linking" of the polymer substance. The ageing of the powder might also result in an increase in melt viscosity due to the molecular weight increase [49].

Another technique for assessing the powder's behavior is DSC, which is used to investigate the thermal properties of polymers, such as the melting temperature (T_m), crystallization temperature (T_c), and degree of crystallization.

The thermal behavior of the powder changes with ageing. By comparing virgin, used, and mixed powder of 50 % used from EOS, it was stated that the powder crystallinity rises with ageing. This can be attributed to crystal growth caused by the co-incorporation of some crystals, which raises the molecular weight of the mixture because of the post-condensation phenomena that occur at high temperatures. This indicates that shorter virgin polymer molecules fold more consistently than older material. As a result, the SLS components created from the aged powders have less crystallinity [49, 260]. On the contrary, PA12 VESTOSINT X1556 shows a decline in the degree of crystallinity with ageing [51, 282].

Divergences can be found in the literature regarding the results of the chemical characterization of powders. Since powder brands and working conditions are different, the degree of crystallinity may increase or decrease after reuse. The microstructural effect on the reprocessed powder provokes changes in the macrostructure and mechanical performances. Various experimental methods have been developed to investigate the fracture behavior of mechanical components [285]. The latter, made with aged powder, reduces part density, hence weaker parts [319, 289]. It is well known that the degree of crystallinity is linked to the strength of the printed parts. Spherulites of SLS parts made from virgin powder have increased crystallinity, which increases intermolecular interactions/locking during mechanical loading and leads to higher stiffness, work hardening, and strength. UTS decreased by 22.9 % in specimens made with 100 % aged powder compared to virgin ones [49].

Studies on successive processing cycles denote that the tensile strength declines when the recycling powder number increases. Tensile strength drops by around 25 % after the sixth build [320]. This can be explained by a decrease in the melt's flowability and an increase in average molecular weight. After eight consecutive build cycles, a significant decrease in the degree of crystallinity and a change in the size and shape distribution of the feedstock powder can be observed. The tensile performance decreased by over 50% compared to when only virgin powder was used [47].

In SLS, the typical layer thickness varies from 100 to 150 μm. Employing smooth particles with high sphericity is preferable to get the desired microstructure in the

final sintered components. The connection between the two layers is weakened because of this impact. Along with tensile strength, ageing causes a decrease in fracture elongation [284, 285]. Although it has been discovered that PA12 material may be reused five to eight times before entirely degrading [57], mixing it with fresh powder is the most frequent way of recovering the characteristics of used polymeric powder. Many studies have been undertaken to discover the reusability limit and ratio of used and fresh PA12 material [62]. An algorithm was implemented to PA12 printed parts manufactured with 0 %, 30 %, and 50 % virgin powder in the powder mixtures that underwent five consecutive printing cycles without refreshing. This algorithm predicted the minimum amount of virgin powder to prevent property loss in terms of Young's modulus, tensile stress at yield, and tensile stress at break. It was demonstrated that the properties loss occurred when only used powder was used in the mixtures, defining that only 30 % of virgin powder is enough for excellent mechanical response [59]. To maximize the reusing potential of aged powder, 30 % virgin powder is added for seven consecutive building cycles. The UTS decreased by 11% compared to extensive reuse of powder [321].

While the characteristics of pure PA12 powder are well known, in different refreshing conditions and various mixing ratios, the properties change along with the final part properties [60, 61]. If the most common mixing ratios used are well studied, such as 100 %, 50 %, and 30 %, little information is available on the capability of other mixing ratios, considering that different brands lead to changes in behavior. Furthermore, each mixture comprises powders under different physical conditions, and the manufacture reproducibility decreases. Moreover, aged powder coalescents are at higher temperatures and have a broader temperature range [318]. It is crucial to ensure homogeneity in the reused powder batch to maintain the reliability of the mechanical properties in parts manufactured with SLS. Any discrepancy in the properties of the powder, whether resulting from the use of distinct batches or contamination during the sieving, handling, or storage phases, can result in inconsistent performance and unpredictable mechanical degradation [57]. The presence of moisture or foreign particles can significantly alter the powder's crystallinity and flowability, which may lead to variations in part strength and structural integrity [318]. Rigorous protocols must be adhered to prevent cross-contamination and guarantee that the reused powder is handled in a controlled environment, thus avoiding the adverse effects that may occur [65, 298].

Extensive studies stated that there is a correlation between the chemical/physical properties of the powder and the mechanical properties of the printed parts, but they do not formalize it in a clear relationship. Moreover, it is necessary to generalize the problem in a way that it is possible to trace the mechanical performances of printed parts starting from PA12 powder and independently from the state of reuse or mixtures since some reports do not reveal the exact building time [49, 287]. In recent years, the growing demand for sustainable manufacturing practices in additive manufacturing has highlighted the need to understand how the progressive reuse of polymeric powders in LS, particularly PA12, affects the mechanical performance of parts. It is important to establish a clear predictive relationship between the properties of reused powder, such as crystallinity, and the strength of the manufactured parts, including their tensile strength. Most studies lack a comprehensive model that can be applied across a range of reuse states of PA12 powder. Furthermore, they do not provide practical tools for optimizing powder reuse without specifying the exact mixture ratios of virgin and aged powders. This study is, therefore, designed to address a gap in the existing literature by quantifying the relationship between powder properties and the strength of the part made from the same powder. In particular, the focus is on the impact of crystallinity on tensile strength. The novelty of this study lies in establishing a clear, predictive relationship between the degree of crystallinity and the UTS of parts manufactured with reused PA12 powder over multiple cycles. In contrast to previous studies, which do not formalize this correlation, our approach provides a robust predictive model that can be applied across different reuse states without specifying the exact powder mixture ratios. This model can be used to optimize powder selection based on the required mechanical performance, thereby supporting sustainable practices in additive manufacturing through the minimization of waste and the maximization of powder reusability in an optic of the circular economy.

The paper is organized as follows: Section 13.2 presents the experimental approach in terms of the material, the manufacturing process, and the ageing condition. A description of the method used for pursuing the material characterization from the DSC and tensile tests is provided. Section 13.3 illustrates the results from the DSC and the results from the mechanical tests conducted on the six sets of specimens. Section 13.4 introduces the proposed model with the validation of the actual set. Finally, Section 13.5 summarizes the funding and future research.

13.2 Materials and method

13.2.1 Characterization of Virgin PA12

The experimental setup used Polyamide 12 Smooth provided by Sinterit®, which has a particle size range of 19-90 μm and a melting point of 185 °C [268]. PA12 was chosen for this application because of its favorable mechanical properties, such as toughness, tensile strength, and impact resistance, widely used in various applications.

13.2.2 SLS process

To analyze the mechanical characteristics of 3D-printed components made of PA12, a tensile sample was created following the ASTM-D 638-22 standard (see Figure 13.1.a). Two internal elements were incorporated into the CAD model for further investigations on the dimensional accuracy that are not a matter of this paper. These adjustments were made specifically in the areas of the specimens that are clamped during mechanical testing, ensuring the integrity of the results. For this work, the printing parameters recommended by the manufacturer were employed: a chamber temperature of 140 °C and a surface printing temperature of 178 °C, utilizing a layer height of 100 μm. All the specimens were printed directly on the build plate, as depicted in Figure 13.1.b.

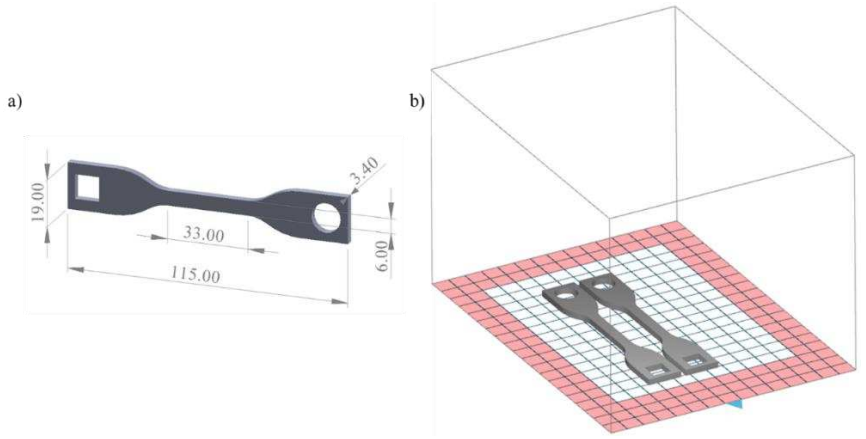


Figure 13.1 (a) Tensile specimen according to ASTM-D 638-99, all dimensions in mm **[109]**; **(b)** Printing preview (screenshot from the pre-processing software Sinterit Studio).

13.2.2.7 Ageing condition

At the end of the printing process, the powder from the feed and printing chambers and the leftover in the bin were collected in a sealed container to protect the powder against humidity. Once the prints were removed and cleaned (see Figure 13.2.a), the powder was put in the Sinterit Powder sieve, shown in Figure 13.2.b, to break the lumps and mix the powder [270]. At the end of each printing process, the powder undergoes a thermal cycle and is considered aged.

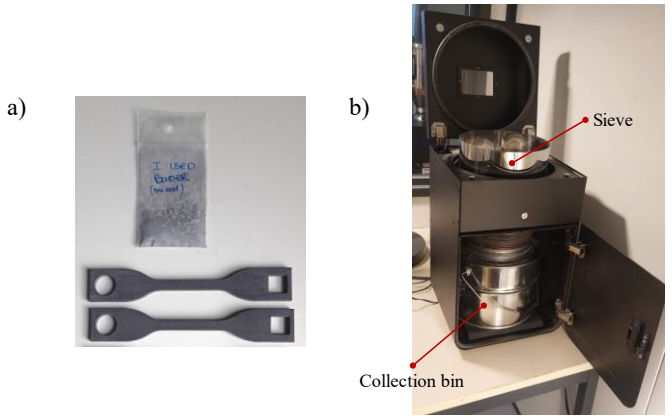


Figure 13.2 (a) Powder sample after sieving and printing specimens after each printing process; **(b)** Sinterit Powder sieve.

At the end of the process, the powder was reused for a new printing cycle without refreshing. The printing cycle was repeated in the same way, i.e., with the same values of the process parameters and involving the same printing parts in the same position inside the machine volume as the first one. This method was used until there was enough material to produce a new printing cycle. In total, six consecutive printing processes were carried out. To better understand the printing cycle, the powder used the first time was called virgin, and the powder used in subsequent cycles was named with the sequence number.

13.2.3 Thermal Analysis using Differential Scanning Calorimetry (DSC)

Samples of powder were collected and stored after each printing process to prevent contamination and moisture absorption (see Figure 13.2.b). Thermal analyses were performed on these samples to evaluate their properties in conformity with the ISO 11357-1 standard [271]. A Mettler Toledo DSC 3+ was used for thermal analysis on the powders. Each sealed sample in aluminum pans weighed 10±0.5

μg and was subjected to a heating ramp from 120 °C to 200 °C at a rate of 10 °C/min. Then, for 5 minutes, the temperature was kept constant, followed by a cooling ramp at the same rate as the heating from 200 °C to 23 °C, with another isothermal stage. The measurements were conducted under a 30 ml/min nitrogen flow rate. The temperatures were considered based on the material's reference melting and crystallization temperatures. To quantify the degradation effect of the printing process, the degree of crystallinity was calculated as follows:

$$Xc(\%) = {}^{\Delta H_m}/_{\Delta H_m^0} * 100 \qquad (13.1)$$

where ΔH_m is the melting enthalpy from the DSC results, and ΔH^o_m is that due to 100 % crystalline PA12, whose value is 209.3 J/g, according to the literature [52].

13.2.4 Mechanical test

The tensile tests were carried out with an MTS Criterion 43 test system using a load cell of 5kN and following the standard ASTM D638 [109] for the definition of the gap between the clamps of 70mm and the classification of the material described in the ASTM D883 [114] to choose the testing speed of 5 mm/min. Two specimens for each recycling condition were tested in the position shown in Figure 13.3.a. The test started until the specimen broke. The rupture occurred within the gauge, as is shown in Figure 13.3.b.

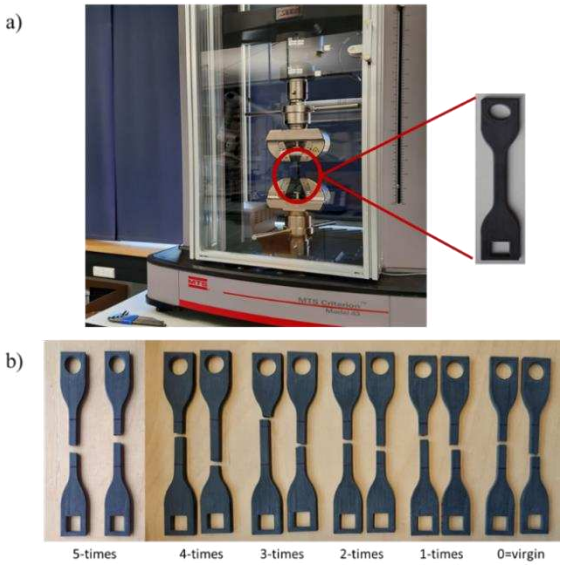


Figure 13.3 (a) Specimens positioning; **(b)** Tensile specimens after the test.

13.3 Results and discussion

13.3.1 Powder characterization

The presence of moisture in reused powders represents a significant concern in SLS, as it can negatively impact both the process and the final part properties. Moisture absorption is a significant issue when working with PA12 powders, which naturally tend to absorb moisture. Thermal degradation and moisture absorption affect the physical properties of the powder itself. Analysis of the virgin powder showed particles with a spherical shape. On the contrary, the high temperatures typically encountered during SLS processes can result in the evaporation of moisture from the powder, leading to potato-shaped particles with the progressive formation of cracks on the surface [62, 297]. Even if the average value of the particles is still 50-60 μm, particles tend to aggregate with successive building cycles [49, 322].

Furthermore, moisture affects the powder's flowability, resulting in inconsistencies in powder bed deposition. This can result in inconsistencies in the part density with the formation of voids and a reduction in the strength of interlayer bonding in the printed parts [49]. To mitigate these issues, it is recommended that powders be adequately dried before reuse, and that the moisture content be monitored carefully to ensure consistent print quality [323].

To achieve the necessary quality, it is crucial to comprehend the powder's thermal behavior; in fact, the SLS process maintains the temperature inside the sintering windows [324]. The primary factor is the adhesion between layers, which guarantees strong mechanical properties and guarantees the melting of all powder particles to prevent unsintered particles in the components. However, aged powder shows a broader sintering window caused by the agglomeration in the powder that postpones the onset of melting temperature and crystallization [61].

Due to the physical changes, the six powders exhibit certain differences in their thermal behavior. $T_{m\text{-}peak}$ and $T_{c\text{-}peak}$ are the temperatures connected to the peak of the heating and cooling curves, respectively, in DSC. ΔH_c is the crystallization enthalpy, and CD is the crystallinity degree obtainable by DSC (see Table 13.1).

Table 13.1 DSC test results.

	The cycle of reuse of the powder					
	0=virgin	**1-time**	**2-times**	**3-times**	**4-times**	**5-times**
$T_{m\text{-}peak}$ (in °C)	179.830	180.297	180.753	180.607	180.550	181.020
$T_{c\text{-}peak}$ (in °C)	152.137	152.680	152.710	152.863	152.887	152.933
ΔH_m (in J/g)	101.710	98.770	98.055	97.370	96.023	94.027
ΔH_c (in J/g)	58.335	57.535	57.543	57.383	58.000	56.927
CD (in %)	49.050	47.190	46.627	46.387	45.880	44.920
Printing process	1°	2°	3°	4°	5°	6°

The melting peak $T_{m\text{-}peak}$ shows an increase of 1.19°C from the virgin powder to the powder used five times, while at the same time, the crystallization peak $T_{c\text{-}peak}$ rises by 0.796 °C. However, these temperature changes do not seem sensitive enough to adequately analyze the powder degradation for recycling purposes [47].

The enthalpy associated with the melting process ΔH_m experiences a decline with successive powder reuse. This decrease could be attributed to powder degradation [279]. The presence of partially sintered particle agglomerates may result in less energy required for the molten phase. It can be suggested that it retains part of its thermal history as the powder ages. Also, chain scission could contribute to powder degradation, forming fragments [61]. Like the melting enthalpy, the crystallization enthalpy ΔH_c also decreases the energy required for crystal growth. This reduction could be attributed to degradation processes, such as further polymerization and cross-linking [280]. The degree of crystallinity CD of subsequent powders shows a progressive reduction of 8.42 % at the fifth reuse. During post-condensation, the amine and carboxyl groups' C-O bonds break to form new amide linkages. The solid-state condensation within the powder during the building cycle contributes to this decrease. This effect may be due to the influence of chain growth and the increase of amorphous content during powder ageing [325]. Furthermore, the decreased crystallinity also indicates that a modest increase in melt temperature is primarily caused by crystalline rearrangement rather than changes in crystallinity. The higher melting enthalpy indicates that more energy is required for the sintering process because the degree of crystallization is higher. The decrease in melting enthalpy may result in more pronounced secondary

sintering of neighboring powders, affecting the surface accuracy of the LS product, such as the occurrence of an "orange peel" effect [51, 287].

13.3.2 Tensile tests

The mechanical properties of laser-sintered PA12 parts are anisotropic. This study examines only the tensile behaviors of parts printed perpendicular to the building direction to ensure maximized mechanical strength and consistency in results. Printing in the XY plane provides superior layer cohesion, as the tensile load is applied parallel to the printed layers, thereby reducing the prevalence of weaknesses in inter-layer bonding that are commonly observed in the Z-axis [289, 325, 288]. Table 13.2 presents the average results μ with their standard deviations σ from the tensile tests. As expected, the reuse of the powder results in a loss of properties in terms of strength and elongation. Previous works also reported this behavior [284, 49, 267].

Table 13.2 Mechanical performances of specimens printed with virgin and reused powder (μ: mean; σ: standard deviation).

Cycles of reuse of the powder	UTS in MPa		True strain in mm/mm	
	μ	σ	μ	σ
0=virgin	65.301	0.297	0.245	0.008
1-time	61.971	1.142	0.220	0.025
2-times	50.133	1.019	0.221	0.008
3-times	47.720	0.136	0.197	0.002
4-times	42.105	1.838	0.194	0.012
5-times	42.201	0.003	0.201	0.001

Reusing the powder with no refreshing operations causes a 35.37 % loss in the part's tensile strength at the fifth reuse. Furthermore, the strain decreases by 17.99 % compared to the specimen manufactured with virgin powder. The reduced coalescence of the reused polyamide 12 particles and the weak solidification between layers explain the lower mechanical characteristics [253, 46]. The typical crystal structure of PA12 is composed of two phases: α and γ. The metastable α-phase, with a higher crystallinity, is presented in the virgin powder. During the sintering process, the chain is transformed into the stable γ-phase. In parts manufactured with aged powder, the decrease in crystallinity is caused by more short

molecule formation [53]. Furthermore, because the material's crystalline capacity is limited, amorphous regions surround lamellae, resulting in coarser spherulites dispersed throughout the matrix. The aged material's longer molecular lengths may have led to greater lamellar thickness and, as a result, a rougher look of the spherulites. The final mechanical characteristics reflect these microstructural changes [65].

The fracture surfaces of aged PA12 samples display a multitude of defects, including the presence of voids and unmolten powder particles. These defects are directly responsible for the initiation and propagation of cracks, which ultimately result in premature failure under tensile stress. It has been demonstrated that cracks in aged PA12 typically originate at these weak points, with subsequent crack growth occurring along the particle boundaries where coalescence is incomplete [288]. Moreover, the degree of crystallinity in the material is of great consequence regarding its fracture behavior. As the degree of crystallinity declines with the passage of time, the material displays increasingly brittle fracture characteristics, accompanied by a diminished capacity to absorb energy prior to failure. This is manifest in the formation of smooth, brittle fracture surfaces with minimal plastic deformation. A reduction in crystallinity is associated with an increase in the rate of crack propagation, which in turn results in a decrease in the overall fracture toughness [326]. Furthermore, the fatigue behavior of SLS is significantly influenced by the orientation of the layered structure. Samples subjected to loading parallel to the layer planes exhibit superior fatigue resistance compared to those loaded perpendicular, as evidenced by fatigue life curves and crack propagation studies. Cracks propagate through the weak interlayer regions, where crazing is a common mechanism responsible for crack nucleation and growth [327]. The combination of porosity and the decrease in molecular cohesion between particles accelerates crack propagation in aged PA12. This phenomenon explains the marked reduction in tensile strength observed in this study, particularly after the third reuse cycle, where defects dominate the fracture mechanism.

13.4 Discussion of the empirical models

Powder ageing changes the microstructure of SLS components. Microstructural variations influence mechanical characteristics. SLS components manufactured from fresh powders have greater tensile strength due to higher crystallinity and fewer inter-lamellar amorphous areas in fibrillar spherulites. The process of

powder ageing has a considerable impact on the microstructure of printed components, which in turn affects their mechanical characteristics. Fresh PA12 powder displays higher crystallinity, a more ordered molecular structure and a reduced number of amorphous regions between the crystalline regions. These attributes contribute to superior mechanical properties in components manufactured from virgin powder [280, 298]. However, as the powder undergoes multiple thermal cycles during reuse, its physical and chemical properties degrade, resulting in a reduction in the performance of the parts [57].

The results of the experiments were collected and statistically analyzed through the software Minitab19 [152]. The relation between the tensile response and reused was investigated. Table 13.3 shows the ANOVA [115] results for the linear model created for the tensile strength as a function of the type of PA12 used.

Table 13.3 ANOVA results of UTS value from tensile tests (DF = Degree of Freedom; Seq SS = Sequential sums of squares; Adj SS = Adjusted sums of squares; Adj MS = Adjusted mean squares).

Source	DF	Seq SS	Contribution	Adj SS	Adj MS	F-Value	p-Value
Regression	1	900.272	91.14 %	900.272	900.272	102.91	0.000
PA12	1	900.272	91.14 %	900.272	900.272	102.91	0.000
Error	10	87.484	8.86 %	87.484	8.748		
Lack-of-Fit	4	81.657	8.27 %	81.657	20.414	21.02	0.001
Pure Error	6	5.827	0.59 %	5.827	0.971		
Total	11	987.756	100.00 %				

Its p-value is extremely low, with an R^2 of 94.14 %, an R^2_{pred} of 90.30 %, and an R^2_{adj} of 92.18 %. According to the F-value, the powder type greatly influences the strength. As previously stated, the recycling state in which the powder affects the mechanical response [49, 253, 46, 53]. A first regression model derived by statistical analysis for predicting the strength of SLS printed parts as a function of the type of PA12 (virgin or reused from 1 to 5 times) is expressed by Equation 13.2:

$$\mathrm{UTS} = 64.25 - 5.072\,\mathrm{PA12} \qquad (13.2)$$

The residuals measure how well the line fits each data point. A residual plot is a graphical representation used to assess the quality of a linear regression model. The graphical representation of the residual values of the regression analysis in Figure 13.4 denotes a p-value of 0.563 and normally distributed errors.

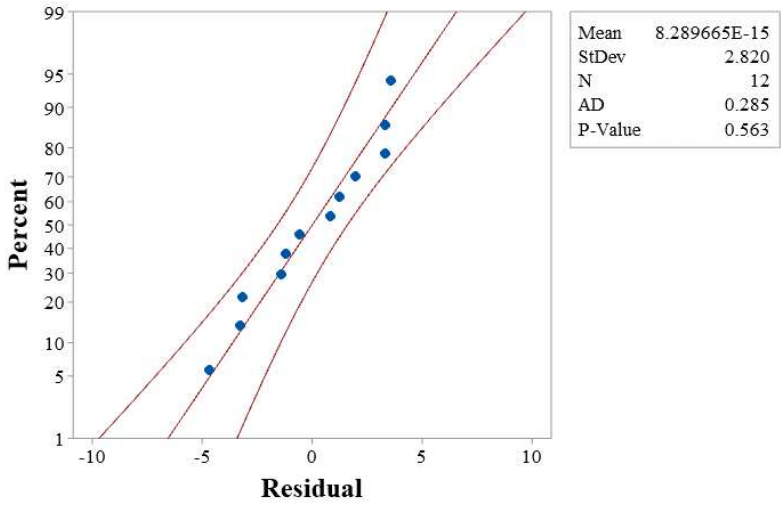


Figure 13.4 Normal probability plot for the residual (based on regression model 1).

The main effect plot of the UTS vs the material reuse is shown in Figure 13.5. The trend demonstrates how increasing powder recycling cycles determine a decreasing UTS of the parts manufactured with that n-times recycled powder. The standard errors on the mean (s.e.m), between 0.002 and 1.299 MPa, show that the UTS values are close to the mean values, so data dispersion is negligible.

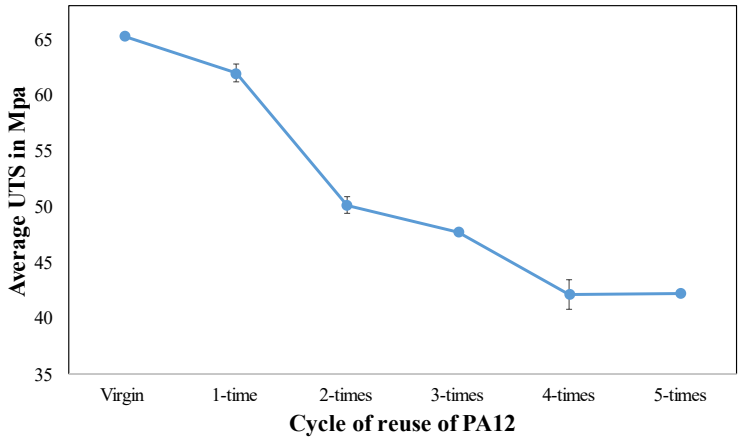


Figure 13.5 The effects of powder reuse on the final part's UTS.

The variation in the degree of crystallinity was also evaluated as a function of the PA12. Table 13.4 shows the ANOVA from the linear model of the degree of

crystallinity CD under the effect of the reused PA12. A linear model was chosen with an R^2 of 92.26 %, an R^2_{pred} of 88.08 %, and an R^2_{adj} of 91.49 %. Also, in this case, the F-value shows that the kind of powder influences the CD.

Table 13.4 ANOVA results of degree of crystallinity from DSC test (DF = Degree of Freedom; Seq SS = Sequential sums of squares; Adj SS = Adjusted sums of squares; Adj MS = Adjusted mean squares).

Source	DF	Seq SS	Contribution	Adj SS	Adj MS	F-Value	p-Value
Regression	1	18.8198	92.26 %	18.8198	18.8198	119.24	0.000
PA12	1	18.8198	92.26 %	18.8198	18.8198	119.24	0.000
Error	10	1.5783	7.74 %	1.5783	0.1578		
Lack-of-Fit	4	1.4313	7.02 %	1.4313	0.3578	14.60	0.003
Pure Error	6	0.1471	0.72 %	0.1471	0.0245		
Total	11	20.3981	100.00 %				

The regression model for the prediction of the degree of crystallinity is:

$$Degree\ of\ crystallinity\ =\ 48.502\ -\ 0.7333\ PA12 \qquad (13.3)$$

The data points are relatively close to the normal distribution line, and the p-value is greater than 0.05 (see Figure 13.6). This means that the data follow a normal distribution.

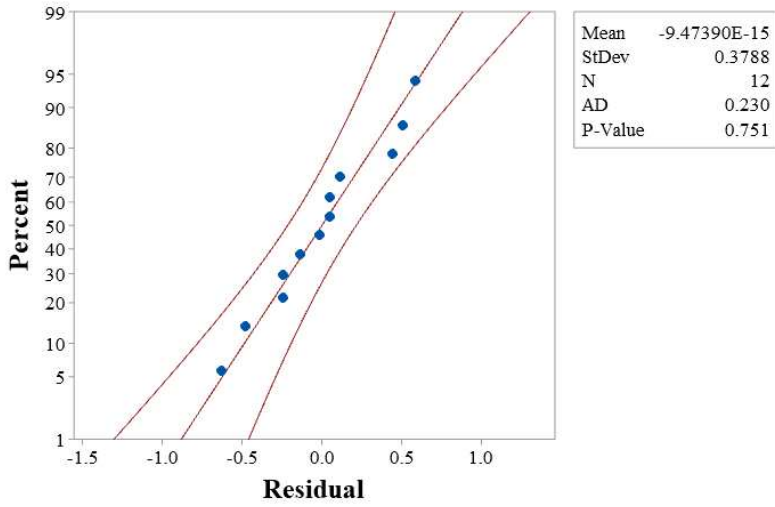


Figure 13.6 Normal probability plot for the residual (based on regression model 2).

Figure 13.7 shows the main effect plot of the CD versus the material reuse. Its trend decreases with the cycle of powder reuse. In this case, the s.e.m. falls between 0.04 and 0.195, demonstrating the data's stability around the mean values. The reuse of PA12 powder results in a reduction of the crystalline content, accompanied by an increase in amorphous regions, due to the occurrence of thermal degradation and molecular chain scission. These changes are directly related to a decline in mechanical properties, as amorphous regions provide less structural integrity than their crystalline counterparts [318]. The findings of the present study illustrate that the degree of crystallinity declines progressively with each reuse cycle, with an 8.42 % reduction observed after five cycles (see Table 13.1). This decline is consistent with previous findings that highlight the detrimental effects of powder ageing on crystallinity and the corresponding mechanical properties [260, 284].

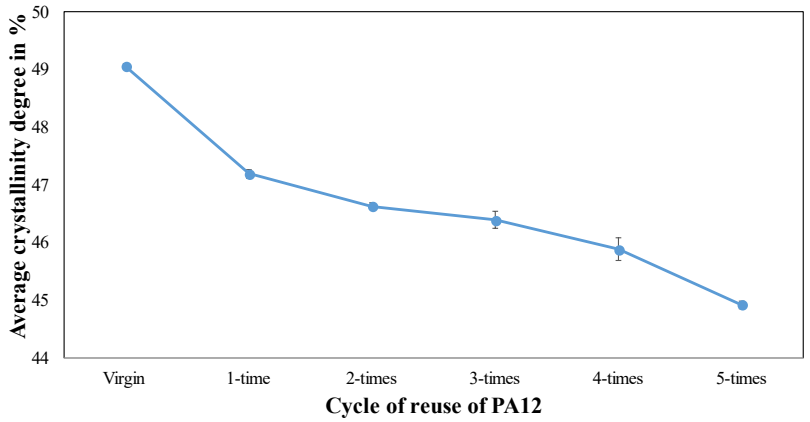


Figure 13.7 The effects of powder reuse on the degree of crystallinity of the powder.

Equation 13.2 can predict the UTS value of printed parts with the subsequential printing process and without the refreshing procedure on the powder. By combining it with Equation 13.3, it is possible to obtain a regression model that can predict the UTS as a function of the degree of crystallinity, which is valid in any work condition, as follows:

$$UTS_{pred} = -271.223 + 6.917\ CD \quad (13.4)$$

Higher crystallinity is associated with stronger intermolecular forces within the polymer, which in turn leads to enhanced mechanical properties. Conversely, as crystallinity decreases, the polymer becomes less rigid and more susceptible to

brittle failure, resulting in an increased propensity for cracks to propagate. This ultimately leads to a reduction in both UTS and overall mechanical integrity [50]. Equation 13.4 was used to predict the UTS, and Table 13.5 displays the variation from the actual value. The expected response has a maximum modulus variation of 12.34 %.

Table 13.5 Comparison between predicted and measured UTS values.

Cycles of reuse of the powder	CD in %	UTS_{meas} in MPa	UTS_{pred} in MPa	Difference in %
0=virgin	49.09	65.51	68.33	4.13
0=virgin	49.01	65.09	67.78	3.97
1-time	47.14	61.16	54.84	-11.52
1-time	47.29	62.78	55.88	-12.34
2-times	46.79	49.41	52.42	5.74
2-times	46.9	50.85	53.18	4.38
3-times	46.06	47.82	47.37	-0.93
3-times	46.35	47.62	49.38	3.56
4-times	45.62	40.81	44.33	7.95
4-times	46.01	43.40	47.03	7.71
5-times	44.95	42.20	39.70	-6.32
5-times	44.82	42.20	38.80	-8.77

13.5 Conclusion

The main conclusions deduced from this analysis are summarized as follows:

- Based on the DSC results on the powder, successive thermal processes lead to a variation in the melting and crystallization enthalpies, with a decrease of 7.55 % and 2.41 %, respectively. Moreover, the degree of crystallinity decreases by 8.42 % from the virgin to the fifth reuse cycle. With ageing, powder exhibits a wider sintering window due to powder agglomeration, which delays the onset of melting temperature and crystallization. The use of partially sintered particle agglomerates may require less energy for the molten phase. The agglomerates may retain some of their thermal history as the powder ages.
- Investigating the mechanical performance connected with the parts manufactured at each cycle denoted a decrease in tensile strength and strain of 35.37 %

and 17.99 %, respectively, at the last printing process. The reduced coalescence of the reused PA12 particles and weak solidification between layers can explain the lower mechanical characteristics.

- The ANOVA tests supported the results, showing a statistical dependency on strength and degree of crystallinity, considering the PA12's cycle of reuse. Considering that there is a correlation between the powder's microstructure and the mechanical properties of the printed parts, it is necessary to generalize the problem so that it is possible to trace the mechanical performances at different reuse states.
- A newly designed regression model was developed to predict the tensile response of a part considering the degree of crystallinity of the powder, starting from a regression model where the UTS is a function of the reused PA12 and combined with a second model able to predict the degree of crystallinity considering the reusing cycles. The expected response has a maximum variation of 12.34 % in absolute value.
- The obtained relationship may be used to boost up the reused powder during printing to minimize production waste in an optic of the circular economy.
- Future works will consider the building orientation of the printed part to have a better accurate predicted UTS. A future study will examine optimum sintering parameters at each recycling stage to develop optimum parts following the requirements.

Summary and Conclusion

Valentina Vendittoli[1]

[1] Department of Civil and Mechanical Engineering, University of Cassino and Southern Lazio, via G. di Biasio 43, 03043 Cassino, Italy

14.1 Key findings and conclusions

This doctoral thesis investigates the optimization of AM processes, focusing on MSLA, FDM and SLS. The work emphasizes the use of AI and material ageing studies to enhance both the geometrical quality and mechanical performance of parts produced through these methods and the sustainability of the AM processes. The research was conducted in three principal sections, initially focusing on MSLA, followed by FDM and subsequently on SLS. This approach enabled a comprehensive examination of the challenges and potential solutions for enhancing AM technologies.

14.1.1 Performance assessment and optimization of MSLA: geometrical accuracy and mechanical strength indices

The research presented in this study was initiated with an investigation into MSLA, which is given in Chapter 2. MSLA, a resin-based AM process, enables the production of high-precision parts with intricate geometries. The study introduced two key performance indices: DPI and PI. Both indices are used to quantify the dimensional accuracy and mechanical strength of parts manufactured through MSLA. These indices provide a reliable means of assessing and comparing the quality of parts made from biodegradable and non-biodegradable resins, thus offering insights into material performance for different applications. In addition, they facilitate a more comprehensive optimization, allowing for a closer alignment between the manufacturing process and the specific requirements of the final product.

14.1.2 AI-driven multi-optimization of FDM: predictive models for mechanical performance and geometrical accuracy

Chapters 4 to 9 examine the optimization of the FDM process. A significant element of this research was using BR artificial neural networks to predict the tensile strength or the geometrical accuracy of PLA components. The study identified critical process parameters, including infill percentage, print speed, and layer height, which significantly impacted the mechanical performance and dimensional accuracy of the printed parts. Furthermore, the DPI and PI were included in the research. These indices provide a comprehensive part quality assessment, considering both mechanical strength and dimensional accuracy. The study

demonstrated that AI-driven models could effectively predict and optimize the FDM process, enhancing part quality. The optimization framework developed through this research paves the way for future studies to enhance FDM-produced components' reliability and efficiency.

14.1.3 Impact of powder ageing in SLS: predicting mechanical properties of PA12 parts

Chapters 11, 12, and 13 aimed to examine the impact of SLS on PA12 parts, specifically investigating the influence of powder degradation and artificial ageing on the mechanical properties of these components. The research introduced a novel method for artificially ageing PA12 powder designed to simulate the effects of repeated use in the SLS process. This method permitted a comprehensive examination of the influence of powder ageing on the UTS and crystallinity of the manufactured parts. The findings indicated that the reuse of powder significantly impacts the mechanical properties of parts manufactured by SLS. The developed AI models were able to predict these changes, thus facilitating more effective management of material ageing in SLS processes. The findings of this research demonstrate the necessity of optimizing process parameters to maintain consistent part quality, even when powder that has undergone ageing is reused.

14.2 Contributions to the field

The findings of this research are of particular significance for industries that utilize additive manufacturing to produce high-performance components. The introduction of DPI and PI in MSLA establishes a new standard for balancing mechanical strength and dimensional accuracy in resin-based AM processes. This is particularly beneficial in sectors that require high precision, such as medical and dental, where biocompatibility and mechanical reliability must coexist with the requirement for complex geometric structures.

The optimization techniques developed for FDM have the potential to result in the production of more reliable and accurate parts, thereby rendering FDM a more viable option for industrial applications. Using AI-driven models, the thesis demonstrates how manufacturers can utilize dynamic adjustments to printing parameters to guarantee that the strength and precision of manufactured parts align

with industrial standards, thereby eliminating the necessity for time-consuming trial-and-error processes.
Similarly, the findings on powder ageing in SLS provide valuable insights into the maintenance of part quality in high-performance applications where material properties are critical. The findings offer practical solutions for industries looking to minimize material waste by introducing methods to extend the usable life of PA12 powder and providing predictive tools to manage powder degradation. Additionally, the insights into powder aging and mechanical property prediction enhance the reliability and consistency of SLS-produced parts, paving the way for broader industrial adoption of sustainable practices in AM.

14.3 Future research

This study has identified several challenges associated with optimizing additive manufacturing processes, particularly those related to MSLA, FDM and SLS. Considering these findings, several recommendations are put forth for further research, aiming to address the challenges associated with material properties and process parameters, as well as deepen the understanding of the underlying mechanisms influencing part quality and performance.

14.3.1 Investigation into the expansion of materials and process parameters in AM

It is recommended that future research concentrates on the creation of new materials that are specifically designed for FDM and SLS processes. This encompasses investigating novel thermoplastic and composite materials for FDM, intending to enhance mechanical performance and the development of new powders for SLS to prevent degradation over multiple reuse cycles. Furthermore, an expansion of the range of process parameters under study, including the investigation of disparate laser powers, scan speeds, and layer heights in the context of SLS, will facilitate the optimization of the mechanical and geometric properties of manufactured parts. Furthermore, the effects of uncertainties [328] of the process parameters (such as geometrical imprecision of the mechanisms for the X-Y-movement are not sufficiently researched. This will further contribute to a robust design of AM processes [329, 330] and a distinct quantification of random and systematic

deviations and thus on a more holistic understanding of the fundamental dependencies within all process steps in AM.
The introduction of advanced material formulations and the fine-tuning of process parameters could result in notable enhancements in the quality and reliability of AM-produced components, particularly in high-performance applications.

14.3.2 AI Integration for Dynamic Process Optimization

It would be beneficial to further investigate the potential of integrating AI, particularly machine learning models, into optimizing AM processes. AI has demonstrated potential in predicting and optimizing outcomes based on real-time data, which can be invaluable in monitoring and dynamically adjusting process parameters to achieve the desired part quality. Future research should concentrate on developing more sophisticated AI algorithms capable of handling the complexity of the multi-variable environments typical of AM processes. Such models could predict the effects of different process parameters on mechanical properties, surface finish, and dimensional accuracy, enabling real-time optimization and increased process efficiency.

14.3.3 Powder Reuse and Aging Studies in SLS

Taking into account the considerable influence that powder degradation exerts on the mechanical characteristics of parts manufactured through SLS, further investigation of the ageing processes of diverse powder materials is imperative. An additional area of investigation would be the effect of repeated use on the crystallinity, particle size distribution and flowability of the powders in question. This could lead to the development of improved guidelines and recommendations for powder reuse, thus ensuring consistent part quality. Furthermore, developing AI models to predict the optimal number of reuse cycles and simulate powder ageing under varying environmental conditions would contribute to achieve more sustainable and cost-effective SLS practices.

14.3.4 Sustainability and environmental Impact of AM

Future research must address the environmental impact of additive manufacturing, particularly concerning material waste and energy consumption. Further research could concentrate on optimizing support structures and reducing material waste in AM processes, in addition to developing recycling techniques for spent

powders and printed components. Furthermore, life-cycle assessments of AM processes, from the initial extraction of raw materials to the eventual recycling of the finished product, would facilitate a comprehensive understanding of their environmental impact and inform the development of more sustainable practices within the industry.

14.4 Concluding Remarks

This thesis has established a foundation for substantial advancements in the optimization of MSLA, FDM and SLS processes, with a particular emphasis on enhancing the mechanical and geometrical properties of AM-produced parts through the integration of AI and the conduct of material studies. The proposed future research directions seek to build upon these findings, offering a framework for further investigation and innovation in the field of AM. Continued research in these areas will be pivotal in realizing the full potential of AM technologies, ensuring their widespread adoption in high-performance industrial applications while maintaining sustainability and efficiency.

References

[1] ISO/ASTM, "ISO/ASTM 52900:2021(En); AdditiveManufacturing—General Principles—Fundamentals and Vocabulary.," ISO: Geneva, Switzerland, [Online]. Available: https://www.iso.org/obp/ui/#iso:std:iso-astm:52900:ed-2:v1:en:sec:A. [Accessed 14 February 2024].

[2] W. Gao, Y. Zhang, D. Ramanujan, K. Ramani, Y. Chen, C. B. Williams, C. C. Wang, Y. C. Shin, S. Zhang and P. D. Zavattieri, "The status, challenges, and future of additive manufacturing in engineering," *Computer-Aided Design,* vol. 69, pp. 65-89, 12 2015.

[3] I. Gibson, D. Rosen and B. Stucker, Additive Manufacturing Technologies, New York, NY: Springer New York, 2015.

[4] T. D. Ngo, A. Kashani, G. Imbalzano, K. T. Nguyen and D. Hui, "Additive manufacturing (3D printing): A review of materials, methods, applications and challenges," *Composites Part B: Engineering,* vol. 143, pp. 172-196, 6 2018.

[5] S. Ford and M. Despeisse, "Additive manufacturing and sustainability: an exploratory study of the advantages and challenges," *Journal of Cleaner Production,* vol. 137, pp. 1573-1587, 11 2016.

[6] C. W. Hull and C. Arcadia, "Apparatus for production of three-dimensional objects by stereolithography". 8 1984.

[7] C. J. Robinson, L. M. Southwell, J. A. Palmer, M. W. Smith, M. B. Sinclair, B. D. Chavez, B. E. Stucker, F. Medina and R. B. Wicker, "Microstereolithography production of integrated Hadamard mask structures," *https://doi.org/10.1117/12.646417,* vol. 6109, pp. 89-93, 1 2006.

[8] A. Divjak, M. Matijević and K. Hajdek, "REVIEW OF PHOTOPOLYMER MATERIALS IN MASKED STEREOLITHOGRAPHIC ADDITIVE MANUFACTURING," *International Symposium on Graphic Engineering and Design,* pp. 431-438, 2022.

[9] N. D. Borra and V. S. N. Neigapula, "Parametric optimization for dimensional correctness of 3D printed part using masked stereolithography: Taguchi method," *Rapid Prototyping Journal,* vol. 29, no. 1, pp. 166-184, 1 2023.

[10] D. Mondal, E. Diederichs and T. L. Willett, "Enhanced Mechanical Properties of 3D Printed Nanocomposites Composed of Functionalized Plant-Derived Biopolymers and Calcium-Deficient Hydroxyapatite Nanoparticles," *Frontiers in Materials,* vol. 9, p. 833065, 2 2022.

[11] Y. Bao, N. Paunović and J. C. Leroux, "Challenges and Opportunities in 3D Printing of Biodegradable Medical Devices by Emerging Photopolymerization Techniques," *Advanced Functional Materials,* vol. 32, no. 15, p. 2109864, 4 2022.

[12] P. T. Smith, b. narupai, J. H. Tsui, S. C. Millik, R. T. shafranek, D.-H. Kim and A. Nelson, "Additive Manufacturing of Bovine Serum Albumin-Based Hydrogels and Bioplastics," *ChemRxiv,* 9 2019.

[13] E. M. Wilts, A. Gula, C. Davis, N. Chartrain, C. B. Williams and T. E. Long, "Vat photopolymerization of liquid, biodegradable PLGA-based oligomers as tissue scaffolds," *European Polymer Journal,* vol. 130, p. 109693, 5 2020.

[14] S. Haudum, S. Lenhart, S. M. Müller, D. Tupe, C. Naderer, T. Dehne, M. Sittinger, Z. Major, T. Griesser, O. Brüggemann, J. Jacak and I. Teasdale, "Amino Acid-Based Polyphosphorodiamidates with Hydrolytically Labile Bonds for Degradation-Tuned Photopolymers," *ACS Macro Letters,* vol. 12, no. 6, pp. 673-678, 6 2023.

[15] B. Nowacki, P. Kowol, M. Kozioł, P. Olesik, J. Wieczorek and K. Wacławiak, "Effect of Post-Process Curing and Washing Time on Mechanical Properties of mSLA Printouts," *Materials 2021, Vol. 14, Page 4856,* vol. 14, no. 17, p. 4856, 8 2021.

[16] D. Lascano, L. Quiles-Carrillo, S. Torres-Giner, T. Boronat and N. Montanes, "Optimization of the Curing and Post-Curing Conditions for the Manufacturing of Partially Bio-Based Epoxy Resins with Improved Toughness," *Polymers 2019, Vol. 11, Page 1354,* vol. 11, no. 8, p. 1354, 8 2019.

[17] J. A. Travieso-Rodriguez, R. Jerez-Mesa, J. Llumà, O. Traver-Ramos, G. Gomez-Gras and J. J. R. Rovira, "Mechanical Properties of 3D-Printing Polylactic Acid Parts subjected to Bending Stress and Fatigue Testing," *Materials 2019, Vol. 12, Page 3859,* vol. 12, no. 23, p. 3859, 11 2019.

[18] B. Nowacki, P. Kowol, M. Kozioł, P. Olesik, J. Wieczorek and K. Wacławiak, "Effect of Post-Process Curing and Washing Time on Mechanical Properties of mSLA Printouts," *Materials 2021, Vol. 14, Page 4856,* vol. 14, no. 17, p. 4856, 8 2021.

[19] B. Orzeł and K. Stecuła, "Comparison of 3D Printout Quality from FDM and MSLA Technology in Unit Production," *Symmetry 2022, Vol. 14, Page 910,* vol. 14, no. 5, p. 910, 4 2022.

[20] J. Zhao, Y. Yang and L. Li, "A comprehensive evaluation for different post-curing methods used in stereolithography additive manufacturing," *Journal of Manufacturing Processes,* vol. 56, pp. 867-877, 8 2020.

[21] A. M. Abdelrhman, W. Wei Gan and D. Kurniawan, "Effect of part orientation on dimensional accuracy, part strength, and surface quality of three dimensional printed part," *IOP Conference Series: Materials Science and Engineering,* vol. 694, no. 1, p. 012048, 11 2019.

[22] Y. A. Al-Dulaijan, L. Alsulaimi, R. Alotaibi, A. Alboainain, S. Akhtar, S. Q. Khan, M. Al-Ghamdi and M. M. Gad, "Effect of Printing Orientation and Postcuring Time on the Flexural Strength of 3D-Printed Resins," *Journal of Prosthodontics,* vol. 32, no. S1, pp. 45-52, 4 2023.

[23] "ISO 22081:2021 - Geometrical product specifications (GPS) — Geometrical tolerancing — General geometrical specifications and general size specifications," [Online]. Available: https://www.iso.org/standard/72514.html. [Accessed 08 10 2024].

[24] "ISO 1101:2017(en), Geometrical product specifications (GPS) — Geometrical tolerancing — Tolerances of form, orientation, location and run-out," [Online]. Available:

https://www.iso.org/obp/ui/#iso:std:iso:1101:ed-4:v1:en. [Accessed 08 10 2024].

[25] S. Junk and C. Kuen, "Review of Open Source and Freeware CAD Systems for Use with 3D-Printing," *Procedia CIRP,* vol. 50, pp. 430-435, 2016.

[26] C. Abeykoon, P. Sri-Amphorn and A. Fernando, "Optimization of fused deposition modeling parameters for improved PLA and ABS 3D printed structures," *International Journal of Lightweight Materials and Manufacture,* vol. 3, no. 3, pp. 284-297, 9 2020.

[27] F. M. Mwema and E. T. Akinlabi, "Basics of Fused Deposition Modelling (FDM)," Springer, 2020, pp. 1-15.

[28] G. Gomez-Gras, R. Jerez-Mesa, J. A. Travieso-Rodriguez and J. Lluma-Fuentes, "Fatigue performance of fused filament fabrication PLA specimens," *Materials & Design,* vol. 140, pp. 278-285, 2 2018.

[29] M. Abas, T. Habib, S. Noor, B. Salah and D. Zimon, "Parametric Investigation and Optimization to Study the Effect of Process Parameters on the Dimensional Deviation of Fused Deposition Modeling of 3D Printed Parts," *Polymers,* vol. 14, no. 17, p. 3667, 9 2022.

[30] V. Cojocaru, D. Frunzaverde, C.-O. Miclosina and G. Marginean, "The Influence of the Process Parameters on the Mechanical Properties of PLA Specimens Produced by Fused Filament Fabrication—A Review," *Polymers,* vol. 14, no. 5, p. 886, 2 2022.

[31] A. Lanzotti, M. Martorelli, S. Maietta, S. Gerbino, F. Penta and A. Gloria, "A comparison between mechanical properties of specimens 3D printed with virgin and recycled PLA," *Procedia CIRP,* vol. 79, pp. 143-146, 2019.

[32] J. Giri, A. Chiwande, Y. Gupta, C. Mahatme and P. Giri, "Effect of process parameters on mechanical properties of 3d printed samples using FDM process," *Materials Today: Proceedings,* vol. 47, pp. 5856-5861, 2021.

[33] L. Adam, O. Lietaer, S. Mathieu and I. Doghri, "Numerical simulation of additive manufacturing of polymers and polymer-based composites," *Structure and Properties of Additive Manufactured Polymer Components,* pp. 115-146, 1 2020.

[34] C. Kousiatza and D. Karalekas, "In-situ monitoring of strain and temperature distributions during fused deposition modeling process," *Materials & Design,* vol. 97, pp. 400-406, 5 2016.

[35] H. R. Vanaei, K. Raissi, M. Deligant, M. Shirinbayan, J. Fitoussi, S. Khelladi and A. Tcharkhtchi, "Toward the understanding of temperature effect on bonding strength, dimensions and geometry of 3D-printed parts," *Journal of Materials Science,* vol. 55, no. 29, pp. 14677-14689, 10 2020.

[36] W. Yu, X. Wang, X. Yin, E. Ferraris and J. Zhang, "The effects of thermal annealing on the performance of material extrusion 3D printed polymer parts," *Materials & Design,* vol. 226, p. 111687, 2 2023.

[37] C. Dudescu and L. Racz, "Effects of Raster Orientation, Infill Rate and Infill Pattern on the Mechanical Properties of 3D Printed Materials," *ACTA Universitatis Cibiniensis,* vol. 69, no. 1, pp. 23-30, 12 2017.

[38] E. E. Cho, H. H. Hein, Z. Lynn, S. J. Hla and T. Tran, "Investigation on Influence of Infill Pattern and Layer Thickness on Mechanical Strength of PLA Material in 3D Printing Technology," *Journal of Engineering and Science Research,* vol. 3, no. 2, pp. 27-37, 4 2019.

[39] V. S. Jatti, M. S. Sapre, A. V. Jatti, N. K. Khedkar and V. S. Jatti, "Mechanical Properties of 3D-Printed Components Using Fused Deposition Modeling: Optimization Using the Desirability Approach and Machine Learning Regressor," *Applied System Innovation 2022, Vol. 5, Page 112,* vol. 5, no. 6, p. 112, 11 2022.

[40] P. Charalampous, N. Kladovasilakis, I. Kostavelis, K. Tsongas, D. Tzetzis and D. Tzovaras, "Machine Learning-Based Mechanical Behavior Optimization of 3D Print Constructs Manufactured Via the FFF Process," *Journal of Materials Engineering and Performance,* vol. 31, no. 6, pp. 4697-4706, 6 2022.

[41] F. Etesami and T. Griffin, "Characterizing the Accuracy of FDM Rapid Prototyping Machines for Machine Design Applications," *Volume 12: Systems and Design,* 11 2013.

[42] M. N. Islam, B. Boswell and A. Pramanik, "An Investigation of Dimensional Accuracy of Parts Produced by Three-Dimensional Printing," *Proceedings of the World Congress on Engineering 2013,* pp. 522-525, 7 2014.

[43] Z. Moza, K. Kitsakis, J. (. D. Kechagias and N. Mastorakis, "Optimizing Dimensional Accuracy of Fused Filament Fabrication using Taguchi Design," 2015.

[44] D. Ahn, H. Kim and S. Lee, "Surface roughness prediction using measured data and interpolation in layered manufacturing," *Journal of Materials Processing Technology,* vol. 209, no. 2, pp. 664-671, 1 2009.

[45] H. Bakhtiari, M. Nikzad and M. Tolouei-Rad, "Influence of Three-Dimensional Printing Parameters on Compressive Properties and Surface Smoothness of Polylactic Acid Specimens," *Polymers,* vol. 15, no. 18, p. 3827, 9 2023.

[46] S. C. Ligon, R. Liska, J. Stampfl, M. Gurr and R. Mülhaupt, "Polymers for 3D Printing and Customized Additive Manufacturing," *Chemical Reviews,* vol. 117, no. 15, pp. 10212-10290, 8 2017.

[47] D. T. Pham, K. D. Dotchev and W. A. Yusoff, "Deterioration of polyamide powder properties in the laser sintering process," *Proceedings of the Institution of Mechanical Engineers, Part C: Journal of Mechanical Engineering Science,* vol. 222, no. 11, pp. 2163-2176, 11 2008.

[48] "File:SLS schematic.svg - Wikimedia Commons," [Online]. Available: https://commons.wikimedia.org/wiki/File:SLS_schematic.svg.

[49] S. Dadbakhsh, L. Verbelen, O. Verkinderen, D. Strobbe, P. Van Puyvelde and J. P. Kruth, "Effect of PA12 powder reuse on coalescence behaviour and microstructure of SLS parts," *European Polymer Journal,* vol. 92, pp. 250-262, 7 2017.

[50] M. Schmid, A. Amado and K. Wegener, "Materials perspective of polymers for additive manufacturing with selective laser sintering," *Journal of Materials Research,* vol. 29, no. 17, pp. 1824-1832, 6 2014.

[51] P. Chen, H. Wu, W. Zhu, L. Yang, Z. Li, C. Yan, S. Wen and Y. Shi, "Investigation into the processability, recyclability and crystalline structure of selective laser sintered Polyamide 6 in comparison with Polyamide 12," *Polymer Testing,* vol. 69, pp. 366-374, 8 2018.

[52] S. Gogolewski, K. Czerntawska and M. Gastorek, "Effect of annealing on thermal properties and crystalline structure of polyamides. Nylon 12

(polylaurolactam)," *Colloid and Polymer Science Kolloid Zeitschrift & Zeitschrift für Polymere,* vol. 258, no. 10, pp. 1130-1136, 10 1980.

[53] H. Zarringhalam, N. Hopkinson, N. F. Kamperman and J. J. de Vlieger, "Effects of processing on microstructure and properties of SLS Nylon 12," *Materials Science and Engineering: A,* Vols. 435-436, pp. 172-180, 11 2006.

[54] A. Kulkarni and H. Dasari, "Current Status of Methods Used In Degradation of Polymers: A Review," 2018. [Online]. Available: https://www.matec-conferences.org/articles/matecconf/abs/2018/03/matecconf_rimes2017_02023/matecconf_rimes2017_02023.html.

[55] J. Vohlidal, "Polymer degradation: A short review," 6 2021. [Online].

[56] P. Mägi, A. Krumme and M. Pohlak, "Recycling of PA-12 in Additive Manufacturing and the Improvement of its Mechanical Properties," *Key Engineering Materials,* vol. 674, pp. 9-14, 2016.

[57] K. Dotchev and W. Yusoff, "Recycling of polyamide 12 based powders in the laser sintering process," *Rapid Prototyping Journal,* vol. 15, no. 3, pp. 192-203, 5 2009.

[58] K. Wudy and D. Drummer, "Aging effects of polyamide 12 in selective laser sintering: Molecular weight distribution and thermal properties," *Additive Manufacturing,* vol. 25, pp. 1-9, 1 2019.

[59] A. C. Lopes, Á. M. Sampaio, C. S. Silva and A. J. Pontes, "Prediction of SLS parts properties using reprocessing powder," *Rapid Prototyping Journal,* vol. 27, no. 3, pp. 496-506, 4 2021.

[60] T. Eggers and F. von Lacroix, "Investigation of the Influence of the Mixing Process on the Powder and Component Properties during Cyclic Reuse of a Polyamide 12 Sinter Material in Selective Laser Sintering," *Powders,* vol. 2, no. 1, pp. 75-96, 2 2023.

[61] P. C. Gomes, O. G. Piñeiro, A. C. Alves and O. S. Carneiro, "On the Reuse of SLS Polyamide 12 Powder," *Materials,* vol. 15, no. 16, 8 2022.

[62] F. M. Mwania, M. Maringa and K. Van Der Walt, "A Review of Methods Used to Reduce the Effects of High Temperature Associated with Polyamide 12 and Polypropylene Laser Sintering," *Advances in Polymer Technology,* vol. 2020, 2020.

[63] K. R. Hart, R. M. Dunn and E. D. Wetzel, "Increased fracture toughness of additively manufactured semi-crystalline thermoplastics via thermal annealing," *Polymer,* vol. 211, p. 123091, 12 2020.

[64] B. Naghshineh, "Additive manufacturing technology adoption for supply chain agility: a systematic search and review," *International Journal of Production Research,* pp. 1-33, 6 2024.

[65] F. Yang, N. Zobeiry, R. Mamidala and X. Chen, "A review of aging, degradation, and reusability of PA12 powders in selective laser sintering additive manufacturing," *Materials Today Communications,* vol. 34, 3 2023.

[66] E. Rich and K. Knight, Artificial intelligence, McGraw-Hill, 1991, p. 621.

[67] J. Schmidhuber, "Deep Learning in neural networks: An overview," *Neural Networks,* vol. 61, pp. 85-117, 1 2015.

[68] Z. Abdelhamid, H. Mohamed and S. Kelouwani, "The use of machine learning in process–structure–property modeling for material extrusion additive manufacturing: a state-of-the-art review," *Journal of the Brazilian Society of Mechanical Sciences and Engineering,* vol. 46, no. 2, p. 70, 2 2024.

[69] N. Leberruyer, J. Bruch, M. Ahlskog and S. Afshar, "Toward Zero Defect Manufacturing with the support of Artificial Intelligence—Insights from an industrial application," *Computers in Industry,* vol. 147, p. 103877, 5 2023.

[70] S. K. Baduge, S. Thilakarathna, J. S. Perera, M. Arashpour, P. Sharafi, B. Teodosio, A. Shringi and P. Mendis, "Artificial intelligence and smart vision for building and construction 4.0: Machine and deep learning methods and applications," *Automation in Construction,* vol. 141, p. 104440, 9 2022.

[71] I. Rojek, J. Kopowski, J. Lewandowski and D. Mikołajewski, "Use of Machine Learning to Improve Additive Manufacturing Processes," *Applied Sciences (Switzerland),* vol. 14, no. 15, p. 6730, 8 2024.

[72] F. Burden and D. Winkler, "Bayesian Regularization of Neural Networks," *Methods in Molecular Biology,* vol. 458, pp. 23-42, 2008.

[73] E. Westphal and H. Seitz, "A machine learning method for defect detection and visualization in selective laser sintering based on convolutional neural networks," *Additive Manufacturing,* vol. 41, p. 101965, 5 2021.

[74] D. P. Guillen, "Machine Learning Applications in Advanced Manufacturing Processes," *JOM,* vol. 72, no. 11, pp. 3906-3907, 11 2020.

[75] S. Kumar, ·. T. Gopi, ·. N. Harikeerthana, ·. Munish, K. Gupta, V. Gaur, ·. Grzegorz, M. Krolczyk, ·. C. Wu, B. Munish, T. Gopi, N. Harikeerthana, G. M. Krolczyk and C. Wu, "Machine learning techniques in additive manufacturing: a state of the art review on design, processes and production control," *Journal of Intelligent Manufacturing 2022 34:1,* vol. 34, no. 1, pp. 21-55, 10 2022.

[76] N. Naik, B. Shivamurthy, B. H. Thimmappa, Z. Guo and R. Bhat, "Bio-Based Epoxies: Mechanical Characterization and Their Applicability in the Development of Eco-Friendly Composites," *Journal of Composites Science 2022, Vol. 6, Page 294,* vol. 6, no. 10, p. 294, 10 2022.

[77] A. Afzal and Y. Nawab, "Polymer composites," Woodhead Publishing, 2021, pp. 139-152.

[78] K. Gopalakrishna, N. Reddy and Y. Zhao, "Biocomposites from Biofibers and Biopolymers," *Biofibers and Biopolymers for Biocomposites: Synthesis, Characterization and Properties,* pp. 91-110, 1 2020.

[79] M. Pagac, J. Hajnys, Q. P. Ma, L. Jancar, J. Jansa, P. Stefek and J. Mesicek, "A Review of Vat Photopolymerization Technology: Materials, Applications, Challenges, and Future Trends of 3D Printing," *Polymers 2021, Vol. 13, Page 598,* vol. 13, no. 4, p. 598, 2 2021.

[80] S. Chaudhary, S. K. Avinashi, J. Rao and C. Gautam, "Recent Advances in Additive Manufacturing, Applications and Challenges for Dentistry: A Review," *ACS Biomaterials Science and Engineering,* vol. 9, no. 7, pp. 3987-4019, 7 2023.

[81] B. Madsen, P. Brøndsted and T. L. Andersen, "Biobased composites: materials, properties and potential applications as wind turbine blade materials," *Advances in Wind Turbine Blade Design and Materials,* pp. 363-386, 1 2013.

[82] E. A. Baroncini, S. Kumar Yadav, G. R. Palmese and J. F. Stanzione, "Recent advances in bio-based epoxy resins and bio-based epoxy curing agents," *Journal of Applied Polymer Science,* vol. 133, no. 45, 12 2016.

[83] M. A. R. Meier, J. O. Metzger and U. S. Schubert, "ChemInform Abstract: Plant Oil Renewable Resources as Green Alternatives in Polymer Science," *ChemInform,* vol. 39, no. 5, pp. no-no, 1 2008.

[84] M. Shibata and M. Shibata, "Bio-Based Nanocomposites Composed of Photo-Cured Soybean-Based Resins and Supramolecular Hydroxystearic Acid Nanofibers," *Soybean - Molecular Aspects of Breeding,* 4 2011.

[85] Q. Tang, Y. Chen, H. Gao, Q. Li, Z. Xi, L. Zhao, C. Peng, L. Li, Q. Tang, Y. Chen, H. Gao, Q. Li, Z. Xi, L. Zhao, C. Peng and L. Li, "Bio-Based Epoxy Resin from Epoxidized Soybean Oil," *Soybean - Biomass, Yield and Productivity,* 11 2018.

[86] B. Sabbatini, A. Cambriani, M. Cespi, G. F. Palmieri, D. R. Perinelli and G. Bonacucina, "An Overview of Natural Polymers as Reinforcing Agents for 3D Printing," *ChemEngineering 2021, Vol. 5, Page 78,* vol. 5, no. 4, p. 78, 11 2021.

[87] E. Skliutas, M. Lebedevaite, S. Kasetaite, S. Rekštytė, S. Lileikis, J. Ostrauskaite and M. Malinauskas, "A Bio-Based Resin for a Multi-Scale Optical 3D Printing," *Scientific Reports 2020 10:1,* vol. 10, no. 1, pp. 1-9, 6 2020.

[88] M. A. Sarabia-Vallejos, F. E. Rodríguez-Umanzor, C. M. González-Henríquez and J. Rodríguez-Hernández, "Innovation in Additive Manufacturing Using Polymers: A Survey on the Technological and Material Developments," *Polymers 2022, Vol. 14, Page 1351,* vol. 14, no. 7, p. 1351, 3 2022.

[89] N. Badanova, A. Perveen and D. Talamona, "Study of SLA Printing Parameters Affecting the Dimensional Accuracy of the Pattern and Casting in Rapid Investment Casting," *Journal of Manufacturing and Materials Processing 2022, Vol. 6, Page 109,* vol. 6, no. 5, p. 109, 9 2022.

[90] R. Brighenti, L. Marsavina, M. P. Marghitas, M. P. Cosma and M. Montanari, "Mechanical characterization of additively manufactured photopolymerized polymers," *Mechanics of Advanced Materials and Structures,* vol. 30, no. 9, pp. 1853-1864, 2023.

[91] A. Tulcan, M. D. Vasilescu and L. Tulcan, "Comparative Study of the Influence of Bio-Resin Color on the Dimension, Flatness and Straightness

of the Part in the 3D Printing Process," *Polymers 2021, Vol. 13, Page 1412,* vol. 13, no. 9, p. 1412, 4 2021.

[92] D. D. Rubayo, K. Phasuk, J. M. Vickery, D. Morton and W. S. Lin, "Influences of build angle on the accuracy, printing time, and material consumption of additively manufactured surgical templates," *The Journal of prosthetic dentistry,* vol. 126, no. 5, pp. 658-663, 11 2021.

[93] T. Hada, M. Kanazawa, M. Iwaki, T. Arakida, Y. Soeda, A. Katheng, R. Otake and S. Minakuchi, "Effect of Printing Direction on the Accuracy of 3D-Printed Dentures Using Stereolithography Technology," *Materials (Basel, Switzerland),* vol. 13, no. 15, pp. 1-12, 8 2020.

[94] O. Poyraz, "Influence of Build Direction and Post Processes on the Material and Part Attributes of Hard Resins Fabricated by Photopolymerization Based Additive Manufacturing," *Materials Research,* vol. 26, p. e20220362, 4 2023.

[95] W. A. Loflin, J. D. English, C. Borders, L. M. Harris, A. Moon, J. N. Holland and F. K. Kasper, "Effect of print layer height on the assessment of 3D-printed models," *American journal of orthodontics and dentofacial orthopedics : official publication of the American Association of Orthodontists, its constituent societies, and the American Board of Orthodontics,* vol. 156, no. 2, pp. 283-289, 8 2019.

[96] C. S. Favero, J. D. English, B. E. Cozad, J. O. Wirthlin, M. M. Short and F. K. Kasper, "Effect of print layer height and printer type on the accuracy of 3-dimensional printed orthodontic models," *American Journal of Orthodontics and Dentofacial Orthopedics,* vol. 152, no. 4, pp. 557-565, 10 2017.

[97] M. A. Boca, A. Sover and L. Slătineanu, "The Printing Parameters Effects on the Dimensional Accuracy of the Parts Made of Photosensitive Resin," *Macromolecular Symposia,* vol. 396, no. 1, p. 2000287, 4 2021.

[98] K. Chockalingam, N. Jawahar and U. Chandrasekhar, "Influence of layer thickness on mechanical properties in stereolithography," *Rapid Prototyping Journal,* vol. 12, no. 2, pp. 106-113, 2006.

[99] D. Miedzińska, R. Gieleta and A. Popławski, "Experimental study on influence of curing time on strength behavior of sla-printed samples

loaded with different strain rates," *Materials,* vol. 13, no. 24, pp. 1-16, 12 2020.

[100] J. Wu, Z. Zhao, C. M. Hamel, X. Mu, X. Kuang, Z. Guo and H. J. Qi, "Evolution of material properties during free radical photopolymerization," *Journal of the Mechanics and Physics of Solids,* vol. 112, pp. 25-49, 3 2018.

[101] N. Chantarapanich, P. Puttawibul, K. Sitthiseripratip, S. Sucharitpwatskul and S. Chantaweroad, "Study of the mechanical properties of photo-cured epoxy resin fabricated by stereolithography process," *Songklanakarin J. Sci. Technol,* vol. 35, no. 1, pp. 91-98, 2013.

[102] C. Zhu, S. Li, X. Cong, X. Liu, C. Zhu, S. Li, X. Cong and X. Liu, "Mechanical Properties of Bio-Based Epoxy Composites Reinforced with Hybrid-Interlayer Ramie and Recycled Carbon Fibres," *Open Journal of Composite Materials,* vol. 10, no. 4, pp. 118-133, 8 2020.

[103] Z. S. Liu, S. Z. Erhan and P. D. Calvert, "Solid freeform fabrication of epoxidized soybean oil/epoxy composites with di-, tri-, and polyethylene amine curing agents," *Journal of Applied Polymer Science,* vol. 93, no. 1, pp. 356-363, 7 2004.

[104] K. Chandrashekhara, S. Sundararaman, V. Flanigan and S. Kapila, "Affordable composites using renewable materials," *Materials Science and Engineering: A,* vol. 412, no. 1-2, pp. 2-6, 12 2005.

[105] F. L. Jin and S. J. Park, "Impact-strength improvement of epoxy resins reinforced with a biodegradable polymer," *Materials Science and Engineering: A,* vol. 478, no. 1-2, pp. 402-405, 4 2008.

[106] V. Vendittoli, W. Polini and M. S. Walter, "Geometrical deviations of green parts due to additive manufacturing: a synthetic geometrical performance index," *Procedia CIRP,* vol. 114, pp. 159-164, 2022.

[107] V. Vendittoli, W. Polini, M. S. J. Walter and G. Moroni, "A synthetic geometric performance index for parts manufactured by VAT photopolymerization," *Manufacturing Technology,* 2024.

[108] L. Rebaioli and I. Fassi, "A review on benchmark artifacts for evaluating the geometrical performance of additive manufacturing processes," *The*

International Journal of Advanced Manufacturing Technology 2017 93:5, vol. 93, no. 5, pp. 2571-2598, 7 2017.

[109] "D638 Standard Test Method for Tensile Properties of Plastics," [Online]. Available: https://www.astm.org/d0638-22.html.

[110] "D790 Standard Test Methods for Flexural Properties of Unreinforced and Reinforced Plastics and Electrical Insulating Materials," [Online]. Available: https://www.astm.org/d0790-17.html.

[111] "PrusaSlicer | Original Prusa 3D printers directly from Josef Prusa," [Online]. Available: https://www.prusa3d.com/page/prusaslicer_424/.

[112] "ATOS 3D scanning," [Online]. Available: https://www.zeiss.com/metrology/en/systems/optical-3d/3d-scanning.html.

[113] "ZEISS INSPECT: Your standard in digital industrial inspection," [Online]. Available: https://www.zeiss.com/metrology/en/software/zeiss-inspect.html.

[114] "D883 Standard Terminology Relating to Plastics," [Online]. Available: https://www.astm.org/d0883-22.html.

[115] "What is ANOVA? - Minitab," [Online]. Available: https://support.minitab.com/en-us/minitab/help-and-how-to/statistical-modeling/anova/supporting-topics/basics/what-is-anova/.

[116] B. Ashrafi, Y. Martinez-Rubi, L. Khoun, A. Derahman and Z. Z. Abidin, "Mechanical properties of bio-epoxy resins and synthetic epoxy resins blends," *IOP Conference Series: Materials Science and Engineering,* vol. 1176, no. 1, p. 012005, 8 2021.

[117] M. Qi, Y. J. Xu, W. H. Rao, X. Luo, L. Chen and Y. Z. Wang, "Epoxidized soybean oil cured with tannic acid for fully bio-based epoxy resin," *RSC Advances,* vol. 8, no. 47, pp. 26948-26958, 7 2018.

[118] W. V. Titow, "Plasticisers," Dordrecht, Springer, Dordrecht, 1990, pp. 177-257.

[119] D. Fico, D. Rizzo, R. Casciaro and C. Esposito Corcione, "A Review of Polymer-Based Materials for Fused Filament Fabrication (FFF): Focus on

Sustainability and Recycled Materials," *Polymers,* vol. 14, no. 3, p. 465, 1 2022.

[120] E. Morse, J.-Y. Dantan, N. Anwer, R. Söderberg, G. Moroni, A. Qureshi, X. Jiang and L. Mathieu, "Tolerancing: Managing uncertainty from conceptual design to final product," *CIRP Annals,* vol. 67, no. 2, pp. 695-717, 2018.

[121] G. D. Kim and Y. T. Oh, "A benchmark study on rapid prototyping processes and machines: Quantitative comparisons of mechanical properties, accuracy, roughness, speed, and material cost," *http://dx.doi.org/10.1243/09544054JEM724,* vol. 222, no. 2, pp. 201-215, 3 2008.

[122] Z. Sun and L. F. Velásquez-García, "Monolithic FFF-printed, biocompatible, biodegradable, dielectric-conductive microsystems," *Journal of Microelectromechanical Systems,* vol. 26, no. 6, pp. 1356-1370, 2017.

[123] V. Shanmugam, M. V. Pavan, K. Babu and B. Karnan, "Fused deposition modeling based polymeric materials and their performance: A review," *Polymer Composites,* vol. 42, no. 11, pp. 5656-5677, 11 2021.

[124] J. Bustillos, D. Montero, P. Nautiyal, A. Loganathan, B. Boesl and A. Agarwal, "Integration of graphene in poly(lactic) acid by 3D printing to develop creep and wear-resistant hierarchical nanocomposites," *Polymer Composites,* vol. 39, no. 11, pp. 3877-3888, 11 2018.

[125] M. M. Hanon, L. Zsidai and Q. Ma, "Accuracy investigation of 3D printed PLA with various process parameters and different colors," *Materials Today: Proceedings,* vol. 42, pp. 3089-3096, 1 2021.

[126] O. A. Mohamed, S. H. Masood and J. L. Bhowmik, "Optimization of fused deposition modeling process parameters: a review of current research and future prospects," *Advances in Manufacturing,* vol. 3, no. 1, pp. 42-53, 3 2015.

[127] M. Á. Caminero, J. M. Chacón, E. García-Plaza, P. J. Núñez, J. M. Reverte and J. P. Becar, "Additive Manufacturing of PLA-Based Composites Using Fused Filament Fabrication: Effect of Graphene Nanoplatelet Reinforcement on Mechanical Properties, Dimensional Accuracy and Texture," *Polymers 2019, Vol. 11, Page 799,* vol. 11, no. 5, p. 799, 5 2019.

[128] E. García, P. J. Núñez, J. M. Chacón, M. A. Caminero and S. Kamarthi, "Comparative study of geometric properties of unreinforced PLA and PLA-Graphene composite materials applied to additive manufacturing using FFF technology," *Polymer Testing,* vol. 91, p. 106860, 11 2020.

[129] E. García Plaza, P. Núñez López, M. Caminero Torija and J. Chacón Muñoz, "Analysis of PLA Geometric Properties Processed by FFF Additive Manufacturing: Effects of Process Parameters and Plate-Extruder Precision Motion," *Polymers,* vol. 11, no. 10, p. 1581, 9 2019.

[130] A. Alafaghani, A. Qattawi, B. Alrawi and A. Guzman, "Experimental Optimization of Fused Deposition Modelling Processing Parameters: A Design-for-Manufacturing Approach," *Procedia Manufacturing,* vol. 10, pp. 791-803, 2017.

[131] L. Santana, J. Lino Alves and A. da Costa Sabino Netto, "DIMENSIONAL ANALYSIS OF PLA AND PETG PARTS BUILT BY OPEN SOURCE EXTRUSION-BASED 3D PRINTING," 8 2019.

[132] B. N. Panda, K. Shankhwar, A. Garg and Z. Jian, "Performance evaluation of warping characteristic of fused deposition modelling process," *International Journal of Advanced Manufacturing Technology,* vol. 88, no. 5-8, pp. 1799-1811, 2 2017.

[133] T. M. Wang, J. T. Xi and Y. Jin, "A model research for prototype warp deformation in the FDM process," *International Journal of Advanced Manufacturing Technology,* vol. 33, no. 11-12, pp. 1087-1096, 8 2007.

[134] T. Müller, A. Elkaseer, J. Wadlinger, M. Salem and S. G. Scholz, "Development of Correction Factors for FDM 3D Printers: Experimental Investigation and ANN Modelling," *Smart Innovation, Systems and Technologies,* vol. 262 SIST, pp. 314-326, 2022.

[135] S. Mahmood, A. J. Qureshi and D. Talamona, "Taguchi based process optimization for dimension and tolerance control for fused deposition modelling," *Additive Manufacturing,* vol. 21, pp. 183-190, 5 2018.

[136] W. Polini and A. Corrado, "Geometric tolerance analysis through Jacobian model for rigid assemblies with translational deviations," *Assembly Automation,* vol. 36, no. 1, pp. 72-79, 2 2016.

[137] P. Grohmann and M. S. Walter, "Speeding up Statistical Tolerance Analysis to Real Time," *Applied Sciences 2021, Vol. 11, Page 4207*, vol. 11, no. 9, p. 4207, 5 2021.

[138] B. S. Rupal, R. Ahmad and A. J. Qureshi, "Feature-Based Methodology for Design of Geometric Benchmark Test Artifacts for Additive Manufacturing Processes," *Procedia CIRP*, vol. 70, pp. 84-89, 1 2018.

[139] "UltiMaker Cura - UltiMaker," [Online]. Available: https://ultimaker.com/software/ultimaker-cura/.

[140] "ISO/ASTM 52902:2023 - Additive manufacturing — Test artefacts — Geometric capability assessment of additive manufacturing systems," [Online]. Available: https://www.iso.org/standard/79683.html.

[141] M. A. Boca, A. Sover and L. Slătineanu, "The dimensional accuracy of plastic parts made by the fused filament fabrication," *IOP Conference Series: Materials Science and Engineering*, vol. 997, no. 1, p. 012021, 12 2020.

[142] F. Gorana, K. Kumar Sahu and Y. Kumar Modi, "Parameter optimization for dimensional accuracy of fused deposition modelling parts," *Materials Today: Proceedings*, vol. 78, pp. 640-646, 2023.

[143] M. Popović, M. Pjević, A. Milovanović, G. Mladenović and M. Milošević, "Printing parameter optimization of PLA material concerning geometrical accuracy and tensile properties relative to FDM process productivity," *Journal of Mechanical Science and Technology*, vol. 37, no. 2, pp. 697-706, 2 2023.

[144] C. Y. Lee and C. Y. Liu, "The influence of forced-air cooling on a 3D printed PLA part manufactured by fused filament fabrication," *Additive Manufacturing*, vol. 25, pp. 196-203, 1 2019.

[145] H. Chokshi, D. B. Shah, K. M. Patel and S. J. Joshi, "Experimental investigations of process parameters on mechanical properties for PLA during processing in FDM," *Advances in Materials and Processing Technologies*, vol. 8, no. sup2, pp. 696-709, 2022.

[146] E. U. Enemuoh, S. Duginski, C. Feyen and V. G. Menta, "Effect of process parameters on energy consumption, physical, and mechanical properties of fused deposition modeling," *Polymers*, vol. 13, no. 15, 8 2021.

[147] H. K. Dave, A. R. Prajapati, S. R. Rajpurohit, N. H. Patadiya and H. K. Raval, "Investigation on tensile strength and failure modes of FDM printed part using in-house fabricated PLA filament," *Advances in Materials and Processing Technologies,* vol. 8, no. 1, pp. 576-597, 1 2022.

[148] V. Vendittoli, W. Polini and M. S. J. Walter, "An overall performance index to quantify dimensional accuracy and mechanical strength of parts manufactured through VAT photopolymerization in biodegradable and non-biodegradable resin," *The International Journal of Advanced Manufacturing Technology,* vol. 128, no. 11-12, pp. 5491-5502, 10 2023.

[149] "UltiMaker S3," [Online]. Available: https://ultimaker.com/3d-printers/s-series/ultimaker-s3/.

[150] "Catalogue of Taguchi designs - Minitab," [Online]. Available: https://support.minitab.com/en-us/minitab/help-and-how-to/statistical-modeling/doe/supporting-topics/taguchi-designs/catalogue-of-taguchi-designs/.

[151] "BASF Ultrafuse PLA 750 gr," [Online]. Available: https://www.crea3d.com/en/basf/486-314-basf-ultrafuse-pla-750-gr.html.

[152] "Data Analysis Software | Statistical Software Package | Minitab," [Online]. Available: https://www.minitab.com/en-us/products/minitab/.

[153] A. Pandzic, D. Hodzic and A. Milovanovic, "Effect of infill type and density on tensile properties of PLA material for FDM process," *30TH DAAAM INTERNATIONAL SYMPOSIUM ON INTELLIGENT MANUFACTURING AND AUTOMATION,* pp. 545-0554, 2019.

[154] T. J. Suteja and A. Soesanti, "Mechanical Properties of 3D Printed Polylactic Acid Product for Various Infill Design Parameters: A Review," *Journal of Physics: Conference Series,* vol. 1569, no. 4, p. 042010, 7 2020.

[155] J. C. Camargo, Á. R. Machado, E. C. Almeida and E. F. M. S. Silva, "Mechanical properties of PLA-graphene filament for FDM 3D printing," *The International Journal of Advanced Manufacturing Technology,* vol. 103, no. 5-8, pp. 2423-2443, 8 2019.

[156] G. Moroni, S. Petrò and W. Polini, "Geometrical product specification and verification in additive manufacturing," *CIRP Annals,* vol. 66, no. 1, pp. 157-160, 2017.

[157] Z. Zhu, N. Anwer, Q. Huang and L. Mathieu, "Machine learning in tolerancing for additive manufacturing," *CIRP Annals,* vol. 67, no. 1, pp. 157-160, 2018.

[158] V. Vendittoli, W. Polini and M. S. Walter, "A numerical approach to introduce and validate a database to foresee dimensional deviations of ABS parts printed through material extrusion," 2024.

[159] "Keyence IM-7000 Series," [Online]. Available: https://www.atecorp.com/atecorp/media/pdfs/data-sheets/keyence-im-7000-datasheet_1.pdf?ext=.pdf.

[160] "W20," [Online]. Available: https://wms2.vistainstrument.com/index.php/he-roughness/w20.

[161] "ISO 16610-21:2011(en), Geometrical product specifications (GPS) — Filtration — Part 21: Linear profile filters: Gaussian filters," [Online]. Available: https://www.iso.org/obp/ui/#iso:std:iso:16610:-21:ed-1:v1:en.

[162] "MATLAB," [Online]. Available: https://www.mathworks.com/products/matlab.html.

[163] R. M. Neal, "Bayesian Learning for Neural Networks," vol. 118, 1996.

[164] P. C. Bürkner, J. Gabry and A. Vehtari, "Efficient leave-one-out cross-validation for Bayesian non-factorized normal and Student-t models," *Computational Statistics,* vol. 36, no. 2, pp. 1243-1261, 6 2021.

[165] D. Chicco, M. J. Warrens and G. Jurman, "The coefficient of determination R-squared is more informative than SMAPE, MAE, MAPE, MSE and RMSE in regression analysis evaluation," *PeerJ Computer Science,* vol. 7, pp. 1-24, 7 2021.

[166] Y. Yang and S. Huang, "Suitability of five cross validation methods for performance evaluation of nonlinear mixed-effects forest models - a case study," *Forestry,* vol. 87, no. 5, pp. 654-662, 12 2014.

[167] D. M. D'Addona, S. J. Raykar, D. Singh and D. Kramar, "Multi Objective Optimization of Fused Deposition Modeling Process Parameters with Desirability Function," *Procedia CIRP,* vol. 99, pp. 707-710, 2021.

[168] A. Jaisingh Sheoran and H. Kumar, "Fused Deposition modeling process parameters optimization and effect on mechanical properties and part

quality: Review and reflection on present research," *Materials Today: Proceedings,* vol. 21, pp. 1659-1672, 1 2020.

[169] S. R. Rajpurohit and H. K. Dave, "Effect of process parameters on tensile strength of FDM printed PLA part," *Rapid Prototyping Journal,* vol. 24, no. 8, pp. 1317-1324, 11 2018.

[170] L. P. T. Huynh, H. A. Nguyen, H. Q. Nguyen, L. K. H. Phan and T. T. Tran, "Effect of Process Parameters on Mechanical Strength of Fabricated Parts using the Fused Deposition Modelling Method," *Journal of the Korean Society for Precision Engineering,* vol. 36, no. 8, pp. 705-712, 8 2019.

[171] N. Alqahtani, S. Alam, I. Aqeel, M. Shuaib, I. Mohsen Khormi, S. B. Khan and A. A. Malibari, "Deep Belief Networks (DBN) with IoT-Based Alzheimer's Disease Detection and Classification," *Applied Sciences (Switzerland),* vol. 13, no. 13, 7 2023.

[172] J. Naskath, G. Sivakamasundari and A. A. S. Begum, "A Study on Different Deep Learning Algorithms Used in Deep Neural Nets: MLP SOM and DBN," *Wireless Personal Communications,* vol. 128, no. 4, pp. 2913-2936, 2 2023.

[173] A. Sheeba, S. N. Bushra, S. Rajarajeswari and C. A. Subasini, "An efficient starling murmuration-based secure web service model for smart city application using DBN," *Artificial Intelligence Review,* vol. 57, no. 3, 3 2024.

[174] D. Guo, Z. Song, N. Liu, T. Xu, X. Wang, Y. Zhang, W. Su and Y. Cheng, "Performance Study of Hard Rock Cantilever Roadheader Based on PCA and DBN," *Rock Mechanics and Rock Engineering,* vol. 57, no. 4, pp. 2605-2623, 4 2024.

[175] M. U. Rehman, I. F. Nizami, M. Majid, F. Ullah, I. Hussain and K. T. Chong, "CN-BSRIQA: Cascaded network - blind super-resolution image quality assessment," *Alexandria Engineering Journal,* vol. 91, pp. 580-591, 3 2024.

[176] J. Lampinen and A. Vehtari, "Bayesian approach for neural networksÐreview and case studies," *Neural Networks,* vol. 14, no. 3, pp. 257-274, 2001.

[177] K. V. Yuen, "Recent developments of Bayesian model class selection and applications in civil engineering," *Structural Safety,* vol. 32, no. 5, pp. 338-346, 2010.

[178] E. Horvitz and D. Mulligan, "Data, privacy, and the greater good," *Science,* vol. 349, no. 6245, pp. 253-255, 7 2015.

[179] J. Ma, F. C. Stingo and B. P. Hobbs, "Bayesian personalized treatment selection strategies that integrate predictive with prognostic determinants," *Biometrical Journal,* vol. 61, no. 4, pp. 902-917, 7 2019.

[180] S. Mekid, T. Schlegel, N. Aspragathos and R. Teti, "Foresight formulation in innovative production, automation and control systems," *Foresight,* vol. 9, no. 5, pp. 35-47, 2007.

[181] S. S. Razvi, S. Feng, A. Narayanan, Y. T. T. Lee and P. Witherell, "A Review of Machine Learning Applications in Additive Manufacturing," *Proceedings of the ASME Design Engineering Technical Conference,* vol. 1, 11 2019.

[182] V. H. Nguyen, T. N. Huynh, T. P. Nguyen and T. T. Tran, "Single and multi-objective optimisation of processing parameters for fused deposition modelling in 3D printing technology," *International Journal of Automotive and Mechanical Engineering,* vol. 17, no. 1, pp. 7542-7551, 1 2020.

[183] K. Manoharan, K. Chockalingam and S. S. Ram, "Prediction of tensile strength in fused deposition modeling process using artificial neural network technique," *AIP Conference Proceedings,* vol. 2311, 12 2020.

[184] L. Carrino, G. Giorleo, W. Polini and U. Prisco, "Dimensional errors in longitudinal turning based on the unified generalized mechanics of cutting approach.: Part II: Machining process analysis and dimensional error estimate," *International Journal of Machine Tools and Manufacture,* vol. 42, no. 14, pp. 1517-1525, 11 2002.

[185] A. Dey and N. Yodo, "A Systematic Survey of FDM Process Parameter Optimization and Their Influence on Part Characteristics," *Journal of Manufacturing and Materials Processing 2019, Vol. 3, Page 64,* vol. 3, no. 3, p. 64, 7 2019.

[186] A. Corrado and W. Polini, "Assembly design in aeronautic field: From assembly jigs to tolerance analysis," *https://doi.org/10.1177/0954405416635033,* vol. 231, no. 14, pp. 2652-2663, 3 2016.

[187] M. F. Afrose, S. H. Masood, M. Nikzad and P. Iovenitti, "Effects of Build Orientations on Tensile Properties of PLA Material Processed by FDM," *Advanced Materials Research,* Vols. 1044-1045, pp. 31-34, 2014.

[188] J. Will and T. Most, "Metamodell of optimized Prognosis (MoP) -an Automatic Approach for User Friendly Parameter Optimization," 2009.

[189] D. J. C. MacKay, "Bayesian Interpolation," *Neural Computation,* vol. 4, no. 3, pp. 415-447, 5 1992.

[190] J. Heaton, "Ian Goodfellow, Yoshua Bengio, and Aaron Courville: Deep learning," *Genetic Programming and Evolvable Machines 2017 19:1,* vol. 19, no. 1, pp. 305-307, 10 2017.

[191] J. D. Olden, M. K. Joy and R. G. Death, "An accurate comparison of methods for quantifying variable importance in artificial neural networks using simulated data," *Ecological Modelling,* vol. 178, no. 3-4, pp. 389-397, 11 2004.

[192] J. D. Olden and D. A. Jackson, "Illuminating the "black box": a randomization approach for understanding variable contributions in artificial neural networks," *Ecological Modelling,* vol. 154, no. 1-2, pp. 135-150, 8 2002.

[193] D. Wu, Y. Wei and J. Terpenny, "Predictive modelling of surface roughness in fused deposition modelling using data fusion," *International Journal of Production Research,* vol. 57, no. 12, pp. 3992-4006, 6 2019.

[194] H. Elhoone, T. Zhang, M. Anwar and S. Desai, "Cyber-based design for additive manufacturing using artificial neural networks for Industry 4.0," *International Journal of Production Research,* vol. 58, no. 9, pp. 2841-2861, 5 2020.

[195] D. Ramón-Lumbierres, F. J. Heredia Cervera, J. Minguella-Canela and A. Muguruza-Blanco, "Optimal postponement in supply chain network design under uncertainty: an application for additive manufacturing," *International Journal of Production Research,* vol. 59, no. 17, pp. 5198-5215, 9 2021.

[196] L.-W. Wong, G. W.-H. Tan, K.-B. Ooi, B. Lin and Y. K. Dwivedi, "Artificial intelligence-driven risk management for enhancing supply chain agility:

A deep-learning-based dual-stage PLS-SEM-ANN analysis," *International Journal of Production Research,* vol. 62, no. 15, pp. 5535-5555, 8 2024.

[197] G. Strano, L. Hao, R. M. Everson and K. E. Evans, "Surface roughness analysis, modelling and prediction in selective laser melting," *Journal of Materials Processing Technology,* vol. 213, no. 4, pp. 589-597, 4 2013.

[198] L. Galantucci, F. Lavecchia and G. Percoco, "Experimental study aiming to enhance the surface finish of fused deposition modeled parts," *CIRP Annals,* vol. 58, no. 1, pp. 189-192, 2009.

[199] T. Feng, L. Sun, A. S. Sohal and D. Wang, "External involvement and firm performance: is time-to-market of new products a missing link?," *International Journal of Production Research,* vol. 52, no. 3, pp. 727-742, 2 2014.

[200] P. K. Rao, J. (. Liu, D. Roberson, Z. (. Kong and C. Williams, "Online Real-Time Quality Monitoring in Additive Manufacturing Processes Using Heterogeneous Sensors," *Journal of Manufacturing Science and Engineering,* vol. 137, no. 6, 12 2015.

[201] D. Patel, C. K. Sahu and R. Rai, "Security in modern manufacturing systems: integrating blockchain in artificial intelligence-assisted manufacturing," *International Journal of Production Research,* vol. 62, no. 3, pp. 1041-1071, 2 2024.

[202] X. Zhao and D. W. Rosen, "A data mining approach in real-time measurement for polymer additive manufacturing process with exposure controlled projection lithography," *Journal of Manufacturing Systems,* vol. 43, pp. 271-286, 4 2017.

[203] M. Abdulrazaq, M. AL-Khafaji and A. Kadauw, "Mechanical Strength Optimization for the Polylactic Acid Printed Parts in Material Extrusion Process Using Artificial Neural Network," *Engineering and Technology Journal,* vol. 0, no. 0, pp. 1-13, 12 2023.

[204] I. Buj-Corral and E. E. Zayas-Figueras, "Comparative study about dimensional accuracy and form errors of FFF printed spur gears using PLA and Nylon," *Polymer Testing,* vol. 117, p. 107862, 1 2023.

[205] M. Seyedzavvar, "A hybrid ANN/PSO optimization of material composition and process parameters for enhancement of mechanical

characteristics of 3D-printed sample," *Rapid Prototyping Journal,* vol. 29, no. 6, pp. 1270-1288, 6 2023.

[206] J. D. Kechagias, N. Vidakis, M. Petousis and N. Mountakis, "A multi-parametric process evaluation of the mechanical response of PLA in FFF 3D printing," *Materials and Manufacturing Processes,* vol. 38, no. 8, pp. 941-953, 6 2023.

[207] R. Teharia, R. M. Singari and H. Kumar, "Optimization of process variables for additive manufactured PLA based tensile specimen using taguchi design and artificial neural network (ANN) technique," *Materials Today: Proceedings,* vol. 56, pp. 3426-3432, 2022.

[208] V. S. Jatti, S. Tamboli, S. Shaikh, N. S. Solke, V. Gulia, V. S. Jatti, N. K. Khedkar, S. Salunkhe, M. Pagáč and E. S. Abouel Nasr, "Optimization of tensile strength in 3D printed PLA parts via meta-heuristic approaches: a comparative study," *Frontiers in Materials,* vol. 10, 1 2024.

[209] J. Bräunig, T. Töppel, B. Müller, M. Burkhardt, T. Hipke and W.-G. Drossel, "Advanced Material Studies for Additive Manufacturing in terms of Future Gear Application," *Advances in Mechanical Engineering,* vol. 6, p. 741083, 1 2014.

[210] R. Ramadani, S. Pal, M. Kegl, J. Predan, I. Drstvenšek, S. Pehan and A. Belšak, "Topology optimization and additive manufacturing in producing lightweight and low vibration gear body," *The International Journal of Advanced Manufacturing Technology,* vol. 113, no. 11-12, pp. 3389-3399, 4 2021.

[211] G. Cybenko, "Approximation by superpositions of a sigmoidal function," *Mathematics of Control, Signals, and Systems,* vol. 2, no. 4, pp. 303-314, 12 1989.

[212] K. Hornik, M. Stinchcombe and H. White, "Multilayer feedforward networks are universal approximators," *Neural Networks,* vol. 2, no. 5, pp. 359-366, 1 1989.

[213] V. Vendittoli, W. Polini, M. S. J. Walter and S. Geißelsöder, "Using Bayesian Regularized Artificial Neural Networks to Predict the Tensile Strength of Additively Manufactured Polylactic Acid Parts," *Applied Sciences,* vol. 14, no. 8, p. 3184, 4 2024.

[214] N. V. Findler, C. Lo and R. Lo, "Pattern search for optimization," *Mathematics and Computers in Simulation,* vol. 29, no. 1, pp. 41-50, 2 1987.

[215] V. Torczon, "On the Convergence of Pattern Search Algorithms," *SIAM Journal on Optimization,* vol. 7, no. 1, pp. 1-25, 2 1997.

[216] K.-E. Aslani, K. Kitsakis, J. D. Kechagias, N. M. Vaxevanidis and D. E. Manolakos, "On the application of grey Taguchi method for benchmarking the dimensional accuracy of the PLA fused filament fabrication process," *SN Applied Sciences,* vol. 2, no. 6, p. 1016, 6 2020.

[217] K. Ninikas, J. Kechagias, N. A. Fountas and N. M. Vaxevanidis, "A study of Fused Filament Fabrication process efficiency: ABS vs PLA materials," *IOP Conference Series: Materials Science and Engineering,* vol. 1235, no. 1, p. 012007, 3 2022.

[218] K. Fayazbakhsh, M. Movahedi and J. Kalman, "The impact of defects on tensile properties of 3D printed parts manufactured by fused filament fabrication," *Materials Today Communications,* vol. 18, pp. 140-148, 3 2019.

[219] S. R. Rajpurohit and H. K. Dave, "Flexural strength of fused filament fabricated (FFF) PLA parts on an open-source 3D printer," *Advances in Manufacturing,* vol. 6, no. 4, pp. 430-441, 12 2018.

[220] J. A. Afonso, J. L. Alves, G. Caldas, B. P. Gouveia, L. Santana and J. Belinha, "Influence of 3D printing process parameters on the mechanical properties and mass of PLA parts and predictive models," *Rapid Prototyping Journal,* vol. 27, no. 3, pp. 487-495, 4 2021.

[221] A. Pulipaka, K. M. Gide, A. Beheshti and Z. S. Bagheri, "Effect of 3D printing process parameters on surface and mechanical properties of FFF-printed PEEK," *Journal of Manufacturing Processes,* vol. 85, pp. 368-386, 1 2023.

[222] H. Gonabadi, A. Yadav and S. J. Bull, "The effect of processing parameters on the mechanical characteristics of PLA produced by a 3D FFF printer," *The International Journal of Advanced Manufacturing Technology,* vol. 111, no. 3-4, pp. 695-709, 11 2020.

[223] R. H. Myers, D. C. Montgomery, G. G. Vining, C. M. Borror and S. M. Kowalski, "Response Surface Methodology: A Retrospective and

Literature Survey," *Journal of Quality Technology,* vol. 36, no. 1, pp. 53-77, 1 2004.

[224] A. I. Khuri and S. Mukhopadhyay, "Response surface methodology," *WIREs Computational Statistics,* vol. 2, no. 2, pp. 128-149, 3 2010.

[225] N. Fountas, J. Kechagias and N. Vaxevanidis, "Statistical Modeling and Optimization of Surface Roughness for PLA and PLA/Wood FDM Fabricated Items," *Journal of Materials and Engineering,* vol. 1, no. 1, pp. 38-44, 2023.

[226] G. Gao, F. Xu and J. Xu, "Parametric Optimization of FDM Process for Improving Mechanical Strengths Using Taguchi Method and Response Surface Method: A Comparative Investigation," *Machines,* vol. 10, no. 9, p. 750, 8 2022.

[227] H. Afshari, F. Taher, S. A. Alavi, M. Afshari, M. R. Samadi and F. Allahyari, "Studying the effects of FDM process parameters on the mechanical properties of parts produced from PLA using response surface methodology," *Colloid and Polymer Science,* vol. 302, no. 6, pp. 955-970, 6 2024.

[228] M. S. Meiabadi, M. Moradi, M. Karamimoghadam, S. Ardabili, M. Bodaghi, M. Shokri and A. H. Mosavi, "Modeling the Producibility of 3D Printing in Polylactic Acid Using Artificial Neural Networks and Fused Filament Fabrication," *Polymers,* vol. 13, no. 19, p. 3219, 9 2021.

[229] J. Grubbs, B. C. Sousa and D. L. Cote, "Establishing a Framework for Fused Filament Fabrication Process Optimization: A Case Study with PLA Filaments," *Polymers,* vol. 15, no. 8, p. 1945, 4 2023.

[230] M. A. Attolico, C. Casavola, A. Cazzato, V. Moramarco and G. Renna, "Effect of extrusion temperature on fused filament fabrication parts orthotropic behaviour," *Rapid Prototyping Journal,* vol. 26, no. 4, pp. 639-647, 12 2019.

[231] L.-A. Chicos, M. A. Pop, S.-M. Zaharia, C. Lancea, G. R. Buican, I. S. Pascariu and V.-M. Stamate, "Infill Density Influence on Mechanical and Thermal Properties of Short Carbon Fiber-Reinforced Polyamide Composites Manufactured by FFF Process," *Materials,* vol. 15, no. 10, p. 3706, 5 2022.

[232] "MTS Criterion® Electromechanical Test Systems," [Online]. Available: https://www.mts.com/en/products/materials/static-materials-test-systems/criterion-electromechanical.

[233] E. Hazir and T. Ozcan, "Response Surface Methodology Integrated with Desirability Function and Genetic Algorithm Approach for the Optimization of CNC Machining Parameters," *Arabian Journal for Science and Engineering,* vol. 44, no. 3, pp. 2795-2809, 3 2019.

[234] B. Akteke-Öztürk, G. W. Weber and G. Köksal, "Desirability Functions in Multiresponse Optimization," *Communications in Computer and Information Science,* vol. 499, pp. 129-146, 2015.

[235] G. Derringer and R. Suich, "Simultaneous Optimization of Several Response Variables," *Journal of Quality Technology,* vol. 12, no. 4, pp. 214-219, 10 1980.

[236] D. Popescu, A. Zapciu, C. Amza, F. Baciu and R. Marinescu, "FDM process parameters influence over the mechanical properties of polymer specimens: A review," *Polymer Testing,* vol. 69, pp. 157-166, 8 2018.

[237] Z. Lianghua, "Research on the Influence of 3D Printing Speed of External Special-Shaped Parts," *Journal of Physics: Conference Series,* vol. 1986, no. 1, p. 012008, 8 2021.

[238] S. Vyavahare, S. Kumar and D. Panghal, "Experimental study of surface roughness, dimensional accuracy and time of fabrication of parts produced by fused deposition modelling," *Rapid Prototyping Journal,* vol. 26, no. 9, pp. 1535-1554, 7 2020.

[239] J. R. C. Dizon, A. H. Espera, Q. Chen and R. C. Advincula, "Mechanical characterization of 3D-printed polymers," *Additive Manufacturing,* vol. 20, pp. 44-67, 3 2018.

[240] S. H. Masood, "Advances in Fused Deposition Modeling," *Comprehensive Materials Processing: Thirteen Volume Set,* vol. 10, pp. 69-91, 1 2014.

[241] Huu Nghi Huynh, Anh Tuan Nguyen, Ngoc Luan Ha and Thi Thu Ha Thai, "Application of fuzzy Taguchi method to improve the dimensional accuracy of Fused Deposition Modeling processed product," *2017 International Conference on System Science and Engineering (ICSSE),* pp. 107-112, 7 2017.

[242] S. K. Padhi, R. K. Sahu, S. S. Mahapatra, H. C. Das, A. K. Sood, B. Patro and A. K. Mondal, "Optimization of fused deposition modeling process parameters using a fuzzy inference system coupled with Taguchi philosophy," *Advances in Manufacturing,* vol. 5, no. 3, pp. 231-242, 9 2017.

[243] A. Peng, X. Xiao and R. Yue, "Process parameter optimization for fused deposition modeling using response surface methodology combined with fuzzy inference system," *The International Journal of Advanced Manufacturing Technology,* vol. 73, no. 1-4, pp. 87-100, 7 2014.

[244] C.-J. Yang and S.-S. Wu, "Sustainable Manufacturing Decisions through the Optimization of Printing Parameters in 3D Printing," *Applied Sciences,* vol. 12, no. 19, p. 10060, 10 2022.

[245] H. Sukanto, D. F. Smaradhana, J. Triyono and P. Wicaksono, "Investigating the Effect of Layer Thickness on the Product Quality of PLA Manufactured by 3D Printing Technique," *Lecture Notes in Mechanical Engineering,* pp. 811-818, 2020.

[246] S. Wang, Y. Ma, Z. Deng, S. Zhang and J. Cai, "Effects of fused deposition modeling process parameters on tensile, dynamic mechanical properties of 3D printed polylactic acid materials," *Polymer Testing,* vol. 86, p. 106483, 6 2020.

[247] S. Khan, K. Joshi and S. Deshmukh, "A comprehensive review on effect of printing parameters on mechanical properties of FDM printed parts," *Materials Today: Proceedings,* vol. 50, pp. 2119-2127, 2022.

[248] S. Cahyati and Y. A. Furqon, "THE LAYER HEIGHT VARIATIONS EFFECT ON TENSILE STRENGTH OF 3D PRINTING PRODUCT PLA MATERIAL BASED," *Jurnal Rekayasa Mesin,* vol. 13, no. 3, pp. 647-657, 12 2022.

[249] T. D. Harpool, I. M. Alarifi, B. A. Alshammari, A. Aabid, M. Baig, R. A. Malik, A. Mohamed Sayed, R. Asmatulu and T. M. A. A. EL-Bagory, "Evaluation of the Infill Design on the Tensile Response of 3D Printed Polylactic Acid Polymer," *Materials,* vol. 14, no. 9, p. 2195, 4 2021.

[250] C. Baechler, M. Devuono and J. M. Pearce, "Distributed recycling of waste polymer into RepRap feedstock," *Rapid Prototyping Journal,* vol. 19, no. 2, pp. 118-125, 2013.

[251] D. Drummer, K. Wudy and M. Drexler, "Influence of energy input on degradation behavior of plastic components manufactured by selective laser melting," *Physics Procedia,* vol. 56, no. C, pp. 176-183, 2014.

[252] "Additive Manufacturing Market Size Report, 2030," [Online]. Available: https://www.grandviewresearch.com/industry-analysis/additive-manufacturing-market.

[253] P. Parandoush and D. Lin, "A review on additive manufacturing of polymer-fiber composites," *Composite Structures,* vol. 182, pp. 36-53, 12 2017.

[254] "SLS powder recycling solution for 3D printing | Engineer Live," [Online]. Available: https://www.engineerlive.com/content/sls-powder-recycling-solution-3d-printing.

[255] M. Galetto, E. Verna and G. Genta, "Effect of process parameters on parts quality and process efficiency of fused deposition modeling," *Computers and Industrial Engineering,* vol. 156, 6 2021.

[256] F. Ciccone, A. Bacciaglia and A. Ceruti, "Optimization with artificial intelligence in additive manufacturing: a systematic review," *Journal of the Brazilian Society of Mechanical Sciences and Engineering,* vol. 45, no. 6, pp. 1-22, 6 2023.

[257] G. Soundarapandiyan, C. Johnston, R. H. Khan, B. Chen and M. E. Fitzpatrick, "A technical review of the challenges of powder recycling in the laser powder bed fusion additive manufacturing process," *The Journal of Engineering,* vol. 2021, no. 2, pp. 97-103, 2 2021.

[258] A. Awad, F. Fina, A. Goyanes, S. Gaisford and A. W. Basit, "3D printing: Principles and pharmaceutical applications of selective laser sintering," 8 2020. [Online]. Available: https://pubmed.ncbi.nlm.nih.gov/32622811/.

[259] C. Yan, Y. Shi and L. Hao, "Investigation into the differences in the selective laser sintering between amorphous and semi-crystalline polymers," 9 2011. [Online]. Available: https://www.degruyter.com/document/doi/10.3139/217.2452/html?lang=en.

[260] V. Vendittoli, W. Polini, M. S. Walter and J. P. Stacheder, "A novel approach on artificial aging of nylon 12 powder for laser powder bed fusion," *Rapid Prototyping Journal,* 8 2024.

[261] S. Weinmann and C. Bonten, "Recycling of pa12 powder for selective laser sintering," *AIP Conference Proceedings,* vol. 2289, 11 2020.

[262] N. Hesse, A. Jaksch, J. Kaschta, D. Groh, D. Drummer, W. Peukert and J. Schmidt, "From trash to treasure in additive manufacturing: Recycling of polymer powders by acid catalyzed hydrolysis," 6 2023. [Online].

[263] Y. Yamauchi, T. Niino and T. Kigure, "Influence of process time and geometry on part quality of low temperature laser sintering," 2017. [Online].

[264] S. Schlicht, S. Greiner and D. Drummer, "Low Temperature Powder Bed Fusion of Polymers by Means of Fractal Quasi-Simultaneous Exposure Strategies," 3 2022. [Online]. Available: https://www.mdpi.com/2073-4360/14/7/1428/htm.

[265] D. Menge and H.-J. Schmid, "Low Temperature Laser Sintering with PA12 and PA6 on a Standard System," *Macromolecurar Symposia,* 2022.

[266] F. M. Mwania, M. Maringa and K. van der Walt, "Mixing and reuse of polymer laser sintering powders to ensure homogeneity - A review," 2020. [Online].

[267] O. A. Alo, I. O. Otunniyi and D. Mauchline, "Correlation of reuse extent with degradation degree of PA 12 powder during laser powder bed fusion and mechanical behavior of sintered parts," *Polymer Engineering and Science,* vol. 63, no. 1, pp. 126-138, 1 2023.

[268] "PA12 Smooth," [Online]. Available: https://sinterit.com/wp-content/uploads/2022/06/PA12-Smooth-EN.pdf.

[269] "Sinterit Lisa," [Online]. Available: https://sinterit.com/3dprinters/lisa/.

[270] "Powder sieve – Sinterit – Manufacturer of compact and industrial SLS 3D printers," [Online]. Available: https://sinterit.com/peripherals/powder-sieve/.

[271] "ISO 11357-1:2023 - Plastics — Differential scanning calorimetry (DSC) — Part 1: General principles," [Online]. Available: https://www.iso.org/standard/83904.html.

[272] "Mastersizer 2000 | Software Downloads | Manuals | Product support | Malvern Panalytical," [Online]. Available: https://www.malvernpanalytical.com/en/support/product-support/mastersizer-range/mastersizer-2000.

[273] "ISO 13320:2020 - Particle size analysis — Laser diffraction methods," [Online]. Available: https://www.iso.org/standard/69111.html.

[274] "ISO 60:2023 - Plastics — Determination of apparent density of material that can be poured from a specified funnel," [Online]. Available: https://www.iso.org/standard/85747.html.

[275] "DIN 66137-2 - 2019-03," [Online]. Available: https://www.dinmedia.de/en/standard/din-66137-2/300301091.

[276] Y. Liu, L. Zhu, L. Zhou and Y. Li, "Microstructure and mechanical properties of reinforced polyamide 12 composites prepared by laser additive manufacturing," 8 2019. [Online].

[277] R. Dai, M. Huang, L. Ma, W. Liu, S. He, H. Liu, C. Zhu, Y. Wang, Z. Zhang and A. Sun, "Study on crystal structure and phase transitions of polyamide 12 via wide-angle X-ray diffraction with variable temperature," 12 2020. [Online].

[278] T. Kaur, J. Nussbaum, S. Lee, K. Rodriguez, N. B. Crane and J. Harmon, "Characterization of PA-12 specimens fabricated by projection sintering at various sintering parameters," 1 2021. [Online].

[279] C. Fosse, A. Bourdet, E. Ernault, A. Esposito, N. Delpouve, L. Delbreilh, S. Thiyagarajan, R. J. Knoop and E. Dargent, "Determination of the equilibrium enthalpy of melting of two-phase semi-crystalline polymers by fast scanning calorimetry," *Thermochimica Acta*, vol. 677, pp. 67-78, 7 2019.

[280] B. Sanders, E. Cant, H. Amel and M. Jenkins, "The Effect of Physical Aging and Degradation on the Re-Use of Polyamide 12 in Powder Bed Fusion," *Polymers*, vol. 14, no. 13, 7 2022.

[281] A. Wörz, K. Wudy, D. Drummer, A. Wegner and G. Witt, "Comparison of long-term properties of laser sintered and injection molded polyamide 12 parts," *Journal of Polymer Engineering,* vol. 38, no. 6, pp. 573-582, 7 2018.

[282] P. Chen, M. Tang, W. Zhu, L. Yang, S. Wen, C. Yan, Z. Ji, H. Nan and Y. Shi, "Systematical mechanism of Polyamide-12 aging and its micro-structural evolution during laser sintering," *Polymer Testing,* vol. 67, pp. 370-379, 5 2018.

[283] A. El Magri, S. E. Bencaid, H. R. Vanaei and S. Vaudreuil, "Effects of Laser Power and Hatch Orientation on Final Properties of PA12 Parts Produced by Selective Laser Sintering," *Polymers,* vol. 14, no. 17, 9 2022.

[284] K. Wudy, D. Drummer, F. Kühnlein and M. Drexler, "Influence of degradation behavior of polyamide 12 powders in laser sintering process on produced parts," *AIP Conference Proceedings,* vol. 1593, pp. 691-695, 2014.

[285] J. Schneider and S. Kumar, "Multiscale characterization and constitutive parameters identification of polyamide (PA12) processed via selective laser sintering," *Polymer Testing,* vol. 86, p. 106357, 6 2020.

[286] D. I. Bower, "An Introduction to Polymer Physics," 5 2002. [Online]. Available: https://www.cambridge.org/core/books/an-introduction-to-polymer-physics/6BF89DF60976AA6D39D05132B6375B55.

[287] F. Yang, A. Schnuerch and X. Chen, "Quantitative influences of successive reuse on thermal decomposition, molecular evolution, and elemental composition of polyamide 12 residues in selective laser sintering," *The International Journal of Advanced Manufacturing Technology,* vol. 115, no. 9-10, pp. 3121-3138, 8 2021.

[288] B. Yao, Z. Li and F. Zhu, "Effect of powder recycling on anisotropic tensile properties of selective laser sintered PA2200 polyamide," *European Polymer Journal,* vol. 141, 12 2020.

[289] P. Obst, M. Launhardt, D. Drummer, P. V. Osswald and T. A. Osswald, "Failure criterion for PA12 SLS additive manufactured parts," *Additive Manufacturing,* vol. 21, pp. 619-627, 5 2018.

[290] V. Vendittoli, M. C. Mascolo, W. Polini, L. Sorrentino, A. Sover and M. S. Walter, "Predictive Modeling of Mechanical Properties from Degraded Polyamide 12 Powder in Laser Powder Bed Fusion".

[291] J. P. Kruth, X. Wang, T. Laoui and L. Froyen, "Lasers and materials in selective laser sintering," *Assembly Automation,* vol. 23, no. 4, pp. 357-371, 2003.

[292] F. Lupone, E. Padovano, F. Casamento and C. Badini, "Process Phenomena and Material Properties in Selective Laser Sintering of Polymers: A Review," *Materials,* vol. 15, no. 1, p. 183, 12 2021.

[293] S. Lekurwale, T. Karanwad and S. Banerjee, "Selective laser sintering (SLS) of 3D printlets using a 3D printer comprised of IR/red-diode laser," *Annals of 3D Printed Medicine,* vol. 6, p. 100054, 6 2022.

[294] P. Avrampos and G. C. Vosniakos, "A review of powder deposition in additive manufacturing by powder bed fusion," *Journal of Manufacturing Processes,* vol. 74, pp. 332-352, 2 2022.

[295] C. Morano and L. Pagnotta, "Additive Manufactured Parts Produced Using Selective Laser Sintering Technology: Comparison between Porosity of Pure and Blended Polymers," *Polymers 2023, Vol. 15, Page 4446,* vol. 15, no. 22, p. 4446, 11 2023.

[296] S. E. Brika and V. Brailovski, "A Novel Apparatus for the Simulation of Powder Spreading Procedures in Powder-Bed-Based Additive Manufacturing Processes: Design, Calibration, and Case Study," *Journal of Manufacturing and Materials Processing,* vol. 7, no. 4, 8 2023.

[297] O. A. Alo, I. O. Otunniyi and D. Mauchline, "Aging due to successive reuse of polyamide 12 powder during laser sintering: extrinsic powder properties and quality of sintered parts," *MATEC Web of Conferences,* vol. 370, p. 03011, 2022.

[298] L. Wang, A. Kiziltas, D. F. Mielewski, E. C. Lee and D. J. Gardner, "Closed-Loop Recycling of Polyamide 12 Powder from Selective Laser Sintering into Sustainable Composites," 2018.

[299] D. Drummer, K. Wudy and M. Drexler, "Modelling of the aging behavior of polyamide 12 powder during laser melting proceb," *AIP Conference Proceedings,* vol. 1664, 5 2015.

[300] A. Martínez, A. Ibáñez, A. Sánchez and M. A. León, "Comparison of aged polyamide powders for selective laser sintering," *AIP Conference Proceedings,* vol. 1431, pp. 5-13, 2012.

[301] J. Benz and C. Bonten, "Temperature induced ageing of PA12 powder during selective laser sintering process," *AIP Conference Proceedings,* vol. 2055, no. 1, p. 140001, 1 2019.

[302] "Universal ovens UNB 100-500 UFB 400-500," [Online]. Available: https://www.memmert.com/index.php?eID=dumpFile&t=f&f=2758&token=604ae7ef54fb25ecbad5b4e96a2444a591d4338c.

[303] "Digital Microscope - VHX-7000 | KEYENCE America," [Online]. Available: https://www.keyence.com/products/microscope/digital-microscope/vhx-7000/models/vhx-7000/.

[304] "Dual objective zoom lens (20 x to 2000 x) - VH-ZST | KEYENCE International Belgium," [Online]. Available: https://www.keyence.eu/products/microscope/digital-microscope/vhx-7000/models/vh-zst/.

[305] Y. M. Akib, E. Marzbanrad, F. Ahmed and J. Li, "A Numerical Study on the Powder Flowability, Spreadability, Packing Fraction in Powder Bed Additive Manufacturing," *Proceedings of ASME 2022 17th International Manufacturing Science and Engineering Conference, MSEC 2022,* vol. 1, 9 2022.

[306] N. Ma, W. Liu, L. Ma, S. He, H. Liu, Z. Zhang, A. Sun, M. Huang and C. Zhu, "Crystal transition and thermal behavior of Nylon 12," *e-Polymers,* vol. 20, no. 1, pp. 346-352, 6 2020.

[307] N. Hiramatsu, K. Haraguchi and S. Hirakawa, "Study of Transformations among α, γ and γ' Forms in Nylon 12 by X-Ray and DSC," *The Japan Society of Applied Physics,* vol. 22, 1983.

[308] L. Li, M. H. Koch and W. H. De Jeu, "Crystalline Structure and Morphology in Nylon-12: A Small- and Wide-Angle X-ray Scattering Study," *Macromolecules,* vol. 36, no. 5, pp. 1626-1632, 3 2003.

[309] N. A. Fountas, I. Papantoniou, J. D. Kechagias, D. E. Manolakos and N. M. Vaxevanidis, "Modeling and optimization of flexural properties of FDM-processed PET-G specimens using RSM and GWO algorithm," *Engineering Failure Analysis,* vol. 138, p. 106340, 8 2022.

[310] A. C. Lopes, A. M. Sampaio and A. J. Pontes, "The influence of the energy density on dimensional, geometric, mechanical and morphological properties of SLS parts produced with single and multiple exposure types," *Progress in Additive Manufacturing*, vol. 7, no. 4, pp. 683-698, 8 2022.

[311] D. Choudhury, S. Ponneganti, P. Radhakrishnanand, U. S. Murty and S. Banerjee, "Selective laser sintering additive manufacturing of solid oral dosage form: Effect of laser power and hatch spacing on the physico-technical behaviour of sintered printlets," *Applied Materials Today*, vol. 35, p. 101943, 12 2023.

[312] P. Karmiris-Obratański, E. L. Papazoglou, N. E. Karkalos and A. P. Markopoulos, "Analysis on the Effect of Energy Density on Mechanical Properties of Selective Laser Sintering Processed Polyamide-12," *Lecture Notes in Mechanical Engineering*, pp. 407-414, 2024.

[313] T. F. Pereira, M. A. Silva, M. F. Oliveira, I. A. Maia, J. V. Silva, M. F. Costa and R. M. Thiré, "Effect of process parameters on the properties of selective laser sintered Poly(3-hydroxybutyrate) scaffolds for bone tissue engineering," *Virtual and Physical Prototyping*, vol. 7, no. 4, pp. 275-285, 12 2012.

[314] N. A. Fountas, J. D. Kechagias and N. M. Vaxevanidis, "Optimization of Selective Laser Sintering/Melting Operations by Using a Virus-Evolutionary Genetic Algorithm," *Machines 2023, Vol. 11, Page 95*, vol. 11, no. 1, p. 95, 1 2023.

[315] P. Karmiris-Obratański, E. L. Papazoglou, N. E. Karkalos and A. P. Markopoulos, "Volume energy density and laser power: key determinants in SLS-processed PA12 mechanical properties," *International Journal of Advanced Manufacturing Technology*, vol. 130, no. 5-6, pp. 2505-2522, 1 2024.

[316] A. Pilipović, P. Ilinčić, M. Tujmer and M. Rujnić Havstad, "Impact of Part Positioning along Chamber Z-Axis and Processing Parameters in Selective Laser Sintering on Polyamide Properties," *Applied Sciences 2024, Vol. 14, Page 976*, vol. 14, no. 3, p. 976, 1 2024.

[317] T. Czelusniak and F. L. Amorim, "Influence of energy density on selective laser sintering of carbon fiber-reinforced PA12," *International Journal of*

Advanced Manufacturing Technology, vol. 111, no. 7-8, pp. 2361-2376, 12 2020.

[318] F. Paolucci, M. van Mook, L. Govaert and G. Peters, "Influence of post-condensation on the crystallization kinetics of PA12: From virgin to reused powder," *Polymer,* vol. 175, pp. 161-170, 6 2019.

[319] S. Nasiri and M. R. Khosravani, "Applications of data-driven approaches in prediction of fatigue and fracture," *Materials Today Communications,* vol. 33, p. 104437, 12 2022.

[320] V. Vendittoli, "Dimensional and geometric deviations of parts in PA12 manufactured by selective laser sintering: numerical and experimental analyses," pp. 198-205, 10 2023.

[321] B. Sanders, E. Cant and M. Jenkins, "Re-use of polyamide-12 in powder bed fusion and its effect on process-relevant powder characteristics and final part properties," *Additive Manufacturing,* vol. 80, p. 103961, 1 2024.

[322] A. Wegner, C. Mielicki, T. Grimm, B. Gronhoff, G. Witt and J. Wortberg, "Determination of robust material qualities and processing conditions for laser sintering of polyamide 12," *Polymer Engineering & Science,* vol. 54, no. 7, pp. 1540-1554, 7 2014.

[323] F. M. Mwania, M. Maringa and J. G. Van Der Walt, "A review of the techniques used to characterize laser sintering of polymeric powders for use and re-use in additive manufacturing," *Manufacturing Review,* vol. 8, p. 14, 2021.

[324] M. Schmid, R. Kleijnen, M. Vetterli and K. Wegener, "Influence of the origin of polyamide 12 powder on the laser sintering process and laser sintered parts," *Applied Sciences (Switzerland),* vol. 7, no. 5, 2017.

[325] M. Wolf and D. Drummer, "Joining laser-sintered with injection-molded parts made of PA12 using infrared welding," *Polymer Engineering and Science,* vol. 61, no. 2, pp. 514-525, 2 2021.

[326] A. J. Cano, A. Salazar and J. Rodríguez, "Effect of temperature on the fracture behavior of polyamide 12 and glass-filled polyamide 12 processed by selective laser sintering," *Engineering Fracture Mechanics,* vol. 203, pp. 66-80, 11 2018.

[327] A. Salazar, A. J. Cano Aragón and J. Rodríguez, "Fatigue life assessment of polyamide 12 processed by selective laser sintering. Damage modelling according to fracture mechanics," *Rapid Prototyping Journal,* vol. 28, no. 5, pp. 814-823, 5 2022.

[328] M. Walter, M. Storch and S. Wartzack, "On uncertainties in simulations in engineering design: A statistical tolerance analysis application," *SIMULATION,* vol. 90, no. 5, pp. 547-559, 4 2014.

[329] G. Moroni, S. Petró and W. Polini, "Robust design of fixture configuration," *Procedia CIRP,* vol. 21, pp. 189-194, 2014.

[330] A. Corrado, W. Polini and G. Moroni, "Robust Design of a Fixture Configuration in the Presence of form Deviations," *Procedia CIRP,* vol. 43, pp. 35-40, 1 2016.

Appendix

The appendix includes three tables that provide detailed data related to the experiments conducted. The first table presents the combinations of FFF input parameters used in the tests.
The second table contains the raw output data concerning the internal and external features of the specimen, with multiple repetitions for each input combination. The third table provides the raw output data related to the mechanical properties and surface quality of the specimen, also with repetitions for each input combination. These tables summarize the key experimental parameters and results that support the findings discussed in the main body of the thesis.

In addition, there are key MATLAB code segments used during the experimental phase. It is included the fitness functions based on the DPI and the PI, which were used for optimization purposes. Furthermore, the PSA along with its option settings is also provided to demonstrate the optimization of the experimental results.

INPUT PARAMETERS							
Run	**Type of Infill**	**Infill in %**	**Print speed in mm/s**	**Layer height in mm**	**Fan speed in %**	**Bed Tempera-ture in °C**	**Extrusion Tempera-ture in °C**
1	1	20	40	0.1	50	50	210
2	1	45	50	0.1	65	60	220
3	1	70	60	0.2	80	50	220
4	1	100	80	0.2	100	60	210
5	2	20	50	0.2	50	60	210
6	2	45	40	0.2	65	50	220
7	2	70	80	0.1	80	60	220
8	2	100	60	0.1	100	50	210
9	3	20	60	0.1	100	60	220
10	3	45	80	0.1	80	50	210
11	3	70	40	0.2	65	60	210
12	3	100	50	0.2	50	50	220
13	4	20	80	0.2	65	50	220
14	4	45	60	0.2	50	60	210
15	4	70	50	0.1	100	50	210
16	4	100	40	0.1	80	60	220

Run	INTERNAL FEATURES in mm			EXTERNAL FEATURES in mm			
	Circle Diameter	Square Length	Square Width	Length	Neck	Width	Thickness
	11.370	9.640	9.693	115.084	6.209	19.110	3.41
	11.168	9.645	9.631	115.092	6.247	19.093	3.40
1	11.463	9.361	9.392	115.184	6.300	19.201	3.41
	11.266	9.569	9.537	115.143	6.277	19.111	3.42
	11.373	9.643	9.625	115.173	6.259	19.182	3.42
	11.378	9.373	9.428	115.292	6.370	19.350	3.44
	11.326	9.295	9.284	115.375	6.397	19.307	3.44
2	11.372	9.349	9.410	115.381	6.351	19.382	3.44
	11.269	9.284	9.315	115.369	6.331	19.298	3.42
	11.373	9.521	9.591	115.316	6.318	19.250	3.45
	11.467	9.371	9.391	115.147	6.362	19.241	3.49
	11.438	9.335	9.294	115.137	6.343	19.243	3.50
3	11.450	9.396	9.352	115.155	6.408	19.266	3.51
	11.423	9.306	9.258	115.156	6.338	19.101	3.52
	11.453	9.432	9.454	115.218	6.293	19.151	3.50
	11.687	9.773	9.850	115.023	6.221	19.118	3.49
	11.623	9.781	9.849	115.023	6.209	19.143	3.47
4	11.681	9.663	9.688	115.016	6.255	19.128	3.49
	11.751	9.746	9.854	115.002	6.352	19.409	3.48
	11.606	9.729	9.959	115.040	6.328	19.487	3.48
	11.717	9.801	9.944	114.990	6.019	19.095	3.50
	11.760	9.797	9.962	114.979	6.030	19.116	3.50
5	11.738	9.800	9.946	114.967	6.007	19.071	3.50
	11.776	9.767	9.989	114.966	6.022	19.210	3.50
	11.769	9.687	9.847	114.965	6.333	19.452	3.49
	11.327	9.134	9.267	115.367	6.241	19.223	3.73
	11.317	9.113	9.286	115.041	6.213	19.164	3.66
6	11.270	9.125	9.287	115.060	6.233	19.186	3.67
	11.270	9.084	9.249	115.068	6.249	19.235	3.70
	11.230	9.042	9.191	115.083	6.281	19.218	3.63
7	11.177	9.305	9.392	115.246	6.319	19.306	3.41

	11.085	9.203	9.26	115.209	6.332	19.273	3.43
	11.069	9.218	9.328	115.224	6.320	19.381	3.44
	11.026	9.154	9.244	115.209	6.331	19.345	3.44
	11.264	9.098	9.196	115.335	6.290	19.390	3.43
	11.743	9.634	9.787	115.155	6.185	19.268	3.45
	11.752	9.622	9.835	115.152	6.212	19.308	3.44
8	11.744	9.619	9.803	115.148	6.199	19.282	3.45
	11.715	9.392	9.63	115.154	6.412	19.515	3.43
	11.622	9.666	9.945	115.171	6.458	19.614	3.43
	11.630	9.525	9.62	115.023	6.120	19.204	3.48
	11.685	9.63	9.719	115.004	6.125	19.255	3.47
9	11.785	9.649	9.551	114.996	6.243	19.242	3.47
	11.742	9.605	9.789	114.984	6.208	19.377	3.46
	11.643	9.304	9.585	114.998	6.349	19.514	3.48
	11.535	9.445	9.519	115.364	6.298	19.324	3.44
	11.458	9.399	9.457	115.201	6.347	19.298	3.47
10	11.452	9.388	9.484	115.198	6.325	19.317	3.46
	11.390	9.357	9.412	115.196	6.342	19.292	3.46
	11.412	9.135	9.271	115.250	6.337	19.276	3.44
	11.064	9.443	9.473	115.245	6.301	19.341	3.58
	10.951	9.025	9.087	115.113	6.375	19.280	3.62
11	11.044	9.368	9.430	115.119	6.304	19.318	3.60
	10.893	9.056	9.090	115.171	6.313	19.280	3.62
	11.029	9.111	9.260	115.178	6.300	19.257	3.59
	11.573	9.414	9.548	115.019	6.165	19.266	3.60
	11.480	9.588	9.748	115.011	6.125	19.225	3.61
12	11.582	9.388	9.533	115.032	6.165	19.296	3.59
	11.593	9.635	9.790	115.009	6.137	19.372	3.54
	11.585	9.449	9.687	115.022	6.300	19.562	3.50
	11.763	9.499	9.667	115.085	6.110	19.194	3.38
	11.787	9.549	9.724	115.022	6.104	19.181	3.40
13	11.757	9.541	9.702	115.048	6.086	19.201	3.39
	11.656	9.775	9.969	115.117	6.264	19.586	3.37
	11.704	9.521	9.706	115.074	6.298	19.487	3.39
14	11.639	9.486	9.567	115.124	6.206	19.179	3.53

	11.559	9.447	9.493	115.094	6.177	19.108	3.54
	11.580	9.413	9.511	115.027	6.207	19.180	3.53
	11.506	9.357	9.410	115.021	6.210	19.104	3.56
	11.477	9.734	9.746	115.005	6.125	19.052	3.51
	11.421	9.425	9.507	115.201	6.325	19.346	3.38
	11.353	9.359	9.409	115.191	6.285	19.257	3.40
15	11.380	9.357	9.443	115.172	6.318	19.312	3.39
	11.336	9.314	9.366	115.168	6.305	19.278	3.40
	11.408	9.655	9.730	115.145	6.241	19.180	3.40
	11.305	9.395	9.422	115.360	6.400	19.445	3.60
	11.284	9.324	9.387	115.315	6.364	19.316	3.60
16	11.262	9.341	9.387	115.190	6.375	19.377	3.59
	11.205	9.249	9.318	115.192	6.437	19.345	3.59
	11.319	9.033	9.183	115.193	6.295	19.223	3.58

	MECHANICAL PERFOR-MANCE in MPa	MICRO-GEOMETRY in μm		
Run	UTS	Ra SQUARE	Ra CENTRAL PART	Ra CIRCLE
	48.587	0.739	4.043	2.124
	45.344	1.973	2.498	1.633
1	46.083	0.722	2.704	1.941
	44.257	1.880	3.669	2.218
	44.724	1.929	4.516	2.340
	42.557	1.077	13.334	3.612
	43.289	1.455	9.233	5.070
2	41.629	1.099	11.668	3.640
	41.534	1.124	10.823	3.299
	40.105	0.912	6.116	2.875
	52.316	2.909	8.608	3.778
	52.207	2.482	14.339	3.657
3	54.380	3.061	11.285	3.539
	52.358	2.648	15.439	3.466
	52.416	3.493	10.970	3.740
	53.670	8.610	10.770	7.617
	53.783	6.752	8.856	7.860
4	53.248	7.559	5.914	7.857
	53.094	6.825	4.136	4.412
	51.772	14.894	11.850	6.446
	50.935	7.005	4.881	7.322
	50.799	6.699	2.795	7.393
5	50.435	6.962	2.841	7.257
	51.360	4.552	3.228	4.892
	47.556	9.254	8.618	5.439
	51.614	9.599	42.520	11.821
	51.673	9.063	39.416	7.864
6	52.539	8.953	34.672	10.562
	52.311	10.944	50.384	8.728
	51.956	7.797	33.664	7.893

	49.369	3.684	5.070	3.006
	48.717	3.295	5.069	3.155
7	48.994	3.460	5.214	2.993
	48.502	3.182	4.441	3.121
	48.463	3.256	4.328	3.378
	51.432	3.040	3.268	2.456
	51.113	3.245	2.507	2.744
8	49.815	3.588	2.440	3.113
	50.159	4.030	2.294	3.043
	50.446	5.918	3.234	3.176
	42.855	3.336	3.199	2.746
	42.932	2.870	3.330	2.112
9	43.452	3.133	4.542	2.244
	43.193	3.966	2.684	2.448
	42.543	4.033	4.065	2.655
	45.466	3.668	4.262	2.691
	46.199	3.505	4.427	2.804
10	45.395	3.832	4.327	2.869
	45.182	3.614	4.407	2.944
	45.370	3.654	3.643	2.974
	56.229	5.130	22.566	5.222
	56.043	4.385	29.780	4.918
11	56.233	5.393	19.247	5.631
	55.557	4.798	28.109	4.961
	55.400	5.245	34.885	5.061
	54.446	6.988	23.126	5.518
	54.647	5.809	23.978	5.116
12	54.952	6.737	23.133	5.391
	55.628	6.923	13.143	4.883
	55.597	7.966	12.527	4.553
	52.608	6.750	3.471	8.074
	51.985	6.369	5.494	7.287
13	52.400	6.340	3.930	7.708
	51.941	12.451	7.261	7.048
	50.868	9.478	6.225	6.362

	54.407	2.944	22.584	3.746
	54.105	2.595	22.074	3.329
14	54.145	2.957	22.407	3.938
	54.058	2.624	17.917	3.538
	54.170	3.378	14.890	3.549
	47.977	2.359	3.151	2.489
	47.945	2.398	2.959	2.520
15	46.767	2.256	2.646	2.417
	48.656	2.271	2.792	2.019
	47.598	2.548	2.985	2.426
	58.996	13.891	44.341	10.598
	58.608	10.494	42.022	11.358
16	58.465	8.344	42.677	10.643
	58.493	8.775	39.694	9.193
	58.674	8.633	38.500	10.208

FITNESS FUNCTION CODE USING DPI EQUATION

```
function fitness = fitnessFunction(optimizedInput)

 load my_workspace_15022024_212634.mat;
 predictedOutput = sim(bestNet, optimizedInput');

 target=0.357;
 fitness1 = sum((predictedOutput(1) - target).^2);
 fitness2 = sum((predictedOutput(2) - target).^2);
 fitness3 = sum((predictedOutput(3) - target).^2);
 fitness4 = sum((predictedOutput(4) - target).^2);
 fitness5 = sum((predictedOutput(5) - target).^2);
 fitness6 = sum((predictedOutput(6) - target).^2);
 fitness7 = sum((predictedOutput(7) - target).^2);

 fitness_dim = sqrt(fitness1^2 + fitness2^2 + fitness3^2 +
 fitness4^2 + fitness5^2 + fitness6^2 + fitness7^2);

end
```

FITNESS FUNCTION CODE USING PI EQUATION

```
function fitness = fitnessFunction(optimizedInput)

  load my_workspace_15022024_212634.mat;
  predictedOutput = sim(bestNet, optimizedInput');

  target=0.357;
  fitness1 = sum((predictedOutput(1) - target).^2);
  fitness2 = sum((predictedOutput(2) - target).^2);
  fitness3 = sum((predictedOutput(3) - target).^2);
  fitness4 = sum((predictedOutput(4) - target).^2);
  fitness5 = sum((predictedOutput(5) - target).^2);
  fitness6 = sum((predictedOutput(6) - target).^2);
  fitness7 = sum((predictedOutput(7) - target).^2);
  fitness8 = predictedOutput(8);

  fitness_dim = sqrt(fitness1^2 + fitness2^2 + fitness3^2
  + fitness4^2 + fitness5^2 + fitness6^2 + fitness7^2);

  fitness=fitness_dim/fitness8;

end
```

PATTERN SEARCH ALGORITHM CODE

```
function [optimizedInput, x, fval, output, optimalFitness]
= opt_pattersearch(y, lb, ub)

 x0 = [0.2,0.2,0.2,0.2,0.2,0.2,0.2];

 options = optimoptions('patternsearch','Algorithm',
 'nups-gps', 'Cache', 'on', 'InitialMeshSize', 10, 'Func-
 tionTolerance', 1e-10, 'ConstraintTolerance', 1e-10,
 'MaxFunctionEvaluations', 14000, 'MaxIterations', 7000,
 'Display', 'iter', 'PlotFcns', ["psplotbestf", "psplot-
 funcount","psplotbestx","psplotmaxconstr","psplot-
 meshsize"]);

 [optimizedInput, x, fval, output] = patternsearch(@fit-
 nessFunction,x0,[],[],[],[],lb,ub,[],options);

 optimalFitness = fitnessFunction(optimizedInput);

 fprintf('Results:\n');
 fprintf('Optimized Input: %s\n', mat2str(optimizedIn-
 put));

end
```

List of publications

V. Vendittoli, W. Polini, and M. S. J. Walter, "Geometrical deviations of green parts due to additive manufacturing: a synthetic geometrical performance index," *Procedia CIRP*, vol. 114, pp. 159–164, Jan. 2022, doi: 10.1016/j.procir.2022.10.036.

V. Vendittoli, W. Polini, and M. S. J. Walter, "An overall performance index to quantify dimensional accuracy and mechanical strength of parts manufactured through VAT photopolymerization in biodegradable and non-biodegradable resin," *The International Journal of Advanced Manufacturing Technology*, vol. 128, no. 11–12, pp. 5491–5502, Sep. 2023, doi: 10.1007/s00170-023-12285-1.

V. Vendittoli, A. Gazzerro, W. Polini, and L. Sorrentino, "Dimensional and geometric deviations of parts in PA12 manufactured by selective laser sintering: numerical and experimental analyses," *Materials Research Proceedings*, pp. 198–205, Sep. 2023, doi: 10.21741/9781644902714-24.

V. Vendittoli, W. Polini, M. S. J. Walter, and S. Geißelsöder, "Using Bayesian regularized artificial neural networks to predict the tensile strength of additively manufactured polylactic acid parts," *Applied Sciences*, vol. 14, no. 8, p. 3184, Apr. 2024, doi: 10.3390/app14083184.

V. Vendittoli, W. Polini, M. S. J. Walter, and J. P. C. Stacheder, "A novel approach on artificial aging of nylon 12 powder for laser powder bed fusion," *Rapid Prototyping Journal*, vol. 30, no. 9, pp. 1836–1845, Aug. 2024, doi: 10.1108/rpj-12-2023-0430.

V. Vendittoli, W. Polini, M. S. J. Walter, and S. Geißelsöder, "Introducing Artificial Neural Networks to predict the dimensional and micro-geometrical deviations of additively manufactured parts," *Procedia CIRP*, vol. 129, pp. 181–186, Jan. 2024, doi: 10.1016/j.procir.2024.10.032.

V. Vendittoli, W. Polini, and M. S. J. Walter, "Two performance indices of parts in Polylactic Acid manufactured through a Material extrusion process: analysis of their dependence on process parameters," *The International Journal of Advanced Manufacturing Technology*, vol. 134, no. 9-10, pp. 4689–4699, Oct. 2024, doi: 10.1007/s00170-024-14380-3.

V. Vendittoli, W. Polini, and M. S. J. Walter, "Artificial intelligence Tool to optimize geometrical and mechanical performances of parts manufactured through Additive Manufacturing processes," Submitted, 2024.

V. Vendittoli, W. Polini, and M. S. J. Walter, "Multi-Response Optimization of the dimensional and mechanical properties of 3D-printed Polylactide Acid part by Response Surface Methodology," Submitted, 2024.

V. Vendittoli, M. C. Mascolo, W. Polini, L. Sorrentino, A. Sover, and M. S. J. Walter, "Overview of structural, mechanical and geometrical characteristics of parts in Polyamide 12 manufactured with Laser Powder Bed Fusion: outcome and future development," Submitted, 2024.

V. Vendittoli, M. C. Mascolo, W. Polini, L. Sorrentino, A. Sover, and M. S. J. Walter, "Predictive Modeling of Mechanical Properties from Degraded Polyamide 12 Powder in Laser Powder Bed Fusion," *Journal of Material Engineering and Performance*, Nov. 2024, doi: 10.1007/s11665-024-10407-8.

V. Vendittoli, W. Polini, and M. S. J. Walter, "A Synthetic Geometric Index of parts manufactured through VAT photopolymerization," Submitted, 2024.

V. Vendittoli, W. Polini, and M. S. J. Walter, "A numerical approach to set up and validate a database to foresee dimensional deviations of ABS parts printed by a material extrusion process," Submitted, 2024.

About the author



Valentina Vendittoli was born on August 20, 1996, in Modena, in Bologna, Italy. In 2015, she began her academic career at the University of Cassino and Southern Lazio, where she obtained a Bachelor of Science in Industrial Engineering in 2019. Subsequently, she proceeded to pursue a master's degree in Management Engineering, graduating cum laude in 2021. She is pursuing a doctorate in "Methods, Models and Technologies for Engineering" at the University of Cassino and Southern Lazio. Her doctoral research is focused on applying AI-based optimization and material ageing studies to enhance the geometric and mechanical performance of components produced through additive manufacturing processes. During her PhD journey, she had the opportunity to spend periods at the University of Applied Sciences in Ansbach, Germany, contributing to international research projects and presenting scientific papers at specialized conferences.

Cover designed by Fabiana Spiridigliozzi

Instagram: _fab3._

E-mail: spiridigliozzi30@gmail.com